ABSTRACT

OH, CHULWOO. Broadband Polarization Gratings for Efficient Liquid Crystal Display, Beam Steering, Spectropolarimetry, and Fresnel Zone Plate. (Under the direction of Dr. Michael Escuti).

Efficient control of light polarization is essential in any optical systems where polarized light is used or polarization information is of interest. In addition to intensity and wavelength, polarization of light gives a very useful/powerful tool to control light itself and observe many interesting optical phenomena in nature and applications. Most available light sources, however, produce unpolarized or weakly polarized light except some of fancy lasers. Therefore, efficient polarization control/generation is important to improve/advance existing or emerging technologies utilizing polarized light. It is also true that polarization can be used to control another properties of light (i.e., intensity, direction).

We have introduced and demonstrated achromatic polarization gratings (PGs) as broadband polarizing beam splitters performing $\sim$ 100% theoretical efficiency over a wide spectral range. The novel design of achromatic PGs and their effective fabrication method will be presented. Experimental demonstration will show that practically 100% efficient diffraction is achieved by achromatic PGs embodied as thin liquid crystal (LC) layers patterned by holographic photoalignment techniques.

Non-ideal diffraction behaviors of the PGs also have been investigated beyond the paraxial limitations via numerical analysis based on the finite-difference time-domain method. We, first, study the effect of the grating regime for this special type of anisotropic diffraction gratings with the minimum assumptions. Optical properties of the PGs at oblique incidence angles and in a finite pixel are numerically predicted and confirmed by experiments. Design and fabrication of small-period PGs are discussed to show how to achieve high diffraction efficiency and large diffraction angles at the same time.

Three key innovative technologies utilizing the unique diffraction properties of the PGs have been introduced and experimentally demonstrated. The first application for light-efficient LC displays is the polymer-PG display, which allows an immediate brightness improvement (up to a factor of two) of conventional LC displays by replacing absorbing polarizers with achromatic PGs as thin, transmissive polymer films. We demonstrate the first proof-of-concept prototype projector based on the polymer-PG display and we also

discuss optical design considerations and challenges toward a viable solution for our ultra-bright pico-projector applications of the polymer-PG display. Second, two novel beam steering concepts based on the PG diffraction have been proposed. The polarization-sensitive diffraction of the PGs provides very attractive beam steering operations with ultra-high efficiency over wide steering angles by all-thin-plate electro-optical systems. We developed a non-mechanical, wide-angle beam steering system using stacked PGs and LC waveplates, and we also demonstrated a continuous beam steering using two rotating PGs, named the Risley grating as a thin-plate version of the Risley prism. The third PG application is in imaging and non-imaging spectropolarimetry. We have shown a snapshot, hyperspectral, full-Stokes polarimeter using inline PGs and quarter-waveplates. The use of PGs as a new polarimetric element for astronomical instruments in the mid-wave IR wavelengths also has been proposed to overcome current limitations of existing IR polarimeters.

In the last part of this Dissertation, we introduce a polarization-type Fresnel zone plates (P-FZPs), comprising of spatially distributed linear birefringence or concentric PG (CPG) patterns. Effective fabrication methods of P-FZPs have been developed using polarization holography based on the Michelson interferometer and photoalignment of LC materials. We demonstrated high-quality P-FZPs, which exhibit ideal Fresnel-type lens effects, formed as both LC polymer films and electro-optical LC devices. We also discuss the polarization-selective lens properties of the P-FZPs as well as their electro-optical switching.

In summary, we have explored the fundamental diffraction behavior of the polarization gratings and their applications in advanced optics and photonics. The achromatic designs of the PGs allow their broadband diffraction operation over a wide range of spectrum, which increases the applicability of the PGs with a great extent. Three novel technologies that directly benefit from the distinct diffraction properties of the PGs have been developed. In addition, a new diffractive lens element operating solely on light polarization has been introduced and experimentally demonstrated. We conclude this Dissertation with our suggestions of a number of potential innovations and advances in technologies that can be enabled by polarization gratings and related technologies.

Broadband Polarization Gratings for Efficient Liquid Crystal Display, Beam Steering, Spectropolarimetry, and Fresnel Zone Plate

by
Chulwoo Oh

A dissertation submitted to the Graduate Faculty of
North Carolina State University
in partial fullfillment of the
requirements for the Degree of
Doctor of Philosophy

Electrical Engineering

Raleigh, North Carolina

2009

APPROVED BY:

Dr. Jan Genzer	Dr. Philip J. Bos
Dr. David Schurig	Dr. David E. Aspnes
Dr. Michael J. Escuti Chair of Advisory Committee	

DEDICATION

To my beloved wife, Suna.

BIOGRAPHY

The author was born to Dae-Kyun Oh and Gui-Nam Lee in 1976 in Seoul, Korea and has two brothers, Won-Seok and Jun-Seok. He married Suna Woo in 2005. In 2003, he graduated from Yonsei University in Seoul, Korea. His undergraduate major was Electrical and Electronics Engineering. In 2006, he earned his master degree in electrical engineering with the research focus in nanoelectronics and photonics at North Carolina State University in Raleigh, NC. He continued his graduate research at the same institution with pursuing his Ph. D. degree. After his degree, he plans to join a bio-imaging research group at University of California, Los Angeles as a postdoctoral scholar.

ACKNOWLEDGMENTS

I wish to express my thanks to my advisor Prof. Michael Escuti for his guidance during my early scientific career. With his complete support, it was possible to work in the encouraging and enjoyable atmosphere. I also would like to thank my colleagues at OLEG, Ravi Komanduri, Brandon Conover, Elena Nicolescu, and Jihwan Kim, for their support and invaluable time to share with them. It was amazing experience for me to work as an OLEGer.

To my committee, Prof. David Aspnes, Jan Genzer, David Schurig, and Philip Bos, I am greatly indebted for their careful review, constructive comments, and thoughtful advices on my career. I specially wish to thank Prof. Philip Bos from Kent State University for allowing his time to serve in the committee and sharing discussions related to this Dissertation research and beyond.

Finally, I would like to thank to my family for their support and to my wife Suna for her understanding and patience. Above all, thank God for his love.

TABLE OF CONTENTS

LIST OF TABLES ..... **viii**

LIST OF FIGURES ..... **ix**

1 Introduction **1**

2 Light Propagation in Anisotropic and Periodic Media **7**
2.1 Electromagnetic Properties of Lightwaves 8
2.1.1 Maxwell's equations and light propagation 8
2.1.2 Polarization of light 10
2.1.3 Jones vector, Stokes parameters, and Poincaré sphere 11
2.2 Light Propagation in Anisotropic and Periodic Media 14
2.2.1 Light propagation in anisotropic media 14
2.2.2 Light propagation in periodic media 18
2.3 Liquid crystals: soft-condensed matters that control light 22
2.3.1 Properties of nematic liquid crystal materials 22
2.3.2 Rubbing techniques of liquid crystal alignment 24
2.3.3 Photoalignment of liquid crystal materials 25
2.3.4 Liquid crystal applications in displays and photonics 30
2.4 Polarization Gratings 35
2.4.1 Essential diffraction properties of polarization gratings 37
2.4.2 Historical record in literature 39
2.4.3 Holographic insights of polarization gratings 41
2.4.4 Polarization holography & LC photoalignment: an effective fabrication method for creating PGs 43

3 Achromatic Polarization Gratings as Broadband Beam Splitters **47**
3.1 Study on the diffraction limits of polarization gratings 48
3.1.1 Numerical analysis of polarization gratings using the FDTD method 48
3.1.2 Beyond the paraxial approximation 51
3.2 Achromatic diffraction by self-compensated twisted polarization gratings .. 58
3.2.1 Achromatic design of polarization gratings 60
3.2.2 Fabrication of achromatic polarization gratings 62
3.2.3 Electrically switchable achromatic liquid crystal polarization gratings on reflective substrates 64
3.3 Super-achromatic diffraction by three-layered polarization gratings with a phase shift 70
3.3.1 Super-achromatic diffraction by three-layered PGs 71
3.3.2 Fabrication of super-achromatic polarization gratings 72
3.4 Fabrication of small-period PGs using high Δn_l materials 75

4 Polymer-PG Displays: a viable solution for polarization-independent displays 79
4.1 Polymer-PG Liquid Crystal Displays 80
4.1.1 Polarization-independent light modulation by the polymer-PG LCD 80
4.1.2 Demonstration of the polymer-PG display with a vertically aligned (VA) LC cell 82
4.1.3 Prototype projector based on the polymer-PG display with a commercial LC microdisplay 84
4.2 Optical Design Consideration: System Acceptance Angle and Extinction Ratio 88
4.2.1 System acceptance angle 88
4.2.2 Extinction ratio enhancement 91

5 Novel Beam Steering Systems using Polarization Gratings 93
5.1 Non-mechanical, wide-angle beam steering using stacked polarization gratings and LC waveplates 94
5.1.1 Basic beam steering operation of polarization gratings 95
5.1.2 Diffraction characterization of single PGs 96
5.1.3 2-stage beam steering system with ±15° steering angles 98
5.2 High-Throughput, Continuous, Beam Steering Using Rotating Polarization Gratings 100
5.2.1 Basic steering operation of the Risley grating 102
5.3 Demonstration of the Risley grating with ±31° field of regard 104

6 Advanced Hyperspectral Polarimeters and Imaging Spectropolarimeters at Visible and Midwave-Infrared Wavelengths Enabled by Polarization Gratings 107
6.1 Snapshot full-Stokes hyperspectral polarimetry based on inline polarization gratings 108
6.1.1 Measurement of the Stokes parameter using PG elements: Jones matrix reasoning 109
6.1.2 Experimental demonstration of simplified spectropolarimeter based on PGs 112
6.2 Polarization Gratings: A New Polarimetric Component for Astronomical Instruments 118
6.2.1 Primary material properties of liquid crystal polymers in MIR . . . 119
6.2.2 Behavior of polarization gratings with illumination in MIR 121
6.2.3 Optimum broadband design using achromatic PGs 123

7 Concentric Polarization Gratings as Vectorial Fresnel Zone Plates: a new opportunity for beam shaping 125
7.1 Fresnel lenses and zone plates as a thin lens 127
7.2 Polarization-type Fresnel zone plates based on a continuous, concentric polarization grating pattern 130
7.3 Fabrication of concentric polarization gratings as a polarization hologram . 131

8 Discussion and Conclusions 136
8.1 Summary and Conclusions 136
8.2 Suggestions for future work 139
8.2.1 Challenges and advances in PG fabrication 139
8.2.2 Polymer-PG display: toward ultra-bright pico-projectors 142
8.2.3 Uni-directional pointing of broadband beam using polarization gratings 143
8.2.4 Polarization holographic elements for vector beam shaping 144

Bibliography 146

Appendices 162

LIST OF TABLES

Table 2.1 Material parameters for two primary types of the polarization gratings 36

Table 5.1 Diffraction characterization of two different types of PGs at 1550nm. 97

LIST OF FIGURES

Figure 1.1 Lightwave propagation and a polarizing beam splitter 2

Figure 2.1 Light polarization: electromagnetic nature of light 10

Figure 2.2 Poincaré sphere for graphical description of light polarization 13

Figure 2.3 Light propagation in a waveplate 15

Figure 2.4 Light propagation in an optically active medium 17

Figure 2.5 Refractive index profiles of conventional phase gratings 18

Figure 2.6 Grating regimes: thick or thin gratings 20

Figure 2.7 Form-birefringence of a subwavelength grating 21

Figure 2.8 Properties of nematic liquid crystal materials 22

Figure 2.9 Polymerizable liquid crystal (reactive mesogen) materials 24

Figure 2.10 Rubbing technologies for LC alignment 25

Figure 2.11 Photoalignment of LCs by azo-containing polymers 26

Figure 2.12 Linear photopolymerization (LPP) photoalignment 27

Figure 2.13 Anchoring energy of the photoalignment layer 29

Figure 2.14 Liquid crystal displays 30

Figure 2.15 LC-based spatial light modulator 32

Figure 2.16 Liquid crystal diffraction gratings 33

Figure 2.17 Polarization-independent light modulation by LC gratings 33

Figure 2.18 Liquid crystal grating with the polymer walls 34

Figure 2.19 Two primary types of the polarization gratings 35

Figure 2.20 Diffraction properties of the circular PG 38

Figure 2.21 Polarization holograms with two orthogonally polarized beams 42

Figure 2.22 Polarization holograms represented on the Poincaré sphere 43

Figure 2.23 LC alignment via linear photopolymerizable polymers (LPP) 44

Figure 2.24 Holography setup for recording polarization gratings 45

Figure 2.25 Fabrication processes of polarization gratings 46

Figure 3.1 FDTD modeling of the polarization gratings 49

Figure 3.2 Basic diffraction properties of a circular PG 50

Figure 3.3 FDTD near-field maps of a polarization grating 51

Figure 3.4 Effect of the grating regime of a circular PG 52

Figure 3.5 Effect of high Δn_l on the maximum efficiency of a circular PG 53

Figure 3.6 Angular response of the PG diffraction 54

Figure 3.7 Diffraction behavior of finite PGs 55

Figure 3.8 Effect of the pixel size of finite PGs 56

Figure 3.9 Diffraction spectra of the circular PG 58

Figure 3.10 Design of the achromatic polarization grating 60

Figure 3.11 Diffraction spectra of the achromatic PG 61

Figure 3.12 Diffraction of white LED light from an achromatic PG 62

Figure 3.13 Measured diffraction efficiency of the achromatic PG 63

Figure 3.14 Design of the reflective achromatic LCPGs 65

Figure 3.15 Fabrication of reflective achromatic LCPGs 66

Figure 3.16 Electro-optical properties of the reflective achromatic PG 67

Figure 3.17 Hysteresis of the voltage response of the reflective achromatic LCPG 68

Figure 3.18 Design of the super-achromatic polarization grating 70

Figure 3.19 Diffraction spectra of the super-achromatic PG 71

Figure 3.20 Fabrication of the super-achromatic PGs 73
Figure 3.21 Measured diffraction efficiency of the super-achromatic PGs 74
Figure 3.22 The 0-order spectra of small-period PGs with different Δn_l 76
Figure 3.23 The first maximum of the first-order efficiency of small-period PGs 77

Figure 4.1 Operation concept of the polymer-PG display 80
Figure 4.2 Transmittance and extinction ratio of parallel and antiparallel PGs 81
Figure 4.3 Polarization-independent light modulation by the polymer-PG LCD 82
Figure 4.4 Polymer-PG display with a VA-mode LCD 83
Figure 4.5 Prototype projector based on the polymer-PG display 85
Figure 4.6 Offset compensator for the polymer-PG display 86
Figure 4.7 Acceptance angle requirements for high-contrast polymer-PG displays 88
Figure 4.8 Effect of polarization leakages on the extinction ratio 89
Figure 4.9 Design consideration of projection optics: acceptance angle and $F/\#$ 90
Figure 4.10 Extinction ratio enhancement by a retardation film 91

Figure 5.1 Concept of a non-mechanical, wide-angle beam steering system 94
Figure 5.2 Non-mechanical beam steering based on stacked PGs and LC waveplates . . 96
Figure 5.3 Experimental setup for the PG diffraction characterization 97
Figure 5.4 2-stage beam steering system using LCPGs with $\pm 15^\circ$ steering angles 99
Figure 5.5 Continuous beam steering using two rotating polarization gratings 101
Figure 5.6 Direction cosine representations of the PG diffraction 103
Figure 5.7 Demonstration of the Risley grating beam steering 104
Figure 5.8 Measured transmittance of the Risley grating 106

Figure 6.1 Hyperspectral polarimetry based on polarization gratings 108

Figure 6.2 Proposed implementation of the full-Stokes, hyper-spectral polarimeter 110
Figure 6.3 Diffraction spectra of three PGs 112
Figure 6.4 Polarization sensitivity of the PG diffraction 113
Figure 6.5 Experimental setup for the PG-based spectropolarimeter 114
Figure 6.6 Experimental results of the PG-based spectropolarimeter 115
Figure 6.7 Concepts of the PG-based imaging spectropolarimeter (PGIS) 116
Figure 6.8 The atmospheric transmission expected for SOFIA 118
Figure 6.9 Material properties of LC polymer films at mid-wave IR wavelengths 120
Figure 6.10 Diffraction properties of a polymer PG sample 121
Figure 6.11 Measured transmittance and diffraction efficiency of polymer PG samples . 122
Figure 6.12 Design of broadband PGs for the MIR polarimeter 123

Figure 7.1 Fresnel-type thin-plate lenses 127
Figure 7.2 Focusing of a Fresnel zone plate 129
Figure 7.3 Concentric polarization gratings as polarization-type FZPs 131
Figure 7.4 Polarization holography setup based on the Michelson interferometer 132
Figure 7.5 Polarizing microscope images of a P-FZP sample 133
Figure 7.6 Polarization-selective lens properties of the P-FZP 134
Figure 7.7 Electrical switching of the P-FZP as a switchable LC device 135

Figure 8.1 Crystallization of reactive mesogen molecules with a high Δn_l 140
Figure 8.2 Fabrication of PGs via the proximity lithography 141
Figure 8.3 Fabrication of a polymer PG on a flexible substrate 142
Figure 8.4 Efficient uni-directional pointing using polarization gratings 144
Figure 8.5 Polarization holographic recording of a fork-shaped grating 145

Figure A-1 Diffraction behavior of the linear PG with the same Δn_l and Δn_c 163

Figure A-2 Diffraction behavior of the linear PG with different Δn_l and Δn_c 164

Chapter 1

Introduction

The electromagnetic nature of light was significantly understood by James Clark Maxwell along with his beautifully simple but rigorous mathematical explanations [1]. In many classical optics (i.e., ray optics and wave theory), light is often treated as a propagating ray/wave without much details of its vectorial properties as an electromagnetic radiation. Although these scalar theories well predict some optical phenomena such as light propagation, interference, and diffraction [2], they only provide approximations of Maxwell's theory under certain conditions (in passive, isotropic media). An electromagnetic wave with full vector description, therefore, has to be considered for accurate solutions wherever the non-scalar nature of light (i.e., non-trivial polarization) takes its place.

Polarization [3] is one particular vectorial property of light, which leads to very interesting optical phenomena such as birefringence, dichroism, Faraday rotation, and Thomson scattering. Human eyes and most other light sensors (photodiodes, charge-coupled devices or CCDs), however, cannot directly detect the polarization properties of light but only count the number of photons. In nature, the effect of polarization is perceived in different forms such as changes in intensity or colors by reflection (e.g., Plusiotis, cuttlefish) or scattering (e.g., atmosphere, interstella dust). To observe or generate polarized light, various techniques have been introduced and developed as polarization science and engineering.

The most common polarizing elements are including absorbing polarizers (polaroid films or wire-grids) and polarizing beam splitters. Excellent polarization contrast and low price make absorbing polarizers very attractive as a practical solution for produc-

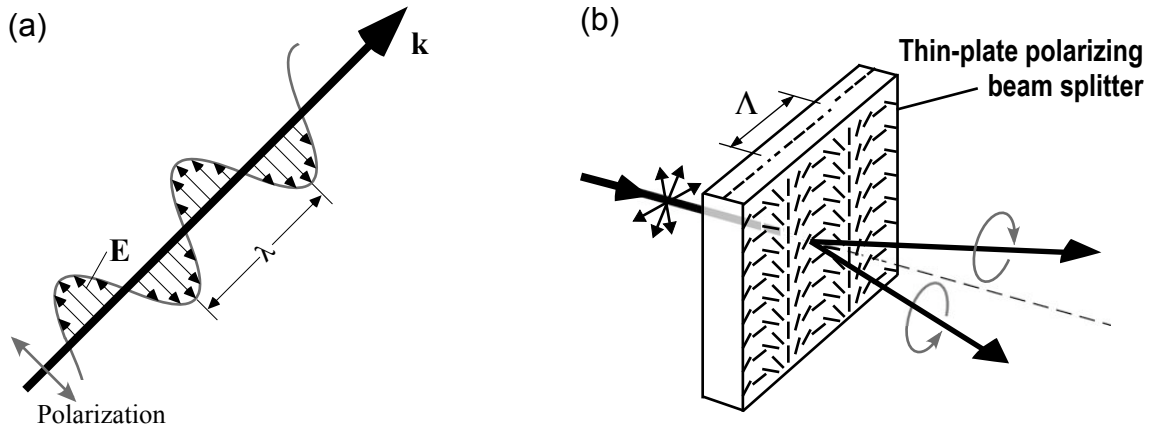

Figure 1.1: Electromagnetic nature of lightwave and a thin-plate polarizing beam splitter: (a) a schematic view of light propagation as the electromagnetic radiation; (b) a thin-plate polarizing beam splitter that generates orthogonal polarization states (i.e., left- and right-handed circular) with a separation angle in the forward direction.

ing/filtering polarized light. The use of polarizers is often subject to substantial losses by absorption ($> 50\%$ with unpolarized light). Polarizing beam splitters operate by separating the beam into two different directions with different polarization states. This beam-splitter type polarizer is typically useful to divide or combine beams. Relatively large volumes and expensive multi-coating process of polarizing beam splitters continue to be major limitations along with poor angular sensitivity and unwanted polarization sensitivity of their properties. Both traditional polarizing elements have limitations of operating wavelengths (not always available for certain wavelength ranges). Therefore, it is natural to consider a thin-film polarizing beam splitter that perform excellent optical properties (high polarization contrast, high throughput, wide angle performance, well-defined beam directions) over a broad range of spectrum.

In recent years, polarization gratings (PGs) [4, 5, 6, 7] have been introduced as efficient polarizing beam splitters and optical switches [8, 9, 10, 11]. The most-studied PGs have its anisotropy profile consisting of a patterned linear birefringence that is both periodic and continuous. Unlike conventional diffraction gratings, this anisotropic grating can manifest a combination of the most advantageous properties of both thick-and thin-gratings (and beyond): 100% diffraction efficiency, strong polarization sensitivity of the ± 1-order diffraction, polarization-independence of the 0-order diffraction, and comparatively

wide bandwidth. These exceptional properties of the PGs offer unique opportunities to improve current technologies that utilize polarization of light.

Until now, the most popular approach to create the PG is using polarization holography with organic materials containing azobenzene moieties [12, 13], which can have modest diffraction efficiencies (80%) and a wide range of grating periods[14, 15]. However, it is limited by absorption at visible wavelengths and irreversible degradation when illuminated or when heated above modest temperatures. An alternative approach employs patterned surfaces which then transfer their anisotropy to a liquid crystal (LC) layer via a photoalignment material [16, 17]. Using this method, we successfully demonstrated defect-free PGs performing their ideal properties [18, 19]. Still, the alignment of liquid crystals remains one of the main fabrication issues and the poor alignment of the LCs causes significant problems of incoherent scattering, especially when the grating period is relatively small. Substantial experimental studies are considered to optimize the fabrication process for small-period PGs by a careful choice of materials.

The ideal diffraction behavior of the PG was significantly investigated by using the Jones calculus in the paraxial domain [6, 19], where light is treated as a ray making a small angle to the optic axis of the system. The theoretical prediction of PG diffraction properties is no longer valid beyond paraxial approximations (i.e., small grating periods or highly oblique incidence). No work adequately deals with the fundamental question of delineating the thin/thick grating regimes in anisotropic gratings. It is, therefore, our desire to investigate PG behavior as the grating period becomes comparable to the wavelength. The study will provide better understanding where the fundamental limits arise and ultimately we seek more practical guidelines for material and processing optimization.

The operation bandwidth of all diffractive elements has a certain limitation [20]. While a polarization grating can perform with extremely high efficiency, its bandwidth for high efficiency is limited by the chromatic dispersion of retardation that light at different wavelengths experiences while traveling through the medium. Several broadband designs of diffraction gratings were proposed to operate with wide-band illumination (i.e., white light) [21]. However, every efforts so far have been plagued by fabrication difficulties or low efficiencies. We designed and demonstrated achromatic polarization gratings with high efficiency over a broad spectrum and at wide angles of incidence. To achieve this achromaticity of grating diffraction, we utilize self-compensation of the retardation dispersions

due to two different polarization mechanisms (linear birefringence and optical activity). This unique achromatic diffraction will lead to more diverse utilities of the PG in many photonics applications.

Our aim in this dissertation is to investigate and apply the polarization grating within many areas of photonics and optoelectronic devices. To this end, we first study diffraction behavior of the PG beyond simplistic, limiting assumptions (i.e., paraxial approximation) via numerical modeling of the PGs. We will prove the broadband design of the PG and experimentally demonstrate the achromatic PGs using liquid crystal materials. This dissertation also focuses on the development of three pioneering technologies based on the PG diffraction: (i) Polymer-PG displays; (ii) novel beam steering systems; (iii) advanced spectro-polarimeters. Finally, we expand our exploitation of polarization-based diffractive elements to shape vectorial beam properties. As one of the examples, the ideal Fresnel lens effect by concentric polarization gratings is explored.

In Chapter 2, we start with Maxwell's equations and then introduce the fundamentals of electromagnetic natures of light. Brief descriptions of the polarization of light and different vector representations for polarized light follow. We also discuss light propagation in anisotropic media with optical anisotropy and periodic structures including conventional phase diffraction gratings. A brief summary of material properties of liquid crystals (LCs) and related technologies in optics and photonics is presented. A technical survey of LC diffractive elements for various applications is also given. Chapter 2 is summarized with an introduction of the polarization grating as highly efficient polarizing beam splitters. The theoretical foundations to understand the PG behavior and the fabrication techniques using polarization holography are included.

Chapter 3 presents our extensive studies on the PG diffraction and the design and fabrication of the achromatic PGs. In the beginning of the Chapter, we examine the properties of the PG and develop a proper evaluation tool to determine the grating regime which the PG falls into. Design considerations for high efficiency with small grating periods (at large diffraction angles) are presented. The broadband design of the PGs have been developed and the properties of the achromatic PG are investigated in both theories and experiments. The Chapter includes experimental results of the achromatic PGs embodied in forms of liquid crystal polymer films (in transmissive mode) and switchable cells (in reflective mode).

In the following three Chapters, we discuss our development of technologies based on the PG diffraction. Chapter 4 introduces the polymer-PG display as a viable solution for highly efficient, polarizer-free LCDs. In this Chapter, we show how to achieve polarization-independent modulation using achromatic PGs and conventional LCDs. We also present preliminary results of a prototype of the polymer-PG projection display using a commercial microdisplay and replacing polarizer films with achromatic PGs. Design considerations of the achromatic PGs and techniques for the extinction-ratio enhancement are also discussed. Novel beam steering systems based on the PG diffraction are presented in Chapter 5. We first demonstrated non-mechanical, wide-angle beam steering using stacked LC polarization gratings and waveplates. Several different system designs are considered and the results of a prototype beam steering device are presented. The second beam steering device is the Risley grating, which is a thin-plate version of the Risley prism. This compact beam steering device utilizes a fair of identical PGs that are individually rotated to scan continuous angles within the field of regard. In Chapter 6, we introduce simplified spectropolarimetry using the polarization sensitive diffraction of the PGs and its experimental demonstration at infrared (IR) wavelengths. We also discuss the use of the PGs as polarizing elements for mid-IR spectropolarimeters, especially for astronomical detection. The preliminary experimental results include material feasibility tests of liquid crystals and the PG diffraction properties in mid-IR.

In Chapter 7, the concept and properties of concentric polarization gratings (CPGs) are examined. The CPG is a vectorial version of the Fresnel zone plate that spatially modulate the polarization state of light leading to lens effects. Unlike conventional Fresnel zone plates operating on phase or intensity modulation, the CPGs can exhibit a single diffraction order with $\sin 100\%$ efficiency in addition to polarization selective lens properties. When a CPG is formed in a liquid crystal cell, an electrically switchable lens can be implemented. In this Chapter, we discuss potential advantages of the CPGs over other Fresnel zone plates (and Fresnel lenses) and also classical volume lenses. We also show preliminary experimental results of CPGs using polarization holography and liquid crystal materials and we summarize the Chapter with discussions on potential applications of the CPGs as lens elements or vector (polarization) beam shapers and other possible variations of spatial polarization modulation for generating/manupulating vectorial beam properties.

Chapter 8 summarizes the results of this dissertation and suggests topics for further

study. Also, practical fabrication techniques for mass production of the PGs are discussed. The Appendix gives a technical and theoretical background about the Jones calculus for the PG diffraction and fabrication details of the polarization holography.

Chapter 2

Light Propagation in Anisotropic and Periodic Media

2.1 Electromagnetic Properties of Lightwaves

The electromagnetic origin of light was significantly understood for the first time by James C. Maxwell [1]. Since his beautiful description of the electromagnetic dynamics, the *concealed* motion of light is captured by simple mathematical expressions now termed "Maxwell's equations." This Section begins with Maxwell's equations and then introduces electromagnetic properties of lightwaves including polarization of light.

2.1.1 Maxwell's equations and light propagation

The electromagnetic field can be defined by two vector quantities: the electric and magnetic fields. Maxwell's equations describe the behavior of these two vector fields in relation to each other and the position and motion of charged particles. In differential form, Maxwell's equations are given by [22]

$$\nabla \times \mathbf{E}(\mathbf{r},t) = -\frac{\partial \mathbf{B}(\mathbf{r},t)}{\partial t} \qquad (Faraday's\ law) \tag{2.1a}$$

$$\nabla \times \mathbf{H}(\mathbf{r},t) = \mathbf{J}(\mathbf{r},t) + \frac{\partial \mathbf{D}(\mathbf{r},t)}{\partial t} \qquad (Ampere's\ law) \tag{2.1b}$$

$$\nabla \cdot \mathbf{D}(\mathbf{r},t) = \rho(\mathbf{r},t) \qquad (Gauss's\ law) \tag{2.1c}$$

$$\nabla \cdot \mathbf{B}(\mathbf{r},t) = 0 \qquad (Gauss's\ law) \tag{2.1d}$$

where $\mathbf{r}$ is the position vector and t is time. The field variables are defined as:

$\mathbf{E}$: *electric field* (V/m) — $\mathbf{H}$: *magnetic field* (A/m)

$\mathbf{D}$: *electric displacement* (W/m^2) — $\mathbf{B}$: *magnetic flux density* (C/m^2)

$\mathbf{J}$: *electric current density* (A/m^2) — ρ : *electric charge density* (C/m^3)

These variables (except ρ, a scalar) are vectors and may have complex amplitudes. ρ is a scalar variable function of space and time.

In order to solve Eq. 2.1, another set of relationships between $\mathbf{E}$ ($\mathbf{H}$) and $\mathbf{D}$ ($\mathbf{B}$) must be known. These are called constitutive relation [23]. These conditions are established by the physical properties of media; the permittivity ε and permeability μ. In a vacuum, these relations are:

$$\mathbf{D}(\mathbf{r},t) = \varepsilon_0 \mathbf{E}(\mathbf{r},t) \tag{2.2a}$$

$$\mathbf{B}(\mathbf{r},t) = \mu_0 \mathbf{H}(\mathbf{r},t) \tag{2.2b}$$

where the subscript '$_0$' refers to the value in a vacuum. $\mathbf{J}$ can generally be found from Ohm's law: $\mathbf{J}(\mathbf{r},t) = \sigma(\mathbf{r})\mathbf{E}(\mathbf{r},t)$, where σ is the conductivity. Since materials of interest in this dissertation are nonmagnetic (at least the effect of magnetic properties is small enough to ignore in normal conditions), μ is assumed as μ_o without any special comment. In linear media, $\varepsilon = \varepsilon(\mathbf{r})$ is a function of position. For anisotropic media, permittivity must be expressed in the form of a tensor $\tilde{\varepsilon}$, which may have different values for each direction of the electromagnetic field vectors. We will discuss more about material properties and light propagation of anisotropic media in Section 2.2.

Maxwell's equations in a source-free space, where $\sigma = \rho = 0$, can be rewritten as

$$\nabla \times \mathbf{E}(\mathbf{r},t) = -\mu \frac{\partial \mathbf{H}(\mathbf{r},t)}{\partial t} \tag{2.3a}$$

$$\nabla \times \mathbf{H}(\mathbf{r},t) = \varepsilon \frac{\partial \mathbf{E}(\mathbf{r},t)}{\partial t} \tag{2.3b}$$

$$\nabla \cdot \mathbf{E}(\mathbf{r},t) = 0 \tag{2.3c}$$

$$\nabla \cdot \mathbf{H}(\mathbf{r},t) = 0 \tag{2.3d}$$

The electromagnetic wave equation can be derived from Eqs. 2.3a and 2.3b. We can eliminate $\mathbf{H}$ by taking the curl of Eq. 2.3a and substituting Eq. 2.3b and we get

$$\nabla \times (\nabla \times \mathbf{E}) = -\mu\varepsilon \frac{\partial^2 \mathbf{E}}{\partial^2 t} \tag{2.4}$$

Applying the vector identity ($\nabla \times \nabla \times = \nabla(\nabla\cdot) - \nabla^2$) and $\nabla \cdot \mathbf{E} = 0$, it is reduced to

$$\nabla^2 \mathbf{E} - \frac{1}{u^2}\frac{\partial^2 \mathbf{E}}{\partial^2 t} = 0 \tag{2.5}$$

where $u = (\mu\varepsilon)^{-1/2}$ is the phase velocity of light propagating in the medium; u in vacuum is given as the special symbol $c = (\mu_0\varepsilon_0)^{-1/2} = 2.998 \times 10^8 (m/s)$, generally called the speed of light. In a dielectric medium, the phase velocity is $u = c/n$ where $n = (\varepsilon/\varepsilon_0)^{1/2}$ is referred to as the index of refraction. Without specifying the precise spatial nature of the wave, the time-harmonic electric field can be rewritten as $\mathbf{E}(\mathbf{r},t) = \mathbf{E}(\mathbf{r})e^{j\omega t}$ where ω is the angular frequency. Substituting it into Eq. 2.5, we have

$$\nabla^2 \mathbf{E}(\mathbf{r}) + k^2 \mathbf{E}(\mathbf{r}) = 0 \tag{2.6}$$

where $k = \omega/u$ is the wavenumber and $\mathbf{k} = \hat{\mathbf{k}}k$ is defined as the wave vector ($\hat{\mathbf{k}}$ is the direction vector of propagation). Eq. 2.6 is known as the Helmholtz equation [2, 24]. A similar expression for $\mathbf{H}$ can be obtained.

2.1.2 Polarization of light

A uniform plane wave is a particular solution of Maxwell's equations with **E** or **H** assuming the same direction, same magnitude, and same phase in infinite planes perpendicular to the direction of propagation ($\hat{\mathbf{k}}$). While its magnitude, sign and direction can vary in time, the electric field resides in what is known as the plane of vibration. Polarization is the property of an electromagnetic wave or light, which shows the pattern of the electric field vibration. In other words, the polarization of a uniform plane wave describes the locus of the **E**'s tip at a given point in space as a function of time [3]. Fig. 2.1(a) shows two special cases of polarization states: linear and circular.

An electric field may have only two other components perpendicular to the propagation direction. For instance, the electric field vector of lightwave propagating along the z-axis ($\hat{\mathbf{k}} \equiv \hat{z}$) can be written as follows

$$\mathbf{E}(z,t) = (\hat{\mathbf{x}}E_x + \hat{\mathbf{y}}E_y)e^{j(\omega t - kz)} \tag{2.7}$$

where E_x and E_y are complex amplitudes of **E** corresponding to $\hat{\mathbf{x}}$ and $\hat{\mathbf{y}}$, respectively. The relative difference in magnitude and phase between x- and y-components determines the polarization state. So it is convenient to rewrite the electric field as

$$\mathbf{E}(z,t) = E_x(\hat{\mathbf{x}} + \hat{\mathbf{y}}Ae^{-j\varphi})e^{j(\omega t - kz)} \tag{2.8}$$

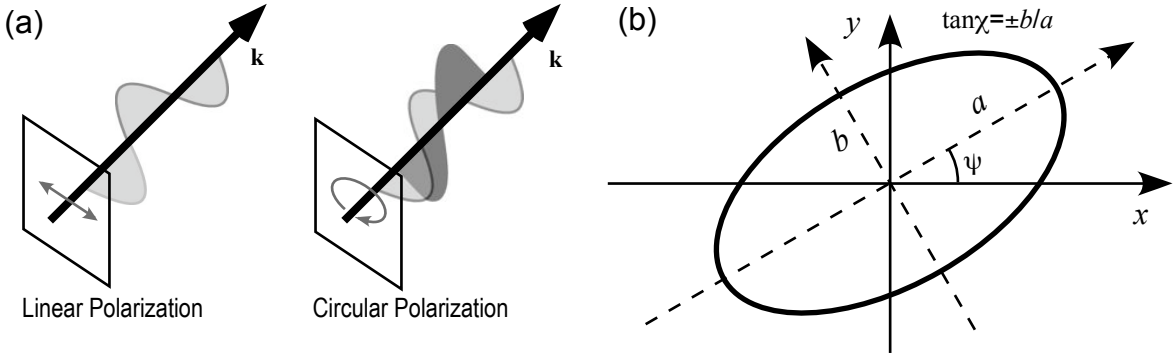

Figure 2.1: Polarization of light: (a) two special polarization states (linear and circular); (b) the polarization ellipse. The polarization state can be described by two characteristic angles of the polarization ellipse: the orientation angle ψ and the ellipticity angle χ as shown in the part (b).

The magnitude A and phase φ allow us to identify three types of polarization states: linear, circular, and elliptical polarization. Note that $A = |E_y/E_x|$ and $\varphi = arg(E_y) - arg(E_x)$.

The polarization property also can be described by two characteristic angles, referred to as the orientation angle ψ and the ellipticity angle χ of the polarization ellipse. ψ is the angle of the major axis of the ellipse from the $+x$-axis and χ is determined by the ratio between the longest diameter 'a' and the shortest diameter 'b' of the polarization ellipse as $\tan\chi = \pm b/a$ (see Fig. 2.1(b)). Both ψ and χ can be written in terms of A and φ by introducing an auxiliary angle $\alpha = \tan^{-1} A$ $(0 \leq \alpha \leq \pi/2)$ as follows

$$\tan 2\psi = \frac{2\tan\alpha}{1-\tan^2\alpha}\cos\varphi \tag{2.9a}$$

$$\sin 2\chi = (\sin 2\alpha)\sin\varphi \tag{2.9b}$$

Readers may refer to Ref. [3] for more detailed descriptions of the polarization ellipse.

For linear polarization states ($\chi = 0$), the locus of $\mathbf{E}$ lies on a line oriented at ψ from the $+x$-axis. One can say that light has a horizontal linear polarization (HLP) when $\psi = n\pi$ and a vertical linear polarization (VLP) when $\psi = (n + \frac{1}{2})\pi$ (n is an integer). For circular polarization states ($\chi = \pm\pi/4$), the polarization ellipse becomes a circle. If $\chi = +\pi/4$, the electric field vector rotates clockwise and it is so called a right-handed circular polarization (RCP). Similarly, if $\chi = -\pi/4$, it is called a left-handed circular polarization (LCP). Elliptical polarization is the most general type of polarization and, if χ and ψ do not satisfy the above conditions, light is elliptically polarized.

2.1.3 Jones vector, Stokes parameters, and Poincaré sphere

The *Jones vector* is one of the simplest ways to describe polarized light [25]. In 1941 [26], R. Clark Jones invented a simple vector representation for the electric field of a planewave as follows

$$\mathbf{E} = \begin{bmatrix} E_{0x}e^{j\varphi_x} \\ E_{0y}e^{j\varphi_y} \end{bmatrix} = E_0 e^{j\varphi_x} \begin{bmatrix} \cos\chi \\ e^{j\varphi}\sin\chi \end{bmatrix} \tag{2.10}$$

where $E_{0x,0y}$ and $\varphi_{x,y}$ are the instantaneous amplitudes and phase factors for the x and y components of $\mathbf{E}$, respectively. E_0 is the total magnitude of the electric field, $E_0^2 = E_{0x}^2 + E_{0y}^2$ and $\tan\chi = E_{0y}/E_{0x}$, and $\varphi = \varphi_y - \varphi_x$ is the relative phase difference. Light propagation in an arbitrary medium can be expressed as a vector product of the Jones vector and a

2×2 matrix that represents the material properties of the medium. This method, often called the *Jones matrix analysis* or *Jones calculus*, is particularly useful to analyze optical properties of planar/stratified media. The extended Jones matrix method also has been developed for oblique incidence analyses [27]. We note that the Jones vector representation can be applied only to perfectly polarized light. We apply the Jones matrix method to derive analytical expressions for ideal diffraction behavior of a special kind of anisotropic diffraction gratings, known as *polarization gratings*.

An important and more general mathematical representation including aspects incoherency for polarized light was developed by G. Stokes in 1852 [28]. He showed that the polarization state of light can be specified by four quantities referred to as the *Stokes parameters* [3], which are given by

$$S_0 = E_x E_x^* + E_y E_y^* + E_{unpol} E_{unpol}^* = E_{0x}^2 + E_{0y}^2 + I_{unpol}^2 \tag{2.11a}$$

$$S_1 = E_x E_x^* - E_y E_y^* = E_{0x}^2 - E_{0y}^2 \tag{2.11b}$$

$$S_2 = E_x E_y^* + E_y E_x^* = 2E_{0x} E_{0y} \cos\varphi \tag{2.11c}$$

$$S_2 = j\left(E_x E_y^* - E_y E_x^*\right) = 2E_{0x} E_{0y} \sin\varphi \tag{2.11d}$$

where S_0 is the total intensity of the light and E_{unpol} is the electric field component corresponding to unpolarized light ($I_{unpol} = |E_{unpol}|^2$). S_1 and S_2 describe the amount of vertical or horizontal polarization and linear $\pm 45^\circ$ polarization, respectively. The last parameter S_3 depicts the amount of either right- or left-handed circular polarization depending on its sign (a positive for RHC and a negative for LHC). For fully-polarized light, the Stokes parameters satisfy $S_0^2 = S_1^2 + S_2^2 + S_3^2$ ($I_{unpol} = 0$), while $S_0^2 \geq S_1^2 + S_2^2 + S_3^2$ for partially polarized light. One can determine the degree of polarization P by use of the Stokes parameters as follows

$$P = \frac{I_{pol}}{I_{tot}} = \frac{I_{tot} - I_{upol}}{I_{tot}} = \frac{\sqrt{S_1^2 + S_2^2 + S_3^2}}{S_0} \tag{2.12}$$

where I_{pol} is the sum of the intensity of the polarization components and I_{tot} is the total intensity. It is often convenient to normalize the Stokes parameters by the value of S_0 as follows

$$\mathbf{S} = \begin{bmatrix} S_0' \\ S_1' \\ S_2' \\ S_3' \end{bmatrix} = \begin{bmatrix} 1 \\ P\cos 2\chi \cos 2\psi \\ P\cos 2\chi \sin 2\psi \\ P\sin 2\chi \end{bmatrix} \tag{2.13}$$

Eq. 2.13 also shows how the Stokes parameters relate to two characteristic angles; the orientation angle (ψ) and the ellipticity angle (χ).

Another useful tool to describe the polarization state of light is the Poincaré sphere [3], which was developed by Henri Poincaré in 1892 as a graphical method of depicting light polarization. The Stokes parameters can be captured in the Poincaré sphere as shown in Fig.2.2. In particular, the Poincaré sphere is useful to describe the change in polarized light when it interacts with polarizing elements.

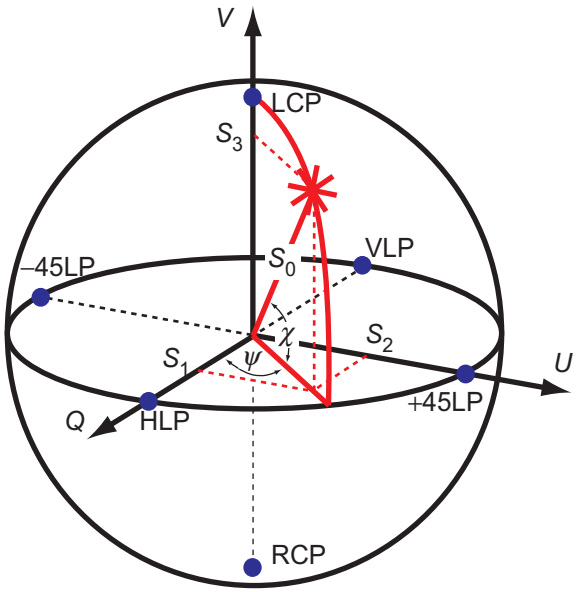

Figure 2.2: Poincaré sphere for graphical description of light polarization. An arbitrary polarization state can be represented as a point within the sphere and the coordinations are determined by the Stokes parameters.

2.2 Light Propagation in Anisotropic and Periodic Media

The vectorial nature of light can lead to different optical properties according to its polarization state when propagation occurs in anisotropic media. In addition, when light travels through/scatters from periodic media, it experiences diffraction or interference, which leads to a spatial modulation of phase or intensity of lightwave. In this Section, we briefly discuss how light interacts with matters while traveling in anisotropic and periodic media.

2.2.1 Light propagation in anisotropic media

Recall the constitutive relation between **E** and **D**. For anisotropic media with a directional dependency of the permittivity, a tensor equation is necessary [25]:

$$\mathbf{D}(\mathbf{r}, t) = \varepsilon_0 \tilde{\varepsilon} \mathbf{E}(\mathbf{r}, t) \tag{2.14}$$

where ε_0 is the dielectric constant in a vacuum and a tilde of $\tilde{\varepsilon}$ signifies a tensor. One can define an arbitrary permittivity tensor $\tilde{\varepsilon}$ as follows

$$\tilde{\varepsilon} = \begin{bmatrix} \varepsilon_{xx} & \varepsilon_{xy} & \varepsilon_{xz} \\ \varepsilon_{yx} & \varepsilon_{yy} & \varepsilon_{yz} \\ \varepsilon_{zx} & \varepsilon_{zy} & \varepsilon_{zz} \end{bmatrix} \tag{2.15}$$

where ε_{mn} $(m, n = x, y, z)$ are the normalized permittivities and they could have complex amplitudes. Note again that we assume non-magnetic material properties ($\mu = \mu_0$).

We first consider a dielectric medium with uniaxial anisotropy in the refractive index only. The permittivity tensor for an arbitrary uniaxial media can be written as

$$\tilde{\varepsilon} = \mathbf{R}^{-1}(\phi, \theta) \begin{bmatrix} \varepsilon_e & 0 & 0 \\ 0 & \varepsilon_o & 0 \\ 0 & 0 & \varepsilon_o \end{bmatrix} \mathbf{R}(\phi, \theta) \tag{2.16}$$

where ε_o and ε_e are the permittivities for the ordinary and extraordinary waves, respectively. The indices of refraction for each characteristic waves are defined as $n_{o,e} = \sqrt{\varepsilon_{o,e}}$. **R** is the transformation matrix, which is specified by two angles as follows

$$\mathbf{R}(\phi, \theta) = \begin{bmatrix} \sin\phi & -\cos\phi & 0 \\ \cos\theta\cos\phi & \cos\theta\sin\phi & -\sin\theta \\ \sin\theta\cos\phi & \sin\theta\sin\phi & \cos\theta \end{bmatrix} \tag{2.17}$$

where ϕ and θ are the azimuthal and polar angles measured from the $+x$- and $+z$-axes, respectively. A difference of the refractive indices Δn_l $(= n_e - n_o)$ is often called *linear birefringence* of the medium [29]. The normal modes for $\mathbf{E}$ corresponding to the ordinary and extraordinary waves can be written as [30]

$$\mathbf{E}_o = \begin{bmatrix} E_{ox} \\ E_{oy} \\ E_{oz} \end{bmatrix} = \begin{bmatrix} \sin\phi \\ -\cos\phi \\ 0 \end{bmatrix} \tag{2.18a}$$

$$\mathbf{E}_e = \begin{bmatrix} E_{ex} \\ E_{ey} \\ E_{ez} \end{bmatrix} = \begin{bmatrix} n_e^2 \cos\theta\cos\phi \\ n_e^2 \cos\theta\sin\phi \\ -n_o^2 \sin\theta \end{bmatrix} \tag{2.18b}$$

Consider linearly polarized light ($\mathbf{E} = E_x\hat{x}$) propagating through a waveplate, which is a dielectric slab with linear birefringence Δn_l. As the light travels through the waveplate, it experiences the optical retardation as shown in Fig. 2.3(a). The Stokes pa-

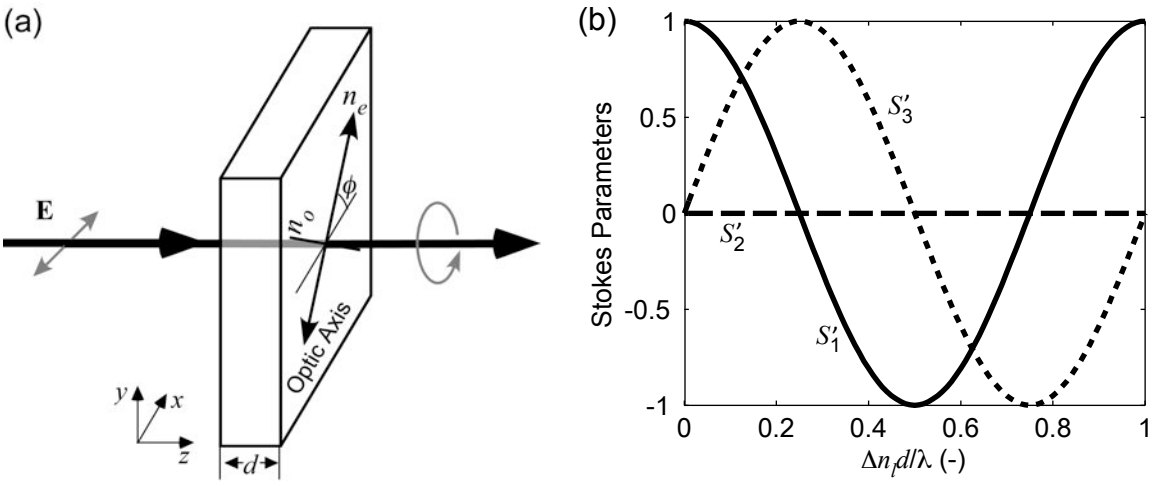

Figure 2.3: Light propagation in a waveplate: (a) a schematic view of a waveplate (i.e., $\phi = \pi/4$ and $\Delta n_l d = \lambda/4$ for a quarter wave retardation); (b) the normalized Stokes parameters of the output beam as a function of the retardation ($\Delta n_l d/\lambda$) of the waveplate, where $\phi = \pi/4$ and $\theta = 0$.

rameters of the emerging light are given by

$$S_1' = \cos^2(2\phi) + \sin^2(2\phi)\cos\left(\frac{2\pi\Delta n_l d}{\lambda}\right) \tag{2.19a}$$

$$S_2' = \cos(2\phi)\sin(2\phi)\left[1 - \cos\left(\frac{2\pi\Delta n_l d}{\lambda}\right)\right] \tag{2.19b}$$

$$S_3' = \sin(2\phi)\sin\left(\frac{2\pi\Delta n_l d}{\lambda}\right) \tag{2.19c}$$

where ϕ is the orientation of the optic axis of the waveplate, d is the thickness of the slab, and λ is the wavelength of light (Fig. 2.3(b)). For a simplification, we assume the polar angle $\theta = 0$. As light travel through the waveplate, it experiences relative phase differences between two characteristic waves (ordinary and extraordinary) depending on the orientation of the optic axis and the polarization orientation, which is often called *retardation*. For example, a linear polarization is converted in to a circular polarization when $\phi = \pi/4$ and $\Delta n d = \lambda/4$ (Fig. 2.3)

Certain substances are found to possess the ability to rotate the plane of polarization of light passing through them as illustrated in Fig.2.4(a). This phenomenon is known as *optical activity* [2]. Consider a simple medium possessing the following permittivity tensor

$$\tilde{\varepsilon} = \begin{bmatrix} \varepsilon_x & -j\varepsilon_g & 0 \\ j\varepsilon_g & \varepsilon_x & 0 \\ 0 & 0 & \varepsilon_z \end{bmatrix} \tag{2.20}$$

where ε_g is the gyration factor. The dispersion relation for a wave propagating along the $\hat{\mathbf{z}}$ direction is given by

$$k = \frac{\omega}{c}\sqrt{\varepsilon_x \pm \varepsilon_g} \tag{2.21}$$

where the upper sign corresponds to right-handed circular polarization and the lower sign to left-handed circular polarization. Accordingly, the refraction indices for the orthogonal, circular polarizations are

$$n_R = \sqrt{\varepsilon_x + \varepsilon_g} \tag{2.22a}$$

$$n_L = \sqrt{\varepsilon_x - \varepsilon_g} \tag{2.22b}$$

where the subscripts '$_R$' and '$_L$' correspond to the right- and left-handed circular polarizations, respectively. The difference of the refractive indices ($\Delta n_c = n_R - n_L$) is often called *circular birefringence* as opposed to linear birefringence [29].

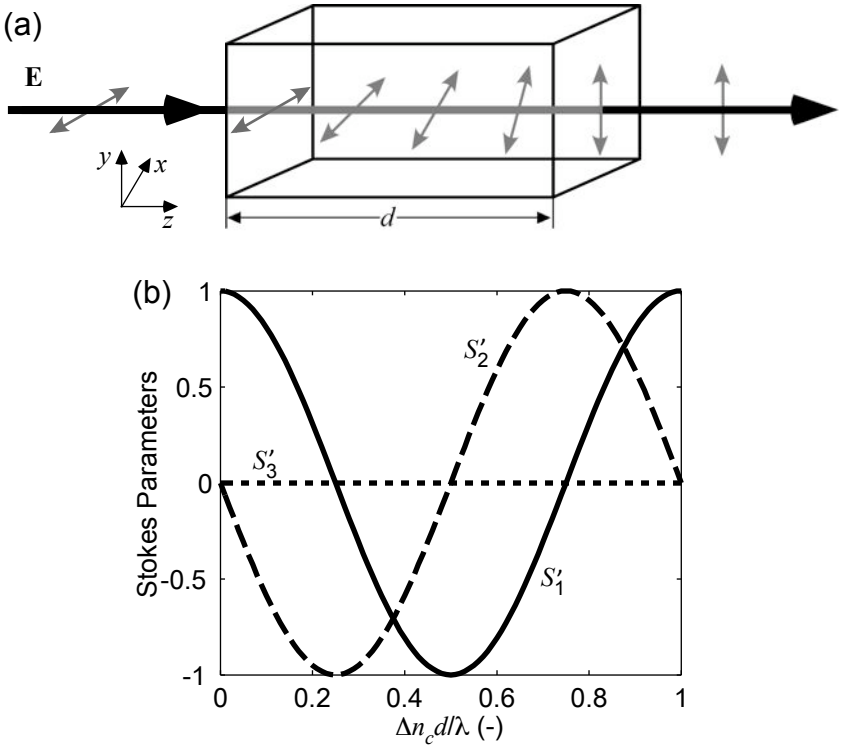

Figure 2.4: Light propagation in an optically active medium: (a) a rotation of the plane of the polarization as light travels in the medium; (b) the normalized Stokes parameters of the output beam as a function of the optical activity ($\Delta n_c d/\lambda$).

Consider linearly polarized light ($\mathbf{E} = E_x\hat{x}$) propagating through a slab with circular birefringence Δn_c. The light experiences the optical rotation as shown in Fig. 2.4(a). The Stokes parameters of the emerging light are given by

$$S_1' = \cos\left(\frac{2\pi\Delta n_c d}{\lambda}\right) \tag{2.23a}$$

$$S_2' = -\sin\left(\frac{2\pi\Delta n_c d}{\lambda}\right) \tag{2.23b}$$

$$S_3' = constant = 0, \tag{2.23c}$$

where d is the thickness of the slab and λ is the wavelength of light (Fig. 2.4(b)). Since the plane of the polarization rotates in the optically active medium, the ellipticity remains a constant in an ideal case.

2.2.2 Light propagation in periodic media

Light propagating through or scattering from periodic structures/surfaces such as gratings experiences diffraction or interference. Conventional diffraction gratings can be classified into two different categories depending on their spatial variations of material properties: phase gratings and amplitude gratings. A phase grating modulates the phase of the propagating wave by its periodically varying refractive index while amplitude gratings modulates the amplitude by its absorption coefficient variation. Although there are interesting aspects of the latter case, we limit our discussion to phase gratings and their properties in this Dissertation. We also briefly cover form-birefringent gratings based on subwavelength structures.

Consider two simple examples of phase gratings with sinusoidal and binary index profiles as shown in Fig. 2.5. These gratings are defined by the grating pitch Λ, average index $\bar{n}$ and index modulation factor n_1 as follows

$$n(x) = \begin{cases} \bar{n} + n_1 \cos(Gx) & \text{for a sinusoidal grating} \\ \bar{n} + n_1 \left\{1 - 2\prod\left[\tan\left(f_t G x\right)\right]\right\} & \text{for a binary grating} \end{cases} \tag{2.24}$$

where G is the grating wave number $(2\pi/\Lambda)$, Λ is the grating period, and $\prod(x)$ is a function that is 0 outside the interval $x = [-1, 1]$ and unity inside it. For binary gratings, the fill factor f_t is a ratio of the area with the higher refractive index $(\bar{n} + n_1)$.

The diffraction orders of a grating can be specified by integer numbers known as the *Floquet* modes $(m = 0, \pm 1, \pm 2, \ldots)$. The diffraction angle θ_m to the m^{th} order is

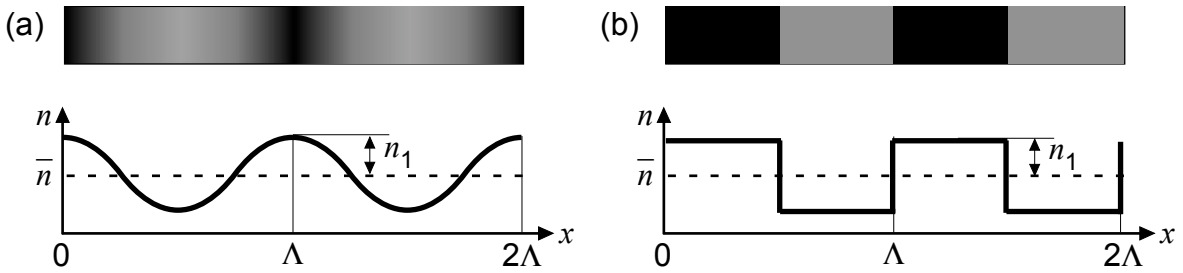

Figure 2.5: The refractive index profiles of conventional phase gratings: (a) a sinusoidal grating; (b) a binary grating. The grating parameters are defined by the period Λ, average index $\bar{n}$, and index modulation factor n_1.

determined by the grating equation [31], defined as follows

$$\sin\theta_m = \frac{m\lambda}{\Lambda} + \sin\theta_{inc} \tag{2.25}$$

where θ_{inc} is the incident angle.

Most phase gratings can be defined into two different grating regimes depending on their grating parameters (i.e., thickness, period, and refractive index): the Bragg and Raman-Nath regimes. Diffraction characteristics differ for gratings in each regime as shown in Fig. 2.6. It is customary to distinguish among the two regimes of diffraction by defining a dimensionless parameter Q known as the *Klein parameter* [32, 33]

$$Q = \frac{2\pi\lambda d}{\bar{n}\Lambda^2} \tag{2.26}$$

where d is the grating thickness. In general cases, gratings with $Q \gg 1$ fall into the Bragg (or thick) grating regime while gratings with $Q < 1$ and $\Lambda \gg \lambda$ into the Raman-Nath (or thin) grating regime. The above descriptions based on Q, however, may be invalid for some extreme cases such as gratings with too large or too small index contrast. Moharam et al. introduced a new dimensionless parameter ρ [34] defined as follows

$$\rho = \frac{\lambda^2}{\bar{n}n_1\Lambda^2} \tag{2.27}$$

, which provides more rigorous descriptions of the grating regime. Similar to the case of Q, the Bragg regime resides in the condition of $\rho \gg 1$ and the Raman-Nath regime in the condition of $\rho \leq 1$. Note that the grating thickness does not enter ρ but it should be chosen to have reasonable diffraction effect of the grating.

For Bragg gratings ($Q \gg 1$ or $\rho \gg 1$), the maximum diffraction occurs where the incident angle satisfies the following condition

$$2\Lambda\sin\theta_{inc} = \lambda \tag{2.28}$$

This angle is known as the Bragg angle θ_B. The diffraction angle of the transmitted wave is given by $\theta_t = \theta_B + \Delta\theta$, where $\Delta\theta$ represents a phase mismatch between the incident and transmitted waves. The maximum diffraction efficiency of a Bragg grating is given by [25]

$$\eta_{max} = \frac{1}{1 + \left[G\Delta\theta/(2\xi)\right]^2} \tag{2.29}$$

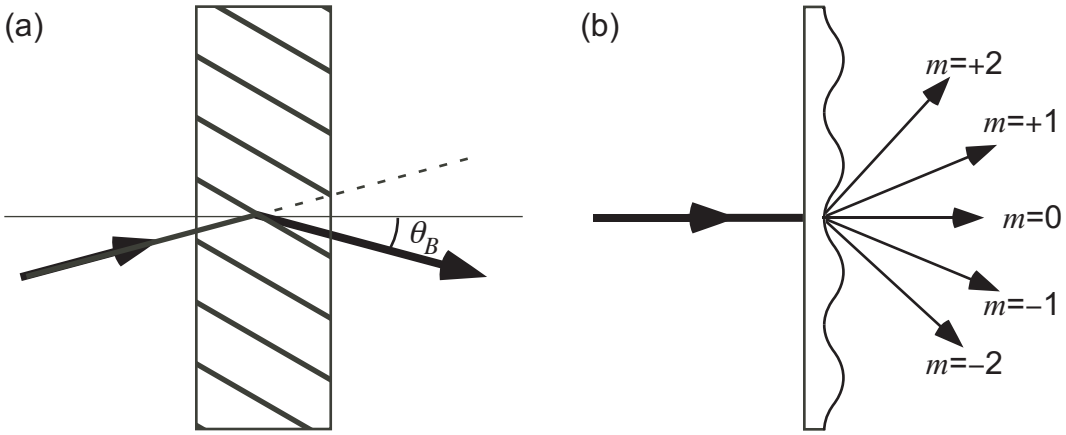

Figure 2.6: The two different grating regimes depending on the grating parameters (i.e., thickness, period, and refractive index): (a) a Bragg or thick grating; (b) a Raman-Nath or thin grating.

where G is the grating number $(2\pi/\Lambda)$ and ξ^2 is given by $(\pi n_1/\lambda)^2(\cos\theta_{inc}\cos\theta_t)^{-1}$. Note that the maximum diffraction efficiency can be 100% when $\Delta\theta = 0$.

For Raman-Nath gratings ($Q \ll 1$ or $\rho \leq 1$), a multiple orders may appear in diffraction as defined in the grating equation (Eq. 2.25). The diffraction efficiencies of sinusoidal phase gratings are given by [25]

$$\eta_m = J_m^2\left(\frac{2\pi\bar{n}d}{\lambda\cos\theta_{inc}}\right) \tag{2.30}$$

where J_m is the m^{th} order Bessel's function. A binary grating with $f_t = \frac{1}{2}$ has diffraction efficiencies of the m^{th} order as follows

$$\eta_m = \begin{cases} \cos^2\varphi & \text{for the } 0^{th} \text{ order} \\ 4(m\pi)^{-2}\sin^2\varphi & \text{for the } m^{th} \text{ order} \end{cases} \tag{2.31}$$

where the phase angle $\varphi = \pi n_1 d/(\lambda\cos\theta_g)$ and θ_g is the refractive angle of the grating, which satisfies $\bar{n}\sin\theta_g = n_0\sin\theta_{inc}$.

Birefringence may arise from an ordered structure of optically isotropic material whose size is small compared with the wavelength of light. We then speak of *form birefringence* [35]. A wave propagating in subwavelength features experiences anisotropy in the effective refractive indicies, which leads to two characteristic waves: an ordinary wave and extraordinary wave.

Consider a periodic structure composed of subwavelength features of two different media shown in Fig. 2.7 and having permittivity distribution as follows

$$n(x) = \begin{cases} n_1 & \text{for } (p \le x/\Lambda \le p + f_1) \\ n_2 & \text{for } (p - f_2 \le x/\Lambda \le p) \end{cases} \tag{2.32}$$

where $\Lambda \lesssim \lambda$, p is an integer, and $f_1 + f_2 = 1$ $(f_1, f_2 > 0)$. The effective dielectric constant n_o for the ordinary wave and n_e for the extraordinary wave are given by

$$n_o = \frac{n_1 n_2}{\sqrt{f_1 n_2^2 + f_2 n_1^2}} \tag{2.33a}$$

$$n_e = \sqrt{f_1 n_1^2 + f_2 n_2^2} \tag{2.33b}$$

and the form-refringence can be defined as $\Delta n = n_e - n_o$. Note that this assembly exhibits uniaxial anisotropy along the x-axis with a negative birefringence ($\Delta n < 0$). One can modulate the refractive index by varying the thickness of features or rotating the effective optic axis. Extensive studies of subwavelength gratings are found in [36, 37, 38, 39, 40, 41]. Subwavelength gratings are essentially equivalent to anisotropic gratings in naturally birefringent media such as liquid crystals [42, 43, 44].

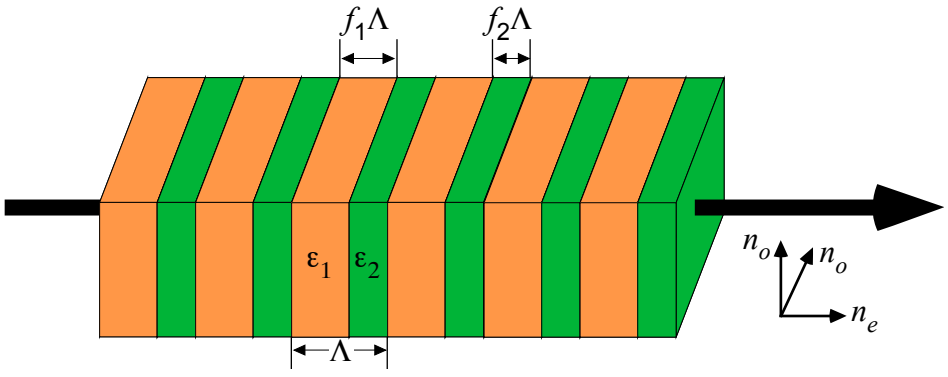

Figure 2.7: Form-birefringence of a subwavelength periodic structure. f_1 and f_2 are the fractions of the pitch (Λ) for the parts of n_1 and n_2 respectively. Note that $\Lambda \lesssim \lambda$.

2.3 Liquid crystals: soft-condensed matters that control light

Liquid crystal [45, 46, 47] is a phase of soft condensed matter that simultaneously exhibits characteristics of both isotropic liquid and crystalline solids. Since the first discovery of cholesteric liquid crystals by Reinitzer in 1888, liquid crystals (LCs) and related technologies have been of great interest to diverse communities in both science and engineering. In this Section, we will briefly review several distinct properties of LC materials and their applications in optics and photonics.

2.3.1 Properties of nematic liquid crystal materials

The liquid crystal phases are often characterized by the nature of ordering: positional and orientational order. The nematic is one of the most common LC phases that has the lowest degree of ordering with a one dimensional orientation order but no long-range positional order (Fig. 2.8(a)). It is convenient to define a unit vector **n**, often called the 'nematic director,' pointing the average direction of an ensemble of molecules (Fig. 2.8(b)). The deviation from the nematic director **n** can be quantified with the order parameter S,

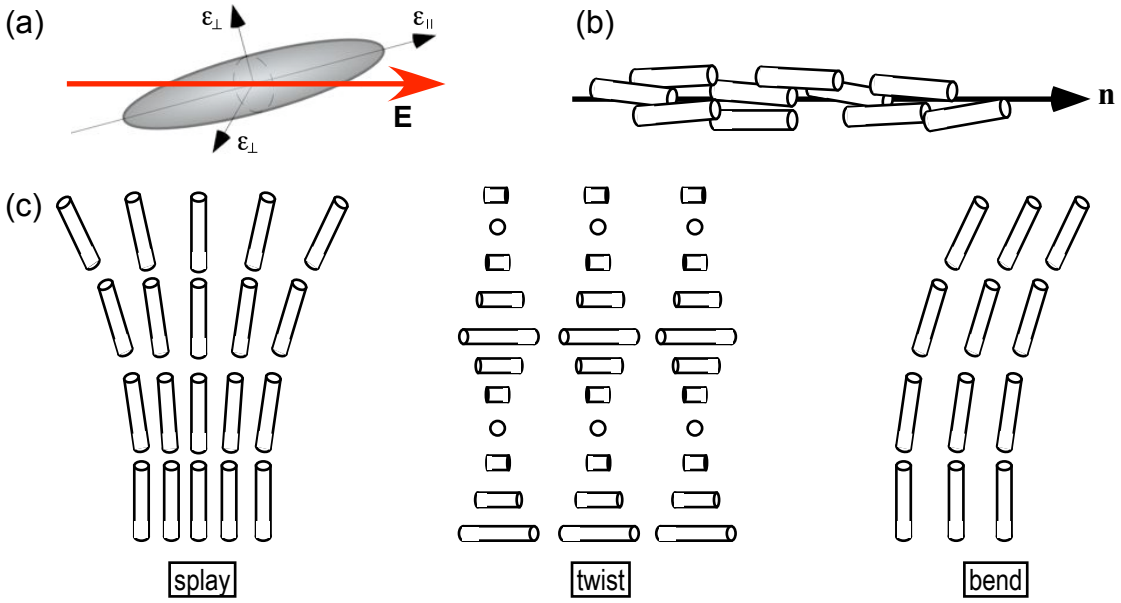

Figure 2.8: Properties of nematic liquid crystal (LC) materials: (a) a LC molecule with an dielectric anisotropy; (b) a nematic director **n**; (c) three basic elastic deformations in LCs (splay, twist, and bend).

defined as $S = \frac{1}{2}(3\cos^2\theta - 1)$ (θ is the orientation angle of individual molecules with respect to $\mathbf{n}$).

The anisotropy in dielectric and optical properties of LCs is a key to enable LCDs and other LC-based electro-optical devices. Consider a nematic LC molecule with the rod-like shape as illustrated in Fig. 2.8(a). The nematic LC exhibits the dielectric anisotropy (expressed as $\Delta\varepsilon = \varepsilon_{\parallel} - \varepsilon_{\perp}$). When an electric field $\mathbf{E}$ is applied, the field tends to polarize the free charges within the molecule and leads to a dipole moment. Due to the dielectric anisotropy, this induced dipole moment makes the nematic molecule reorient either parallel ($\Delta\varepsilon > 0$) or perpendicular ($\Delta\varepsilon < 0$) to the applied electric field as shown in Fig. 2.8(a). At optical frequencies, the nematic LC also shows the optical anisotropy, conveniently quantified by a linear birefringence $\Delta n_l = \Delta n_{\parallel} - \Delta n_{\perp}$ and light passing through the LC medium may experience phase retardation ($\Delta n_l d/\lambda$). The ability of the electro-optic control of optical anisotropy makes liquid crystals uniquely useful for many applications in optics and photonics. We also note that any static deformation of LCs by external fields and surface interactions can be described by the three basic elastic deformations: splay, twist, and bend (Fig. 2.8(c)).

The elastic continuum theory well explains LC ordering in a finite geometry and applied electric fields [48]. In Ossen-Frank theory, the static free energy density w_f of a LC volume can be expressed as follows

$$w_f = \frac{1}{2}K_{11}[\nabla \cdot \mathbf{n}]^2 + \frac{1}{2}K_{22}[\mathbf{n} \cdot \nabla\times\ \mathbf{n}]^2 + \frac{1}{2}K_{33}[\mathbf{n} \times \nabla \times \mathbf{n}]^2 \tag{2.34}$$

where K_{11}, K_{22}, and K_{33} are the elastic constants corresponding to the splay, twist, and bend deformations, respectively (Fig. 2.8(c)). Electric fields that are applied across the volume contribute the total energy density by the addition of an extra term: $w_{elec} = -\frac{1}{2}\varepsilon_0\Delta\varepsilon|\mathbf{E}\cdot\mathbf{n}|^2$. Due to chemical and microscopic structural interactions, LCs will typically exhibit a preferred orientation with respect to a surface. This surface influence to LC ordering can be quantified by another extra term: $w_{surf} = \frac{1}{2}(w_\theta \sin^2\phi + w_\phi \sin^2\phi)$ where w_θ and w_ϕ are surface anchoring strengths (θ and ϕ are the polar and azimuth angles of the nematic director). The equilibrium states for a given set of conditions can be found where the sum $w = w_f + w_{elec} + w_{surf}$ is minimized. The resulting configuration of the nematic director can then be used to find many electro-optical properties.

We now discuss another class of liquid crystal materials relevant to this disser-

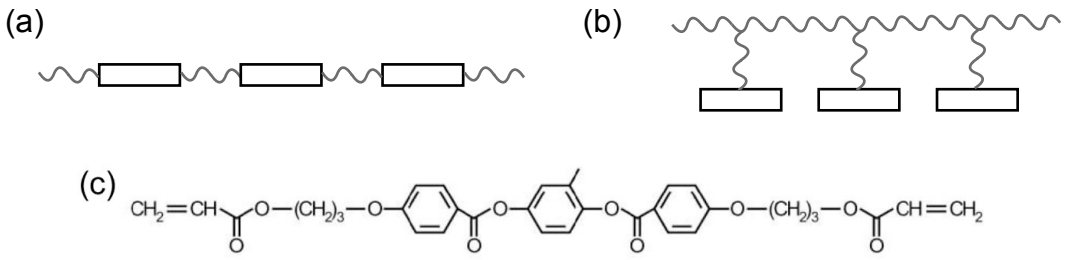

Figure 2.9: Types of polymerizable liquid crystal (reactive mesogen or RM) materials: (a) a main-chain LC polymer; (b) a side-chain LC polymer; (c) a chemical structure for a typical RM monomer (RM257 from Merck).

tation. Reactive mesogens (RMs) are liquid crystalline materials with polymerizable end groups [49, 47, 50]. Polymerization of RMs with two or more polymerizable groups leads to densely crosslinked networks in which the liquid crystalline order is permanently fixed. Figs. 2.9(a) and 2.9(b) show two main kinds of reactive mesogens: main-chain and side-chain RMs, respectively. A typical LC diacrylate molecule (RM257 from Merck) is also shown in Fig. 2.9(c). Many interesting applications using these RM materials have been suggested [51, 52, 53, 54, 55, 56, 57, 58]; for example, optical compensation films for LCDs, reflective color filters, and micro-actuators for biomedical applications.

2.3.2 Rubbing techniques of liquid crystal alignment

Although the nematic director is free to point in any direction, LCs typically exhibit a preferred orientation with respect to a surface due to chemical and microscopic structural interactions [47]. If the alignment condition is poor (weak anchoring or discontinuity), alignment-related defects may appear, such as disclination lines, reverse twist, and reverse tilt. These defects usually lead to considerable light scattering and have large effects on the electro-optical properties of LC devices. It is therefore very important to control the alignment conditions for most LC applications.

Rubbing is the most conventional LC alignment process. When a thin polymer film (i.e., polyimide) is rubbed using a cloth, liquid crystal molecules tend to be aligned by surface interactions. The alignment strength of a uniformly rubbed surface can be quantified by the azimuthal anchoring energy w_ϕ (typically, $\sim 10^{-3} J \cdot m^{-2}$) defined as follows[59]:

$$w_\phi = \frac{1}{4} K_{11} A^2 q \tag{2.35}$$

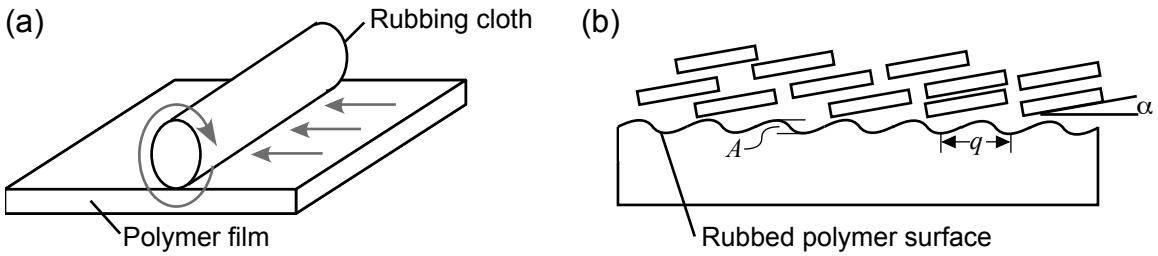

Figure 2.10: Rubbing technologies for LC alignment: (a) rubbing of a polymer film; (b) LC alignment by a rubbed polymer surface (groove height A, pitch q) with a pretilt angle α.

where K_{11} is the splay elastic constants of the LC and A and q are the depth (several μm) and pitch (tens of μm) of surface relief structures, respectively. The rubbing also generates a polar directional alignment, called the pretilt angle. Although the polymer rubbing is a simple and effective method for aligning LCs in a large scale, it is often subject to several problems: static charges, non-uniformity, and surface impurities. A number of non-rubbing alignment techniques have been developed, including photoalignment, chemically treated surfaces, and oblique evaporation [60].

2.3.3 Photoalignment of liquid crystal materials

Photoalignment of LCs has become of great interest in display industries due to its capability of the multi-domain alignment for viewing angle improvement of LCDs. The first reports on photoalignment techniques was found in 1988 and 1991 using azobenzene materials [61, 62]. Soon after, in 2002 [16], Schadt and coworkers reported photoalignment by dimerization of poly (vinyl cinnamate) photopolymer exposed to linearly polarized UV light, which is known as the linear photo-polymerization (LPP) polymer due to its anisotropic crosslinking selectively responding to linearly polarized light. Although only a few limited types of photoalignment materials were considered in the early development of this alignment techniques, significant improvements have been done during the last decade with more types of photoalignment techniques and increased choices of materials [63, 64, 65]. Applications of photoalignment materials with liquid crystal polymers also successfully draw substantial interests in optical retardation films and color filters.

Photoalignment via a reversible *cis-trans* transformation (photoisomerization) of azo-dye molecules was observed by Ichimura et al. [61]. The azobenzene molecule undergoes

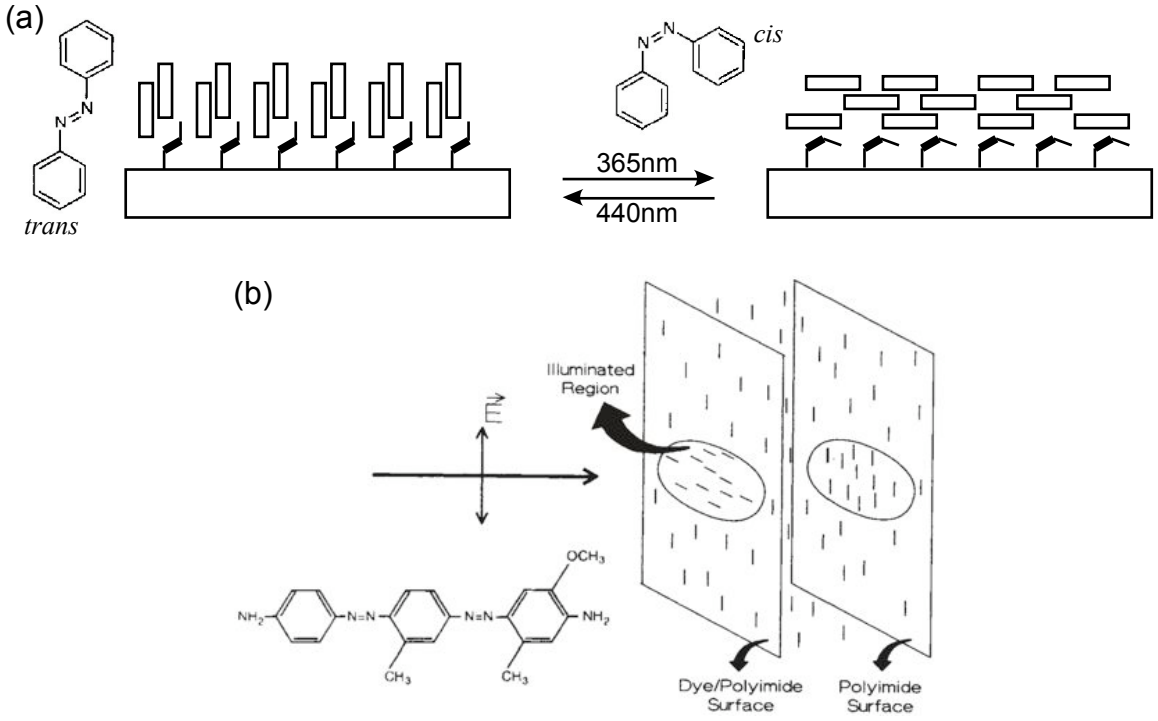

Figure 2.11: Photoalignment of LCs by the photoisomerization of azo-containing polymers: (a) homogeneous to homeotropic transition by a 'command surface' treated as aligned azo-dye monolayer (from Ref. [61]); (b) in-plane (or azimuthal) alignment of LCs using the effect of rotation of the azo-dye absorption oscillator (from Ref. [62]).

photoisomerization to the *cis* form upon UV exposure (at 365nm) and the *trans* form upon visible light exposure (at 440nm) as shown in Fig. 2.11(a). If the dye molecules are directly attached to the surface (a so-called "command surface"), the reorientation of LC molecules between homeotropic and planar configurations can be achieved by subsequent illumination of UV-visible light (Fig. 2.11(a)). Azimuthal alignment by the dichroism or reorientation of azo-dye side-chain polymers was also reported [62]. Due to the dichroism of the azobenzene molecule, molecules in the *trans* form is isomerized to the *cis* form with linearly polarized UV light (at 365nm) parallel to the molecular long axis. The relative population of molecules in the *trans* form whose long axes are perpendicular to the polarization axis increases and the LC molecules become aligned perpendicular to the polarization axis as shown in Fig. 2.11(b). Another important mechanism for photoalignment of azobenzene molecules is a molecular reorientation upon the polarized light illumination. The molecular reorientation

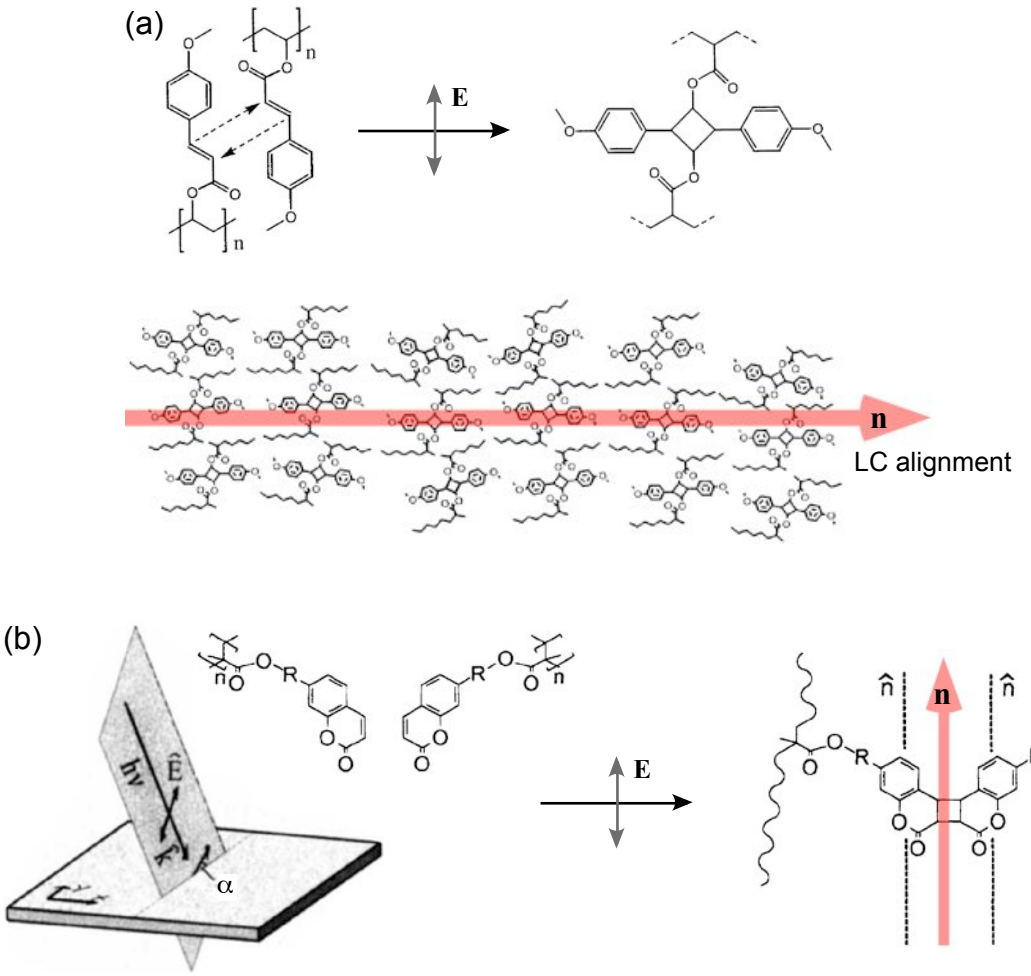

Figure 2.12: Photoalignment of LCs via linear photopolymerization (LPP): (a) crosslinking of polyvinyl 4-methoxy-cinnamate perpendicular the polarization axis (from Ref. [16]); (b) crosslinking of coumarin side-chain polymer parallel to the polarization axis of the illumination light. The latter shows a biased tilt angle θ with oblique illumination in the polarization plane (from Ref. [67]).

involves a molecular axis that actually moves during tis conformation change. A diffusion model of the azo-dye absorption oscillator (chromophore) has been developed to describe this reorientation phenomena [66].

LC alignment by the photo-induced crosslinking of polyvinyl 4-methoxy-cinnamate (PVMC) was experimentally demonstrated in 1992 [16]. The mechanism of crosslinking in PVMC is described as linear photo-polymerization (LPP) which leads to a preferred depletion of the cinnamic side chain molecules along the polarization axis due to the (2+2)

cycloaddition reaction as shown in Fig. 2.12(a). This causes an anisotropic distribution of cyclobutane molecules with their long axis preferably aligned perpendicular to the polarization axis and LC alignment also perpendicular to the polarization axis. Thus anisotropic Van der Waals interactions of the rigid cores of the anisotropically corsslinked photoproducts are primarily responsible for the alignment of liquid crystals on the LPP surface with two additional factors (anisotropic steric interactions with their partly aligned hydrocharbon polymer chains and anisotropically depleted prepolymer molecules). In 1996, Schadt et al. reported a modified LPP process based on coumarin side-chain polymers [67]. Similar photo-induced crosslinking can be achieved by the (2+2) cycloaddition reaction as shown in Fig. 2.12(c). There are two very important improvements in comparison with cinnamate side-chain polymers: (i) coumarin molecules do not give photoisomerization; (ii) the anisotropic crosslinking occurs parallel to the polarization axis and it also leads to LC alignment along the polarization axis. The former removes an issue of alignment stability in case of the cinnamoyl moiety. The latter shows, for the first time, an azimuthal alignment direction parallel to the electric field of the illumination light. Development of modified LPP photoalignment materials based on endo cinnamic ester polymer molecules and its applications in displays and optical thin films was reported in Ref. [68].

Another important photoalignment mechanism is photodegradation in polyimide materials. The successful photoalignment of a polyimide is considered to be an important technological goal, because of the high thermal stability of polyimides and their acceptance as the alignment layer of choice by the LC display industry. Hasegawa and Taira [69] first reported photoalignment of polyimide by polarized light exposure at 257 nm. Homogeneous LC alignment was obtained in a direction perpendicular to the polarization of the incident UV beam. This is the direction of the maximum density of unbroken polyimide chains on exposure. Therefore, alignment was attributed to the anisotropic depolymerization of the polyimide.

Photoalignment mechanism by anisotropic light desorption was introduced by Nazarenko et al. [70]. This approach may extend the research on photoalignment materials with a great extent from very complex molecular engineering of specialized functional polymers to any possible substrates for liquid crystal devices.

The anchoring energy is one of the most important parameters to characterize the LC alignment quality. To avoid the formation of surface walls and to provide a fast

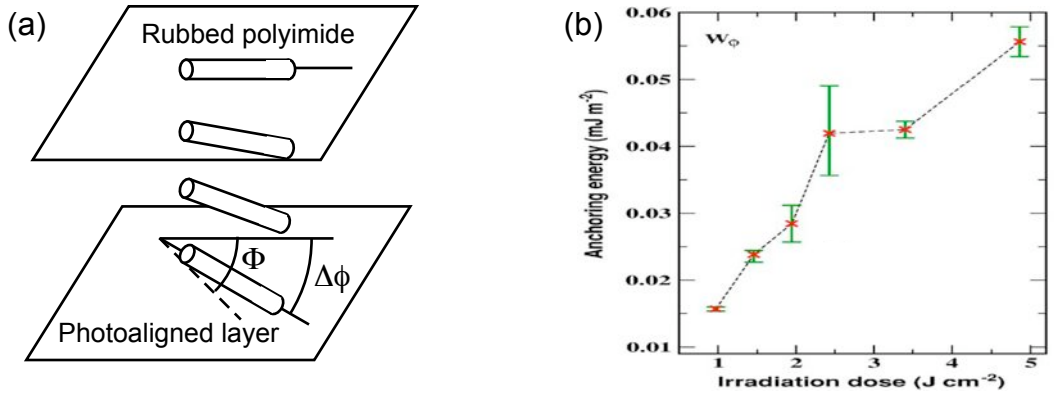

Figure 2.13: Anchoring energy of the photoalignment layer: (a) measurement of the azimuthal anchoring energy using a twisted LC cell with the in-plane sliding mode; (b) the effect of the exposure energy on the anchoring energy. (from Ref. [71])

switching 'off' time, the anchoring energy should sufficiently high (e.g., $w_\phi > 10^{-4}\mathrm{J/cm^2}$), comparable with that of the rubbed polymer surface.

Recall the surface anchoring strengths defined as $w_s = \frac{1}{2}(w_\theta \sin^2\phi + w_\phi \sin^2\phi)$. The azimuthal anchoring energy w_ϕ can be measured using a Φ-twisted nematic LC cell assembled with a rubbed polyimide alignment layer on a substrate and a photoalignment layer on the other as shown in Fig. 2.13(a). The value of the apparent twist angle in the LC cell is lower than that the one set by the preferred azimuthal director alignment on the substrates (Φ), because the strong azimuthal anchoring substrate affects the director alignment on the weak azimuthal anchoring one with a photoalignment layer [72]. Assuming the infinite anchoring energy of the rubbed surface, the azimuthal anchoring energy of the photoalignment layer can be calculated from the torque balance equation in the LC cell as follows

$$w_\phi = \frac{2K_{22}\Delta\phi}{d\sin 2(\Phi - \Delta\phi)} \tag{2.36}$$

where $\Delta\phi$ is the measured apparent twist angle. $w_\phi \approx 10^{-5}$ to $10^{-6}\mathrm{J/m^2}$ was reported from photoalignment layers based on polyvinyl cinnamate derivatives, about one to two orders of magnitude smaller than that of rubbed polyimide layers [73]. Subsequently higher azimuthal anchoring energy $w_\phi > 10^{-4}\mathrm{J/m^2}$, comparable with the anchoring energy of the rubbed polyimide layer, was measured from azo-dye photoalignment layers [74]. Even though the surface interactions are predominantly responsible for aligning LCs, the thinck-

ness of the photoalignment layer can strongly affects the alignment quality. For a ultra-thin photoalignment layers, the film may not be uniform or even continuous and the discontinuous layer exhibits a lower anchoring energy. However, once a continuous film is obtained, LC alignment can be achieved with good anchoring properties. Another important factor for the anchoring energy of the photoalignment layers is the exposure energy/dose. Fig. 2.13(b) shows the azimuthal LC anchoring energy of the azo-dye layers depending on the UV dose with varying the exposure time [71].

2.3.4 Liquid crystal applications in displays and photonics

Liquid crystal technology has had a major effect many areas of science and engineering, as well as device technology. Applications for this special kind of material are still being discovered and continue to provide effective solutions to many different problems. In this Section, we review three different examples of liquid crystal applications in displays and photonics: (i) flat panel displays, (ii) spatial light modulators, and (iii) diffractive optical elements.

Liquid crystal displays (LCDs) are one of the most popular LC devices with a hugh success of commercialization that utilize distinct electro-optical properties of LC materials. The twisted nematic (TN) LC is the first successful mode of LCDs [75]. Fig. 2.14 illustrates

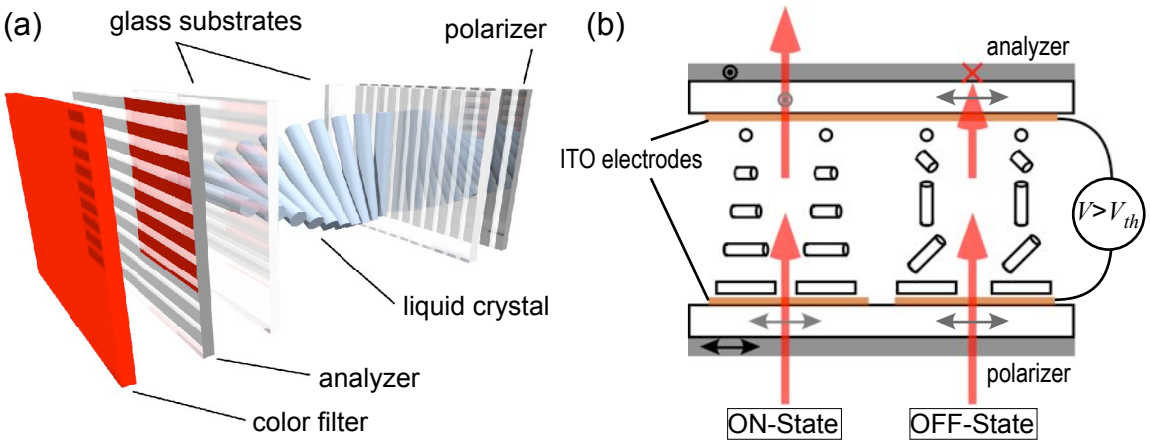

Figure 2.14: Liquid crystal displays: (a) a single pixel of LCDs with a twisted-nematic (TN) LC layer between crossed polarizers (from `http://en.wikipedia.org/wiki/Liquid_crystal_display`); (b) basic light switching operations of a TN-LCD.

the operation principle of TN-LCDs consisting of a 90°-twisted LC cell sandwiched between crossed polarizers. In the 'ON' state ($V = 0$), the polarization vector of the incident beam follows the twist of the liquid crystal directors, which is often called the adiabatic following or waveguiding in the TN-LC. On the other hand, light passes without experiencing waveguiding in the 'OFF' state ($V > V_{th}$) where the LC directors are mostly reoriented normal to the surface.

There are a number of advantages of LCDs as compared to traditional displays using the cathode ray tube (CRT). Since a LCD is formed in two sandwiched glass substrates with a few μm gap, the size and weight is dramatically reduced and this flat panel display has been replacing CRT displays in the last decade. The scalability of LCDs from microdisplays to big screen TVs is another important advantage over even other types of flat panel displays such as plasma displays and digital imaging devices based on MEMS technologies. Even though the LCD technology requires external light sources, it generally shows a low power consumption as compared with that of the CRT. However, some technical challenges remain to improve, including light efficiency, viewing angle, contrast ratio, and response time. While the most advanced LCDs suggest potential solutions for most of these problems, the use of absorbing/reflective polarizers and color filters limit the light efficiency.

LC-based spatial light modulators (SLMs) have become popular to control an optical wave-front by altering the phase distribution [76, 77, 78, 79]. A spatial light modulator is a device that imposes some form of spatially-varying modulation (either phase or intensity or both simultaneously) on a beam of light. A typical LC-SLM consists of a liquid-crystal-on-silicon (LCoS) backplane, a LC layer, and a glass substrate coated with a transparent electrode as shown in Fig. 2.15. With combination of the electro-optic control of the LC directors, advanced Si technologies provide a number of attractive characteristics of LC-SLMs such as compactness, high density integration, and low cost. Utilities of LC-SLMs can be found in various photonics applications [80, 81, 79]; for example, holographic data recording, adaptive optical systems, beam steering, optical communication, and projection displays. More recently, holographic optical tweezers have been developed using a high resolution LC-SLMs [82].

Several concepts of liquid crystal gratings have been proposed as optical diffractive elements for various photonics applications which include beam steering/shaping [44, 83], tunable filters [84], and displays [85]. Both a relatively large optical anisotropy and the

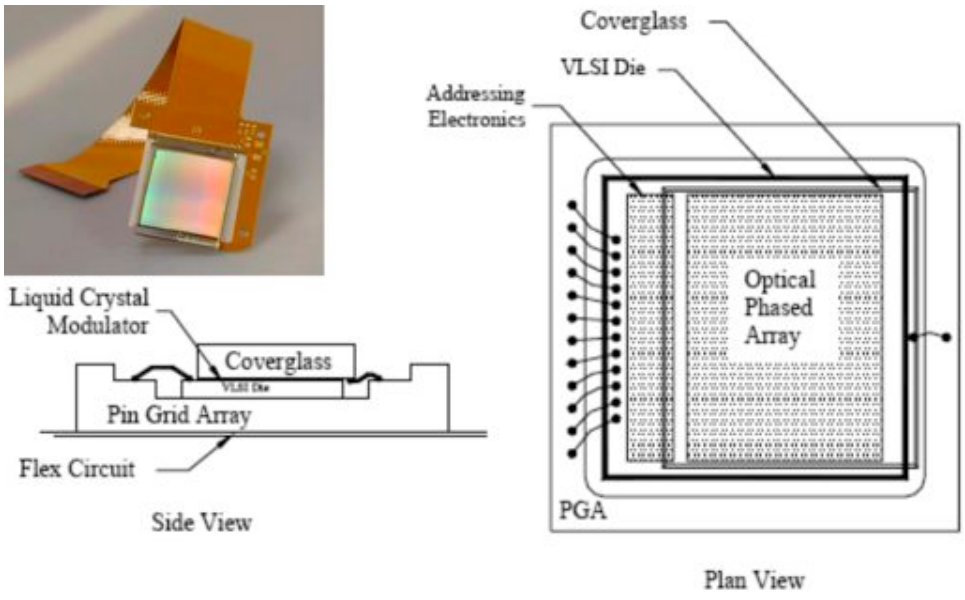

Figure 2.15: LC-based spatial light modulator (LC-SLM) (from Boulder Nonlinear Systems, Inc.)

ability to control the director configuration by surfaces and applied fields uniquely makes LC materials attractive to form grating structures with with advanced functions including electro-optical switching/tuning and polarization sensitivity/selectivity.

One possibility is to use surface structures to form LC micro-prisms [83] or LC-filled groove structures [42] as shown in Fig 2.16(a). If the surface structure is patterned using a dielectric material with the ordinary index of the liquid crystal, a polarization selective diffraction can be achieved; light with a linear polarization parallel to the LC long axis experiences diffraction due to the index difference between two regions with and without LCs, while light with a linear polarization perpendicular to the LC long axis simply travels through without experiencing diffraction. An electrical switching of diffraction also can be done by applying a voltage across two substrate electrodes and then no diffraction will occur. Fig. 2.16(b) shows a LC blazed phase grating by using patterned electrodes with differential applying fields within a grating period, which alter the LC directors to effectively form the gradient index profile. This LC blazed gratings have been studied in beam steering applications because of their high efficiency (up to $\sim$ 90%) into a single diffracted order [86, 87]. General problems of most LC gratings may include scattering due to defects in the LC, non-ideal index profiles, and problems related to fine alignment

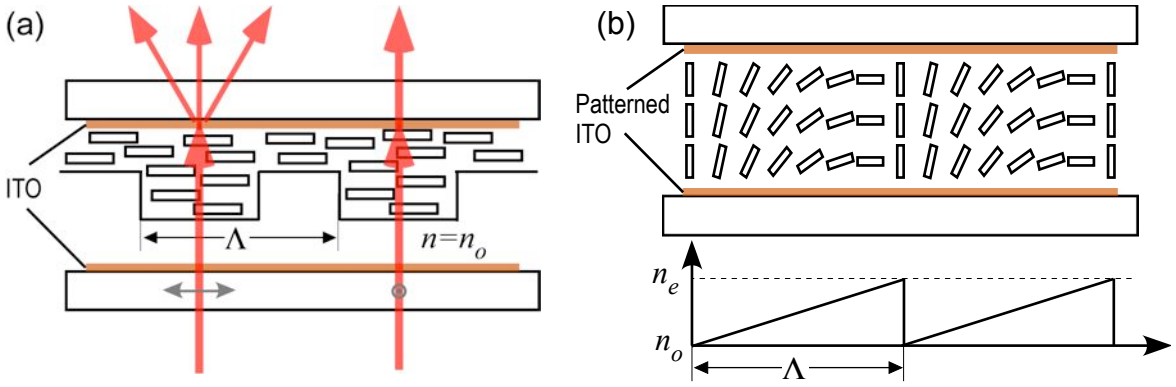

Figure 2.16: Liquid crystal diffraction gratings: (a) a surface-groove LC binary phase grating (Ref. [42]); (b) an electrically addressed LC blazed phase grating (Ref. [83]).

patterns.

Polarization sensitivity of diffraction properties also could be a concern where light polarization cannot be properly controlled. A stack of two LC gratings with the orthogonal LC profiles may be considered to compensate the effect of polarization. More recently, grating structures employing hybrid LC configurations have been proposed as a polarization-independent light modulator that exhibits optical switching/diffraction insensitive to the polarization of incident light (Figs. 2.17(a) and 2.17(b)) [89, 88, 90] and $\sim 100\%$ theoretical efficiency. One major problem of binary LC configurations is disclinations (line defects) along the boundaries between two different domains. One can avoid such a problem using a uniform LC alignment as an initial state and the grating profile is created by applying a voltage across the LC cell. However the fringe fields between electrodes and interactions between neighboring LCs affect a non-ideal LC profile.

An interesting idea of using polymer walls between LC domains was introduced [91,

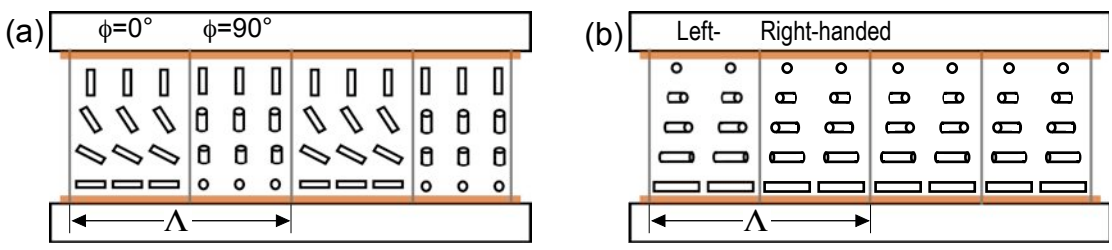

Figure 2.17: Polarization-independent light modulators based on LC diffraction gratings: (a) a hybrid LC configuration (Ref [88]); (b) a reverse twist configuration (Ref. [89]).

92]. The polymer walls are formed via polymer diffusion process during selective UV exposure as shown in Fig. 2.18(c). Since the LC orientation in the polymer wall is locked and it does not response to the electric field, the phase profile more close to the ideal case can be obtained. A very high efficiency $\sim 97\%$ was also reported. This polymer-wall grating, however, is limited by problems with creating narrow polymer walls (currently, tens of μm) and the effect of the polymer surface still causing non-ideal phase profiles.

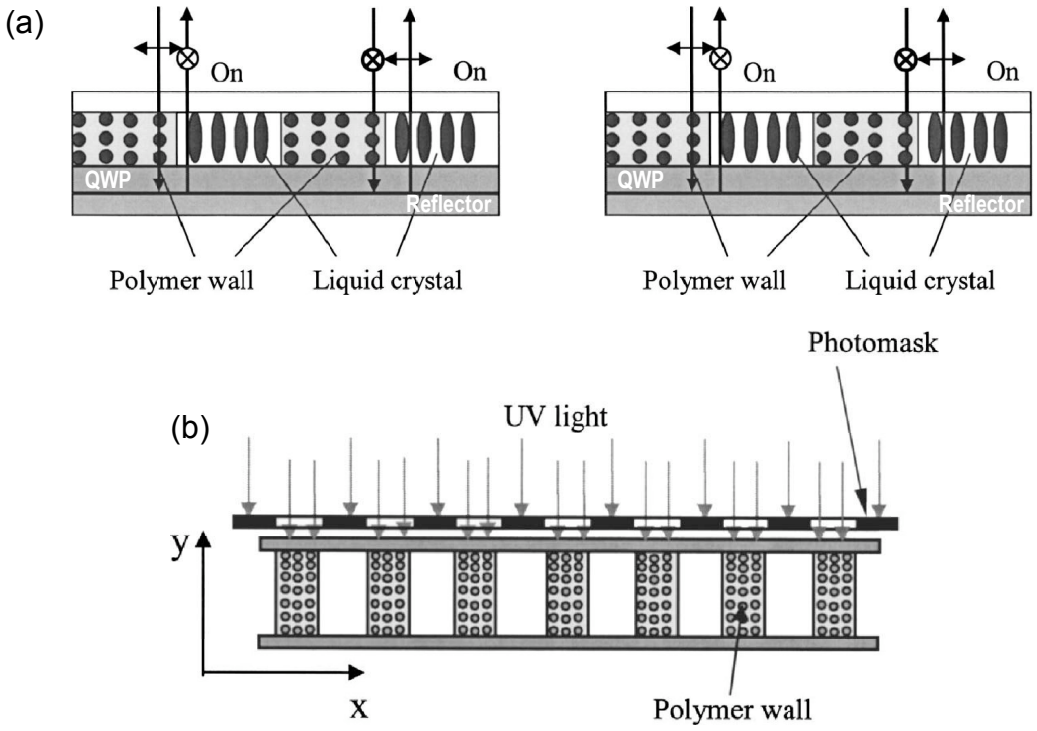

Figure 2.18: Liquid crystal grating with the polymer walls (from Ref. [92]): (a) the basic concept for polarization-independent modulation; (b) the fabrication of the polymer wall via the polymer diffusion process during selective UV exposure.

2.4 Polarization Gratings

Polarization gratings (PGs) [4, 93, 6] are generally described as periodic profiles of spatially-varying optical anisotropy. Unlike conventional phase or amplitude gratings, this special type of anisotropic gratings operates by locally modifying the polarization state of lightwaves passing through them. The most-studied PG profiles are continuous and transparent, which we classify into two primary types based on their local anisotropy: *circular* PGs consisting of a spiralling, constant-magnitude, linear birefringence (Fig. 2.19(a)); and *linear* consisting of a varying-magnitude circular and linear birefringence PGs (Fig. 2.19(b)). They manifest a unique combination of optical properties that can include 100% diffraction into a single order, diffracted orders with a fixed polarization state controlled by the PG profile, and efficiencies that are highly polarization sensitive. These make PGs useful for numerous applications in a variety of fields, including polarimeters [5, 94, 95, 96, 19], displays [10, 97, 98], polarizing beam-splitters [99, 8], beam-steering [100, 101], and polarization multiplexers [102]. (add more of our application papers)

The profiles of the two primary PG types (circular and linear) can now be fully defined by their anisotropy profile (ϕ, n_o, n_e, and ϵ_g) in terms of material parameters ($\bar{n}$, Δn_l, and Δn_c) and geometry (thickness d and effective optical period Λ). The permittivity

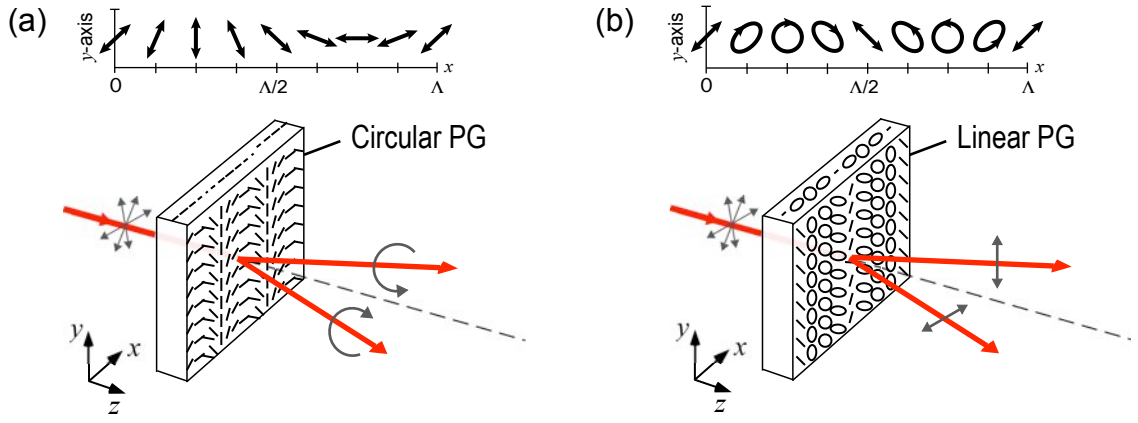

Figure 2.19: Periodic birefringence profiles for the two primary types of polarization gratings (PGs): (a) *circular* PG and (b) *linear* PG. The direction/handednesses of the total local anisotropy are illustrated as arrows. (Λ is the effective optical grating period/pitch.)

tensor $\tilde{\epsilon}$ can be written as follows

$$\tilde{\epsilon} = \mathbf{R}^{-1}(\phi, 0)\left[\tilde{\epsilon}_l + \tilde{\epsilon}_c\right]\mathbf{R}(\phi, 0) \tag{2.37}$$

where $\phi(x)$ is the azimuthal orientation of spatial-variant linear birefringence, and $\tilde{\epsilon}_l$ and $\tilde{\epsilon}_c$ are tensor elements corresponding to linear and circular anisotropy, respectively, which can be written as follows

$$\tilde{\epsilon}_l = \begin{bmatrix} n_e^2 & 0 & 0 \\ 0 & n_o^2 & 0 \\ 0 & 0 & n_o^2 \end{bmatrix} \tag{2.38a}$$

$$\tilde{\epsilon}_c = \begin{bmatrix} 0 & -i\epsilon_g & 0 \\ i\epsilon_g & 0 & 0 \\ 0 & 0 & 0 \end{bmatrix} \tag{2.38b}$$

where $n_{o,e}(x)$ are the ordinary and extra-ordinary refractive indices of the anisotropic medium, respectively, and the linear birefringence is defined as $\Delta n_l = n_e - n_o$. The gyration factor $\epsilon_g(x) = \bar{n}\Delta n_c$ is symmetric about the z-axis (where $\bar{n} = \frac{1}{2}(n_o + n_e)$ is the average index of refraction and the circular birefringence is identified as Δn_c). Table 2.1 summarizes these material and geometric parameters for both circular and linear types of PGs. We note that the azimuthal orientation of the anisotropy is changing along the x-axis (or the grating axis) for the circular PG with a constant value of birefringence ($\Delta n_l \neq 0$, $\Delta n_c = 0$) while the magnitudes of linear and circular birefringence vary along the grating axis but at the same azimuthal angle (i.e., $\phi = \pi/4$) for the linear PG.

The both circular and linear polarization gratings can exhibit several unique features as shown in Figs. 2.19(a) and 2.19(b) that include: (i) only three orders are potentially

Table 2.1: Material parameters for two primary types of the polarization gratings

	Circular PG	Linear PG
$\phi(x)$	$x\pi/\Lambda + \pi/4$	$\pi/4$
$n_e(x)$	$\bar{n} + \Delta n_l/2$	$\bar{n} + (\Delta n_l/2)\cos(x\pi/\Lambda)$
$n_o(x)$	$\bar{n} - \Delta n_l/2$	$\bar{n} - (\Delta n_l/2)\cos(x\pi/\Lambda)$
$\epsilon_g(x)$	0	$\bar{n}\Delta n_c \sin(x\pi/\Lambda)$

non-zero ($\eta_{|m|\geq 2} = 0$, unlike thin phase gratings); (ii) the first orders are circularly/linearly polarized regardless the input polarization state; (iii) all three orders can have efficiencies from 100% to 0%. Theoretical descriptions for these ideal properties of the PGs have been developed using the Jones matrix method for paraxial diffraction.

2.4.1 Essential diffraction properties of polarization gratings

In what follows, we derive a concise summary of the properties of the circular PG, based in part on Jones matrix reasoning [6, 19]. We begin by assuming an infinite grating and express the (far-field) electric field D_m for each diffraction order m as the Fourier transform of the (near-field) output. Under this set of assumptions, we can express the far-field electric field of the diffraction order m as follows

$$\mathbf{D}_m = \frac{1}{\Lambda}\int_0^{\Lambda} \mathbf{T}(x)\mathbf{E}_{in}e^{-j2\pi mx/\Lambda}dx \tag{2.39}$$

The transfer matrix T is given by

$$\mathbf{T}(x) = \mathbf{R}\left(-\frac{\pi x}{\Lambda}\right)\begin{bmatrix} e^{-j\pi\Delta n_l d/\lambda} & 0 \\ 0 & e^{j\pi\Delta n_l d/\lambda} \end{bmatrix}\mathbf{R}\left(\frac{\pi x}{\Lambda}\right) \tag{2.40}$$

where $\Delta n_l d/\lambda$ is the normalized retardation and $\mathbf{R}$ is the rotation matrix. Assuming an incident plane-wave (uniform in the x direction), we can rewrite Eq. 2.39 as follows

$$\mathbf{D}_m = \mathbf{T}_m\mathbf{E}_{in} \tag{2.41}$$

where the grating transfer matrix is defined as $\mathbf{T}_m = \Lambda^{-1}\int_0^{\Lambda}\mathbf{T}(x)e^{-i2\pi mx/\Lambda}dx$. Since PGs have non-zero solutions only for $m = -1, 0, +1$, Eq. 2.41 can be summarized as follows

$$\mathbf{D}_0 = \mathbf{E}_{in}\cos\left(\frac{\pi\Delta n_l d}{\lambda}\right) \tag{2.42a}$$

$$\mathbf{D}_{\pm 1} = \frac{1}{2}\mathbf{E}_{in}\sin\left(\frac{\pi\Delta n_l d}{\lambda}\right)\begin{bmatrix} -j & \mp 1 \\ \mp 1 & j \end{bmatrix} \tag{2.42b}$$

We can now solve for the diffraction efficiency as the ratio of output to input intensity ($\eta_m = |\mathbf{D}_m|^2/|\mathbf{E}_{in}|^2$) as follows

$$\eta_0 = \cos^2\left(\frac{\pi\Delta n_l d}{\lambda}\right) \tag{2.43a}$$

$$\eta_{\pm 1} = \frac{1}{2}(1 \mp S_3')\sin^2\left(\frac{\pi\Delta n_l d}{\lambda}\right) \tag{2.43b}$$

where $S_3' = S_3/S_0$ is the normalized Stokes parameter corresponding to ellipticity of the incident light. Furthermore, it can be shown that the polarization states of the ±1-orders will be orthogonal and circularly polarized (hence the label 'circular' PG). Jones analysis for more general cases of the polarization grating (including the linear PGs) can be found in Ref. [103].

The expressions above are derived using the paraxial approximation (that all waves of interest propagate along directions close to the z-axis), which necessarily implies that the gratings are considered 'thin'. Several unique features are apparent: (i) only three orders are potentially non-zero ($\eta_{|m|\geq 2} = 0$, unlike thin phase gratings); (ii) the first orders are circularly polarized regardless the input polarization state as shown in Fig. 2.20(a); (iii) all three orders can have efficiencies from 100% to 0%; (iv) both η_0 and the sum of $\eta_{\pm 1}$

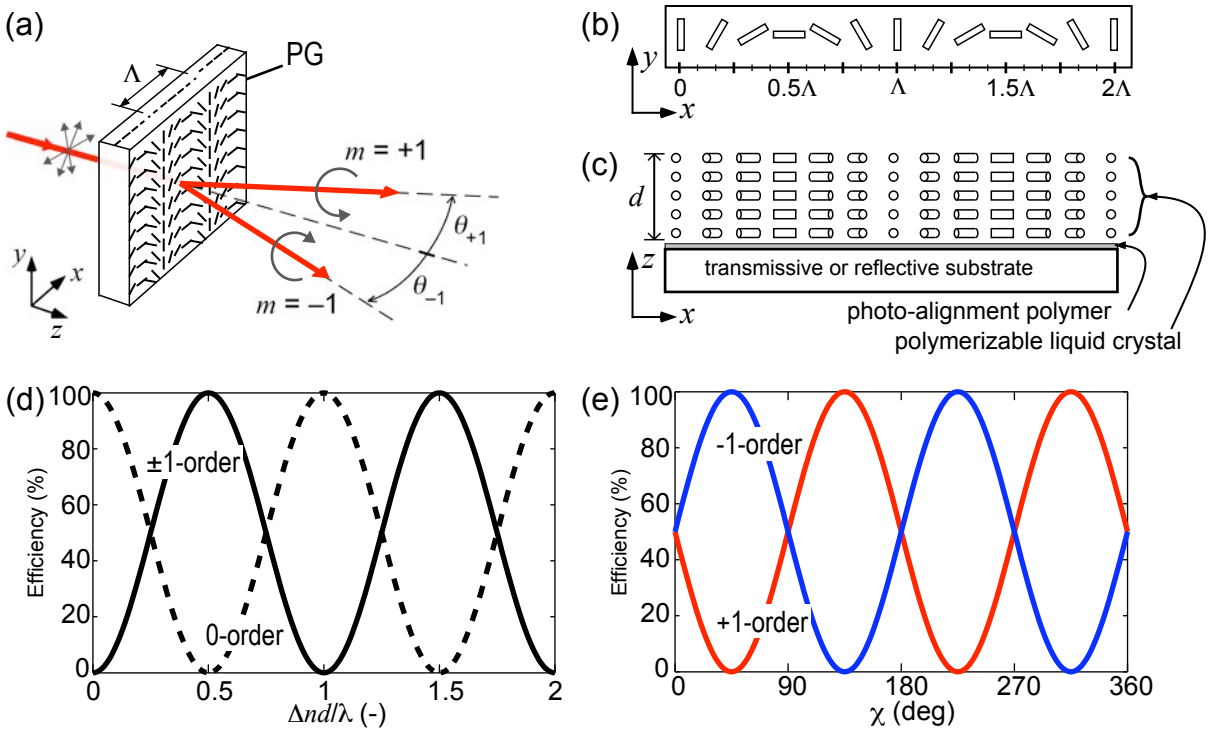

Figure 2.20: Diffraction properties of the circular PG: (a) the first-order diffraction with orthogonal circular polarization states; a schematic view of the circular PG embodied as a liquid crystal layer – (b) plane- and (c) side-view; diffraction efficiencies of the circular PG as a function of (d) the normalized retardation $\Delta n_l d/\lambda$ and (e) the ellipticity angle χ (related to the Stokes parameter by $S_3' = \sin(2\chi)$) of the input polarization.

depend only on the normalized retardation $\Delta n_l d/\lambda$ (see Fig. 2.20(d)). It is also important to note that the efficiencies of the ± 1-orders are strongly coupled by the polarization state of incident light as shown in Fig. 2.20(e).

A circular PG has moderate diffraction bandwidths (through $\Delta nd/\lambda$ in Eqs. 2.43(a) and 2.43(b)) and reasonable angular response when compared with other conventional gratings. The spectra of diffraction efficiencies of this grating are very similar to those of binary phase gratings while the maximum efficiency can be $\sim 100\%$. The PG also shows similar high efficiency and polarization properties over a fairly wide angles of incidence (i.e., $\pm 30^\circ$). For Bragg gratings, $\sim 100\%$ efficiency can be obtained in special conditions (i.e., $\theta_{inc} \approx \theta_B$). However, diffraction efficiencies of both blazed and Bragg gratings are highly sensitive to incident angle variation. We will discuss more on the diffraction bandwidth and angular sensitivity of PGs in Chapter 3, and we will also show how to make achromatic PGs in the same Chapter.

2.4.2 Historical record in literature

The concept of polarization gratings was first proposed in 1972 [104] as spatially modulated linear/circular polarizer patterns to create polarization moiré in interferometry applications. Theoretical foundations to understand diffraction behavior of these absorbing gratings was developed using the Jones matrix analysis and the basic optical properties were also confirmed by initial experimental demonstrations. The author of the paper in 1972 also presented very interesting interferometer configurations using polarization gratings and some important aspects of this special type of anisotropic gratings were hinted in the same paper, which are also very useful for many different applications including polarimetric imaging, beam steering, light modulation, and so on. These marvelous theoretical and experimental works, however, were not quite well recognized in literatures and not so much works had been reported after this first appearance of the polarization grating. One of the reasons may be no practical means to create such complex patterns using polarizer films with a high resolution although several techniques utilizing electro-optical materials and polarization-sensitive recording materials were suggested. The initial experiments employed Ronchi rullings (few mm wide) of polarizer films.

Soon after, in 1974 [105], a method of holographic recording of polarization gratings was proposed with extended mathematical descriptions for general polarization holograms

including grating patterns. Polarization-sensitive materials of which birefringence can be induced under the action of polarized coherent light was considered as a holographic recording medium. Nikolova and Todorov reported a summary of distinct properties of special types of polarization gratings [4] and their development of organic polarization-sensitive materials (containing azo dye molecules) [12, 106], which publications successfully draw hugh interests in both material and optics communities. Perhaps, more importantly, it was first time to prove theoretical 100% efficiency from paraxial-domain (or thin-grating regime) diffractive elements [4, 107, 6]. Polarization gratings based on dichroism (anisotropic absorption) rather than birefringence were simultaneously reported in both theory and experiment [108, 109].

The most popular means to create PGs is using polarization holography with anisotropic organic recording materials (especially azobenzene-containing polymers [14, 110, 111, 112]), among other materials [113, 114, 15]. PGs also can be formed by sub-wavelength features [99, 115]. Several related approaches use patterned surfaces via micro-rubbing or photoalignment to align a liquid crystal layer [116, 17, 10], which have recently been implemented experimentally with ideal optical properties [18, 19, 11].

The first application of polarization gratings was suggested as a polarizing component for advanced interferometric imaging systems to create polarization-type Moiré-fringe patterns [104]. While the use of polarization gratings in imaging systems has become of a great interest, this interesting work, however, was not quite recognized because of fabrication complexity at the time when it is published. A simplified polarimetry concept based on PG diffraction was proposed by Gori [5] and many other publications of PG applications as a polarizing beam splitter followed [99, 94, 117, 8]. Polarization detection methods using PGs in optical communication were also proposed [102, 118]. Most previous attempts could not lead to successful development of applications and limited because of poor optical performance (low efficiency, incoherent scattering, low polarization contrast) of actual PGs, far away from its ideal properties. A new fabrication process that separates holographic recording and liquid crystal alignment via the photoalignment surface layer was proposed to overcome the complexity of volume holographic recording (usually limited by recording efficiency and low induced birefringence of the recording medium) and the difficulty of liquid crystal alignment in such a complex spatial pattern using rubbing techniques [119, 17]. With benefits of development of new liquid crystal materials and photoalignment techniques [18, 96],

more practical applications arose in displays [10, 9, 98, 120, 121], imaging/nonimaging polarimeters [96, 19, 122, 123], imaging/nonimaging spectrometers [124, 125, 126], beam steering [100, 127], and optical switching/imaging [128].

2.4.3 Holographic insights of polarization gratings

Holography is a photographic technique to create an interference pattern using multiple beams of coherent light [129]. While most conventional holography uses an intensity modulation as shown in Fig. 2.21(a), polarization holography involves a modulation of the polarization state as a result of interference of light with different polarization. Interesting interference patterns can be created when two beams have orthogonal polarization states with each other. Figs. 2.21(b)–2.21(d) show polarization holograms for three special cases of orthogonal polarizations (linear vertical and horizontal, linear at $\pm 45^\circ$, and right- and left-handed circular). The circular PG is one type of these polarization interference patterns with two orthogonal, circularly polarized light (Fig. 2.21(d)). Polarization holograms can be represented as circles on the Poincaré sphere. One interesting view of polarization gratings is that all above polarization holograms based on two orthogonal beams with the same intensity make great circles on the sphere as shown in Figs. 2.22(a)–2.22(c). A polarization hologram of any circle on the sphere can be achieved by adjusting the relative intensities of orthogonal beams (Fig. 2.22(d)).

The birefringence pattern of the circular PG can be interpreted as the interference of two circularly polarized beams (left- and right-handed) of which electric fields are:

$$\boldsymbol{E}_L = \frac{E_0}{2} \begin{bmatrix} 1 \\ -i \end{bmatrix} e^{(i\pi x/\Lambda)} \tag{2.44a}$$

$$\boldsymbol{E}_R = \frac{E_0}{2} \begin{bmatrix} 1 \\ i \end{bmatrix} e^{(-i\pi x/\Lambda)} \tag{2.44b}$$

where $\Lambda = \lambda_R/(2\sin\theta)$ is the modulation period, λ_R is the wavelength of the recording beams, and $\pm\theta$ is the incident angle of the recording beams. The Jones vector for the resulting polarization is given by $\boldsymbol{E} = \boldsymbol{E}_L + \boldsymbol{E}_R = E_0[\cos(\pi x/\Lambda), \sin(\pi x/\Lambda)]^T$. This spatially modulated polarization pattern can be directly recorded in a volume by illuminating polarization-senstive holographic materials, which can exhibit induced birefringence as a product of photochemical reaction. The most effective way to capture such a polarization

pattern is to record it in polarization-sensitive materials which then transfer their anisotropy

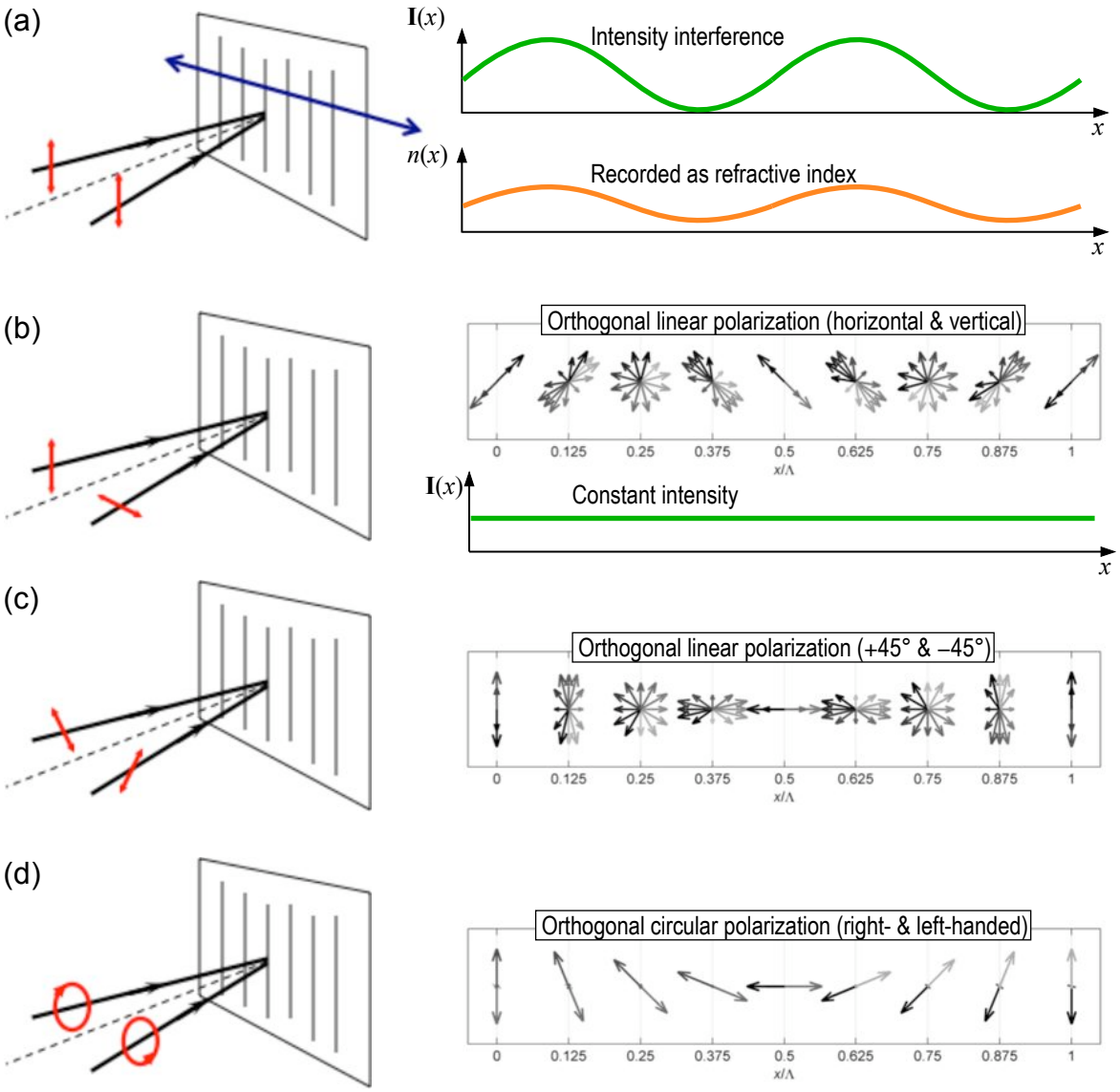

Figure 2.21: Polarization holograms by two beam interference with orthogonal polarizations: (a) classical intensity interference with two linear beams with the same polarization; (b)–(d) polarization interference patterns with two orthogonal beams with linear ((b) vertical & horizontal, (c) $+45°$ & $-45°$) and circular ((d) right- & left-handed) polarizations. While the intensity profile is captured as a modulated refractive index of the recording medium for the conventional holography, the polarization pattern is recorded as a distribution of the orientation of the induced birefringence.

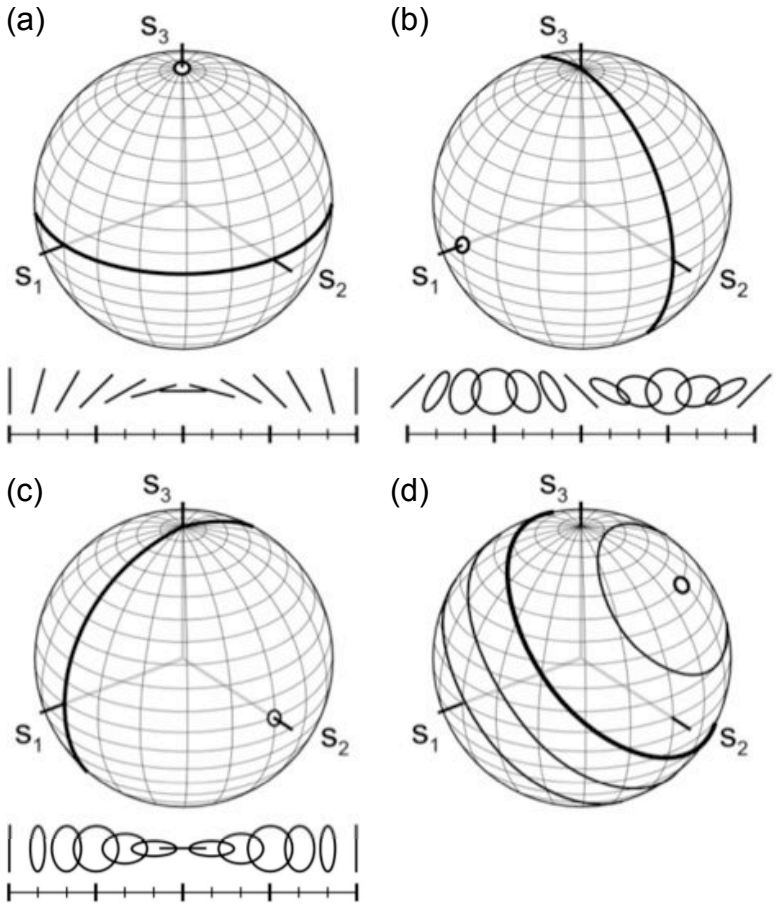

Figure 2.22: Polarization holograms represented on the Poincaré sphere. Polarization grating patterns created by two orthogonal beams with the same intensity can be described as great circles on the sphere (see (a)–(c)). An arbitrary polarization hologram can be also represented as circles on the sphere (see (d)).

to a liquid crystal layer via surface alignment of LCs.

2.4.4 Polarization holography & LC photoalignment: an effective fabrication method for creating PGs

The most popular means to create PGs is using polarization holography with anisotropic organic recording materials (especially azobenzene-containing polymers [14, 110, 111, 112]), among other materials [113, 114, 15]. PGs also can be formed by sub-wavelength features [99, 115]. Several related approaches use patterned surfaces to align a liquid crystal layer [116, 17, 10], which have recently been implemented experimentally with ideal optical

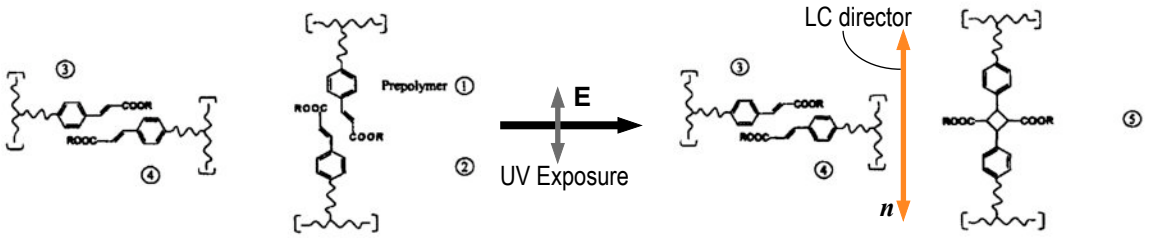

Figure 2.23: LC photoalignment using a linear photopolymerizable polymer (LPP). Anisotropic LPP-distribution via cross-linking on the function of linearly polarized UV exposure leads to directional alignment of LCs through Van der Waals interactions [68].

properties [18, 19, 11].

We have developed an effective fabrication method for creating defect-free PGs with ultra-high efficiency and low incoherent scattering by adopting polarization holography and liquid crystal materials. The key of the fabrication technique is the use of photo-alignment techniques that allow the separation of hologram recording and grating structure amplification and a careful optimization of materials (photoalignment materials, liquid crystals) and processing parameters (exposure doses, spin processing).

In particular, we utilize a linear photopolymerizable polymer (LPP) ROP-103/2CP (Rolic), which manifests a strong orientational photo-chemical reaction in response to the local direction of linearly polarized UV light [68]. Figs. 2.23(a) and 2.23(b) illustrate intermolecular reaction and the anisotropic molecular configuration, respectively, when the LPP is exposed with a linearly polarized UV light. This new alignment technology allows generation of high resolution azimuthal LC director patterns and optically patterned devices. A proper choice of the exposure fluence ($\mathrm{J{\cdot}cm^{-2}}$) is essential to obtain the strong alignment condition, which is degenrally dependent on the surface pattern and LC material properties.

We have developed PG fabrication processes for two different forms of a switchable cell and a polymer film as shown in Figs. 2.24(a)–2.24(e). We first prepare a thin (typically, $<$ 100nm) film of LPP on a glass substrate by spin-coating. The LPP substrate is then exposed to a polarization hologram from a UV laser (i.e., HeCd, 325nm) with orthogonal circular polarizations as shown in Fig. 2.24(b). The typical recording dose of choice is around a few $\mathrm{J{\cdot}cm^{-2}}$ depending on liquid crystal materials and grating parameters (i.e., thickness d and period Λ).

We use polymerizable liquid crystals (reactive mesogen, RM) to form a polymer PG (now called a RMPG). As shown in Figure 2.25(a), the fabrication of RMPGs proceeds with following four basic steps: first, a LPP layer is coated on a glass substrate; second, the LPP substrate is exposed to UV recording beams, leading to a polarization hologram for PG patterns; third, a RM mixture (including liquid crystal monomers, solvents, photo-initiators, and surfactants) is coated on the LPP layer and made to be aligned according to the surface pattern; finally, the RM layer is photopolymerized with a blanket ultraviolet exposure to permanently fix the largely structured optical anisotropy. Virtually any grating thickness can be achieved by multiple coating of thin RM layers while the maximum cell thickness ($\leq d_C$) is limited for LCPG samples. The resulting PG exhibits all the properties predicted by theory with unsurpassed fidelity; $>$ 99% first-order efficiency, $>$ 4000 : 1 polarization contrast ratio, and $<$ 0.1% incoherent scattering.

For a switchable liquid crystal PG sample (now called a LCPG), we prepare two ITO-glass substrates coated with a LPP layer and make a cell with a uniform gap (a few μm) (Fig. 2.25(b)). For the maximum diffraction efficiency ($\sim$ 100%), the cell gap can be designed for a half-wave retardation ($\Delta nd = \frac{1}{2}\lambda$) at a target wavelength. After UV exposure

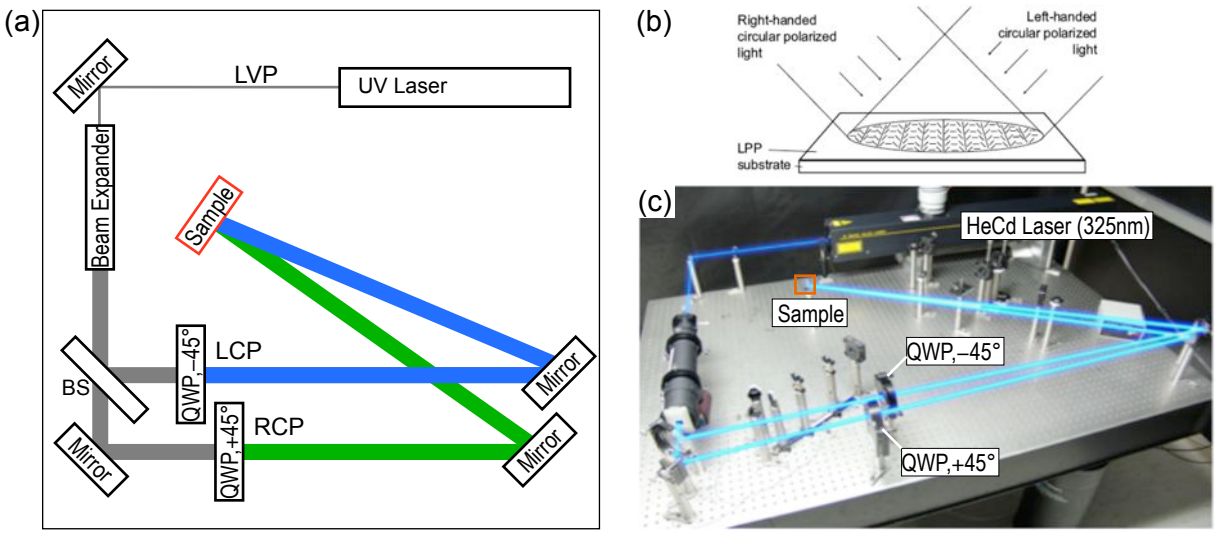

Figure 2.24: Holography setup for recording polarization gratings: (a) a modified Mach-Zehnder interferometer setup for UV holographic recording; (b) a polarization interference pattern recorded from two circularly polarized coherent beams; (c) our UV holography setup using a HeCd laser (325 nm).

to a polarization hologram (with two orthogonal, circularly polarized beams), we fill the cell with liquid crystals via capillary action, typically above the isotropic temperature. As cooling the cell, liquid crystal molecules are aligned by the surface pattern of the LPP layer to form a polarization grating profile. Applying a voltage above the threshold across the ITO electrondes, one can modulate light by altering the diffraction efficiencies. The electro-optical properties of LCPGs have been studied in both theory and experiments and referring readers to Refs. [9, 121, 130, 131] for details.

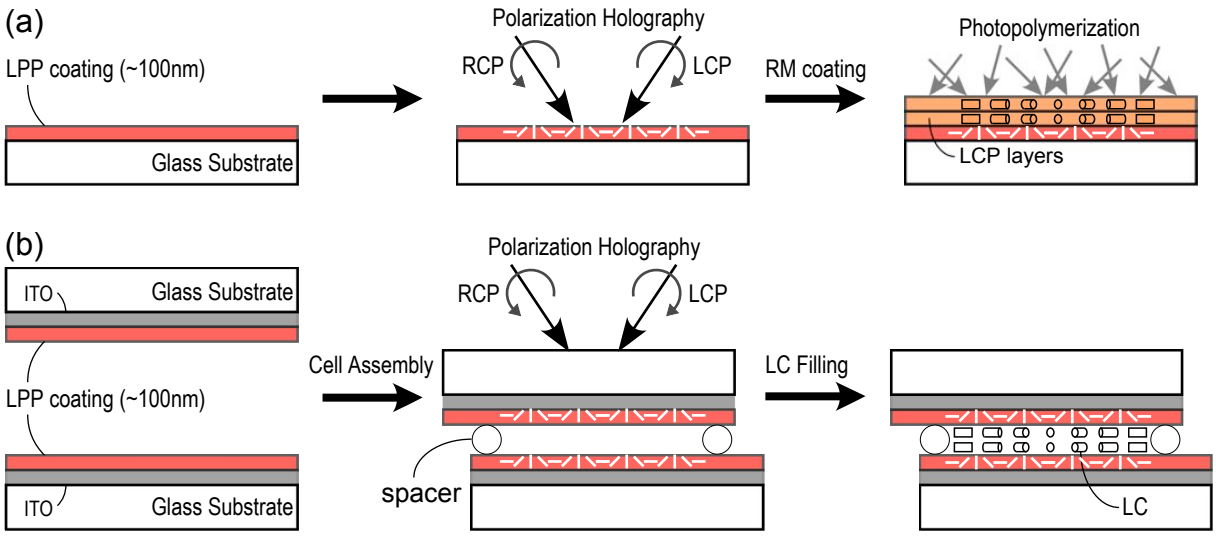

Figure 2.25: Fabrication of polarization gratings using polarization holography and photoalignment of LCs: (a) fabrication process for polymer RMPGs; (b) fabrication process for switchable LCPGs.

Chapter 3

Achromatic Polarization Gratings as Broadband Beam Splitters

3.1 Study on the diffraction limits of polarization gratings

We have done an extensive numerical analysis of the optical properties of PGs using the finite-difference time-domain (FDTD) method [132]. While concise analytic expressions for the diffraction properties of PGs have been derived [4, 6] using Jones calculus [26], these are limited by their assumptions to large grating periods, normal incidence, and infinite gratings. Furthermore, even the most unabridged coupled-wave analysis [93] is limited to slowly-varying envelopes, and has only been developed for pure volume holograms.

Most conventional gratings may fall into two grating regimes, *thin* or *thick* gratings, depending on both their material properties and physical structures. When a grating is well defined in one of these grating regimes, its behavior is usually well understood and analytical descriptions for optical properties (such as efficiency, diffraction angles) are often available for many grating types. These explanations, however, may fail to predict actual diffraction behavior of gratings in intermediate situations between the thin and thick grating regimes. Some literatures reported comprehensive studies on the effect of the grating retime on diffraction properties of phase gratings and suggested how to interpret given grating parameters to determine a proper grating regime [32, 34]. Still, no work adequately deals with the fundamental question of delineating the thin/thick grating regimes in anisotropic gratings.

Therefore, we focus to investigate two issues: First and most prominently, we seek to understand PG behavior as the grating period becomes comparable to the wavelength; Second, we predict the angular response and the behavior of a finite grating. To this end, we numerically analyze the PG diffraction using the open-source software package *WOLFSIM-Wideband OpticaL Fdtd SIMulator*, developed at NCSU for efficient modeling of periodic anisotropic media.

3.1.1 Numerical analysis of polarization gratings using the FDTD method

We have developed an efficient FDTD algorithm for wide-band analysis of periodic anisotropic media [133, 134], now available as an open-source software WOLFSIM [135]. WOLFSIM incorporates a two-dimensional 2D spatial grid containing media with an arbitrary three-dimensional, nondispersive permittivity tensor. Off-axis illumination, monochromatic and wideband Gaussian-pulse sources, and periodic boundaries are

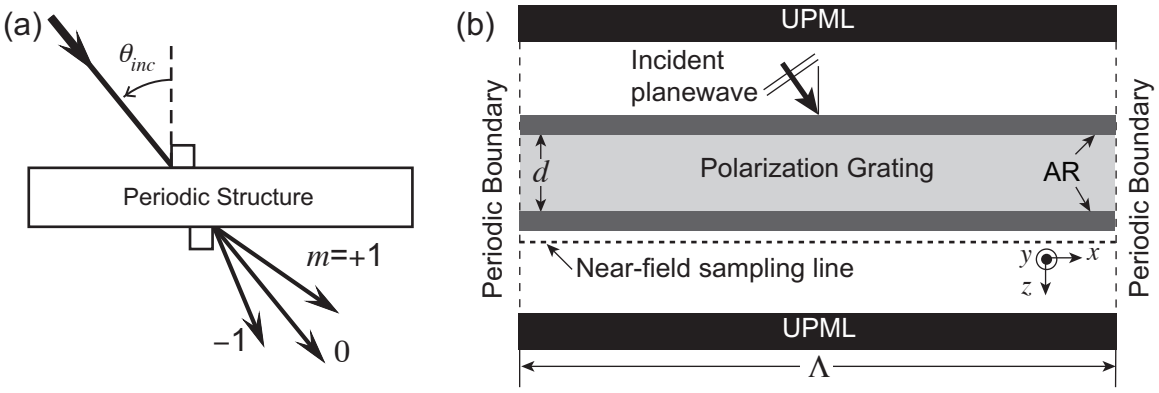

Figure 3.1: Numerical analysis of the polarization grating (PG) using the finite-difference time-domain (FDTD) method: (a) light diffraction from periodic structures at oblique incidence; (b) a layout of the FDTD simulation space. Note that the simulation space includes only one period of the PG structure (the x-width = Λ) for most our simulations.

explicitly incorporated.

We consider structures with 1D periodicity along the x-axis. Fig. 3.1 illustrates a 2D FDTD simulation space for PG analysis. The heart of the simulation is a modified split-field method, adapted for arbitrary anisotropic media with input illumination at a general angle of incidence. The finite simulation space is implemented by applying the periodic boundary conditions along the x-axis and placing uniaxial perfectly matched layers (UPML) at the boundaries along the z-axis. To appropriately isolate the effect of the PGs themselves from Fresnel reflection effects, we also place gradient-index antireflection layers [136] at the air-PG interfaces. The computational grid spacing Δu was selected as $\lambda_{min}/(20n_{max})$, where λ_{min} is the shortest wavelength of interest and n_{max} is the maximum index of refraction in the media. The time resolution was chosen as $\Delta t = \Delta u/3c$ to ensure numerical stability, where c is the speed of light. The expected accuracy of the FDTD simulation is 0.05% meansquare error. A more complete description of the details can be found in Ref. [7].

The diffraction angle θ_m of the m-order propagating wave (Fig. 3.1(a)) is determined by the grating equation $\sin\theta_m = m\lambda/\Lambda + \sin\theta_{inc}$, where θ_{inc} is the angle of incidence. The complex vector amplitude $\mathbf{E}_m$ in the far-field of the m-order propagating wave is calculated by a (Fourier) vector transformation applied to a line sampled immediately following the structure (defined explicitly in Eqs. (18) in Ref. [134]). Except where noted, diffraction

efficiencies (or intrinsic efficiencies) are calculated as the ratio of the intensity of wave m to the total intensity of the forward propagating waves:

$$\eta_m = |\mathbf{E}_m|^2 / |\mathbf{E}_{tot}|^2 \tag{3.1}$$

where $|\mathbf{E}_{tot}|^2 = \sum_{m=-\infty}^{+\infty} |\mathbf{E}_m|^2$.

We now revisit the analytic expressions for the diffraction efficiency of a circular PG (see Eqs. 2.43): $\eta_0 = \cos^2(\pi \Delta n_l d/\lambda)$ and $\eta_{\pm 1} = \frac{1}{2}(1 \mp S_3') \sin^2(\pi \Delta n_l d/\lambda)$, where λ is the wavelength, η_m is the diffraction efficiency of the m-order, Δn_l is the linear birefringence, d is the grating thickness, and $S_3' = S_3/S_0$ is the normalized Stokes parameter of the input light.

The numerically calculated diffraction efficiencies of a circular PG are shown in Fig. 3.2(a), compared to the analytic prediction. The grating parameters for the FDTD simulations are: $\Lambda = 20\lambda_0$, $d = 5\lambda_0$, $\bar{n} = 1.6$, and $\Delta n_l = 0.2$ (e.g., $\Lambda = 10\mu$m, $d = 2.5\mu$m for $\lambda_0 = 500$nm), where λ_0 is the center-wavelength of the input source. As expected, only three diffraction orders $(0, \pm 1)$ are non-zero ($> 0.01\%$), and the maximum first-order efficiency approaches 100% (actually 99.96%). We also verified the polarization states of each diffraction order; the 0-order has the same linear polarization state as the input and the $+1$- and -1-orders have right- and left-hand circular polarizations, respectively.

The polarization sensitivity of the first-orders is shown in Fig. 3.2(b), which plots the calculated first-order efficiencies for different ellipticity angles χ of the incident polar-

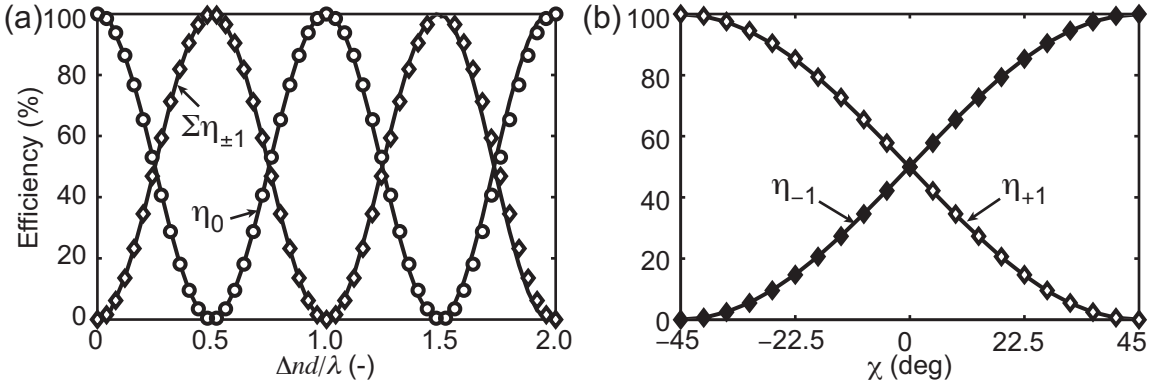

Figure 3.2: Diffraction behavior of a circular PG numerically calculated (curves) and analytically estimated (◯, ◇, and ♦) using Eqs. 2.43: (a) diffraction efficiency spectra as a function of the normalized retardation ($\Delta n_l d/\lambda$); (b) polarization response of the first-order efficiencies when $\Delta n_l d/\lambda = \frac{1}{2}$. ($\Lambda = 20\lambda_0$, $\bar{n} = 1.6$, $\Delta n_l = 0.2$)

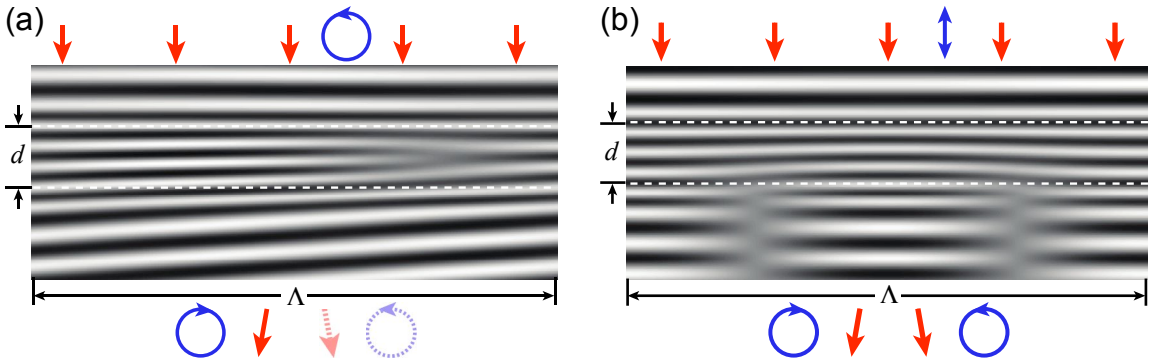

Figure 3.3: FDTD near-field maps of the electric fields from a circular polarization grating with circular (a) and linear (b) incident polarizations. ($\Lambda = 20\lambda$, $\bar{n} = 1.6$, $\Delta n_l = 0.2$, $d = 2.5\lambda$)

ization when $\Delta n_l d = \lambda/2$ (i.e., when $\eta_0 \simeq 0$). The ellipticity angle χ is related to the normalized Stokes parameter by $S_3' = \sin(2\chi)$. The FDTD electric field maps in the near field, captured using a monochromatic source, are presented in Figs. 3.3(a) and 3.3(b) for circular ($\chi = \pi/4$) and linear ($\chi = 0$) incident polarizations, respectively. Overall, the FDTD calculation correlates extremely well to the analytic expressions.

3.1.2 Beyond the paraxial approximation

While excellent agreement is observed between the FDTD results and analytical solutions for the paraxial case, the small-angle assumptions used in the derivation of Eqs. 2.43 suggest that they may not describe diffraction if Λ/λ becomes relatively small (and large diffraction angles). Several fundamental questions therefore remain unanswered: For what PG parameters do the analytic equations properly apply? Is the Klein parameter Q useful to distinguish grating regimes in PGs, or is another parameter more descriptive? For a given λ and Λ (or for a fixed diffraction angle), what choice of d, Δn_l, and $\bar{n}$ enables high efficiencies?

The best way to address these questions is to consider a parameter-space defined by the normalized retardation $\Delta n_l d/\lambda$ and grating period Λ/λ_0 (similar to Ref. [137] for phase gratings). This is essentially a summary of diffraction spectra versus grating period. In Fig. 3.4, we present a map of the total first-order diffraction for a relatively high ($\Delta n_l = 0.2$) and low ($\Delta n_l = 0.04$) birefringence. We plot the FDTD result as solid-line

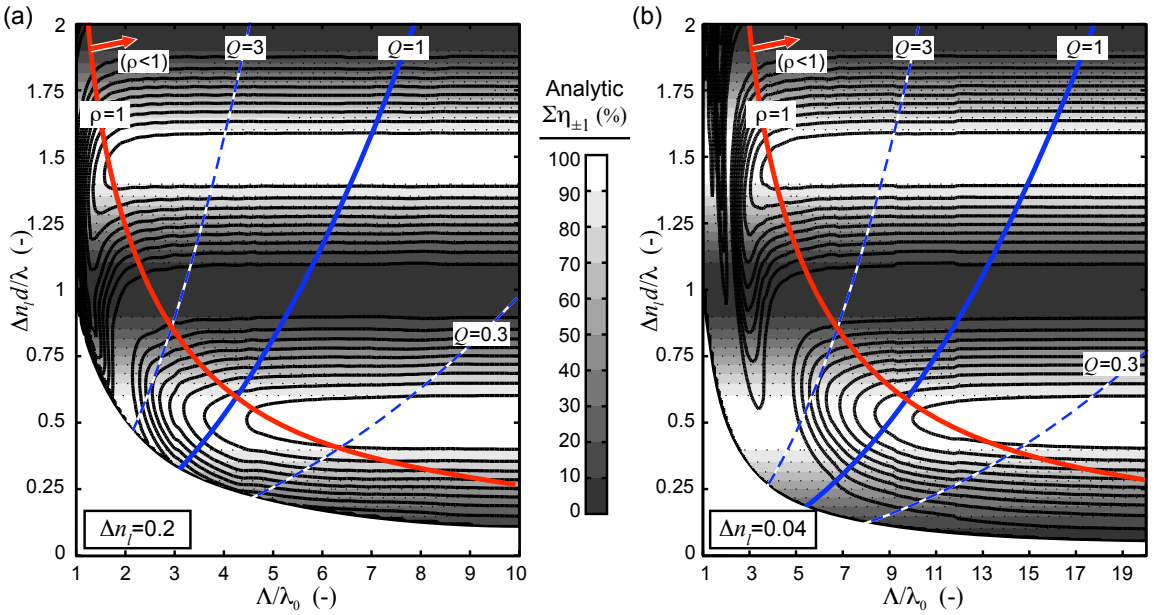

Figure 3.4: The behavior of the circular PG diffraction with respect to grating regime (thin or thick), from the perspective of Q and ρ parameters [33, 138, 34]. The contour plots show the total first-order diffraction $\Sigma\eta_{\pm 1}$ versus normalized retardation $\Delta n_l d/\lambda$ and normalized grating period Λ/λ_0. A comparison between numerical FDTD calculation (black solid-line contours) and analytical estimate (grayscale levels) is shown for a high ($\Delta n_l = 0.2$) and low ($\Delta n_l = 0.04$) birefringence in parts (a) and (b), respectively. We note that diffraction best follows the analytic expressions when $\rho < 1$, the thin-grating regime. (from Ref. [7])

contours, and plot the analytic expressions (Eqs. 2.43) as grayscale levels. Note that these are well correlated for larger values of Λ/λ_0, but become dramatically different for smaller grating periods.

The FDTD calculation was generated as follows: for each setting of Λ/λ_0, a Gaussian-pulsed planewave [134] was input with linear, vertical polarization, and the normalized spectral output ($\Sigma\eta_{\pm 1}$ versus $\Delta n_l d/\lambda$) was calculated. Additionally, $d = \lambda_0/2\Delta n_l$ and $\bar{n} = 1.6$.

It is instructive to segment this first-order efficiency map into grating regimes, often described as either *thin* or *thick*. In classical grating analysis, two dimensionless parameters Q [33, 138] and ρ [34] are frequently used to identify the grating regimes: $Q = 2\pi\lambda d/\left(\bar{n}\Lambda^2\right)$ and $\rho = 2\lambda^2/\left(\bar{n}\Delta n_l \Lambda^2\right)$. The contours of both parameters are superimposed on the map in Fig. 3.4.

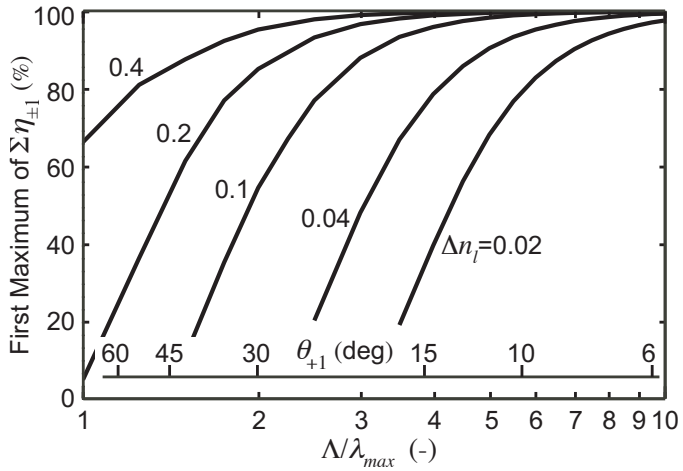

Figure 3.5: The first maximum of the first-order diffraction $\Sigma\eta_{\pm1}$ of the circular PG (calculated numerically). The normalization factor λ_{max} is the wavelength at which maximum diffraction occurs. Note that the axis for θ_{+1} shows the angle of diffraction for the given ratio Λ/λ_{max}.

The condition $Q < 1$ is most popularly used to identify the thin-grating (Raman-Nath) regime, and it is appropriate to note that the analytic equations (Eqs. 2.43) correspond well to the FDTD solution under this same condition. However, it is important to note that this is sufficient, but not necessary: for some regions with $Q > 1$, it is still possible for the FDTD solution to be nearly identical to the analytic solutions (especially for larger values of $\Delta n_l d/\lambda$). This suggests that Q is not the best indicator of the thin-grating regime boundary. In fact, this is generally true for phase gratings [34], but is particularly noticeable in circular PGs since their birefringence can be high.

A contour for the parameter $\rho = 1$ is also shown in Fig. 3.4. Note that because the FDTD and analytic solutions correlate strongly when $\rho < 1$, this parameter is the most robust indication of when Eqs. 2.43 are valid. The usefulness of ρ over Q is particularly important when large diffraction angles are desired (i.e., Λ/λ approaching 1). Assuming normally-incident light, we therefore predict that the following conditions must be met for $\approx 100\%$ diffraction in PGs: $\rho < 1$ and $\Delta n_l d/\lambda = \frac{1}{2} + a$, where a is a non-negative integer.

A complementary view of circular PG behavior is shown in Fig. 3.5. A series of FDTD simulations were performed with a normally-incident, linearly polarized, Gaussian-pulsed planewave input for a range of Λ and Δn_l. The first maximum of the first-order

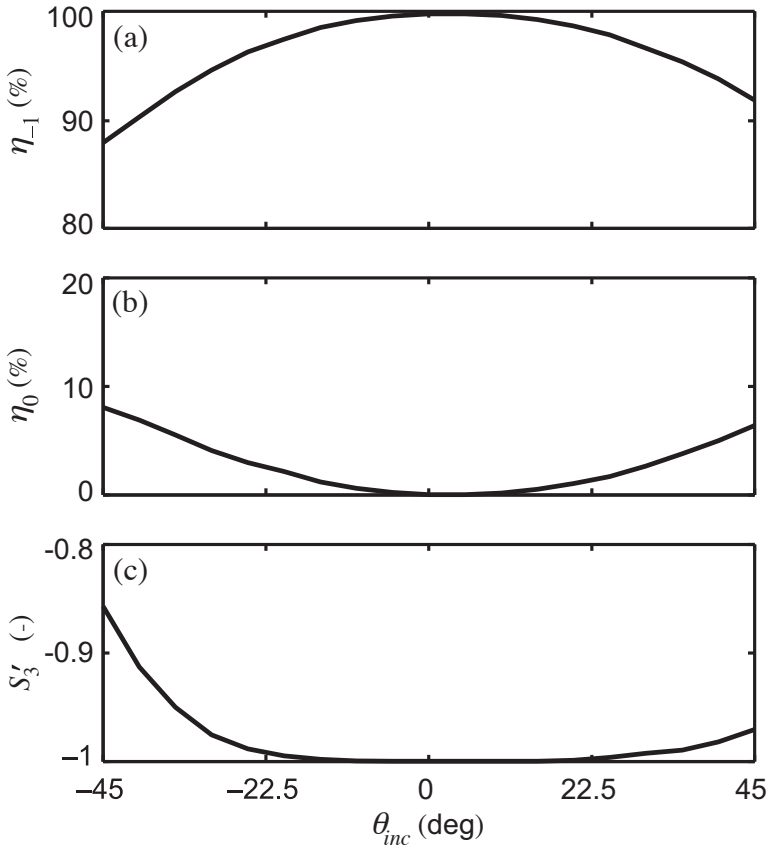

Figure 3.6: Angular response of a circular PG when illuminated at oblique incidence with right-handed circular polarization input ($\chi = 45°$): (a) First-order and (b) zero-order diffraction efficiency; (c) Polarization state of the diffracted -1-order. PG parameters are set for halfwave retardation. ($\Lambda = 20\lambda$, $d = 5\lambda$, $\bar{n} = 1.6$, and $\Delta n_l = 0.2$)

diffraction efficiency $\Sigma\eta_{\pm 1,max}$ (which appears at or near the $\Delta n_l d/\lambda = 0.5$ line in Fig. 3.4) decreases as Λ approaches λ. We normalize with respect to the actual wavelength λ_{max} at which each maximum occurs. One apparent lesson about circular PGs is therefore that materials that possess a high linear birefringence are needed in order to achieve high diffraction efficiencies *and* large diffraction angles. We will return to this topic in latter Section 3.4 with experimental demonstration of highly efficient, small-period grating using liquid crystal materials with high Δn_l values.

The angular response is shown in Fig. 3.6, where the impact of oblique illumination is highlighted (a topic not yet theoretically studied, to our knowledge). For small angles of incidence θ_{inc}, only the -1-order has appreciable power ($\approx 100\%$) and manifests a nearly

perfect right-handed circular polarization ($S_3' \simeq 1$). For $|\theta_{inc}| > 20°$, the -1-order efficiency decreases (with the leakage passing into the 0-order), and its polarization state becomes increasingly elliptical. We note that the angular response is asymmetric with respect to $\theta_{inc} = 0$. We consider all of these off-axis effects as being primarily related to a change in the effective optical path length experienced by the incident lightwave as θ_{inc} increases. We also note that the $+1$-order remains very small (≤ 1) for all the cases.

In many application contexts (most notably in displays [97, 98]), finite-size PGs are inherently involved because the transverse direction of the grating is bounded in some way (e.g., by pixel edges). It is therefore important to quantify the diffraction of this finite grating as its lateral size L becomes comparable to the grating period Λ. To accomplish this, we have created a pixel model by surrounding a circular PG in the lateral direction by absorbing materials.

The near-field and far-field diffraction of an example pixel ($L = 2\Lambda$) with a Circular PG ($\Lambda = 10\lambda$, $\Delta n_l d = \lambda/2$ and $\bar{n} = 1.6$) and an isotropic dielectric slab are shown in Figs. 3.7(a) and 3.7(b), respectively. A monochromatic planewave with right-hand circular polarization was input with normal incidence, and the far-field intensity calculated with the standard Kirchhoff integral method for finite apertures (e.g., Ref. [2]). Since the far-field intensity profiles follow the classical single-slit aperture diffraction ($I(\theta) \propto$

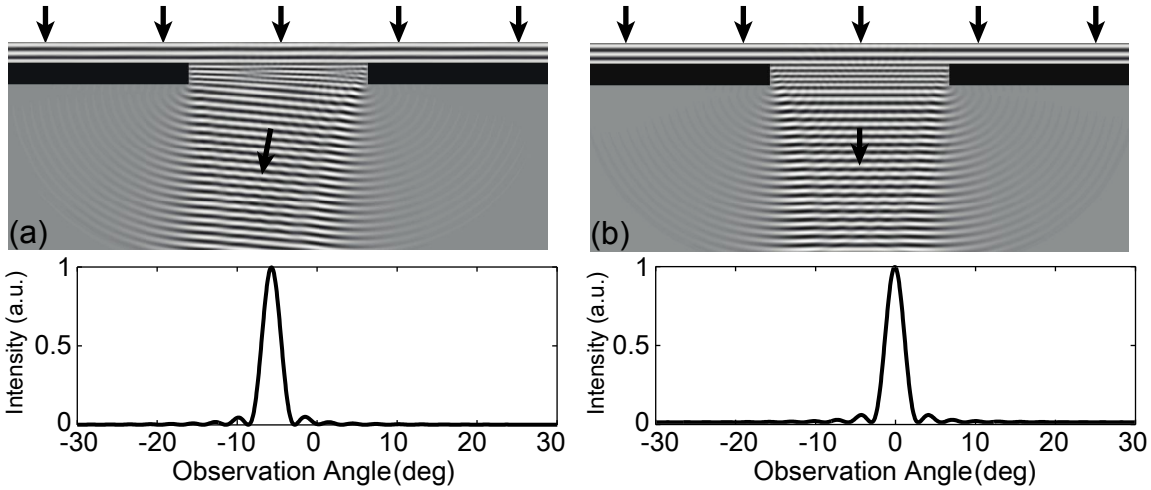

Figure 3.7: Diffraction behavior of finite circular PGs with circularly polarized light: (a) FDTD near-field map of a pixelated circular PG with two periods ($L = 2\Lambda$, $\Lambda = 10\lambda$); (b) FDTD near-field map of a dielectric slab with the same width.

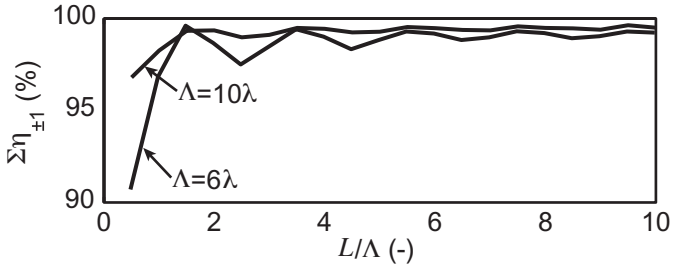

Figure 3.8: The diffraction efficiency of finite circular PGs with two different pixel widths ($\Lambda = 6\lambda$ and $\Lambda = 10\lambda$).

$\mathrm{sinc}^2\left(\pi \sin(\theta - \theta_m)L/\lambda\right)$, with $\theta_m = 0$ for the dielectric slab), the diffraction efficiency is no longer strictly a scalar. However, we can still make useful comparisons between the two cases of Fig. 3.7 by defining the diffraction efficiency for finite PGs as:

$$\eta = \frac{(I_{peak}/I_{tot})_{PG}}{(I_{peak}/I_{tot})_{SLAB}}, \tag{3.2}$$

where I_{peak} and I_{tot} are the maximum and total intensities in the far-field in the two simulations. In this way, we isolate the diffraction effect of the grating as opposed to the aperture.

Fig. 3.8 shows the -1-order efficiency when $\Lambda = 10\lambda$ and 6λ. As might be expected, we observe that as L/Λ increases, the efficiency asymptotically approaches the value (99.5%) of the comparable infinite PG. Furthermore, a weak oscillation away from this maximal value becomes increasingly pronounced for smaller grating periods (Λ/λ). However, this analysis suggests that a high efficiency can still be achieved even with a small pixel size (e.g. $L \approx 12$ μm, for $\lambda = 550$ nm and $\Lambda = 3.3$ μm).

This work is the first rigorous numerical analysis of polarization gratings and presents their diffraction behavior on a fundamental level with as few assumptions as possible. Using our newly developed FDTD method for periodic anisotropic media, we found strong correspondence with the analytic expressions previously developed for 'thin' PGs (i.e., with small diffraction angles and normally incident illumination). We explored the thin-thick grating regime transition, and identified $\rho < 1$ as the most robust condition (as opposed to $Q < 1$) to delineate the grating regime. It is also apparent that materials with large linear birefringence are most likely to support a high diffraction efficiency and large diffraction angle simultaneously. In studying off-axis illumination, we found that PGs can

retain high diffraction efficiencies for modest incident angles ($< 20°$). We also studied the behavior of a finite grating, and found that first-order diffraction remains nearly identical in magnitude to that of a comparably small aperture (i.e. high diffraction efficiency occurs even for only a few grating periods). We also present further numerical analysis of a different type of polarization gratings comprising of both linear and circular birefringence (namely, 'linear' PGs) in Appendix A.

3.2 Achromatic diffraction by self-compensated twisted polarization gratings

Since its first appearance in literature, many aspects of the polarization grating which are not available in classical scalar diffractive elements have been recognized by different groups of researchers, and recent advances in fabrication technologies significantly improve or even eliminate problems associated with fabrication challenges (i.e., incoherent scattering, limited grating period, and discontinuity of birefringence profile), which often result in poor optical properties. In last five years, we have developed fabrication process for high-quality PGs using UV polarization holography and photoalignment of LC materials. We routinely make PGs with a wide range of grating periods (typically, from 2 μm to 20 μm) as electrically controlled liquid crystal devices and thin liquid crystal polymer films depending on requirements for different applications. Our numerical study of the circular PG also suggests a more realistic guideline for the design of grating parameters (i.e., thickness, period, and birefringence) along with the elastic continuum analysis that provides a prediction of the physical behaviors of liquid crystal molecules (i.e., alignment condition, voltage threshold, and switching times).

Wavelength sensitivity of diffraction efficiency is often a concern in applications where broadband illumination is required (i.e., white light). A circular PG shows a modest bandwidth for high efficiency as compared with conventional phase gratings (but substan-

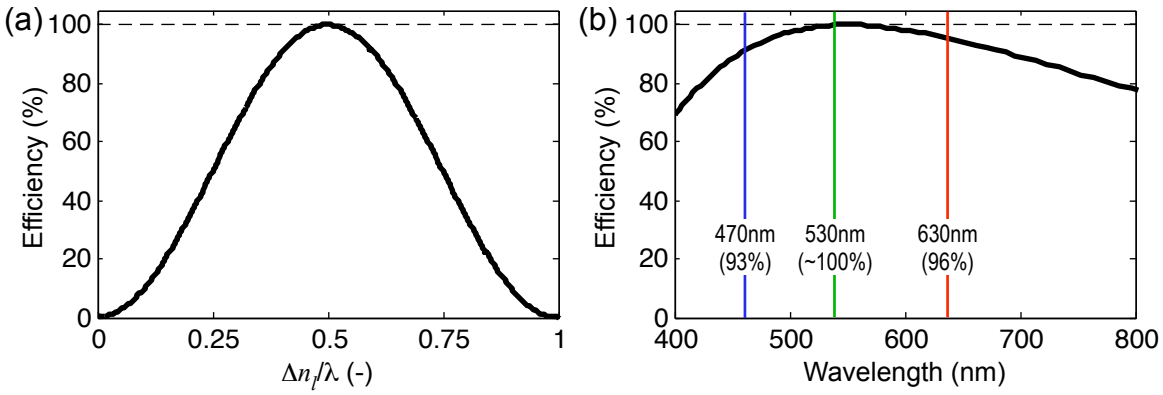

Figure 3.9: Wavelength sensitivity of the diffraction efficiency of a circular PG: the first-order efficiency as a function of (a) retardation ($\Delta n_l d/\lambda$) and (b) wavelength.

tially broader than Bragg or volume-holographic gratings that show similar high efficiency). Since the PG operates on a spatial modulation of local polarization states by retardation of the medium (i.e., liquid crystals), its spectral characteristics rely on the optical retardation that light at different wavelengths experiences while propagating through the PG. Fig. 3.9(a) shows the first-order efficiency as a function of retardation ($\Delta n_l d/\lambda$). It is clear that the maximum efficiency can be obtained when $\Delta n_l d = \lambda/2$ and high efficiency is available only near the center wavelength. For a PG optimized for $\sim$ 100% at a green wavelength ($\sim$530 nm), small but apparent reductions of efficiency are predicted for other visible wavelengths (i.e., 93% at 470 nm, 96% at 630 nm) as shown in Fig. 3.9(b). Broadband designs, therefore, are desired to make the nearly ideal PG properties available for all wavelengths of interest. An interesting design of achromatic gratings was proposed by Lajunen et al. [139, 21]. The suggested design approach using subwavelength features, however, is limited by no practical method of creating fine structures (i.e., few nanometers for optical frequencies).

Here, we demonstrate a broadband, thin-film, polarizing beamsplitter (Fig. 3.10(a)) based on an anisotropic diffraction grating composed of reactive mesogens (polymerizable liquid crystals). This achromatic polarization grating (PG) manifests high diffraction efficiency ($\sim$100%) and high extinction ratio ($\geq$1000:1) in both theory and experiment. We show an operational bandwidth $\Delta\lambda/\lambda_0 \sim 56\%$ (roughly spanning visible wavelength range) that represents more than a four-fold increase of bandwidth over conventional PGs (and significantly larger than any other grating). The diffraction angle and operational region (visible, near-infrared, mid-wave infrared, and ultraviolet wavelengths) may be easily tailored during fabrication. The essence of the achromatic design is a stack of two chiral PGs with opposite twist sense, and employs the principle of retardation compensation. We fully characterize its optical properties and derive the theoretical diffraction behavior.

This achromatic PG comprises two antisymmetric chiral circular PGs with opposite twist sense, where the nematic director $\mathbf{n}$ follows

$$\mathbf{n}(x,z) = [\cos\phi(x,z),\ \sin\phi(x,z),\ 0] \tag{3.3a}$$

$$\phi(x,z) = \begin{cases} \pi x/\Lambda + \Phi\, z/d & \text{if } 0 \leq z \leq d \\ \pi x/\Lambda - \Phi z/d + 2\Phi & \text{if } d < z \leq 2d \end{cases} \tag{3.3b}$$

where ϕ is the azimuth angle of the director field, Λ is the grating period, d is the thickness, and Φ is the twist angle of each chiral layer. Figs. 3.10(b) and 3.10(c) illustrate this profile.

Reactive mesogens [53] are ideal to create this anisotropy pattern since their orientation can be initially established by surfaces and chiral dopants, and indefinitely fixed via photo-polymerization.

3.2.1 Achromatic design of polarization gratings

The diffraction efficiency η_m of order m may be calculated using Jones calculus under the paraxial (small-angle) approximation, a method employed previously by several authors for conventional PGs [6, 19, 103]. Since the derivation for our anisotropy profile (Eq. (3.5)) involves lengthy expressions, here we will only summarize the approach and include the final result (referring the reader to Ref. [140] and Appendix B for details). First, we find the spatially-varying 2×2 transfer matrix $\mathbf{T}_{APG}(x)$, incorporating all grating geometry and material anisotropy. The achromatic PG profile is expressed as multiple thin layers of Circular PGs with a small lateral phase shift between them, akin to the analysis of twisted nematic LC modes as stratified media [30]. Second, we find the electric field of diffraction order m far from the grating as $\mathbf{D}_m = (1/\Lambda)\int_0^{\Lambda} \mathbf{T}_{APG}(x)\mathbf{E}_{in}e^{-i2\pi mx/\Lambda}dx$. Finally, we determine the diffraction efficiency as $\eta_m = |\mathbf{D}_m|^2/|\mathbf{E}_{in}|^2$, which may be analytically summarized by the following:

$$\eta_0 = \left[\cos^2(X) + \left(\Phi^2 - \Gamma^2\right)\mathrm{sinc}^2(X)\right]^2 \tag{3.4a}$$

$$\eta_{\pm 1} = A^2\left(\frac{1 \mp S_3'}{2}\right)\left(\cos^2(X) + \Phi^2\mathrm{sinc}^2(X)\right) \tag{3.4b}$$

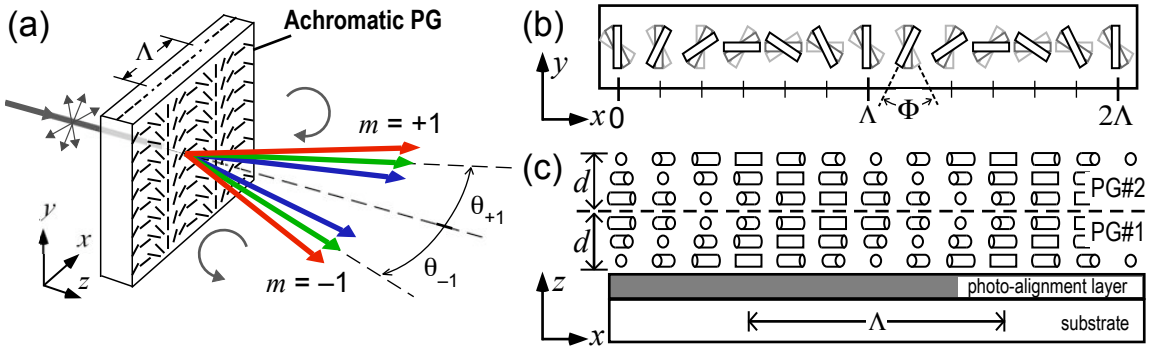

Figure 3.10: Achromatic polarization grating (PG): (a) diffraction geometry (note only the $m = \pm 1$ orders emerge; nematic director profile (a) plan- and (b) side-view.

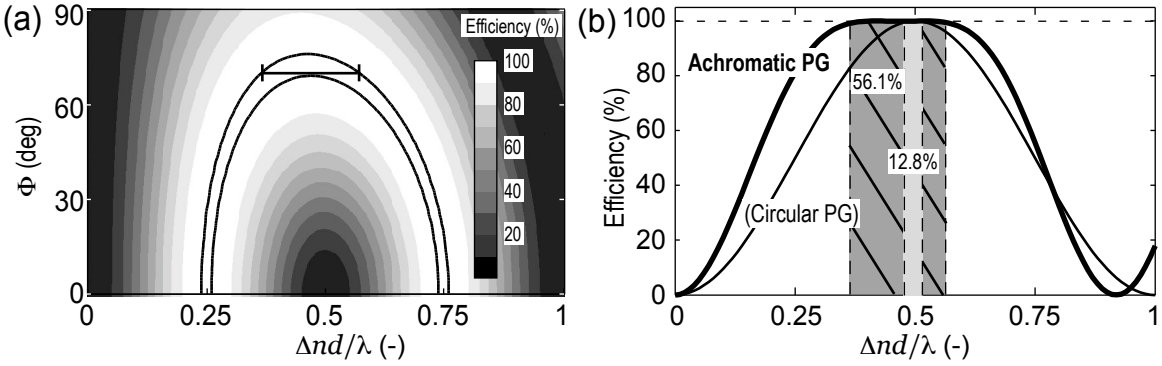

Figure 3.11: Theoretical diffraction of the achromatic PG: (a) First-order efficiency spectra vs twist angle Φ ($\Sigma\eta_{\pm 1} \geq 99\%$, red outlined region); (b) First-order efficiency spectrum for $\Phi = 70^\circ$ compared to the circular PG.

where $\Gamma = \pi\Delta n_l d/\lambda$, $X = \sqrt{\Phi^2 + \Gamma^2}$, $A = 2\Gamma \mathrm{sinc} X$, and $\mathrm{sinc}(X) \equiv \sin(X)/X$. The term $S_3' = S_3/S_0$ is a normalized Stokes parameter. The grating equation $\sin\theta_m = m\lambda/\Lambda \pm \sin(\theta_{inc})$ governs diffraction angles (Fig. 3.10(a)).

Several important properties should be noted in Eqs. (3.4) and in Ref. [141]. *First*, only three diffraction orders (0 and ± 1) exist, which depend on both the retardation $\Delta n_l d/\lambda$ and the twist angle Φ. We will show that $\Sigma\eta_{\pm 1} \approx 100\%$ over a wide wavelength range by balancing the effect of retardation and twist. *Second*, the first-orders have orthogonal circular polarizations (Fig. 3.10(c)). *Third*, the first-order efficiencies are strongly sensitive to the incident polarization state through S_3' (akin to circular PGs). *Overall*, we understand the achromaticity of the two antisymmetric chiral layers as self-compensation, via counteracting chromatic dispersions in the linear and twist-induced circular birefringences [142].

To enable quantitative evaluation, we define bandwidth as $\Delta\lambda/\lambda_0$, the ratio of the spectral range $\Delta\lambda$ (over which high diffraction efficiency $\Sigma\eta_{\pm 1} \geq 99\%$ occurs) to the center wavelength λ_0. We employ Eq. (3.4b) to generate a map of total first-order diffraction efficiency as a function of the retardation and the twist angle (shown in Fig. 3.11(a)). The maximum bandwidth ($\simeq 56.1\%$) for $\geq 99\%$ efficiency is found when $\Phi = 70^\circ$. Note, this is more than a four-fold enhancement as compared with a conventional Circular PG ($\simeq 12.8\%$), as shown in Fig. 3.11(b) with relative bandwidths highlighted. Numerical studies at oblique incidence and near the paraxial limit are also found in Ref. [140].

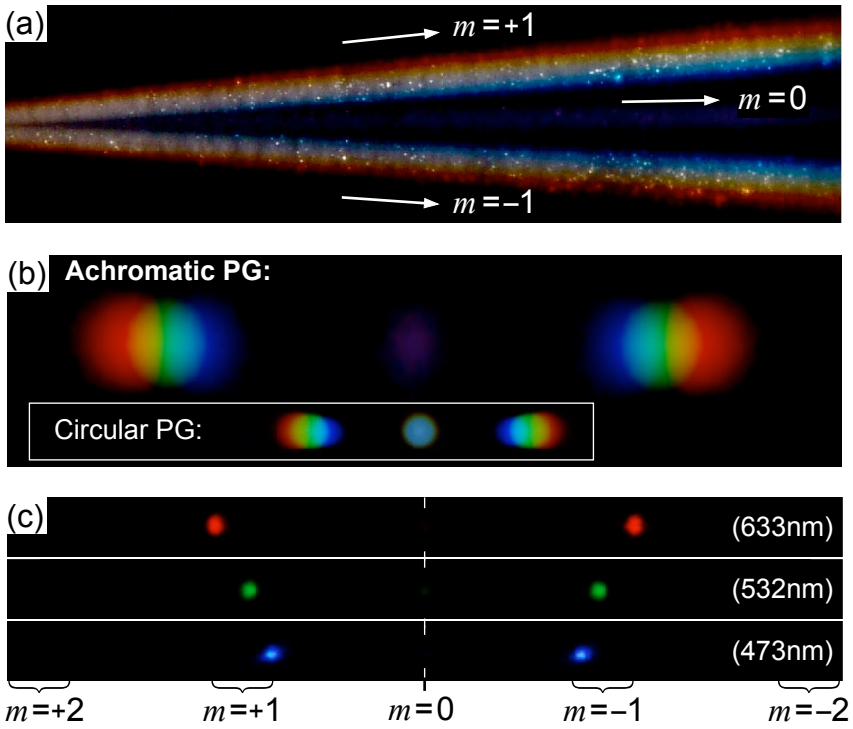

Figure 3.12: Photographs of achromatic PG diffraction: unpolarized, white LED light, as seen from (a) plan-view (intersecting a white card), and (b) projected screen-view; and (c) linearly polarized laser light. ($\Lambda = 6.5$ μm)

3.2.2 Fabrication of achromatic polarization gratings

We have experimentally realized this achromatic PG formed as a reactive mesogen (RM) film by polarization holography and photo-alignment techniques. Again, we utilized a linear photopolymerizable polymer (LPP) [68] ROP-103 (Rolic) as a photo-alignment material. The surface alignment pattern with a period of $\Lambda = 6.5$ μm was recorded in the LPP layer by orthogonal circular-polarized beams from a HeCd laser (at 325 nm). After holographic exposure, RM films were spin-coated on the LPP-coated substrate. The first PG layer was composed of the RM prepolymer/solvent mixture RMS03-001 (Merck, $\Delta n_l \simeq 0.159$ at 589 nm) doped with a small amount (0.34%) of the chiral molecule CB15 (Merck, right-handed). A thickness $d \simeq 1.7$ μm was chosen so that halfwave retardation $\Gamma = \pi/2$ (at $\lambda \simeq 550$ nm) and a twist $\Phi = +70^\circ$ occurred simultaneously. The second PG layer was deposited directly on the top of the first, and was composed of RMS03-001 doped with a small amount (0.25%) of the chiral molecule ZLI-811 (Merck, left-handed),

resulting in the same thickness and opposite twist angle ($\Phi = -70°$). As these RM films are highly crosslinked acrylate films, they are known [49, 53] to have high thermal and optical stability. Reproducibility and fabrication process sensitivity are similar to other spin-coated RM films.

These achromatic PGs exhibit practically ideal properties, with high first-order efficiency, high polarization selectivity, low scattering, and low non-first-order leakage. As shown in Fig. 3.12, nearly 100% of incident light can be directed into the first-orders alone, for both light-emitting-diode (LED) and laser light (wavelengths in Fig. 3.12(c)). Note the substantially reduced zero-order leakage of the achromatic PG compared to the circular PG (see Fig. 3.12(b)). Note also that both unpolarized and linearly polarized light are split equally (since $S_3' = 0$).

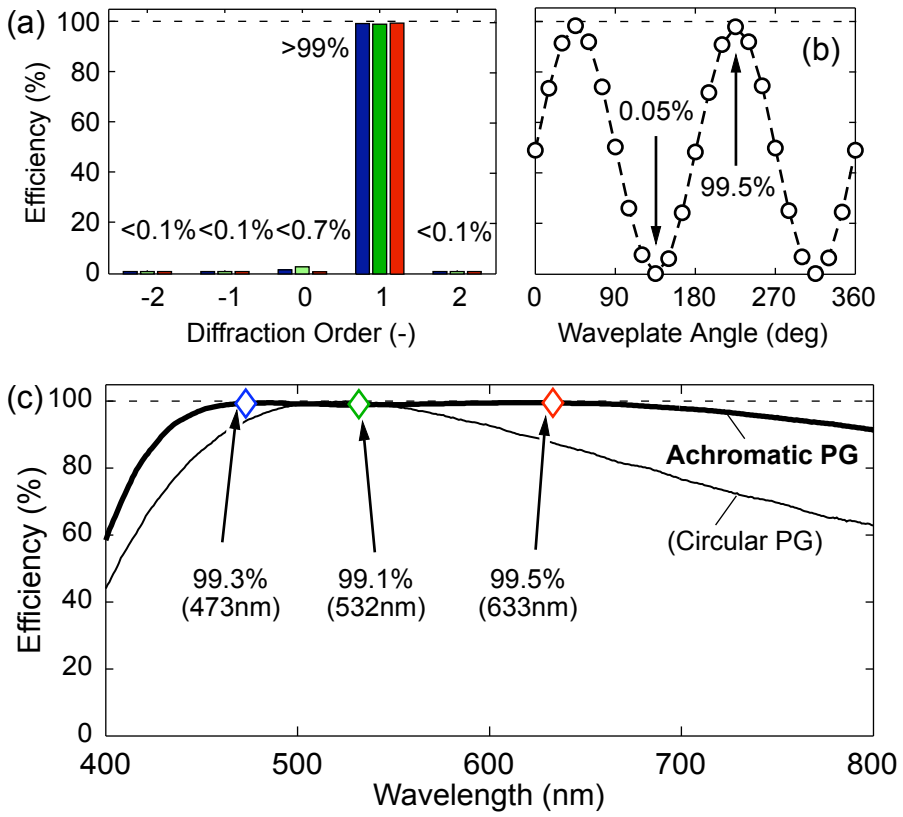

Figure 3.13: Measured diffraction of the achromatic PG: (a) the efficiencies with circularly-polarized incident laser light (same wavelengths as in Fig. 3.12(c)); (b) the polarization sensitivity of the $m = +1$ order with a rotating quarter-waveplate, and (c) the first-order efficiency spectrum from spectrometer (curves) and laser (diamonds) measurements.

The measured diffraction efficiencies of the achromatic PG with circularly-polarized incident laser light are summarized in Fig. 3.13(a). Very high efficiencies of $\geq 99\%$ within a single order ($m = +1$) were observed throughout the visible spectrum (since $S_3' = -1$). Most other diffraction orders ($m = -2, -1, +2$, and higher) manifest $\leq 0.1\%$, while the worst case leakage of $< 0.7\%$ arose in the zero-order ($m = 0$) for the green wavelength. We define diffraction efficiency as $\eta_m = I_m / I_{REF}$, where I_m is the measured intensity of the m^{th} transmitted diffracted order, and where I_{REF} is a reference transmission intensity for a glass substrate. Incoherent scattering was measured as $\leq 0.3\%$ above 400 nm.

We also measured the polarization sensitivity of the first-orders, by arranging and rotating quarter-waveplates in between the achromatic PG and the linearly-polarized lasers. Fig. 3.13(b) shows the +1-order response for the red laser (as the best example wavelength). The efficiency varies as the incident light is varied from linear ($\simeq 50\%$), to circular ($\simeq 99.5\%$, right handed), to linear ($\simeq 50\%$), and finally back to circular ($\simeq 0.05\%$, left handed). The extinction ratio is therefore $99.5/0.05 \simeq 2000 : 1$ (or 33 dB), an excellent measure for polarizing beamsplitters of any kind. The green and blue wavelengths were slightly lower, but nevertheless maintained $\geq 1000 : 1$ (30 dB) extinction ratios.

Finally, we examined the spectrum of the achromatic PG by measuring η_0 using a spectrophotometer (with $\eta_{|m|\geq 1}$ blocked) and estimating $\Sigma\eta_{\pm 1} \simeq 100\% - \eta_0$ (due to the difficulty of its direct measurement). The result is shown in Fig. 3.13(c), with the exact efficiencies measured using lasers (which match up well). The achromatic PG clearly manifests high diffraction efficiency ($\geq 99\%$) across almost all visible wavelengths, which is a substantial improvement over the conventional circular PG.

3.2.3 Electrically switchable achromatic liquid crystal polarization gratings on reflective substrates

We also report on our successful implementation of electrically switchable achromatic LCPGs on a reflective substrate (Fig. 3.14), which manifest polarization-independent modulation with high efficiencies ($\geq 95\%$). To pattern a spiraling, periodically varying LC profile, we utilize polarization holography and photoalignment techniques. Use of reflective substrates enables the same retardation compensation of double-layer achromatic PGs. In addition, perhaps most importantly, the single cell structure allows the electro-optical switching/modulation by applying an electric field across the cell. The achromatic LCPG

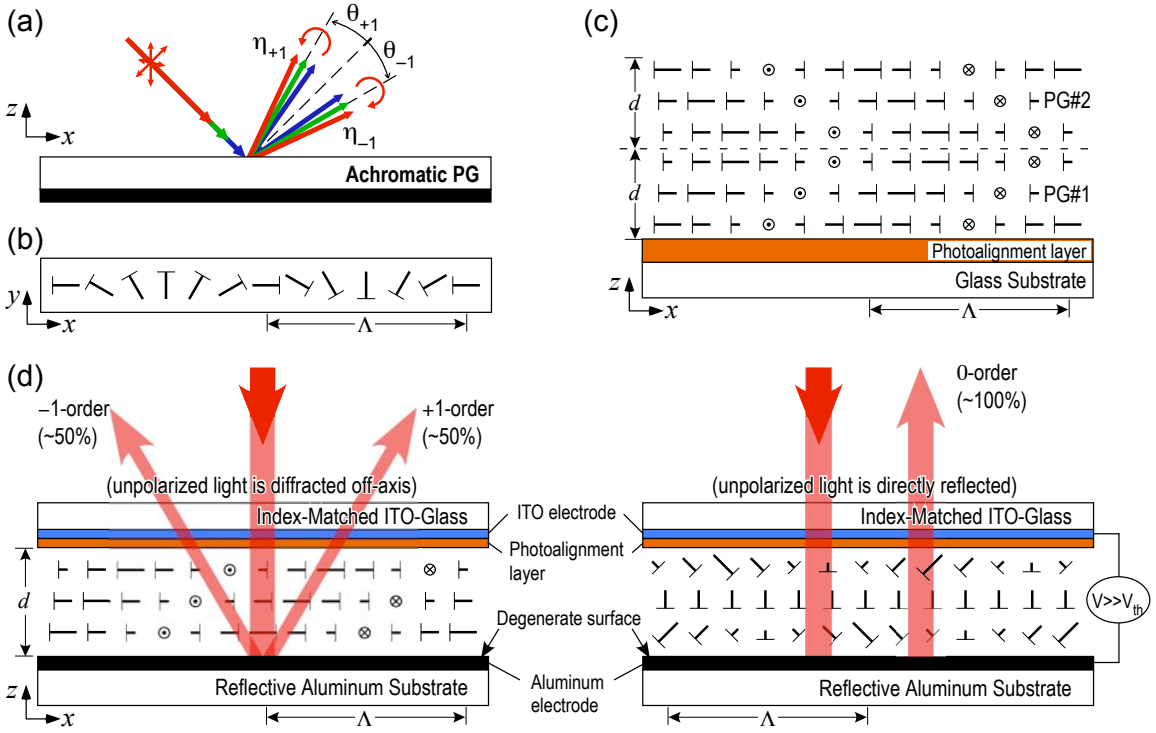

Figure 3.14: Basic structure and light switching of a reflective achromatic LCPG: (b) diffraction from reflective achromatic PGs; (b) a spiraling, periodically varying anisotropy profile of Circular PGs; (c) a schematic view of transmissive achromatic PG; (d) a reflective achromatic LCPG and its electro-optical switching.

sample shows steeper voltage responses and less spectral shifts while operating in grayscale with respect to previously reported LCPGs. Relatively faster switching times (∼6 msec for 3 μm-thickness) were measured compared to a conventional LCPG with the same thickness (∼10 msec). Interesting electro-optical behaviors were also observed including zero-voltage threshold and a hysteresis in the voltage response.

We introduce a simple but effective way to implement a reflective version of the achromatic PG. Use of a reflective substrate effectively captures the self-compensation of retardation dispersion within a single cell. In addition, the degenerate surface allows to control the twist angle only by the amount of chiral dopants without precision substrate registrations. The achromatic LCPG consists of a cell structure of a transmissive substrate with a LC alignment layer on a transparent electrode (i.e., ITO) and a reflective substrate (i.e., aluminum coated glass), whose surface is treated for degenerate anchoring of LCs.

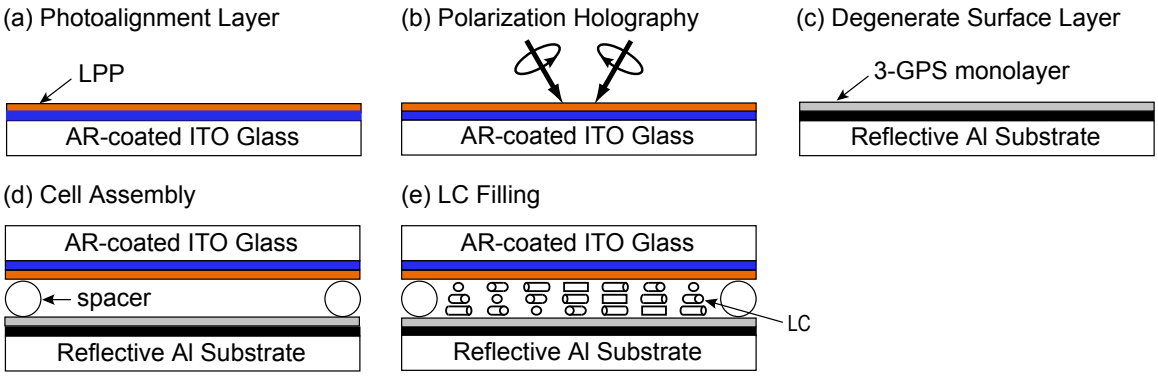

Figure 3.15: Fabrication procedures for reflective achromatic LCPGs using the polarization holography and photo-alignment techniques for LCs. A spiraling anisotropy profile is patterned on the photoalignment layer (LPP) surface and the reflective surface is coated with 3-GPS for for degenerate anchoring of LCs. Then, both substrates are assembled to form a cell to fill with LC mixtures.

The cell thickness d is determined to deliver a half-wave retardation (i.e., $\Delta n_l d = \lambda/2$) and a proper twist angle ($\sim 70°$). The cell is filled with a nematic liquid crystal mixture, which are doped with chiral agents, to form the grating as shown in Fig. 3.14(d), which is controlled by surface alignment and amount of chiral dopants in the LC mixture.

The following process was used for the results reported here(Fig. 3.15. An index-matched ITO glass substrate (from Thin Film Devices Inc.) with a broadband AR coating was used to minimize Fresnel losses due to index mismatch (i.e., reflections at an air-glass interface). We coated the ITO substrate with a photoalignment material ROP103-2CP (from Rolic, with standard recommended coating processing). A HeCd laser (325 nm) delivering a dose of 5 J/cm^2 with orthogonal circularly polarized beams was used to expose a surface periodic alignment pattern with a period of Λ =9 μm. A standard aluminum-coated glass substrate (from Edmund Optics) was coated with (3-glycidoxypropyl) trimethoxysilane (also called 3-GPS) to form a dense, homogeneous monolayer, which allows in-plane degenerate surface anchoring of LCs. The ITO and Al substrates were assembled to to form a 3 μm-thickness cell. We prepared a LC mixture of nematic liquid crystal MLC-12100-000 (from Merck, Δn_l = 0.113, T_{NI} = 92 °C, K_1 = 11.4 pN, K_3 = 13.8 pN, $\Delta\varepsilon$ = 8.5, γ_1 = 183 mPa-sec) with a small amount ($\sim$ 0.22%) of chiral dopant CB15 (from Merck, right-handed, HTP $\simeq$ 7.3 μm^{-1}), chosen so that the twist angle $\Phi = 70°$. Isotropic filling of the LC mixture was done on a hotplate at 130 °C.

We also demonstrated electrical switching of broadband light (i.e., white light or red, green, blue LEDs) using reflective achromatic LCPGs. The voltage response of a reflective LCPG ($\Lambda = 9\ \mu m$, $d = 3\ \mu m$) is shown in Fig. 3.16(a). The grating efficiency and reflectance (of the first-orders) were measured with unpolarized red, green, and blue LEDs (collimated for this measurement to $\sim 4°$). We observe that the achromatic LCPG diffracts all RGB LEDs with efficiency $\Sigma\eta_{\pm 1} \geq 95\%$ and reflectance $R \geq 90\%$ without voltage modulation. Diffraction efficiencies for red and green LEDs ($\geq 98\%$) reach nearly the 100% theoretical value while the blue LED produces a slightly lower value ($\sim 95\%$) due to the dispersion of LC birefringence (in general, larger values for shorter wavelengths). Further optimization can be done by a fine tuning of the thickness and the amount of chiral dopants in the LC mixture. Losses in reflectance predominantly result from electrode-absorptions. Note that the achromatic LCPG sample does not show a voltage threshold.

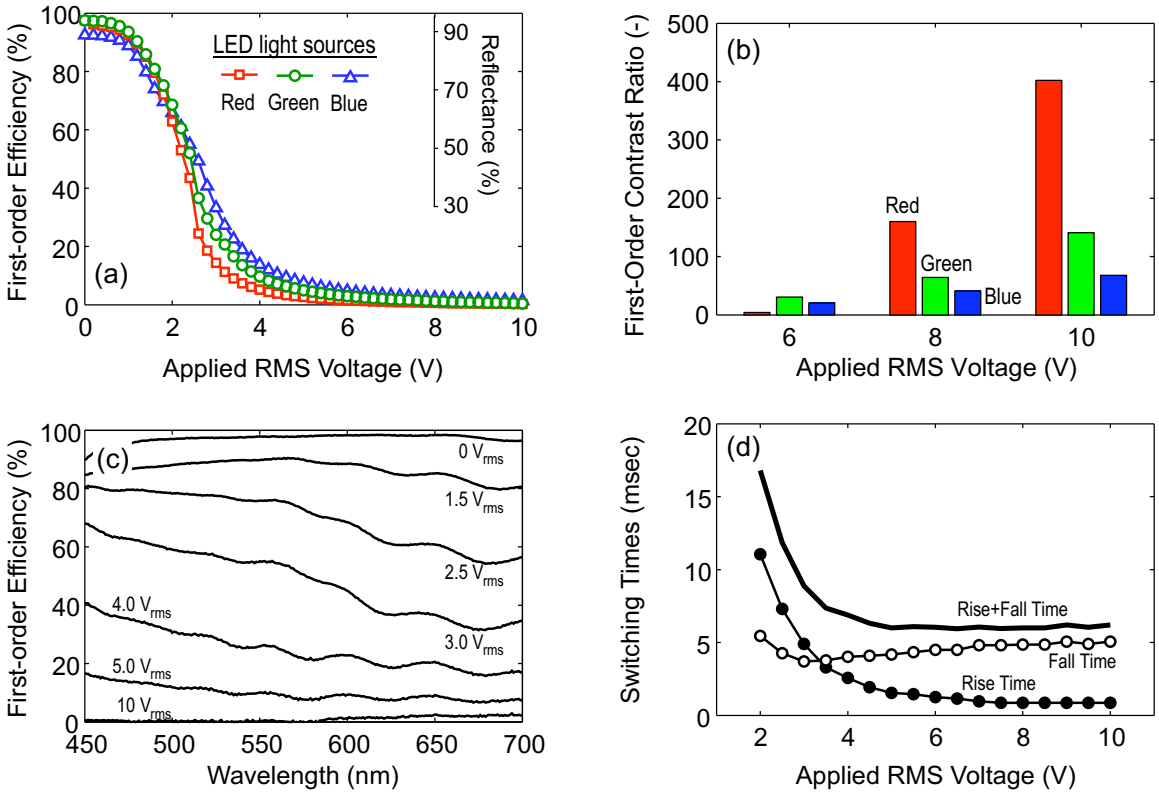

Figure 3.16: Electro-optical properties of the reflective achromatic LCPG sample: (a) voltage response of the first-order efficiency for RGB LED light; (b) contrast ratios at 6, 8, 10 V; (c) diffraction spectra with various applied voltages; (d) switching times.

The contrast ratios were also measured by comparing first-order diffracted powers without applied voltage (0 V) with respect to diffracted powers at three different applied voltages (6, 8, 10 V). As shown in Fig. 3.16(b), the maximum contrast ratio $\geq$ 400 was measured with red LED light (contrast ratios of 140 and 70 with green and blue LEDs, respectively), which is much higher than the best previous report of conventional reflective LCPGs [143] (i.e., CR$\geq$ 50 at 13 V applied voltage). We believe that the effect of twist and degenerate surface anchoring of LCs result in such a low voltage threshold and high contrast ratios.

To characterize the grayscale operation, we also measured diffraction spectra of the achromatic LCPG with varying applied voltages. We estimated the first-order efficiency from the zero-order reflection spectra ($\Sigma\eta_{\pm 1} \approx \eta_0$) because of difficulty of its direct measurement. Fig. 3.16(c) shows estimated first-order efficiencies at different RMS voltages (0, 1.5, 2.5, 3, 4, 5, 10 V). The diffraction spectrum moves mostly up-and-down without noticeable spectral shifts. In addition, the achromatic LCPG exhibits a steeper grayscale curve than the conventional LCPGs [131].

The dynamic response was also characterized, where a few ms total switching times are typical for conventional LCPGs [98]. Fig. 3.16(d) shows the rise and fall times (10% – 90% transitions) of the achromatic LCPG switching from 0V to the indicated applied voltage. The total switching times $\sim$ 6 ms was measured. The general trend is similar to other LC modes: rise-time is strongly dependent on voltage, while fall-time is roughly

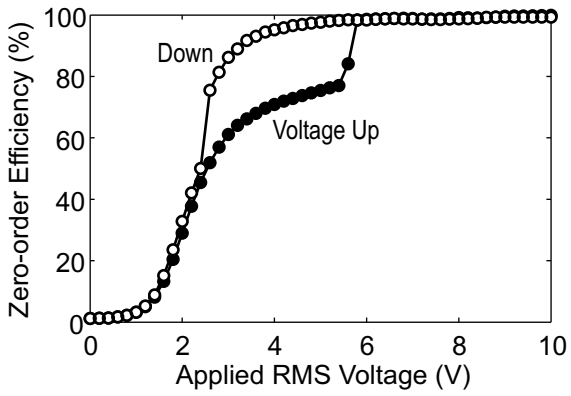

Figure 3.17: Voltage response of the zero-order efficiency with HeNe red laser light. A hysteresis is observed and the transitions occur at $\sim$ 6 V and $\sim$ 2.5 V while increasing and decreasing applied voltages, respectively.

constant. These switching times are ~ 2 times faster than a conventional LCPG with a same thickness while a normal LCPG requires a 1/4-wave thickness instead of a 1/2-wave thickness. Since the switching times are generally proportional to a square of the thickness, the increase of switching times due to doubled thickness of the reflective achromatic LCPG is only two-times rather than four-times with respect to those of a conventional reflective LCPG.

Somewhat surprisingly, we noticed two very interesting characteristics from the voltage response of the achromatic LCPG diffraction. First, we observed no obvious threshold of the applied voltage. The zero-order transmittance almost immediately starts to increase when even a very small voltage is applied as shown in Fig. 3.17. No proper explanation for such a zero-threshold behavior is found in literature to the author's knowledge. Second, there is a hysteresis in the voltage response curve of diffraction efficiencies (both zero- and first-order), also shown in Fig. 3.17. We believe that such a hysteresis has its origin in the presence of twist in the LCPG cell [144, 145]. Transitions for the hysteresis are always found at certain applied voltages across many samples as shown in Fig. 3.17; one transition occurs at ~ 6 V while increasing the voltage and the other occurs at ~ 2.5 V while decreasing the voltage. This effect appears more evident in the voltage response of the zero-order efficiency, while it is also seen from the first-order diffraction. More investigation on these interesting electro-optical behaviors of such a LC structure (with all three types of deformations (spray, bend, twist) in a periodic way) is suggested.

3.3 Super-achromatic diffraction by three-layered polarization gratings with a phase shift

There is a well-known technique to implement achromatic waveplates using a stack of two or three birefringent layers. When three identical waveplates are stacked with the middle layer oriented at a certain angle with respect to the others, a uniform retardation can be obtained over an very broad spectrum range [146, 147, 148, 149]. The key of this structure is the self-compensation of retardation due to the relative phase differences in the optic axes of the waveplates. Since the polarization grating diffraction relies on spatially modulated retardation of the birefringent medium, a similar approach can be employed to enhance its broadband performance. A broadband design using three-layered polarization gratings (Fig. 3.18) was proposed by the Author [133], and the design parameters for the bandwidth optimization were developed for highly diffraction efficiencies over a extremely wide range of spectrum, so called *super*-achromatic diffraction.

In this Section, we demonstrate super-achromatic polarization gratings composed of thin liquid crystal polymer films. This achromatic PG manifests high diffraction efficiency ($> 99\%$) and high polarization extinction ratio in both theory and experiment. We show an operation bandwidth $\Delta\lambda/\lambda_0 \sim 78\%$ that represents more than a six-fold increase of bandwidth over conventional PGs (and 40% increase compared with another achromatic

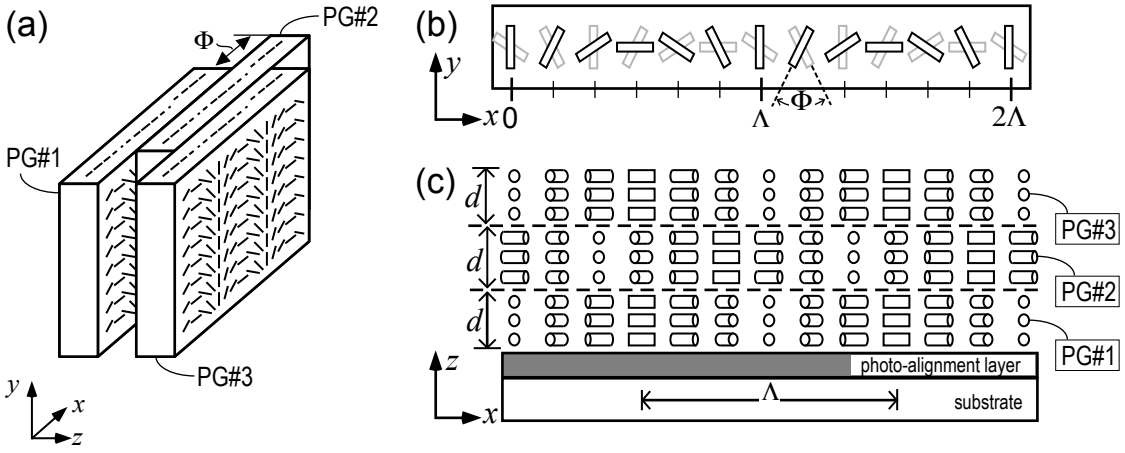

Figure 3.18: Super-achromatic polarization grating (PG): (a) triple-layered broadband PG design with a phase shift at an angle Φ (i.e., 55°) in the director profile of the middle PG; Nematic director profile (b) plane- and (c) side-view.

PGs with double twisted layers). We confirm excellent optical properties (i.e., high efficiency, excellent polarization sensitivity) of the super-achromatic PGs that are optimized at visible and infrared wavelangths.

This achromatic PG comprises three identical circular PG layers with a relative phase shift in the birefringence profile of the second PG layer, where the nematic director $\mathbf{n}$ is described as follows

$$\mathbf{n}(x) = [\cos\phi(x),\ \ \sin\phi(x),\ \ 0] \tag{3.5a}$$

$$\phi(x,z) = \begin{cases} \pi x/\Lambda & \text{if } 0 \le z \le d \text{ and } 2d < z \le 3d \\ \pi x/\Lambda + \Phi & \text{if } d < z \le 2d \end{cases} \tag{3.5b}$$

where ϕ is the azimuth angle of the director field, Λ is the grating period, d is the thickness, and Φ is the shift angle of the second PG layer. Figs. 3.18(b) and 3.18(c) illustrate this profile. The phase shift in the grating profile can be implemented by using thin chiral liquid crystal polymer layers with opposite handedness as described in Ref. [133].

3.3.1 Super-achromatic diffraction by three-layered PGs

We can apply Jones calculus to derive the analytic expressions for three-layered PGs that describe the diffraction efficiency and polarization properties of the diffraction orders. Here we present only a summary of the analytical results (referring readers to Appendix C for more detailed mathematical descriptions). The diffraction efficiency of a

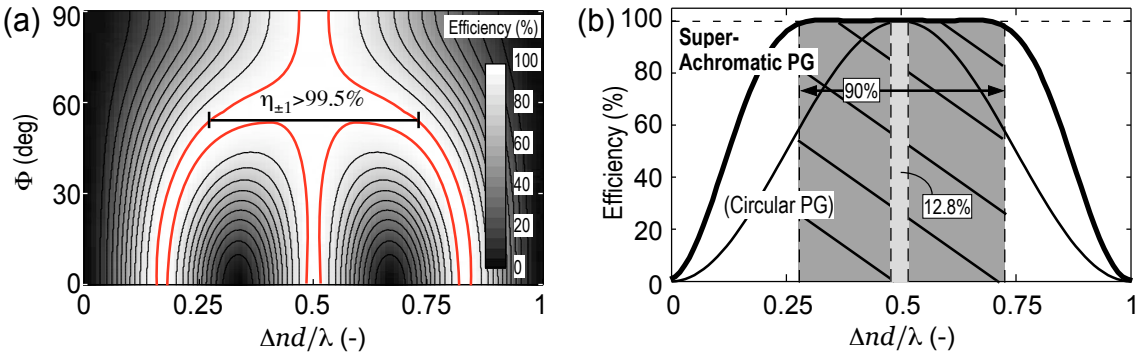

Figure 3.19: Theoretical diffraction of the super-achromatic PG: (a) first-order efficiency spectra vs the phase shift angle Φ ($\Sigma\eta_{\pm1} \ge 99\%$, red outlined region); (b) first-order efficiency spectrum for $\Phi = 55^\circ$ compared to the circular PG.

stack of three PGs with a phase shift Φ of the middle layer is given by

$$\eta_0 = \{\cos^3(\Gamma) - [1 + 2\cos(2\Phi)]\cos(\Gamma)\sin^2(\Gamma)\}^2 \tag{3.6a}$$

$$\eta_{\pm 1} = \frac{1 \mp S_3'}{2}\sin^2(\Gamma)\left\{1 - 4[1 + \cos(2\Phi)]\cos(2\Phi)\cos^2(\Gamma) + 4[1 + \cos(2\Phi)]^2\cos^4(\Gamma)\right\} \tag{3.6b}$$

where $\Gamma = \pi\Delta n_l d/\lambda$. The term $S_3' = S_3/S_0$ is a normalized Stokes parameter. The grating equation $\sin\theta_m = m\lambda/\Lambda \pm \sin\theta_{inc}$ governs diffraction angles. Note that we assume a discrete shift in the grating profile between the second and the first or third layers without taking account of the optical effect of the thin chiral layers.

Several important properties should be noted in Eqs. (3.6). *First*, only three diffraction orders (0 and ± 1) exist, which depend on both the retardation $\Delta n_l d/\lambda$ and the shift angle Φ. We will show that $\Sigma\eta_{\pm 1} \approx 100\%$ over a wide wavelength range by a careful choice of the shift angle Φ ($\sim 55^\circ$). *Second*, the first-orders have orthogonal circular polarizations. *Third*, the first-order efficiencies are strongly sensitive to the incident polarization state through S_3' (akin to circular PGs). *Overall*, we understand the achromaticity of the three layers with a relative phase shift, via self-retardation compensation.

To enable quantitative evaluation, we define bandwidth as $\Delta\lambda/\lambda_0$, the ratio of the spectral range $\Delta\lambda$ (over which high diffraction efficiency $\Sigma\eta_{\pm 1} \geq 99\%$ occurs) to the center wavelength λ_0. We employ Eq. (3.6) to generate a map of total first-order diffraction efficiency as a function of the retardation and the shift angle (shown in Fig. 3.19(a)). The maximum bandwidth $\simeq 90\%$ for $\geq 99\%$ efficiency is found when $\Phi = 55^\circ$. Note, this is more than a 7-fold enhancement as compared with a non-achromatic PG ($\simeq 12.8\%$), as shown in Fig. 3.19(b) with relative bandwidths highlighted.

3.3.2 Fabrication of super-achromatic polarization gratings

We have experimentally realized this super-achromatic PG, optimized for visible and near-infrared wavelength, formed as a reactive mesogen (RM) film by polarization holography and photo-alignment techniques. The fabrication steps include UV holographic exposure and multiple coating of RM/chiral layers as illustrated in Fig. 3.20. Again, we utilized a linear photopolymerizable polymer (LPP) [68] ROP-103 (Rolic) as a photo-alignment material. The surface alignment pattern with a period of $\Lambda = 6.5$ μm was recorded in the

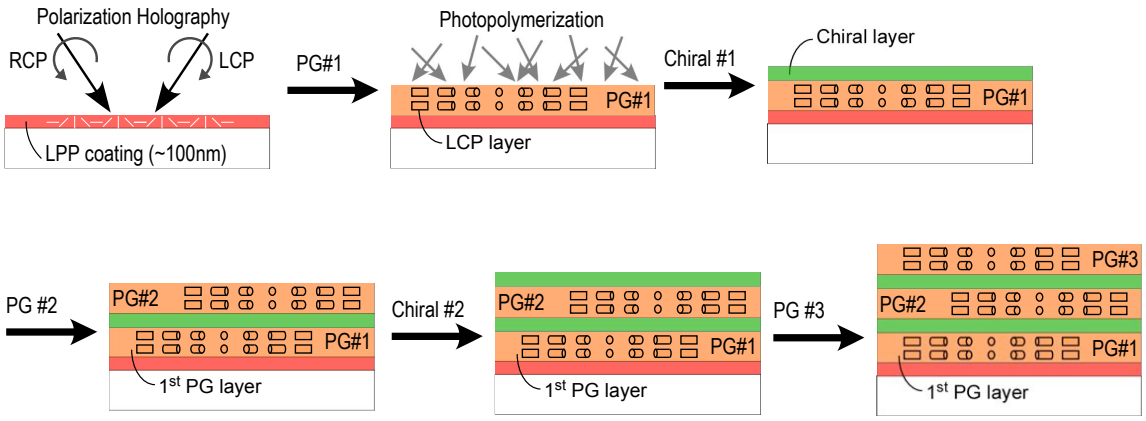

Figure 3.20: Fabrication steps for super-achromatic PGs with three-layer PGs with a phase shift in the middle PG layer by Φ. Each chiral layer delivers either $\Phi = +55°$ or $\Phi = -55°$ by opposite handedness of its chirality.

LPP layer by orthogonal circular-polarized beams from a HeCd laser (at 325 nm). After holographic exposure, RM films were spin-coated on the LPP-coated substrate. The first PG layer was composed of the RM prepolymer/solvent mixture RMS03-001 (Merck, $\Delta n_l \simeq 0.159$ at 589 nm) with a thickness for a halfwave retardation $\Gamma = \pi/2$ ($d \simeq 1.7$ μm at 550 nm, $d \simeq 4.5$ μm at 1400 nm). The first chiral layer was deposited directly on the top of the first PG layer, and was composed of RMS03-001 doped with a small amount (2.32 wt-%) of the chiral molecule ZLI-811 (Merk, left-handed), resulting in the twist angle $\Phi = -55°$ within a thin layer, which provides the required phase shift for the next RM layer. The second PG layer was coated identical to the first PG (with the same thickness, $d \simeq 1.7$ μm, but the grating profile shifted by $\Phi = -55°$). Another thin chiral layer of RMS03-001 doped with a small amount (2.9 wt-%) of another chiral molecule CB15 (Merk, right-handed) to implement the opposite shift angle $\Phi = +55°$. The third PG layer was coated again with the same thickness of RMS03-001 and its grating profile is exactly matched to the first PG. As these RM films are highly crosslinked acrylate films, they are known [52] to have high thermal and optical stability. Reproducibility and fabrication process sensitivity are similar to other spin-coated RM films.

These super-achromatic PG samples exhibit practically ideal properties, with high first-order efficiency, high polarization selectivity, low scattering, and low non-first-order leakage. We examined the spectrum of the achromatic PG by measuring η_0 using a spec-

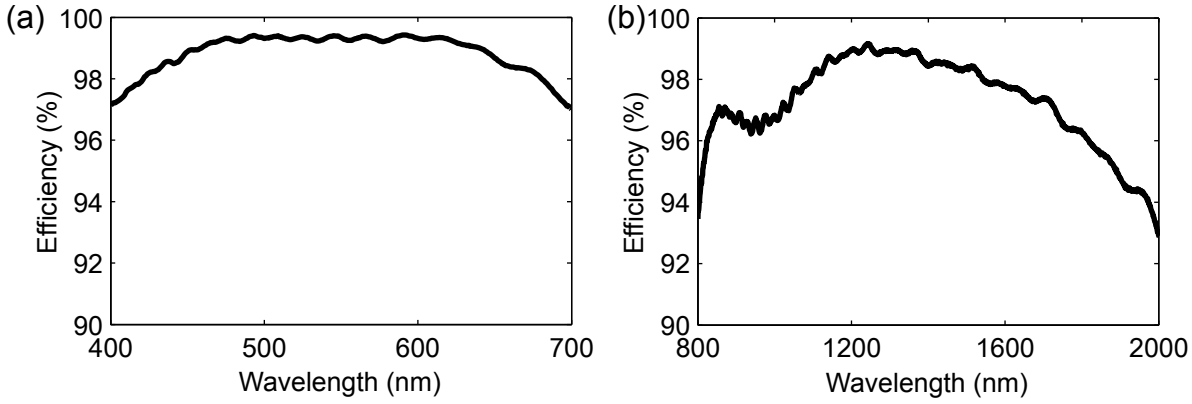

Figure 3.21: Diffraction efficiency of two different super-achormatic PG samples optimized for (a) visible and (b) near-infrared wavelengths. Both samples exhibit high efficiency (95%–99%) over very wide ranges of spectrum, high polarization selectivity, low scattering, and low non-first-order leakage.

trophotometer (with $\eta_{|m|\geq 1}$ blocked) and estimating $\Sigma\eta_{\pm 1} \simeq 100\% - \eta_0$ (due to the difficulty of its direct measurement). The results are shown in Figs. 3.21(a) and 3.21(b) for RMPG samples optimized for visible and IR wavelengths, resepctively. The both super-achromatic PG clearly manifest high diffraction efficiency (95% – 99%) across very wide ranges of spectrum in both wavelength regions, which is a substantial improvement over the conventional circular PG and also the first kind of achromatic PGs with two chiral layers. We also confirmed the +1-order response for a monochromatic beam (from a HeNe laser at 633 nm). The efficiency varies as the incident light is varied from linear ($\simeq$ 50%), to circular ($\simeq$ 99.3%, right handed), to linear ($\simeq$ 50%), and finally back to circular ($\simeq$ 0.13%, left handed). The extinction ratio is therefore $99.3/0.03 \simeq 550 : 1$ (or 27.4 dB), an excellent measure for polarizing beamsplitters of any kind.

3.4 Fabrication of small-period PGs using high Δn_l materials

Until now, we have shown great potentials of polarization gratings as a broadband polarizing beam splitter that can operate at $\sim 100\%$ efficiency. This thin-plate beam splitter embodied as liquid crystal cells or liquid crystal polymer films has a number of distinct advantages over other conventional beam splitting elements that include high polarization contrast (between two emerging beams), good response over a fairly wide range of incidence angles, capability of electrooptical switching/tunning (for LCPGs), excellent optical transparency from visible to midwave IR wavelengths, ease of integration with other optical elements or multiple stacks, and no need for specialized substrates in general. Novel designs for achromatic PGs suggest significant improvement of performance even with broadband illumination, which can enhance existing optical systems by replacing polarizing elements or even lead to new applications.

Fabrication of high-quality PGs is essential for many practical applications where large angular dispersion/separation is required. In recent five years, we have developed fabrication technologies for creating PGs utilizing polarization holography and photoalignment of LC materials, and demonstrated PGs showing nearly ideal properties for a wide range of grating periods (from $\sim$ 2 μm to a few 100's μm) and various operating wavelengths (visible, near-infrared, mid-infrared). In this Section, we report our most recent advances of fabrication of PGs with small periods using liquid crystal materials with high Δn_l. We also discuss our choice of different materials and fabrication challenges.

We fabricated non-achromatic, reactive mesogen PG samples with different periods for comparison. To observe the effect of Δn_l on optical properties of PGs, we also prepared RMPG samples at the same periods using following RM prepolymer/solvent mixtures (all from Merk): (i) RM1: RMS03-001C ($\Delta n_l = 0.159$ at 589 nm); (ii) RM2: RMS08-075 ($\Delta n_l = 0.25$ at 589nm); (iii) RM3: RMS09-025 ($\Delta n_l = 0.33$ at 589 nm); (iv) RM4: RMS09-038 ($\Delta n_l = 0.39$ at 589nm). We utilized a new linear photopolymerizable polymer LIA-01 (from Dainippon Ink and Chemical) as a photoalignment material. The general fabrication process consists of the following four steps: First, substrate cleaning and LPP coating/drying; Second, surface alignment pattern via UV exposure with orthogonal ciruclar-polarized beams from a HeCd laser (at 325 nm) (typical dose $\sim$5 J/cm^2); Third, after holographic exposure, RM coating/photopolymerization.

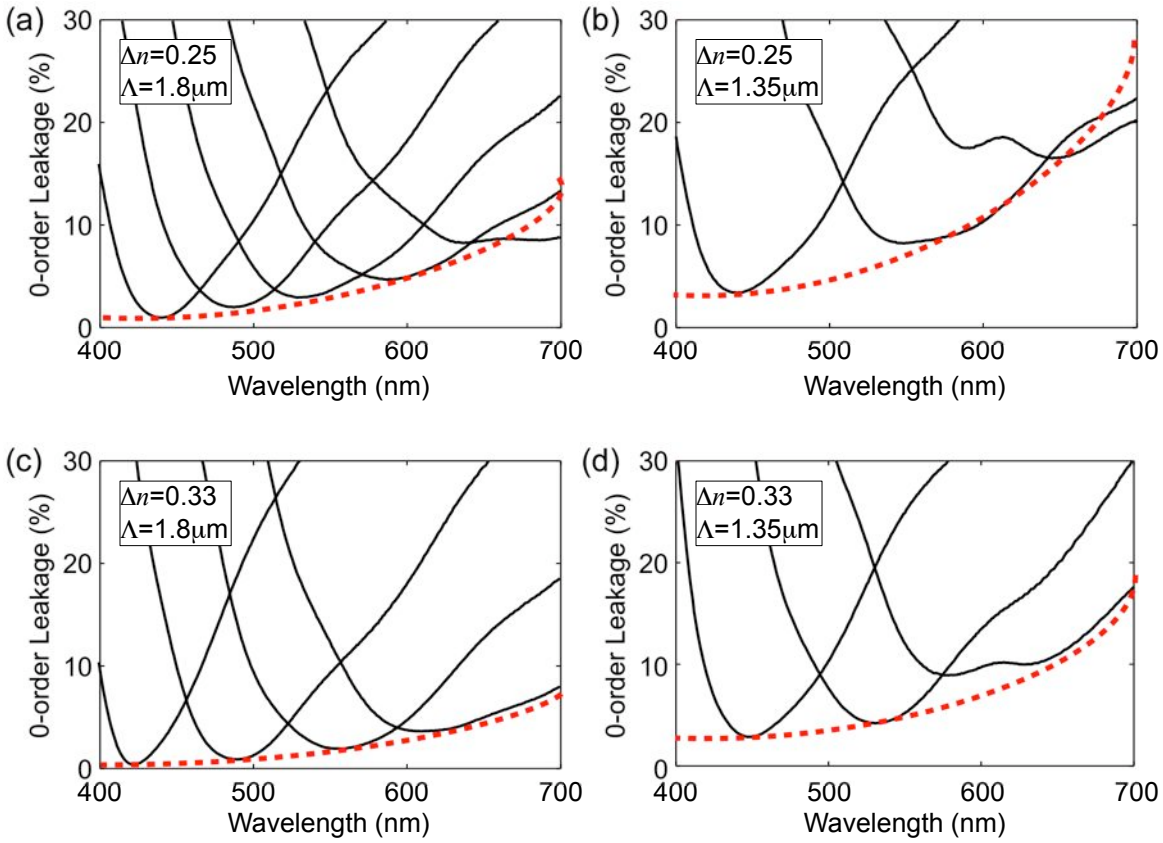

Figure 3.22: The 0-order spectra of reactive mesogen (RM) PG samples at different grating periods (Λ = 1.8 μm and 1.35μm) using two RM materials, RMS08-075 (Δn_l = 0.25 at 589 nm) and RMS09-025 (Δn_l = 0.33 at 589 nm). Note that the 0-order transmittance was measured at every coating steps for RM layers to get spectra with different thicknesses. Also note that dotted lines are predicted guidelines to show the trend in the 0-order leakage as wavelength increases for the same grating period and same material Δn_l. No measurable high-order diffraction was observed other than the 0- and first-orders for all RMPG samples.

Figs. 3.22(a)–3.22(d) show spectra of the 0-order leakage of RMPG samples with 1.8 μm (i.e., $\theta_{\pm 1} \approx \pm 20^\circ$ at 632.8 nm) and 1.35 μm (i.e., $\theta_{\pm 1} \approx \pm 28^\circ$ at 632.8 nm) periods for two different RM mixtures (RM2 and RM3). The 0-order spectra of the same RMPG sample were taken after every RM coating. The 0-order leakage substantially increases for longer wavelengths and this trend is more obvious for the case of RM2 than RM3 at both grating periods. We should note that our observation across most of RMPG samples is less 0-order leakages (or high first-order efficiencies) for larger grating periods and higher Δn_l values, which is already predicted as the effect of ρ parameter in Section 3.1. To confirm

the rule of $\rho \leq 1$ for high efficiency of PGs, we also plot the maximum diffraction efficiency (calculated from the 0-order efficiency as $\eta_{max} = 100\% - \eta_{0,min}$) for different period of RMPGs with alll the above RM materials (RM1-RM4) in Fig. 3.23, which is similar to Fig. 3.5. The results show very good agreement with numerically predicted trends for different values of Δn_l. A small discrepancy between the experimental results and the numerical prediction can be explained as the effect of the dispersion of Δn_l (Δn_l generally decreases as wavelength increases) of which was not taken account in the numerical results.

We have achieved $\sim 95\%$ efficiency even at $\pm 29^\circ$ diffraction angles using RM4 (RMS09-038 with $\Delta n_l = 0.39$ at 589 nm). We also experimentally prove the general trend in the maximum diffraction efficiency at different diffraction angles with various choices of Δn_l materials, which is well predicted from the numerical analysis in Section 3.1. High Δn_l has a significant impact on the maximum efficiency when the grating period become comparable to wavelength (i.e., $\Lambda \leq 5$) while all RMPGs show very high efficiency ($> 95\%$) for larger grating periods. These relationships between the maximum achievable efficiency and the ρ parameter (determined by Λ and Δn_l) provide us a very useful guideline for the

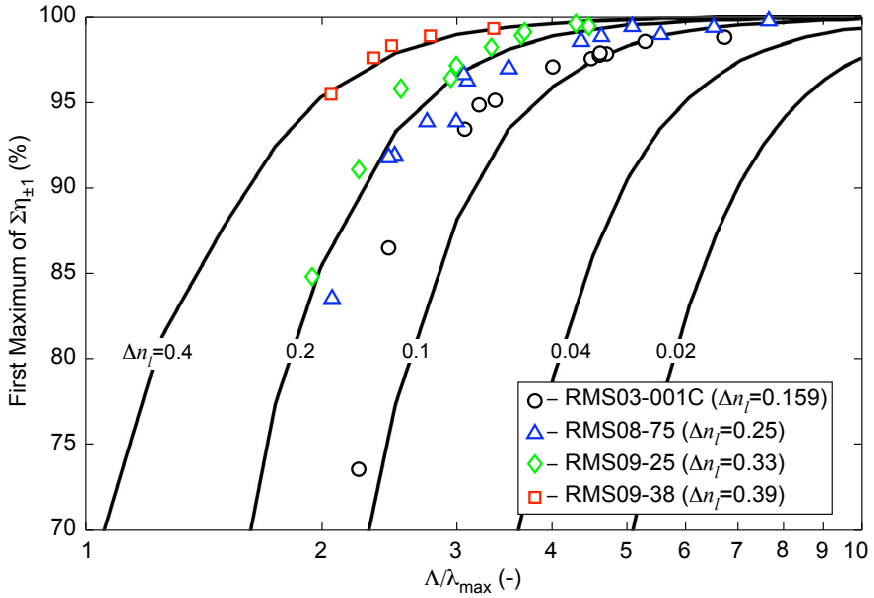

Figure 3.23: The first maximum of the first-order diffraction efficiency $\Sigma\eta_{\pm 1}$ of the RMPG samples, calculated from the 0-order transmittance as $100\% - \eta_0$. It is clear that high Δn_l materials have advantages to achieve high diffraction efficiency even at small grating periods.

choice of materials and grating periods depending on requirements for different applications.

We also should note that the layer-by-layer process of RM materials has many advantages especially for fabrication of small-period PGs. Since multiple thin polymer layers can be coated to achieve a desired thickness, conditions for LC alignment is very relaxing compared to a LCPG cell and, more importantly, the limit of the critical thickness (no in-plane alignment beyond a certain thickness) can be avoided by controlling the thickness of each RM layer. This thin-film coating process is promising to make high-quality PGs with any grating periods even close to wavelengths. Another important advantage is its potential of mass production with large areas using conventional thin film fabrication techniques (i.e., slot coating). A raster scanning of a fractional area for exposure to cover the entire size can be considered to maximize productivity keeping the same cost for the exposure system.

Chapter 4

Polymer-PG Displays: a viable solution for polarization-independent displays

We introduce a polarization-independent microdisplay, namely "polymer-PG display," employing standard liquid crystal display (LCD) panels and multiple polymer polarization gratings (PGs). The PGs replace conventional (absorbing or reflecting) polarizers, and inherently double light efficiency by enabling direct modulation of unpolarized-light by virtually any LCD modes. Unlike other previous approaches of polarization-independent modulation, no modification to the LC microdisplay is required.

4.1 Polymer-PG Liquid Crystal Displays

We introduce a deceptively simple method of doubling the light efficiency of liquid crystal (LC) microdisplays by replacing the polarizers in common LCDs with polarization gratings (PGs) as transparent polymer, thin-film, broadband polarizing beam-splitters. We employ achromatic PGs, reactive mesogen (polymerizable LC) films shown in Fig. 4.1(a), in such a way so that they act as both polarizer and analyzer. The operation concept of polarization-independent modulation is illustrated in Fig. 4.2(b). The result is that both orthogonal polarizations (i.e. all of the unpolarized light) can be directed through the microdisplay simultaneously, so that the display has $\sim$ 100% (brightness) efficiency (as opposed to $<$ 50% efficiency when using polarizers). We term this a "polymer-PG display" system, requiring little-or-no modifications to commercial, off-the-shelf LC microdisplays.

4.1.1 Polarization-independent light modulation by the polymer-PG LCD

The key elements of the polymer-PG display system are achromatic polarization gratings, which replace absorbing film polarizers or polarizing cube bean splitters of conventional LCDs. It is convenient to understand the polarization filtering based on PGs by analogy with parallel and crossed polarizers. Figs 4.2(a) and 4.2(b) illustrate parallel and antiparallel configurations of two identical PGs, respectively. For parallel PGs which are equivalent to parallel polarizers, an incoming beam (unpolarized) is diffracted into the first orders by the first PG and redirected back to the original direction by the second PG. For antiparallel PGs equivalent crossed polarizers, the beam is again diffracted by the first PG

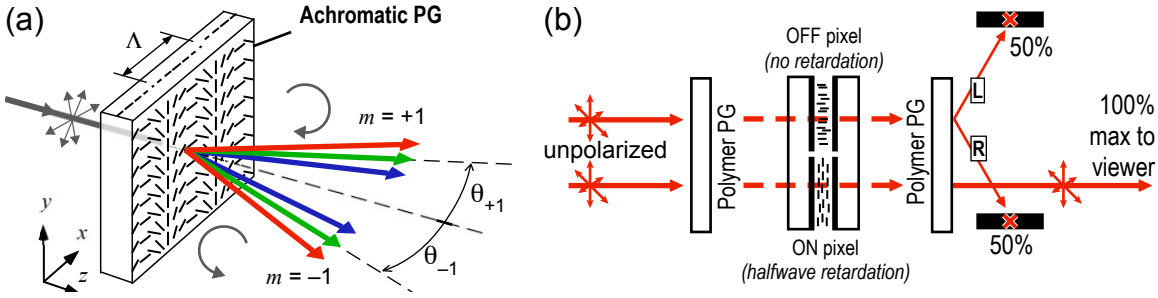

Figure 4.1: Operation concept of the polymer-PG display: (a) achromatic polarization grating (PG) diffraction; (b) polarization-independent light modulation using a liquid crystal display and achromatic PG films.

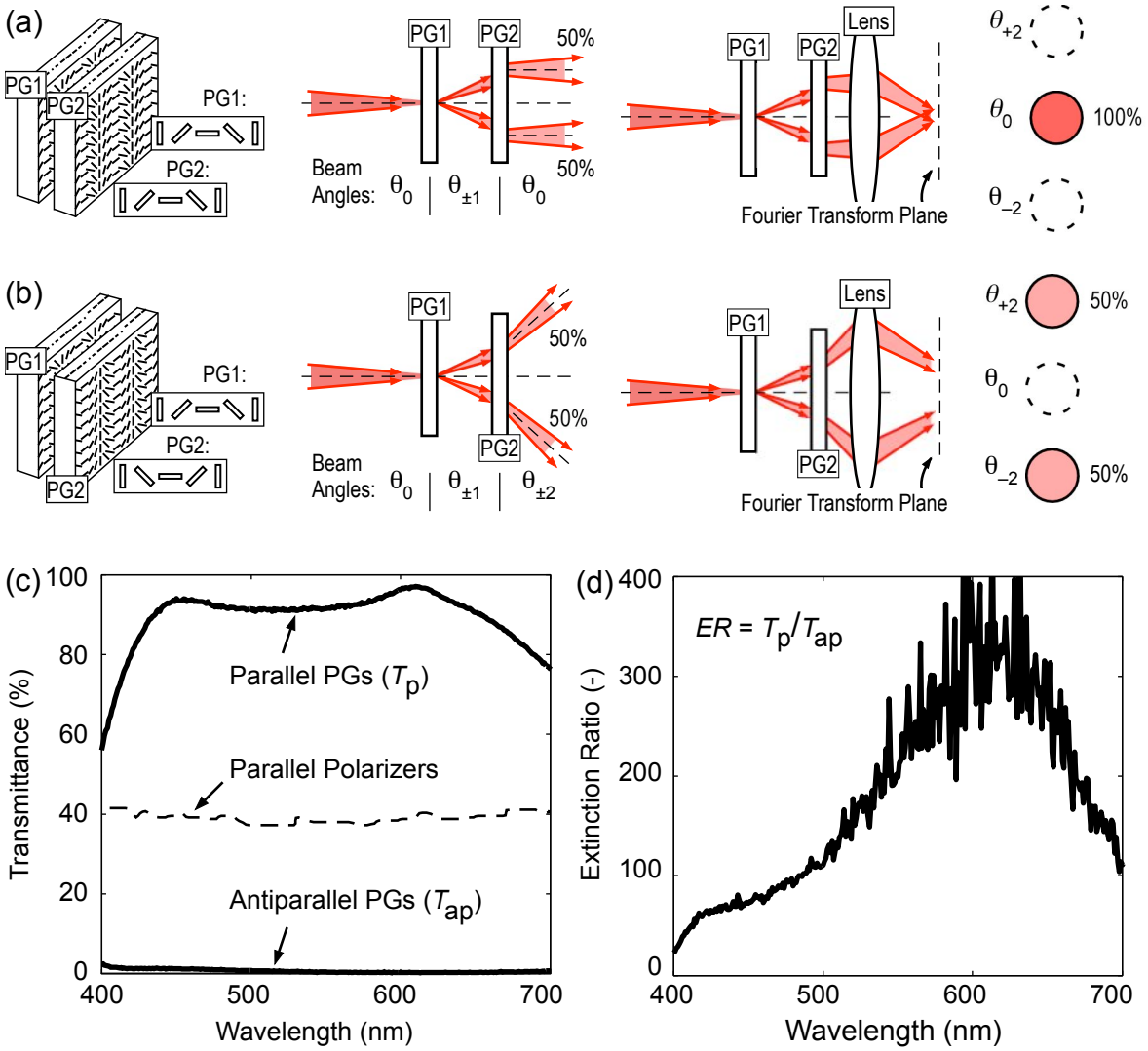

Figure 4.2: Angle filtering of polarization by (a) parallel and (b) anti-parallel PGs and (c) measured transmission spectra of each (along with parallel polarizers); (d) extinction ratio of anti-parallel PG is also calculated ($ER = T_{\mathrm{p}}/T_{\mathrm{ap}}$).

but it is diffracted at even higher angles ($\theta_{\pm 2}$) by the second PG. Light switching can be done by using aperture stops and lenses to filter the diffraction orders (either the 0- or higher-orders).

As in conventional LCDs, LC switching leads to light modulation by altering polarization states of light passing through the LC layer. The first PG outputs circular polarizations in the first orders, the handedness of which is affected by LC switching and the

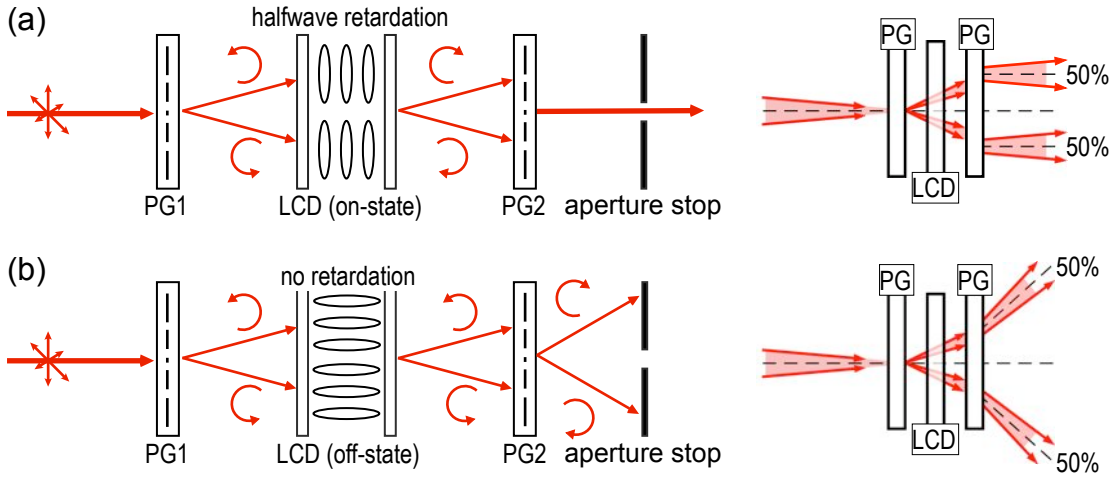

Figure 4.3: Polarization-independent light modulation by the polymer-PG LCD: (a) on-state and (b) off-state of the LC retardation. LC switching leads to light modulation by changing the polarization state of light from the first PG. Note that two PGs are aligned in an anti-parallel configuration.

relative orientation between the first and second PG (see Figs. 4.3(a) and 4.3(b)). The second PG either diffracts the light into higher angles or directs it toward the normal direction based on the polarization handedness of light from the LC layer. We limit our discussion to the anti-parallel alignment of PGs, bearing in mind that there would be a number of varied designs possible.

4.1.2 Demonstration of the polymer-PG display with a vertically aligned (VA) LC cell

For our initial demonstration of the basic operation of the polymer-PG display concept, we prepared a pair of achromatic PG polymer films (grating period = 3 μm) with high efficiencies ($> 95\%$) for red, green, and blue LED lights with divergence angle $\sim \pm 5°$. We again utilized a linear-photopolymerizable polymer (LPP) ROP-103/2CP (Rolic) as the photo-alignment material a reactive mesogen (RM) RMS03-001C (Merck, $\Delta n_l = 0.159$ at 589 nm) with small amount (0.25%) of chiral dopants CB15 (Merck, right-handed) and ZLI-811 (Merck, left-handed).

We first highlight the maximum achievable brightness and contrast ratios of our current Polymer-PG Displays. As described above, we prepared a pair of achromatic PG

polymer films (grating period = 3 μm) with high efficiencies ($>$ 95%) for red, green, and blue LED lights with divergence angle $\sim \pm 5^{\circ}$. To obtain the upper limits of light efficiency and contrast ratios, we aligned two PG samples in parallel and anti-parallel orientations (Figs. 4.2(a) and 4.2(b)), which are nearly equivalent to the bright-state and dark-state of an ideal display system, respectively. Fig. 4.2(c) presents the true transmittance spectra of both configurations, for unpolarized input light. Parallel PGs manifest $\sim$ 90% transmittance, while anti-parallel PGs leak $\sim$ 0.5% for visible light (450-650 nm). Fig. 4.2(d) shows the extinction ratio of anti-parallel PGs (analogous to crossed-polarizers) is $\geq$ 100, and has a peak of $\sim$ 400 in the red.) as shown in Fig. 2c. Note we expect this can be improved by optimized PG film-coating processing. Note that we used anti-reflection coated glass (ColorLink in Japan) to reduce Fresnel losses.

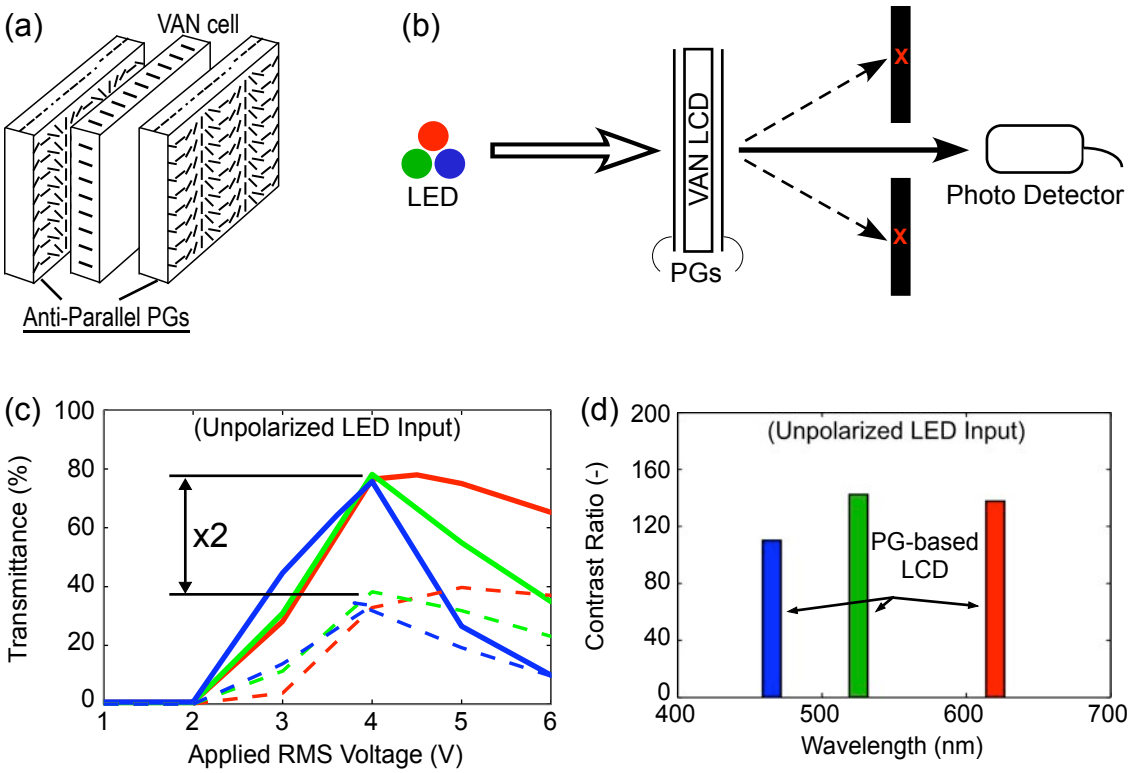

Figure 4.4: Polymer-PG LC display experimental data with VA-mode LC pixel and for unpolarized LEDs (red at 625 nm, green at 530 nm, blue at 470 nm): (a) the polymer-PG LCD configuration; (b) a measurement setup with LED illumination; (c) the transmittance vs. voltage curve (solid lines), compared to those of a polarizer-based VA-LCD (dashed lines); (d) the contrast ratios (bright/dark).

We demonstrate electro-optical switching with a single monolithic pixel with a conventional LC cells (with vertical-alignment (VA) mode, prepared with MLC-6610 Merck LC, SE-1211 Nissan homeotropic polyimide, and 6 μm cell gap). We arranged two achromatic Polymer PGs in anti-parallel orientations to the LC cell (Fig. 4.4(a)), which controls the polarization of light passing through it. Recall that the VA-mode cell with an applied voltage ($\sim$ 4V) applied will present a half-wave retardation due to its predominantly planar alignment, and will therefore reverse the polarizations of the two beams (simultaneously) passing through it (from the first PG). This light will then be directed toward the normal direction by the second PG (Fig. 4.4(b)), and subsequently projected to the screen/viewer/detector. However, when zero voltage is applied to the VA-mode cell, it presents very little retardation, and light subsequent to the first PG entering the LC layer will retain its original polarization (simultaneously) and be diffracted to even higher angles by the second PG.

The transmittance vs. voltage curves for the Polymer-PG and polarizer-based VA-mode are compared in Fig. 3a, for unpolarized light from RGB LEDs. The voltage applied was a 4 kHz square wave with zero DC bias. Note that the switching curves are similar and reach a maximum at around 4V. Most remarkably, as Fig. 4.4(b) shows, the true transmittance to unpolarized light for the polymer-PG LCD is $\sim$ 80%, more than double that of a conventional polarizer-based display, while still maintaining modest contrast ratios (114:1 to 140:1, Fig. 3c). Note that retardation compensation for the VA-LC pixel (not used in these measurements), would likely enhance the contrast similarly to conventional LCDs.

4.1.3 Prototype projector based on the polymer-PG display with a commercial LC microdisplay

To confirm the imaging properties of the polymer-PG display, we have built a prototype projector using a commercial LC microdisplay panel (transmissive, 0.41" VGA, planar-alignment mode) with our achromatic PG films. We used a Golden-eye LED light source (supporting color-sequential operation) limited to a $\pm 6^\circ$ divergence angle. We removed the polarizers from the commercial microdisplay, and added our own retardation compensation film (RM-based, +A plate). Here, Polymer-PGs (with 2.5 μm period) were aligned in anti-parallel configuration. Simple lenses were used to achive a magnification was

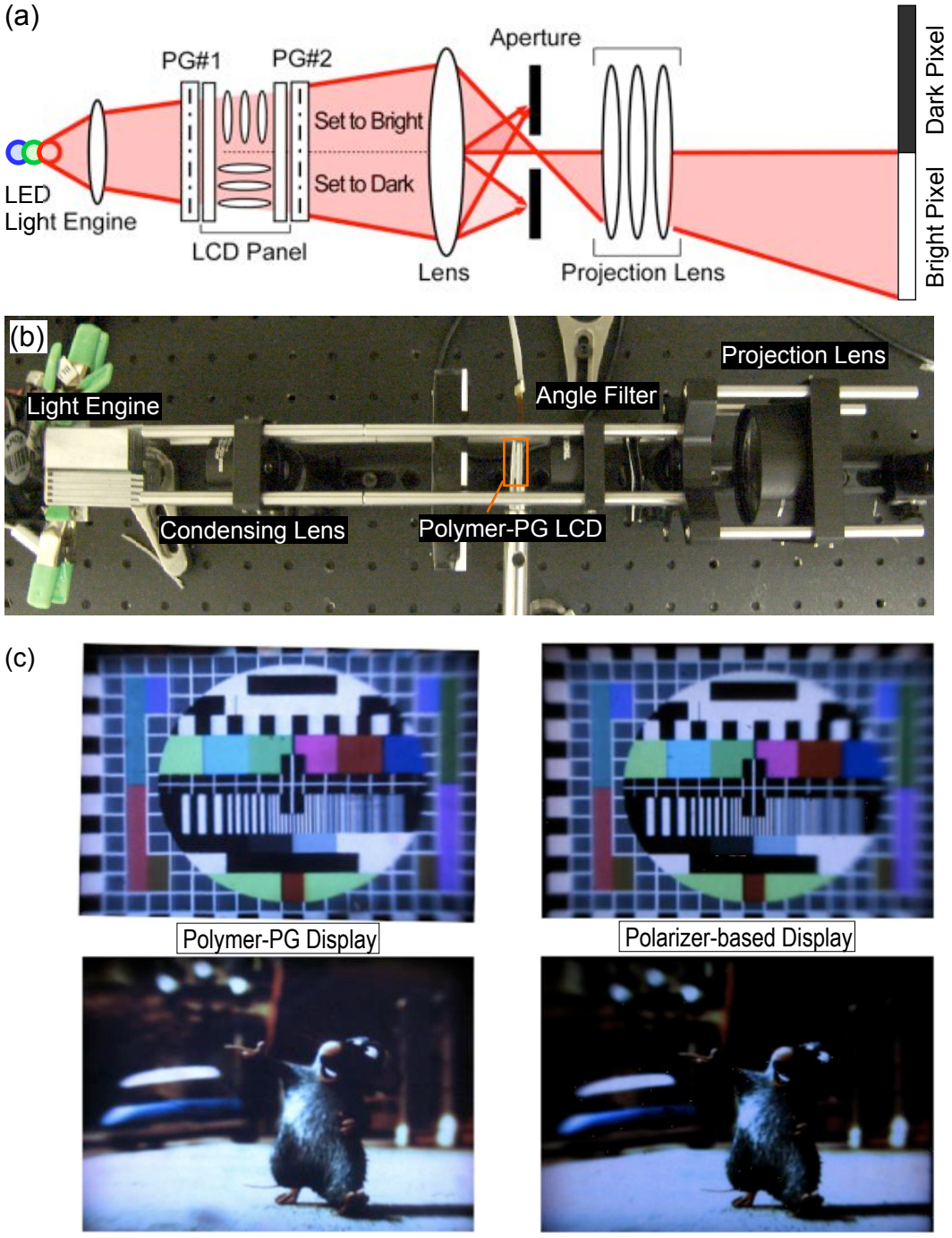

Figure 4.5: A prototype projector using a commercial LC microdisplay and our Polymer-PGs: (a) illustration of the projection system geometry; (b) photograph of the prototype projector; (c) projected images of the polymer-PG projector and a polarizer-based projector.

~ 20, with a throw of ~ 2 ft. The overall system is shown in Fig. 4.5(a), and a photo in Fig. 4.5(b).

A comparison (Fig. 4.5(c)) of projected images from the original display and our polymer-PG display shows equivalently sharp edges, nearly identical color saturation, and excellent image focus. The full-on and full-off transmittance values of the Polymer-PG LCD (R: 24%, G: 45%, B: 33%) are more than double the values of the unmodified polarizer-based LCD (R: 9.4%, G: 20%, B: 18%) for the unpolarized LED input. This includes in both cases all losses within the display itself (e.g. electrode absorption, fill-factor blocking, interfaces) and the PGs and polarizers. The contrast ratios of polymer-PG LCD (around 30:1 for all colors) are admittedly not nearly as high as the polarizer-based LCD (around 60:1 for all colors), which we feel is predominantly related to the sub-optimal retardation compensation film we fabricated for the Polymer-PG Display. Improving this remains one of our primary continuing efforts.

Note we observed parallax in projected images with a small spatial offset, which we attribute to the distance (glass thickness) between the imaging plane and the second PG. To avoid this, we place two additional parallel PGs (identical to the PGs already chosen) with the same gap thickness as the glass after the second PG, which perfectly compensates for the offset, as Fig. 4.6 shows. This set of PGs with a spacing is now so called an "offset compensator" throughout this dissertation. The offset compensator can be inserted anywhere after the second PG to fix the parallax problem, which also can be

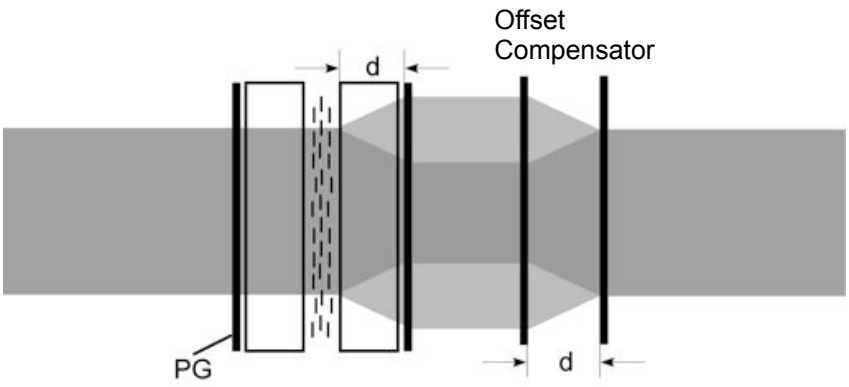

Figure 4.6: The offset compensator using a fair of identical PGs with a spacing, which cancels a spatial offset causing parallax in projected images due to the distance between the imaging plane and the second PG.

eliminated by inserting the second PG inside of the LCD panel.

The Polymer-PG Display improves the light efficiency of LC microdisplays simply by replacing polarizers with diffractive transparent polymer thin films. Brightness of (unmodified) commercial LC microdisplays can be roughly doubled, and standard étendue-limited light sources may be used. Improvement for low contrast ratios and limited divergence angles of light sources is suggested and will be discussed in the following Section 4.2.

4.2 Optical Design Consideration: System Acceptance Angle and Extinction Ratio

4.2.1 System acceptance angle

All projection systems are deeply influenced by the maximum acceptance angle of the most restricting optical element (e.g. defining the useful divergence angle of the light source and F/# of the lenses). In any system based on the polymer-PG display, the PG-LCD-PG stack presents this key limitation. In this Section, we detail this constraint, and discuss the design trade-off between the acceptance angle and the extinction ratio.

Acceptance angle and extinction ratio are uniquely related polymer-PG enabled projection displays. In order to quantify these, we must begin by considering the realistic versus ideal properties of PGs. Recall that a single PG ideally diffracts into two off-axis directions (only the ±1-orders, as in Fig. 4.7(a)). Furthermore, if an LCD and a second PG follow this, the PG-LCD-PG assembly ideally diffracts into three possible directions (only the 0- and ±2-orders) depending on the state of the LCD. However, realistic PGs will have

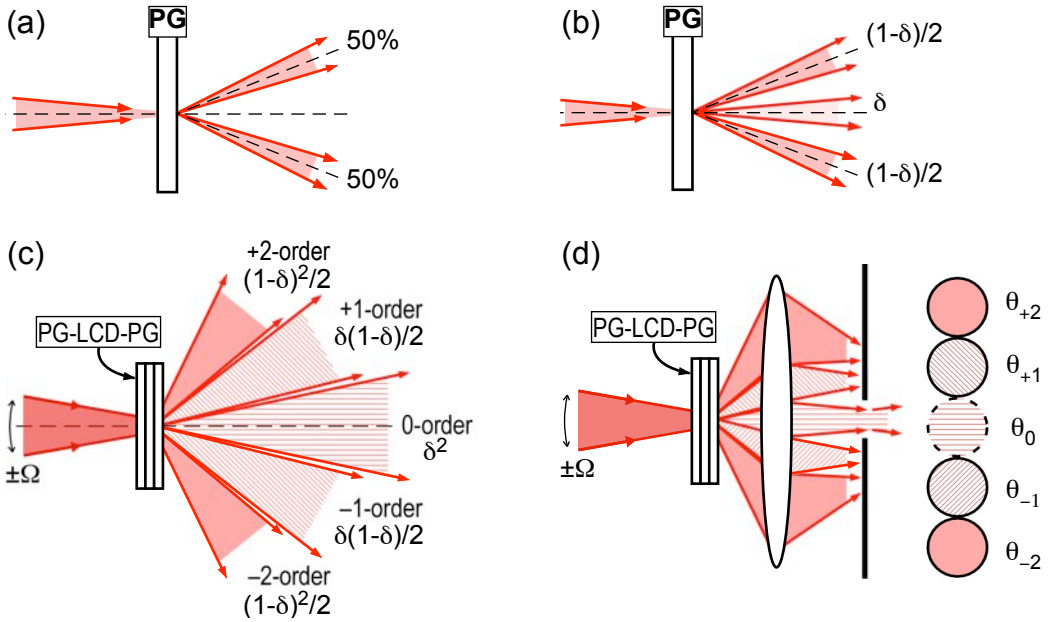

Figure 4.7: Optical design consideration of the polymer-PG display: (a) ideal PG diffraction; (b) non-ideal PG diffraction with a leakage δ; (c) and (d) diffracted beams (the 0-, ±1-, and ±2-orders) from the PG-LCD-PG assembly with and without angle filtering, respectively.

some non-ideal zero-order leakage that complicates this picture somewhat (Fig. 4.7(b)).

If we account for a small leakage δ in each PG (e.g. a few %), then a single grating can be described as having the following efficiencies across the entire spectral range as follows

$$\eta_0 = \delta(\lambda) \tag{4.1a}$$

$$\eta_{\pm 1} = \frac{1}{2}\left[100\% - \delta(\lambda)\right] \tag{4.1b}$$

In this situation, a single PG diffracts into three orders, and the PG-LCD-PG assembly diffracts into five possible orders (the 0-, ±1-, and ±2-orders, as in Fig. 4.7(c)). If we configure a projection system so that all orders are angularly separate, then total transmittance of the dark- and bright-states of the display are given by

$$T_{dark} = \delta^2(\lambda) \tag{4.2a}$$

$$T_{bright} = 100\% - 2\delta(\lambda) + 2\delta^2(\lambda) \approx 100\% - 2\delta(\lambda) \tag{4.2b}$$

The maximum extinction ratio is calculated as $ER = T_{bright}/T_{dark}$, which can be $\sim 1000:1$ even for 3% of the 0-order leakage ($\delta \leq 3\%$).

The actual extinction ratios of achromatic PGs, however, were measured less than the values suggested from Eqs. 4.2b. We found that a substantial amount of light of the first diffraction order from the first PG is diffracted back to the global normal direction by

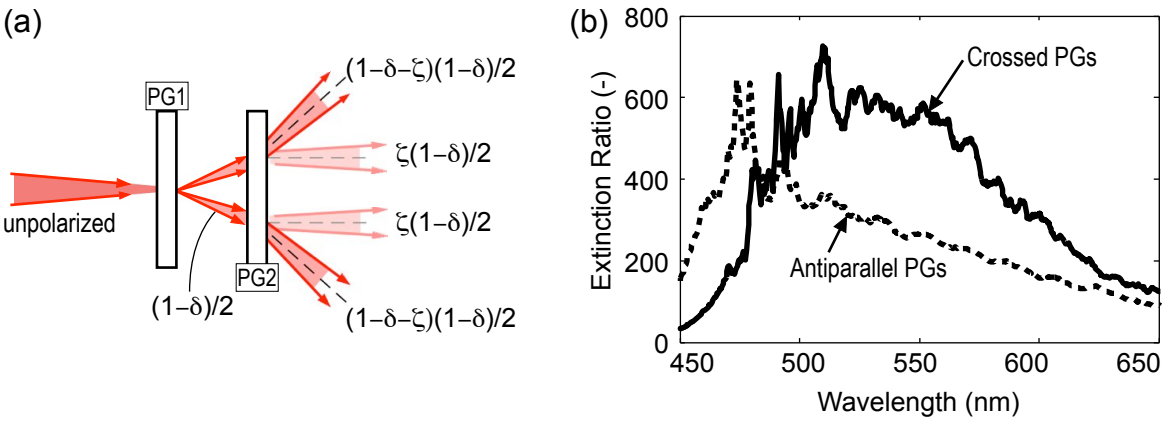

Figure 4.8: Effect of polarization leakages on the extinction ratio of antiparallel PGs: (a) light leakage (ζ) from the global first orders (± 1) due to the polarization mismatch; (b) Extinction ratio comparison of anti-parallel PGs (dotted line) and crossed PGs (solid line).

the second PG as shown in Fig. 4.8(a). If we account for this leakage ζ, then Eqs. 4.2b for the total transmittance are re-written as follows

$$T_{dark} = \delta^2(\lambda) + \zeta(1-\delta) \approx \delta^2(\lambda) + \zeta \tag{4.3a}$$

$$T_{bright} = 100\% - (2+\zeta)\delta(\lambda) + 2\delta^2 - \zeta \approx 100\% - 2\delta(\lambda) - \zeta \tag{4.3b}$$

This leakage is mainly due to the polarization mismatch between the polarization state of the first order and the ideal polarization condition for the second PG [121]. We can indirectly measure this leakage by comparing the extinction ratios of PGs in anti-parallel and crossed configurations. When two gratings are aligned as their grating axis are orthogonal (90°) to each other, these leakages do not affect the extinction ratio and the maximum achievable extinction ratio (from Eqs. 4.2b) is obtained. Fig. 4.8(b) shows extinction ratios of both anti-parallel and crossed gratings. A significant reduction in the extinction ratio is observed for the anti-parallel case and this result indicates the polarization leakage can be a few % of the input intensity, comparable to the 0-order leakage of individual PGs (δ). We have discovered that a relatively simple retardation film can dramatically improve the extinction ratio of anti-parallel PGs. We will discuss on this extinction ratio improvement techniques in the following Section.

The acceptance angle (Ω) of the above configurations can be determined as follows

$$\Omega = \frac{1}{2}\theta_1 = \frac{1}{2}\sin^{-1}\left(\frac{\lambda}{\Lambda}\right) \tag{4.4}$$

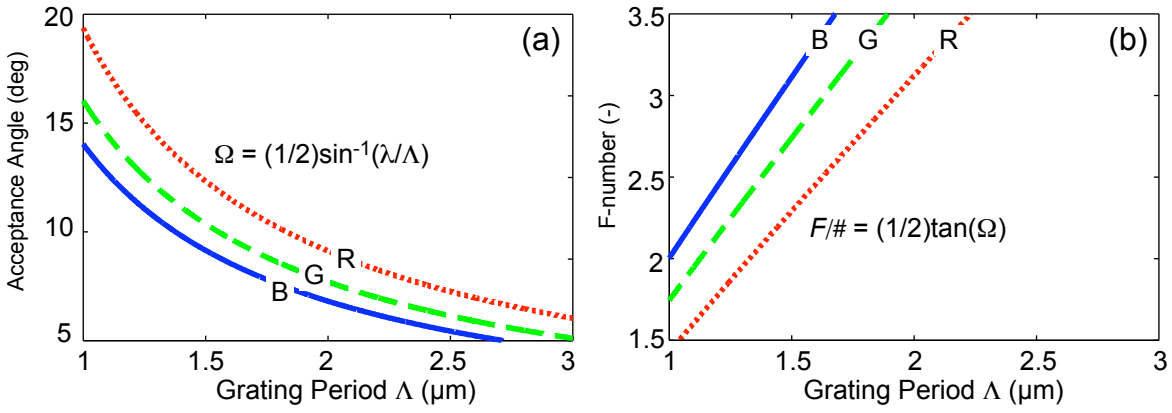

Figure 4.9: System requirements for high-contrast polymer-PG displays: (a) acceptance angle and (b) $F/\#$ of projection optics.

As is well known, a projector system has an aperture that is angularly limited to a cone of half angle Ω, the F/# (defined as ratio of a lens focal length to its diameter) can be determined as $F/\# = \frac{1}{2}\tan\Omega$. These are calculated and shown in Fig. 4.9 for three wavelengths (red, green, blue) corresponding to the peak wavelengths of popular high-brightness LEDs. For obvious reasons, we focuses on achieving the lowest 0-order leakage and smallest grating period possible, since these aims lead to higher extinction ratio and larger acceptance angle, respectively.

4.2.2 Extinction ratio enhancement

The parallel and anti-parallel configurations of two achromatic PGs are directly analogous to parallel and crossed polarizers, respectively. Most importantly, note that the transmittance of parallel PGs is approximately double that of parallel polarizers. However, the raw extinction-ratio from anti-parallel PGs (typically, at small periods $\sim 2\mu$m) are significantly lower than expected and are limited to $\leq$100:1, mainly related to leakage illustrated in Fig. 4.10(a).

We have discovered that a fractional +a-plate placed immediately after the first PG can dramatically improve the extinction-ratio of anti-parallel PGs. The relative orientation of this extinction-ratio enhancement film (EEF) is shown in Fig. 4.9(b). We found that the best matched EEF has a retardation $\sim 0.04\lambda$, and it improves the peak extinction-ratio by

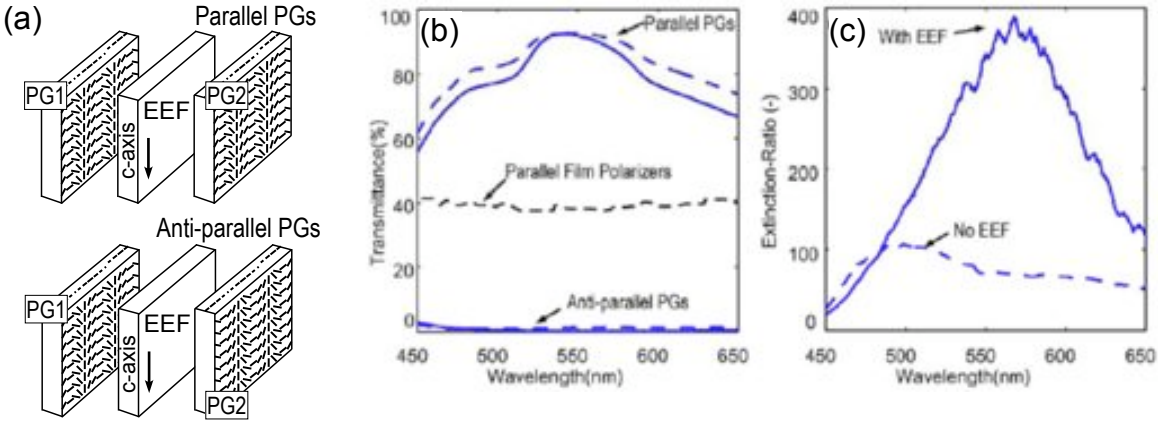

Figure 4.10: Effect of the extinction-ratio enhancement film (EEF): (a) polarization leakage; (b) anti-parallel PGs with an EEF; (c) transmittance of parallel and antiparallel PGS; (d) improvement on the extinction ratio by an EEF.

nearly a factor of four (up to 400:1 versus 100:1, Figs. 4.9(c) and 4.9(d)). The EEF adjusts the polarization of the diffracted orders from the first PG to match the eigen-polarizations of the second grating, thus reducing the leakage into the redirected beam at the output, even at large diffraction angles. Although the retardation of this film may vary with the grating period, we find in general that such thin retardation films nearly always offer a significant enhancement.

Chapter 5

Novel Beam Steering Systems using Polarization Gratings

The ability of precise beam pointing is crucial to any optical systems such as free-space optical communications, remote sensing, laser cutting/milling, fiber optic connections, optical data storage, displays, even laser-guided weaponry, and related technologies where directional control of collimated light is essential. The most common approaches employ large mechanically controlled mirrors (i.e., Ginballed mirros). While this technology is mature, conventional mechanical steering is still limited by difficulties of rapid pointing, stability issues, requirement of large weight and volume, mechanical design complexity, and high costs. To overcome these limitations of the current mechanical beam steering systems, there are increasing demands for compact, robust, and cost effective devices for beam steering.

In this Chapter, we introduce and demonstrate a beam steering device based on a stack of polarization gratings and waveplates. This all-thin-plate beam steering design enables wide-angle steering at extremely high-efficiency with a large aperture beam in a compact, light-weight, nonmechanical system. We also introduce a new beam steering concept *Risley Grating* using rotating, inline polarization gratings as a thin-plate version of the Risley prism. The Risley grating suggests the same mechanical stabilities and precisions of the Risley prism but a much more compact design with larger apertures over large angular range.

5.1 Non-mechanical, wide-angle beam steering using stacked polarization gratings and LC waveplates

Nonmechanical beam steering has been of great interest for many application especially where mechanical parts are not acceptable (i.e., due to vibration/thermal fluctuation) or a large-aperture beam is required in a limited space and weight [101]. One approach to nonmechanical beam steerng is an optical phased array (OPA) enabled by MEMS-based micro-mirros [150] and liquid crystal technologies [86] to create a phase profile by tilting micro-mirrors or changing liquid crystal arrangement. Several other approaches based on acousto-optic devices, electro-optic polymer devices, micro-prism or micro-lens elements [83, 151], birefringent prisms [87], holographic glass [152], and electrowetting devices [153]. Significant advances have been made in key performance areas such as size, rapid pointing, power, and design simplicity. However, viable solutions for wide-angle beam steering have not been established yet.

Liquid crystal technologies have several advantages of high birefringence, excellent electro-optical properties including fast switching and low operation voltages, and well-established techniques (e.g., liquid crystal displays). While these exceptional properties make LC devices attractive as a nonmechanical beam steering device, continuous steering over large angular range still remains an important challenge to advance the current beam steering technology. The LC-based OPA concept has been developed in the last decade but often limited to small-aperture, small-angle steering. A combination of this LC-OPA

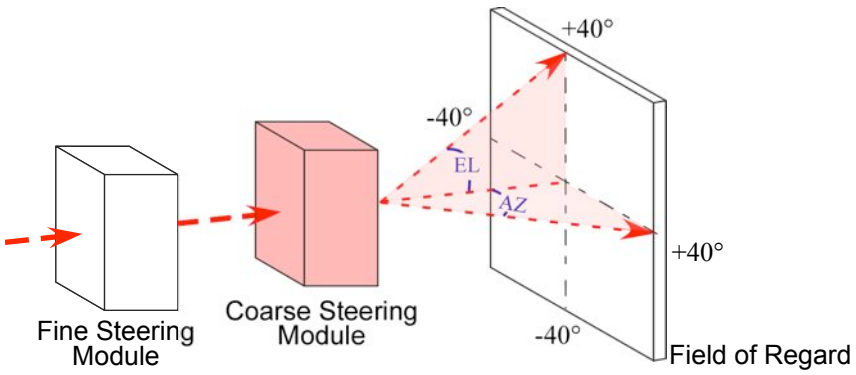

Figure 5.1: Concept of a beam steering system combining a continuous, narrow-angle steering device and a coarse, wide-angle beam steering device to achieve a large field of regard.

with other large angle, discrete steering techniques was also suggested to enable continuous, wide-angle steering. A few different types of LC phase gratings (i.e., binary or blazed) for large angle, discrete steering have been investigated. However, one important disadvantage of all these LC gratings has proven to be their poor steering efficiency at large angles.

In this Section, we introduce a novel non-mechanical beam steering device based on the polarization sensitive properties of liquid crystal polarization gratings (PGs) [100]. They can function as highly efficient beam steering elements, by deflecting all of the incident light into one of the three diffraction orders (0 and ± 1), based on the input polarization and the applied voltage. The unique properties of PGs can give very high experimental diffraction efficiency ($\sim 100\%$) for various diffraction angles, and the thickness of PGs is independent of the aperture size so it allows for wide angle steering with large aperture. Multiple stacks of PGs with LC waveplates enables all electrically controlled, wide-angle beam steering in a remarkably thin package and with light weight. As shown in Fig. 5.1, high throughput, continuous steering with a large aperture size over a large FOR can be obtained by combining of a fine-angle, but continuous beam steering device (i.e., LC-OPA).

5.1.1 Basic beam steering operation of polarization gratings

We have identified several combinations of PGs and LC waveplates, that can perform a three-way steering. These designs can be implemented with switchable (active) or polymer (passive) PGs, with each approach having its own advantages and disadvantages. We will discuss two representative cases of PG beam steering, compare the fabrication procedures involved, and measure their individual performance.

We first consider an active PG beam steering stage, which contains one LCPG and one LC half-waveplate as shown in Fig. 5.2(a). In this scheme, a circular incident polarization is assumed and the notations for circular polarizations are given as right-handed (RCP) and left-handed (LCP). The LC waveplate, which can lead to a half-wave retardation ($\Delta n_l d = \lambda/2$), determines the handedness of polarization (RCP or LCP). With no external field, the beam is diffracted from the LCPG cell and its direction (either the $+1$- or -1-order, $\theta_{\pm 1} = \sin^{-1}(\lambda/\Lambda)$) is determined by the beam polarization state. Note that the handedness of output polarization is again flipped by PG diffraction (RCP to LCP or LCP to RCP). When a voltage is applied to the LCPG cell, the beam passes through without changing its direction. Hence a unique steering operation with three beam

directions corresponding to the diffraction orders (0 and ±1) is enabled by individually switching two LC elements. We note that this approach may involve 4 glass substrates and 4 transparent-conducting-electrodes (i.e., ITO).

Fig. 5.2(b) shows a passive PG steering stage, which is also able to steer an incident beam into three different directions. This stage includes each pair of RMPGs and LC half-waveplates to essentially perform in the same manner as the active PG steering stage. Since RMPGs diffract the beam into desired directions depending on the polarization handedness that is determined by LC waveplates, the final steering angle can be controlled by switching the two LC waveplates. Note that the number of active elements (for electrical switching) remains same but the steering angle becomes the second order of diffraction ($\theta_2 = \sin^{-1}(2\lambda/\Lambda)$) instead of the first order ($\theta_1 = \sin^{-1}(\lambda/\Lambda)$) for an active PG stage with the same grating period. We again note that each stage may involve 6 glass substrates and 4 transparent-conducting-electrodes, which means more interfaces than the active PG case.

5.1.2 Diffraction characterization of single PGs

We prepared two sets of PGs with 5° ($\Lambda \approx 18\mu$m) and 10° ($\Lambda \approx 9\mu$m) diffraction angles using the reactive mesogen mixture RMS03-001C (Merck, Δn_l=0.14 at 1550 nm) for passive RMPGs and nematic LC MDA-06-177 (Merck, Δn_l=0.13 at 1550 nm) for active LCPGs. The thickness of the gratings is $\sim 6\mu$m for a halfwave retardation at 1550nm ($\Delta n_l d = 1/2$). We measured the power of three possible diffraction orders with both RMPGs and LCPGs with an infrared laser beam (1550nm), which was right-handed, circularly

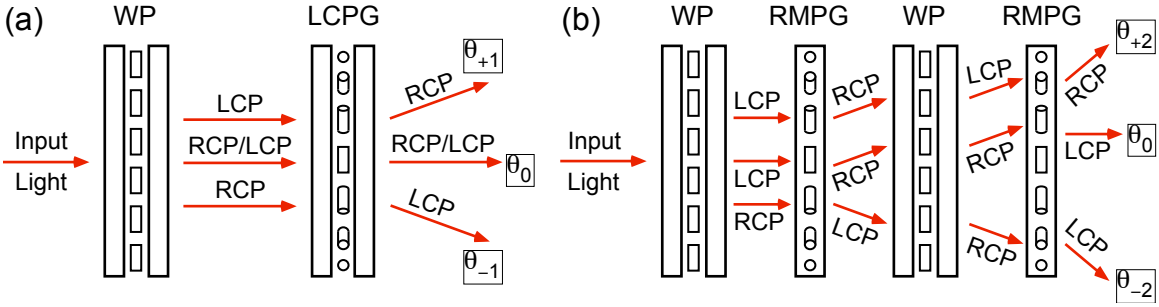

Figure 5.2: Non-mechanical beam steering based on PGs: (a) switchable (active) LCPG configuration and (b) polymer (passive) RMPG configuration. The notations 'RCP' and 'LCP' represent right- and left-handed circular polarization, repsectively. Note that both LC waveplates (WPs) and PGs are optimized for a half-wave retardation ($\Delta n_l d = \lambda/2$).

polarized (see Fig. 5.3). In order to quantitatively evaluate the diffraction properties, we define a number of different parameters including the input power I_{in}, the transmitted power of a reference substrate/cell filled with glue I_{ref}, the power of the m-th diffracted order I_m, the transmittance of the m-th order $T_m = I_m/I_{in}$, the absolute efficiency of the m-th diffracted order $\eta^a_m = I_m/I_{ref}$, and the intrinsic efficiency of the m-th diffracted order $\eta^i_m = I_m/(\cdots + I_{-1} + I_0 + I_{+1} + \cdots)$. Table 5.1 summarizes our measurements of these two sets of PGs.

Intrinsic efficiency quantifies the inherent diffraction efficiency of the grating alone, normalizing out the effects of the substates and any scattering. From this data, it is apparent that diffraction from individual gratings is extremely efficient ($> 99.7\%$ for all cases). For the absolute efficiency measurement including scattering, both RMPG perform with high

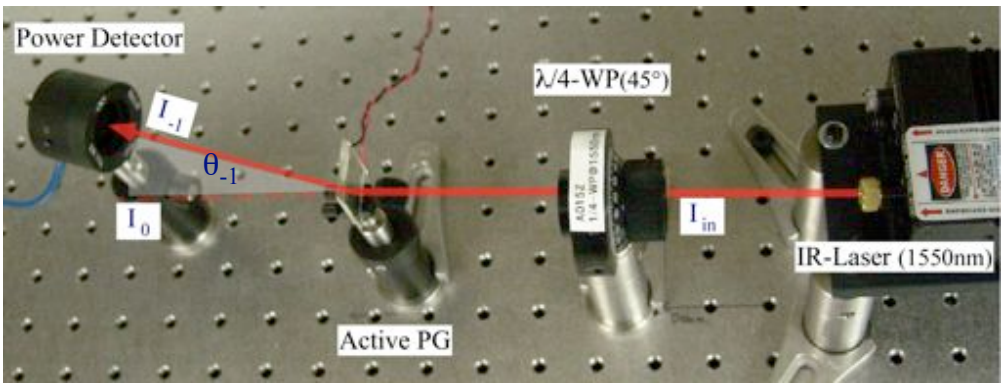

Figure 5.3: Experimental setup for characterization of basic diffraction properties of PG samples. Note that the IR laser beam is circularly polarized at the grating sample and the beam is diffracted predominantly into one of the first order.

Table 5.1: Diffraction characterization of two different types of PGs at 1550nm.

Type of PG	$\theta_{\pm1}$ (deg)	I_{in} (mW)	I_{ref} (mW)	I_{-1} (mW)	T_{-1} (%)	η^a_{-1} (%)	η^i_{-1} (%)
RMPG	±5	41.32	37.91	37.83	91.4	99.6	99.8
RMPG	±10	41.32	37.91	37.44	91.1	99.3	99.8
LCPG	±5	41.71	35.68	35.63	85.3	99.7	99.8
LCPG	±10	41.82	35.68	33.71	80.6	94.5	99.7

efficiencies ($> 99.3\%$) while the LCPG with 10° diffraction angle shows lower efficiency ($\sim 94.5\%$) that indicates more scattering. The actual transmittance was measured between 80% and 91% for all PG samples. It is important to note that almost all of the losses, therefore, were due to the substrate absorption and interfaces. We expect that as we reduce reflection-related losses by acquiring more optimum glass substrates (AR-coated and index-matched), we will be able to dramatically improve the overall transmittance.

We now discuss some trade-offs between these two approaches using either RMPGs or LCPGs as beam steering elements. One clear advantage of RMPGs over LCPGs is larger steering angles using the same period gratings (i.e., 20° steering from 10° diffraction angle). Another important advantage is layer-by-layer processing of RMPGs, which allows small grating periods without limitation of the critical thickness. RMPGs, however, require two more substrates (4 more interfaces) for each stage. Since every interface likely involves scattering and reflection losses, minimum substrates in use is always preferred. Therefore, RMPGs can be employed in steering stages for high angles where LCPGs cannot perform with high efficiencies or beyond the critical thickness.

5.1.3 2-stage beam steering system with ±15° steering angles

We built a simple active PG beam steering system that are composed of two LCPGs and two LC waveplates and demonstrated electrically controlled beam steering into seven different angles within ±15°. The same LCPG samples (with 5° and 10° diffraction angles) were used for this system. We also prepared two LC waveplates with a half-wave thickness ($d = 6\mu$m) for 1550nm using nematic LC MDA-06-177 (Merck, $\Delta n_l \approx 0.13$). These LCPGs and LC waveplates are stacked as shown in Fig. 5.4(a).

The stage can selectively control steering angles from $-15°$ to $+15°$ with 5° steps by switching individual gratings and waveplates. Fig. 5.4(b) shows pictures of diffraction spots at seven different steering angles (on an IR sensitive detecting card located 40cm off from the steerer). All diffraction spots are well aligned each other and no significant walk-off was observed, which is another advantage of this thin-plate beam steering system. Experimentally demonstrated intrinsic efficiency (steering efficiency) ranges from 99.5% to 99.6% for all seven diffraction beams with the case of 15° diffraction angle shown in Fig. 5.4(c).

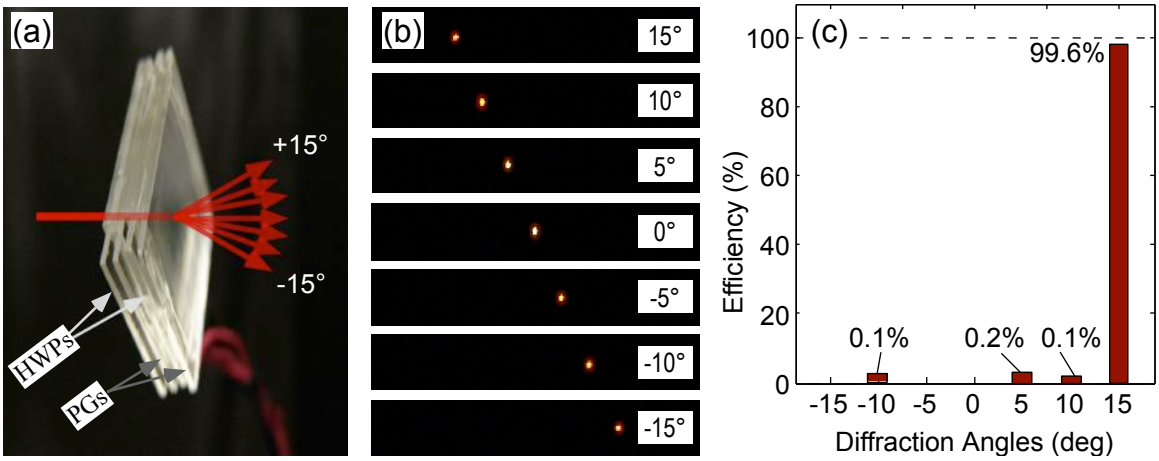

Figure 5.4: Beam steering system using LCPGs with ±15° steering angles: (a) photograph of 2-stage steerer with two LCPGs and two LC waveplates; (b) steered beam at seven different angles; (c) intrinsic efficiencies for 15° steering angle.

5.2 High-Throughput, Continuous, Beam Steering Using Rotating Polarization Gratings

The ability of precise beam pointing is crucial to any optical system such as free-space optical communications, countermeasure, laser weapons, and fiber optic switches where beam alignment and target tracking are required. With increasing demands for compact, robust, and cost-effective devices for beam steering, *Risley Prisms* [154, 155, 156, 157, 158, 159] comprising pairs of wedge prisms have long been used for its high degree of accuracy and stability. Their utility, however, is often limited by small deflection angles and poor size scaling properties (due to bulky prismatic elements) where wide angles and modest/large apertures are required.

Here, we introduce an arrangement of two independently rotating, inline polarization gratings (Fig. 5.5(a)), which we term *Risley Gratings*, to achieve a remarkably efficient and compact beam steering device (Fig. 5.5(b)). The single-order diffraction, high efficiency, polarization behavior, and wide acceptance angle of the polarization gratings [7] (PGs) described here enable a unique opportunity for beam steering with high throughput and low sidelobes. Several liquid crystal (LC) grating structures (i.e., blazed or binary types) were proposed as a beam steering element [42, 83]. The practical use of such LC gratings, however, is limited by their poor angle performance, limited peak efficiency, and low transmittance, and they are not applicable for the Risley gratings. A nonmechanical beam steering system based on stacked LCPGs and LC waveplates was first introduced and demonstrated by Kim et al. [100]. A similar steering operation by rotating two PGs was also reported in Ref. [128], but the Risley grating concept was not yet clearly captured. The two PGs can be formed on are thin substrates (eg, glass, Si) can be placed in close proximity (total thickness of few mm) and can be made with wide areas (easily many cm^2), exhibiting a dramatic aspect ratio improvement as compared to *Risley Prisms*. A further benefit is that our arrangement manifests practically no beam walk-off, and can be tailored to operate at nearly any wavelength from visible to midwave-infrared.

In this Section, we will show the basic concept and its operation principles of this new beam steering device based on PGs and demonstrate a Risley grating that performs continuous steering of a laser beam (at 1550 nm) with the maximum deflection angle of $\pm 31^\circ$ and up to 92% throughput. The angle of the emerging beam from the Risley grating

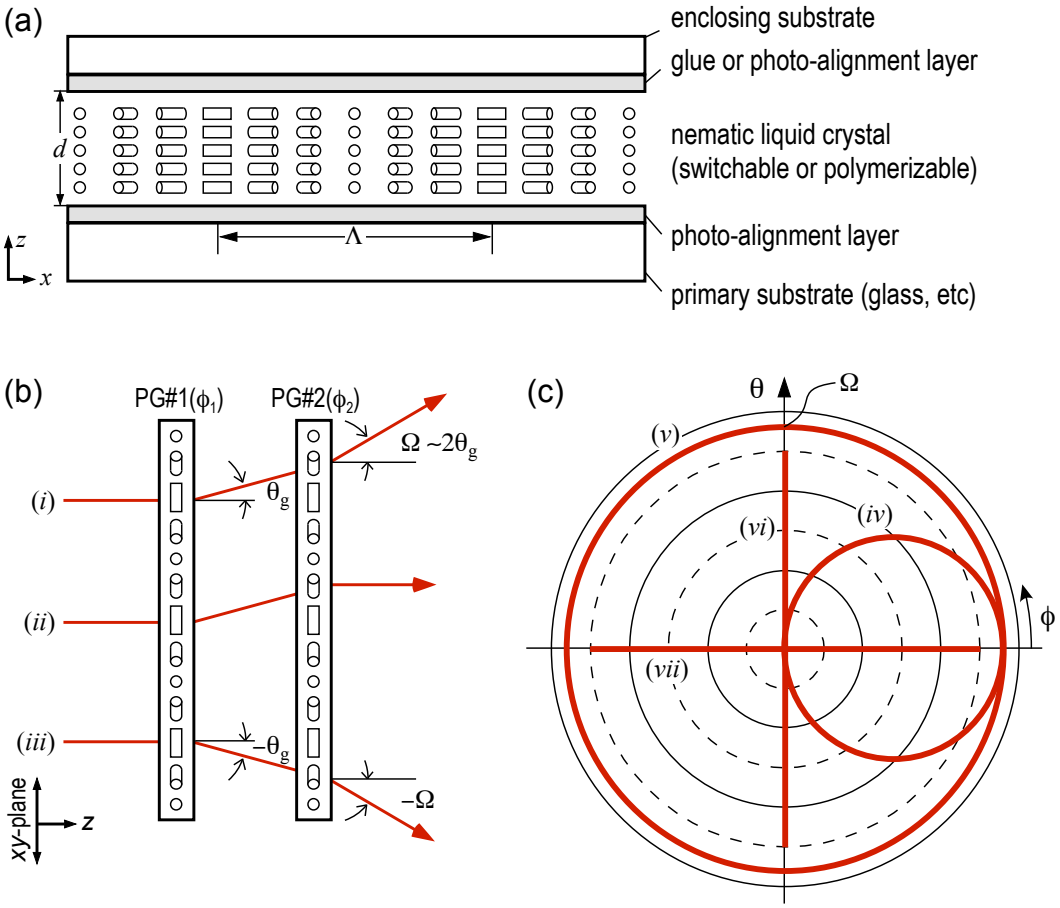

Figure 5.5: Risley gratings as a thin-plate, continuous beam steering element using rotating polarization gratings (PGs): (a) a PG formed in a thin liquid crystal layer; (b) beam steering from two inline PGs (with azimuthal orientation angles at ϕ_1 and ϕ_2); (c) simple scanning patterns of the Risley grating. Note that the maximum deflection angle Ω is determined by the diffraction angle θ_g (e.g., $\theta_g = 15°$) of the PGs as $\sin\Omega = 2\sin\theta_g$ (e.g., $\Omega_g = 31°$). The field-of-regard (FOR) of such a beam steering system is defined as 2Ω (e.g., $\theta_g = 62°$). Several different steering conditions are described here as: (i) the beam is diffracted into the +1-order at both the PG stages and the final steering angle is the maximum deflection angle Ω; (ii) the beam is first diffracted into the +1-order by the first PG but redirected back to the normal by the second PG and the final steering angle is 0°; (iii) the beam is diffracted into the −1-order at both the PG stages and final steering angle is $-\Omega$; (iv) the first PG is fixed at $\phi_1 = 0$ and the second PG is rotated by 360° to scan an inner circle; (v) the two PGs are aligned in an antiparallel orientation and both are rotated by 360° to scan a most outer circle within the FOV; (vi) and (vii) the two PGs are aligned in an antiparallel orientation and counter-rotated with each other (i.e., the first PG is rotated in clockwise while the second in counterclockwise) to scan linear lines within the FOR.

is calculated using the direction cosine space method and confirmed by experimental results. The steering patterns and sidelobes will be also discussed.

5.2.1 Basic steering operation of the Risley grating

In general [4, 6], PGs are diffractive elements composed of periodic profiles of spatially varying optical anisotropy, and as such, often manifest unique behavior. Here, we employ "Circula"-type PGs [7], defined by a spiraling, constant-magnitude, uniaxial birefringence (Fig. 5.5(a)). Remarkably, this PG exhibits some of the best properties of both the thin- (Raman-Nath) and thick (Bragg) grating regimes, including 100% theoretical efficiency into a single diffraction order and a wide angular acceptance angle. As long as the parameter $\rho = 2\lambda^2/\bar{n}\Delta n_l \Lambda^2 << 1$, the first-order diffraction efficiency can be accurately approximated as follows [7]: $\eta_{\pm 1} = \frac{1 \mp S_3'}{2} \cos^2\left(\frac{\pi \Delta n_l d}{\lambda}\right)$, where Δn_l is the birefringence, $\bar{n}$ is the average index, d is the grating thickness, Λ is the grating period, λ is the wavelength, and $S_3' = S_3/S_0$ is the normalized Stokes parameter describing polarization ellipticity of the incident light. Note that a single first-order efficiency can indeed be 100% when $\Delta n_l d = \lambda/2$ and when circularly polarized light (ie, $S_3' = \pm 1$) is incident, as illustrated in Fig. 5.5(b). Note that first-order diffracted light will have the reverse handedness of the input, and is always circularly polarized regardless of the input. Also note that within our modest assumptions, efficiency does not depend on either Λ or the angle of incidence θ_{in}, enabling significant design flexibility (especially compared to Bragg gratings, another common high efficiency grating). The propagation angle $\theta_{\pm 1}$ light transmitted into the first-orders is determined by the classic grating equation: $\sin\theta_{\pm 1} = \pm\lambda/\Lambda + \sin\theta_{in}$ (when the incident light is coplanar with the grating vector).

Here, we arrange two independently rotating, inline PGs, to achieve a remarkably efficient and compact beam steering device (Fig. 5.5(b)). The principle of operation is described as follows. A circularly polarized, collimated, narrowband beam is arranged normally incident on the first PG. With nearly 100% efficiency, this light is redirected into the polar angle $\theta_g = \sin^{-1}(\lambda/\Lambda)$ with an azimuthal direction set by the azimuth angle ϕ_1 of this first PG. The second PG then receives this beam, and redirects it again with a nonlinear dependence on its diffraction angle θ_g and azimuth angle ϕ_2.

Since the angle relationship is nonlinear, it is often convenient to introduce the direction cosine space where diffraction at an arbitrary incident angle can be described by

simple, linear vector representations as shown in Figs. 5.6(a) and 5.6(b) [160]. The direction cosines of the steered beam are given by

$$\alpha = \sin\theta_g \left(\cos\phi_1 - \cos\phi_2\right) \tag{5.1a}$$

$$\beta = \sin\theta_g \left(\sin\phi_1 - \sin\phi_2\right) \tag{5.1b}$$

$$\gamma = \sqrt{1 - \alpha^2 - \beta^2}, \tag{5.1c}$$

By definition, $\alpha^2 + \beta^2 \leq 1$. The net azimuth and polar angles of the transmitted beam can be determined from Eqs. 5.1 as

$$\phi = \tan^{-1}\left(\beta/\alpha\right) \tag{5.2a}$$

$$\theta = \cos^{-1}\left(\gamma\right). \tag{5.2b}$$

The maximum deflection angle Ω is defined as $\sin\Omega = 2\sin\theta_g$, and the device can steer to any angle within a $\pm\Omega$ cone (as shown in Fig. 5.5(c)), with a field-of-regard (FOR) $= 2\Omega$. The author refers readers to Appendix **??** for more details on mathematical descriptions for the steering angles. Chromatic dispersion in this simple two PG device will follows typical diffractive dispersion.

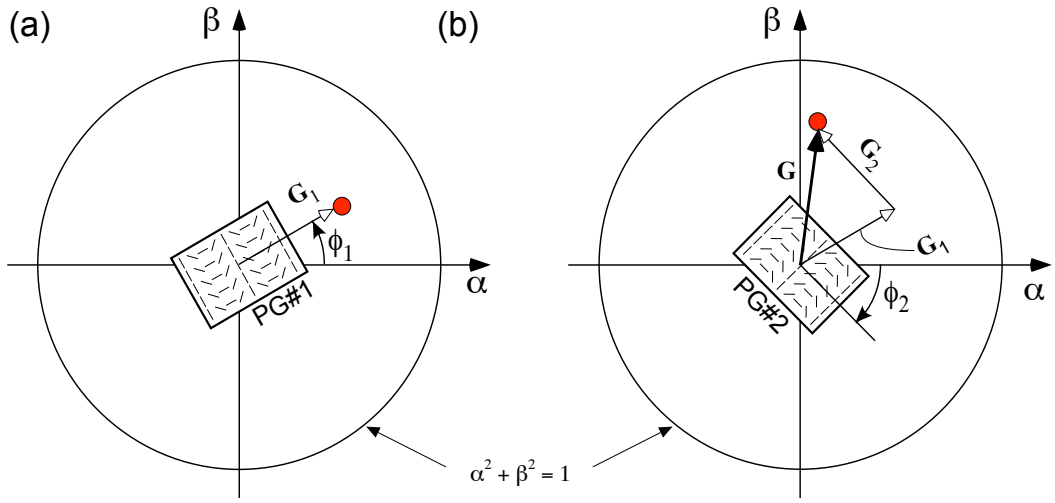

Figure 5.6: Vector representations of the PG diffraction in the direction cosine space: (a) the first PG diffraction $\mathbf{G}_1$; (b) the second PG diffraction $\mathbf{G}_2$. The final direction can be expressed as a simple vector sum $\mathbf{G} = \mathbf{G}_1 + \mathbf{G}_2$.

5.3 Demonstration of the Risley grating with $\pm 31^\circ$ field of regard

We demonstrate the Risley grating beam steering with the maximum deflection angle $\Omega = 31^\circ$ at 1550 nm using a pair of PGs (each with Λ =6 μm, and $\theta_g = 15^\circ$). Two PGs are mounted in separate rotation stages to independently set their grating orientations.

Our defect-free PGs were formed as LC cells, using polarization holography and photo-alignment materials, as well described elsewhere [18, 11, 17]. We utilized a linear-photopolymerizable polymer (LPP) (ROP-103/2CP, from Rolic) and nematic LC (LCMS-102, from Boulder Nonlinear Systems, $\Delta n_l = 0.31$ at 1550 nm). After coating glass substrates with LPP using standard processing (3000 krpm spin, 130°C bake for 10 min), we formed a cell with 2.5 μm thickness (using silica spacers). The PG pattern was recorded with orthogonal, circularly polarized beams from a HeCd laser (325 nm), with an exposure energy of 2 J/cm^2. Then the exposed cell was filled with LC in the isotropic state (at 150°C) at atmospheric pressure. The individual PGs exhibit nearly ideal PG diffraction as Eq. 2.43 with $> 98\%$ first-order efficiency, with no observable higher orders or scattering. Note that both air/glass interfaces were treated with anti-reflection coatings to reduce reflection losses.

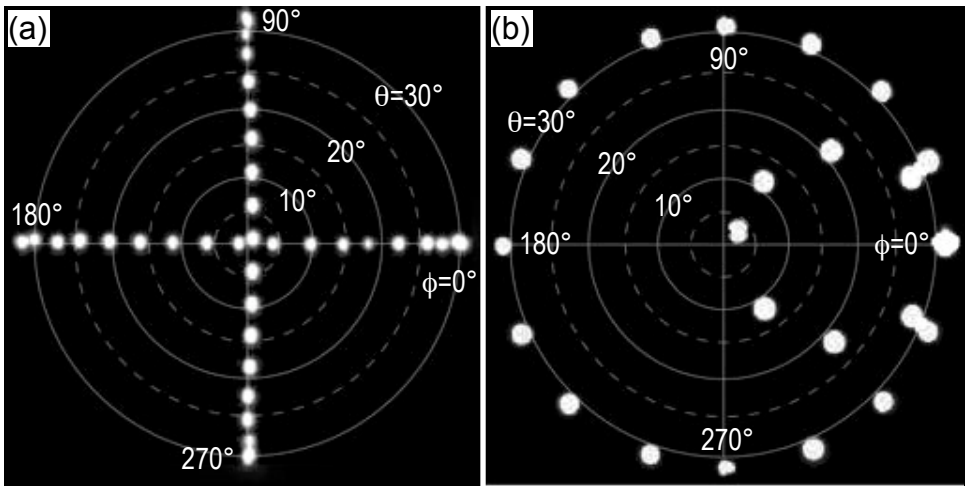

Figure 5.7: Demonstration of the Risley grating beam steering with a 62° FOR at 1550 nm wavelength. Note that the pictures of the steered beam on an IR sensitive detecting screen were taken and post-processed onto the angle space.

Fig. 5.7 shows images of the steered beam (from a linearly polarized IR laser passed through a quarter-waveplate) directed incident on a planar screen, showing a variety of simple scans (lines and circles) within the entire field-of-regard (FOR). These correspond to the curves indicated in Fig. 5.5(c), validating Eqs. 5.2. Each image is a superposition of individual pictures taken of the beam incident on a fluorescent infrared viewing-card in a dark room.

We confirmed continuous beam steering within $\pm 31^\circ$ with $\sim$ 92% throughput (i.e., transmittance defined as $T = P_{out}/P_{in}$, where P_{in} is the input power and P_{out} is the power in the steered direction). We also calculate the diffraction efficiency, a normalization that removes the effect of the substrates and allows direct comparison to Eq. 2.43, defined as $\eta = P_{out}/P_{tot}$, where P_{tot} is the total transmitted power into the output hemisphere. Fig. 5.8(a) shows transmittance and efficiency of the steered beam at the (intended) steered angle. This shows high transmittance (from 92% to 89%), with some variation depending on the steering angle. Since we estimate that each of our glass/LC interface has a $\sim$ 1% Fresnel-type reflection loss, the substrates cause roughly 4% of the transmittance loss. The remaining loss is due to leakage into sidelobe directions, as better characterized in Fig. 5.8(b). Note that the diffraction efficiency is even higher, since the loss due to substrates is normalized away. In order to explore the severity of sidelobe leakage (for the two extreme and center angles), we show in Fig. 5.8(b) the fraction of transmitted power measured at observation angles when the PGs were fixed. In all cases, the sidelobe leakage occurred at angles that were multiples of θ_g, and were in the range of 1% to 6%. This leakage primarily results from oblique incidence to the second PG, and can be reduced by the use of higher birefringence LC materials and additional retardation compensation films in between the two PGs (similar to the display application [**?**]). Within our measurement error, we noticed $< 0.5\%$ absorption and scattering. We note that the reflection loss and any absorption can be further improved with the use of enhanced index-matched (glass/LC) substrates.

While these tests were performed at 1550 nm with $\sim$ 5 W/cm^2 intensity without degradation, we have also conducted preliminary tests with similar PGs at 1064 nm at several 100s W/cm^2 intensities with the same result. We speculate that polymer PGs formed with commercial materials on index-matched substrates could steer very high beam powers (perhaps many kW/cm^2 at near-infrared wavelengths).

We demonstrated that two rotating, inline PGs is a highly efficient beam steering

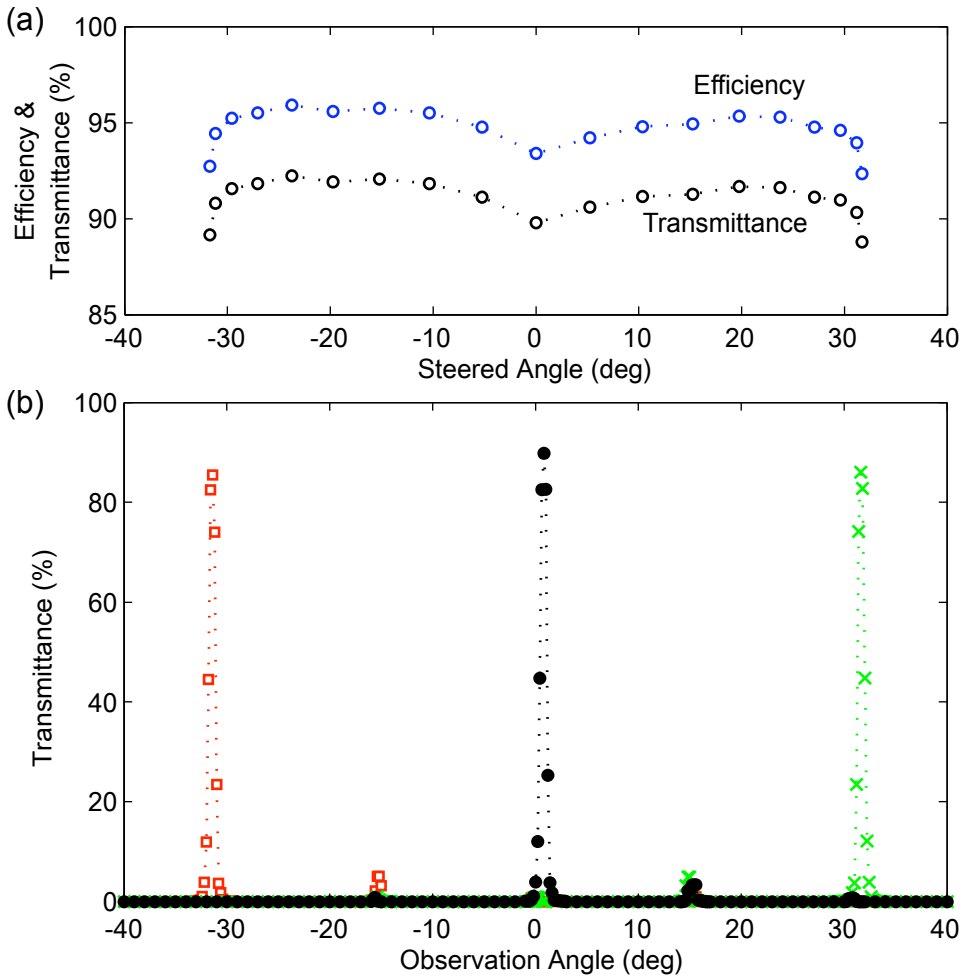

Figure 5.8: High throughput from 92% to 89% of the Risley grating: (a) transmittance and efficiency for different steered angles; (b) transmittance at observation angles across ±40° for three steering angles (0° and ±31°).

device, with an ultra-compact and lightweight form factor. Our prototype continuously steers within a FOR = 62°, and manifests a transmittance as high as 92% into the steered direction, with sidelobe leakage on the order of a few percent. We employ two identical PGs (with $\Lambda = 6$ μm) with ±31° maximum deflection angles at 1550 nm wavelength. Each PG is a thin-plate and can be formed at almost arbitrarily large areas, and practically eliminates beam walk-off. Larger steering angles, further loss reduction, and implementation at other wavelengths are certainly possible through continued optimization of substrates and PG materials, as discussed.

Chapter 6

Advanced Hyperspectral Polarimeters and Imaging Spectropolarimeters at Visible and Midwave-Infrared Wavelengths Enabled by Polarization Gratings

6.1 Snapshot full-Stokes hyperspectral polarimetry based on inline polarization gratings

The measurement of complete polarimetric parameters for a broad spectrum of wavelengths is challenging because of the multi-dimensional nature of the data and the need to chromatically separate the light under test. As a result, current methods for spectropolarimetry and imaging polarimetry are limited because they tend to be complex and/or relatively slow. Here we experimentally demonstrated an approach to measure all four Stokes parameters [3] using three polarization gratings and four simultaneous intensity measurements, with potential to dramatically impact the varied fields of air/space-borne remote sensing, target detection, biomedical imaging/diagnosis, and telecommunications.

We suggest that an ideal spectropolarimeter would (i) determine the full Stokes vector through only four simultaneous intensity measurements per wavelength, (ii) require no polarizers at all (avoiding their expense, bulk, and wavelength limitations), (iii) offer the potential to operate across wavelengths ranging from 0.4μm to mid-infrared with easy calibration, (iv) be robust to photo/mechnical/chemical/thermal degradation, and (v) have ability to be easily fabricated with clear apertures of several cm^2 or more. The inline PG spectropolarimeter we describe and validate here achieves all of these properties.

While the details of polarimetry using PGs depend on the specific implementation, a generic description capturing the basic elements of the approach is illustrated Fig. 6.1(a). An inline arrangement of polarization-sensitive diffraction gratings allows for the detection

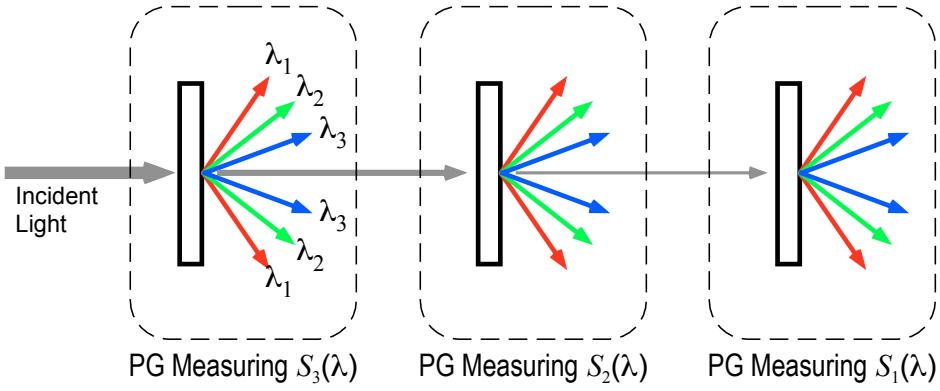

Figure 6.1: Hyperspectral polarimetry based on polarization gratings (PGs) with parallel detection of the full Stokes parameters.

at each stage of at least one of the Stokes parameters by the measurement of the diffracted intensities. Wavelength separation occurs inherently (governed by the grating equation), and detection can be done in a fashion similar to conventional spectrometers using linear photodetector arrays or two-dimensional focal-plane-arrays. We utilize three PG elements along with two achromatic quarter-waveplates to implement the spectropolarimeter, as shown in Fig. 6.2.

6.1.1 Measurement of the Stokes parameter using PG elements: Jones matrix reasoning

We now revisit the Jones matrix reasoning for describing PG diffraction, which is described in Section 2.4. The far-field electric field of the diffraction order m can be written as follows

$$\mathbf{D}_m = \frac{1}{\Lambda}\int_0^{\Lambda} \mathbf{T}(x)\mathbf{E}_{in}e^{-j2\pi mx/\Lambda}dx \tag{6.1}$$

The transfer matrix T is given by

$$\mathbf{T}(x) = \mathbf{R}\left(-\pi x/\Lambda\right)\begin{bmatrix} e^{-j\Gamma} & 0 \\ 0 & e^{j\Gamma} \end{bmatrix}\mathbf{R}\left(-\pi x/\Lambda\right) \tag{6.2}$$

where $\Gamma = \pi\Delta n_l d/\lambda$ is the normalized retardation and R is the rotation matrix. Assuming an incident plane-wave (uniform in the x direction), we can rewrite Eq. 6.1 as follows

$$\mathbf{D}_m = \mathbf{T}_m\mathbf{E}_{in} \tag{6.3}$$

where the grating transfer matrix is defined as $\mathbf{T}_m = \Lambda^{-1}\int_0^{\Lambda}\mathbf{T}(x)e^{-j2\pi mx/\Lambda}dx$. Since PGs have non-zero solutions only for $m = -1, 0, +1$, we can rewrite Eq. 6.3 as follows

$$\mathbf{D}_0 = \mathbf{E}_{in}\cos\Gamma \tag{6.4a}$$

$$\mathbf{D}_{\pm1} = \frac{1}{2}\mathbf{E}_{in}\sin\Gamma\begin{bmatrix} -j & \mp1 \\ \mp1 & j \end{bmatrix} \tag{6.4b}$$

We can now solve for the diffraction efficiency as the ratio of output to input intensity ($\eta_m = |\mathbf{D}_m|^2/|\mathbf{E}_{in}|^2$) as follows

$$\eta_0 = \cos^2\Gamma \tag{6.5a}$$

$$\eta_{\pm1} = \frac{1}{2}(1 \mp S_3')\sin^2\Gamma \tag{6.5b}$$

where $S_3' = S_3/S_0$ is the normalized Stokes parameter corresponding to ellipticity of the incident light.

It should be clear that these three unique properties make it suitable to implement the first element in Fig. 6.1, allowing the measurement of both S_0 and S_3 each wavelength knowing only the parameters of the PG and the first-order intensities $I_{+1}(\lambda)$ and $I_{-1}(\lambda)$.

$$S_0 = (I_{+1} + I_{-1}) \cos^{-2} \Gamma \tag{6.6a}$$

$$S_3 = (I_{-1} - I_{+1}) \sin^{-2} \Gamma \tag{6.6b}$$

Additionally, we have discovered that this PG may also be configured to measure the other two Stokes parameters when combined with achromatic quarter-waveplates, enabling a simple implementation of the second two elements in Fig. 6.1.

Consider the assembly in Fig. 6.2, where the second stage is implemented as a quarter-waveplate (symmetry axes parallel to the x-axis ($\phi = 0°$)) placed immediately before the PG. The Jones transfer matrix for a quarter-waveplate at an angle ϕ from the x-axis can be expressed as follows

$$\mathbf{J}_{\lambda/4}^{\phi} = \frac{1}{\sqrt{2}} \begin{bmatrix} 1 + j\cos 2\phi & j \sin 2\phi \\ j \sin 2\phi & 1 - j \cos 2\phi \end{bmatrix} \tag{6.7}$$

If we consider this assembly in isolation (apart from the first stage), the electric-field of the diffracted orders can be found simply by replacing $\mathbf{E}_{in}$ with $\mathbf{J}_{\lambda/4}^{\phi}\mathbf{E}_{in}$ in Eqs. 6.4 as follows

$$\mathbf{D}_{\pm 1} = \mathbf{T}_{\pm 1}\mathbf{J}_{\lambda/4}^{0°}\mathbf{E}_{in} = \frac{1}{2\sqrt{2}}\mathbf{E}_{in} \sin \Gamma \begin{bmatrix} 1 - j & \mp(1 + j) \\ \mp(1 + j) & 1 + j \end{bmatrix} \tag{6.8}$$

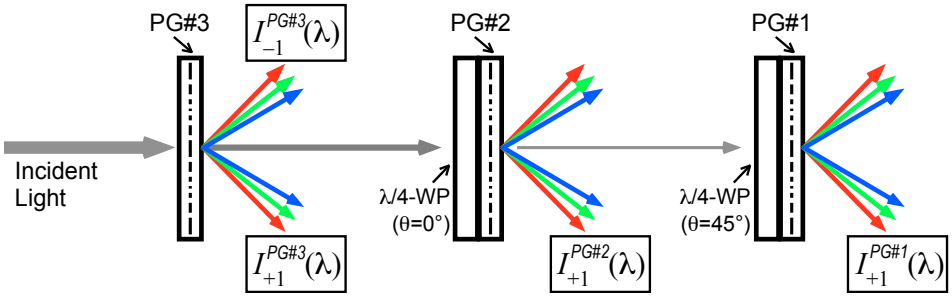

Figure 6.2: Proposed implementation with three PGs and two quater-waveplates enabling detection of the complete Stokes vector information with only four simultaneous intensity measurements per wavelength.

The diffraction efficiency of this quarter-waveplate ($\phi = 0°$) and PG assembly is therefore

$$\eta_{\pm 1} = \frac{1}{2}(1 \pm S_2') \sin^2 \Gamma \tag{6.9}$$

where $S_2' = S_2/S_0$ is the normalized Stokes parameter corresponding to the component of incident light linearly polarized in the $\pm 45°$ directions. The 0-order diffraction efficiency η_0 remains the same as Eq. 6.5.

Finally, consider an assembly with two quarter-waveplates placed immediately before the PG. If the first waveplate has its symmetry axis at 0° and the second at 45°, the electric-field of the diffracted orders can be expressed as follows

$$\mathbf{D}_{\pm 1} = \mathbf{T}_{\pm 1} \mathbf{J}_{\lambda/4}^{45°} \mathbf{J}_{\lambda/4}^{0°} \mathbf{E}_{in} = \frac{1}{4} \mathbf{E}_{in} \sin \Gamma \begin{bmatrix} (-1+j) \pm (1-j) & (-1+j) \mp (1+j) \\ -(1+j) \mp (1+j) & (1+j) \mp (1+j) \end{bmatrix} \tag{6.10}$$

The diffraction efficiency of this double-waveplate ($\phi = 0°, 45°$) and PG assembly is therefore

$$\eta_{\pm 1} = \frac{1}{2}(1 \mp S_1') \sin^2 \Gamma \tag{6.11}$$

where $S_1' = S_1/S_0$ is the normalized Stokes parameter corresponding to the component of incident light linearly polarized in the horizontal (0^{circ}) and vertical (90°) directions. The 0-order diffraction efficiency η_0 remains the same as Eq. 6.5.

We can determine the Stokes parameters using the following simple relationships:

$$S_0(\lambda) = \frac{I_{+1}^{PG\#3}(\lambda) + I_{-1}^{PG\#3}(\lambda)}{\sin^2 \Gamma_3} \tag{6.12a}$$

$$S_1(\lambda) = \frac{I_{-1}^{PG\#1}(\lambda) - I_{+1}^{PG\#1}(\lambda)}{\sin^2 \Gamma_1 \cos^2 \Gamma_2 \cos^2 \Gamma_3} \tag{6.12b}$$

$$S_2(\lambda) = \frac{I_{+1}^{PG\#2}(\lambda) - I_{-1}^{PG\#2}(\lambda)}{\sin^2 \Gamma_2 \cos^2 \Gamma_3} \tag{6.12c}$$

$$S_3(\lambda) = \frac{I_{-1}^{PG\#3}(\lambda) - I_{+1}^{PG\#3}(\lambda)}{\sin^2 \Gamma_3} \tag{6.12d}$$

where the subscripts refers to the parameters of the respective PG ($\Gamma_i = \pi \Delta n_{l,i} d_i / \lambda$, $i = 1, 2, 3$). Using the relationships between the Stokes parameters, all four Stokes parameters can be found by measuring four intensities at each wavelength as follows

$$\begin{bmatrix} S_0(\lambda) \\ S_1(\lambda) \\ S_2(\lambda) \\ S_3(\lambda) \end{bmatrix} = \begin{bmatrix} 0 & 0 & C & C \\ -A & 0 & C & C \\ 0 & B & -C & -C \\ 0 & 0 & C & -C \end{bmatrix} \begin{bmatrix} I_{+1}^{PG\#1}(\lambda) \\ I_{+1}^{PG\#2}(\lambda) \\ I_{+1}^{PG\#3}(\lambda) \\ I_{-1}^{PG\#3}(\lambda) \end{bmatrix} \tag{6.13}$$

with

$$A = 2(\gamma \sin^2 \Gamma_1 \cos^2 \Gamma_2 \cos^2 \Gamma 3^{-1}) \tag{6.14a}$$

$$B = 2(\gamma^2 \sin^2 \Gamma_2 \cos^2 \Gamma 3^{-1}) \tag{6.14b}$$

$$C = (\gamma^3 \sin^2 \Gamma_3)^{-1} \tag{6.14c}$$

where the subscripts refers to the parameters of the respective PG ($\Gamma_i = \pi \Delta n_{l,i} d_i / \lambda$, $i = 1, 2, 3$). The factor γ is the total transmittance of each PG stage, which includes the influence of the material absorption and Fresnel reflection losses at the interfaces. We assume here that this factor is the same for each PG stage.

6.1.2 Experimental demonstration of simplified spectropolarimeter based on PGs

In order to prove the principle-of-operation of the proposed spectropolarimeter (Fig. 6.2), three reactive mesogen PGs with were prepared on borosilicate glass substrates. Their grating period ($\Lambda = 5\mu$m) and birefringence (measured at $\Delta n_l \approx 0.144$ at 1550 nm) were the same for each, and the thicknesses were 6, 3, and 2μm for PG#1, PG#2, and PG#3 respectively. The 0-order efficiency spectra are shown in Fig. 6.3, and each had an area of $\sim 1\text{cm}^2$. These were designed such that each PG stage diffracts approximately 1/3 of the incident light into its respective first-orders, insuring equal signal strength for each measurement. The absorption of the substrates and Fresnel air-glass reflections led to the

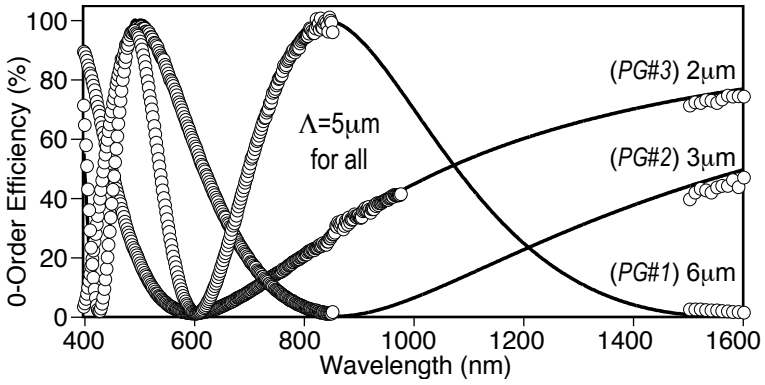

Figure 6.3: Measured diffraction efficiencies (0-order) of the polarization gratings (PGs) used for the spectropolarimeter implementation. Note that $\Lambda = 5\mu$m, $\Delta n_l = 0.144$, and that they were optimized for measurements around 1550nm.

transmittance $T \approx 0.7$ at 1550 nm.

First, we quantitatively measured the polarization-dependent diffraction properties using the setup in Fig. 6.4(a), where a linearly polarized probe laser was arranged such that it would be modulated by the rotation of a waveplate. In Fig. 6.4(b) and 6.4(c), a quarter-waveplate was rotated to vary the probe light between circular and linear polarizations as the +1- and −1-order diffraction efficiencies were measured. An excellent match with Eq. 6.13 is observed. The polarization contrast ratio (between left and right handedness) in the first-orders was remarkably $> 4000 : 1$. The response to a half-waveplate was also measured, and revealed an almost constant ∼50% for both first-orders regardless of the orientation of the input linearly polarized light (Fig. 6.4(d) and 6.4(e)), as expected.

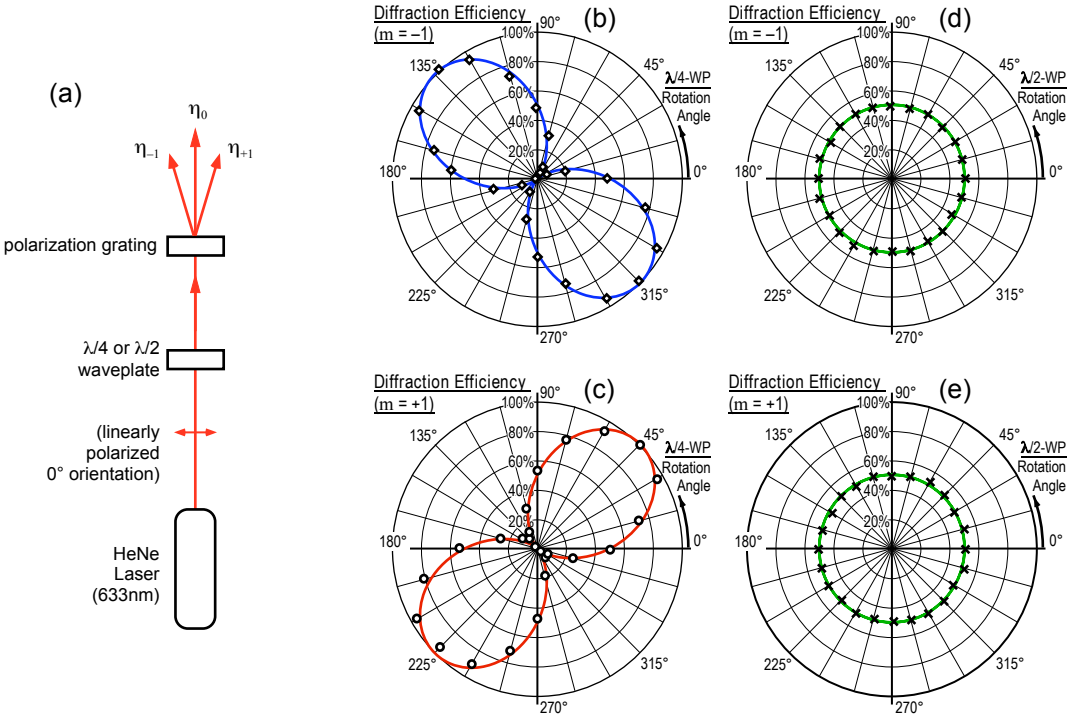

Figure 6.4: Polarization sensitivity of the reactive mesogen PGs: (a) measurement setup including a linearly polarized laser with waveplates modulating the polarization incident on the PG; (b)measured −1-order and (c) +1-order di?raction response to the rotation of a quarter-waveplate, showing strong experimental sensitivity (from ∼ 0% to ∼ 100%); (d) measured −1-order and (c) +1-order di?raction response to the rotation of a half-waveplate, showing almost constant ∼ 50%. Discrete points correspond to experimental data and solid lines correspond to the theoretical response (Eq. 6.5).

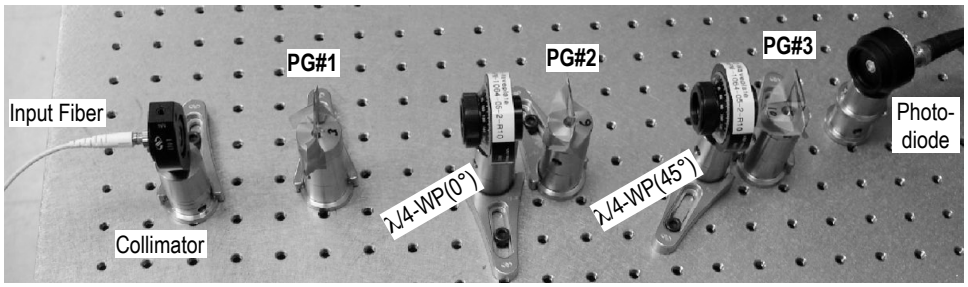

Figure 6.5: Photograph of the basic spectropolarimeter based on three polarization gratings (PGs) and two quarterwaveplates (WPs). Note that the polarizer used to set the test-input polarization state was placed immediately after the collimator (not shown for clarity).

A near-infrared tunable fiber laser with output-collimator was arranged as the test-source, along with two zero-order quarter-waveplates, as shown in Fig. 6.5. The six intensities were measured with a photo-diode across 1525nm to 1625nm (slightly more than the C- and L-bands). An infrared-polarizer was used to set the polarization state of the test-light at 22.5° from the horizontal direction (Fig. 6.4(a)). The normalized Stokes parameters for this fully-polarized test input are therefore $S_1' = 0.707$, $S_2' = -0.707$, and $S_3' = 0$ across the entire wavelength range.

The six first-order diffraction intensities were measured for the linearly-polarized test input, and are shown in Fig. 6.4(b), where the nominal intensity of the tunable laser was set to 0.5mW for all wavelengths. Using only the four measured intensities identified in Eq. 6.13, the resulting Stokes parameters from this measured data were calculated and are shown in Fig. 6.4(c). The measured intensity of the input signal S_0 was within ±5% of the nominal value. The other Stokes parameters S_1, S_2, and S_3 were approximately constant, and matched the ideal values within ±5% even in this very preliminary spectropolarimeter setup. The degree-of-polarization ($\sqrt{S_1^2 + S_2^2 + S_3^2}/S_0$) was also calculated from the measured data, and resulted in a value within ±3% of the actual value (100%). A small amount of measurement error was introduced by the use of zero-order quarter-waveplates (instead of truly achromatic waveplates), by the potential non-uniformity in the IR-absorption of the PG substrates, as well as by the imperfect positioning of the photo-diode that was manually aligned for each measurement.

Nevertheless, the strong correspondence between measurement and actual value clearly demonstrates the ability of this PG spectropolarimeter to detect all four Stokes pa-

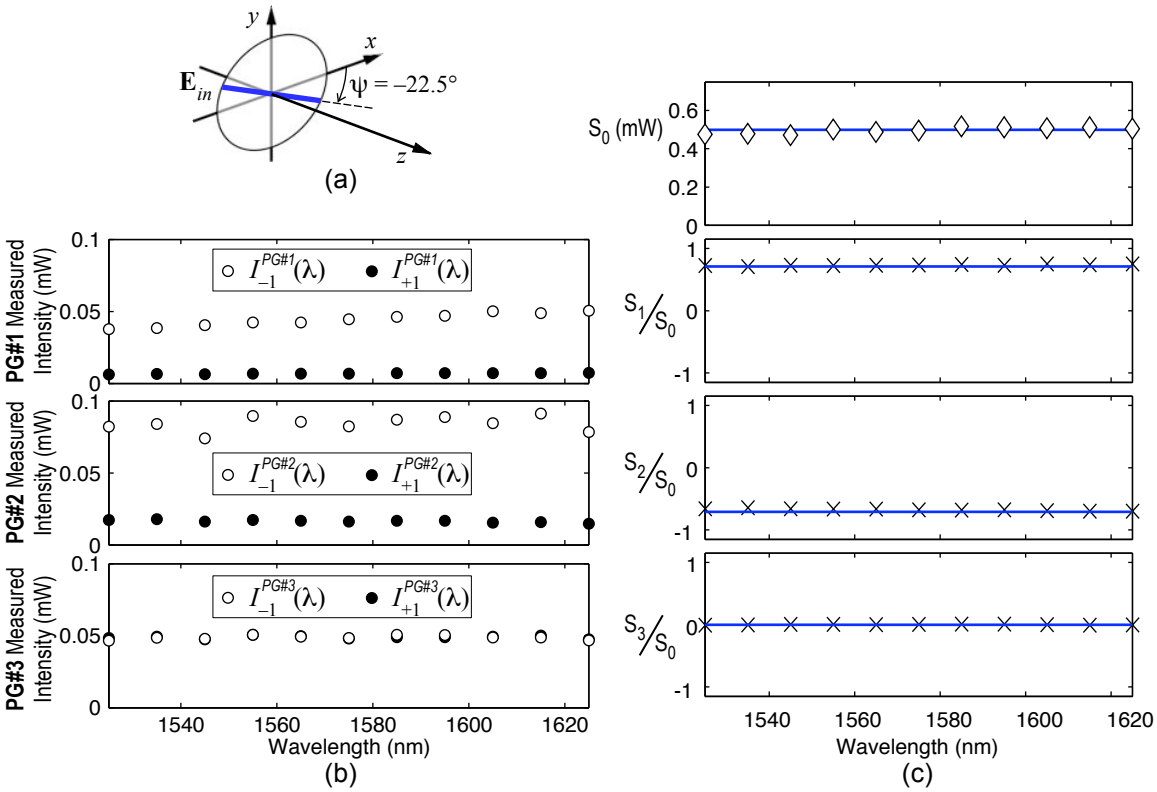

Figure 6.6: Results of the PG-based spectropolarimeter measuring linearly polarized input light at $-22.5°$: (a) Input light propagating along Z-direction; (b) Measured first-order intensities; and (c) Measured Stokes parameters calculated only from the four measured intensities $I_{+1}^{PG\#1}(\lambda)$, $I_{+1}^{PG\#2}(\lambda)$, $I_{+1}^{PG\#3}(\lambda)$, and $I_{-1}^{PG\#3}(\lambda)$.

rameters in a wavelength-parallel fashion using only four simultaneous intensity measurements. Its spectral resolution and sampling rate is limited primarily by the implementation of the photo-detection elements, and could most likely be designed with resolution and speed commensurate with conventional spectrometers for the same wavelength range and application (MHz or more). The bandwidth of this detection system is potentially very large, and can be estimated by considering the wavelength range over which all three PGs diffract more than 10% into their first orders ($\Delta\lambda/\lambda_0 \approx 70\%$ of the center wavelength).

While the representative experiment reported here tested a point-light source, it should be noted that one and two-dimensional (1D/2D) images could also be implemented without much modification. Figs. 6.6(a) and 6.6(b) show two different image registration schemes using a single detector (CCD or photo-detector arrays) for a hyper-spectral imaging

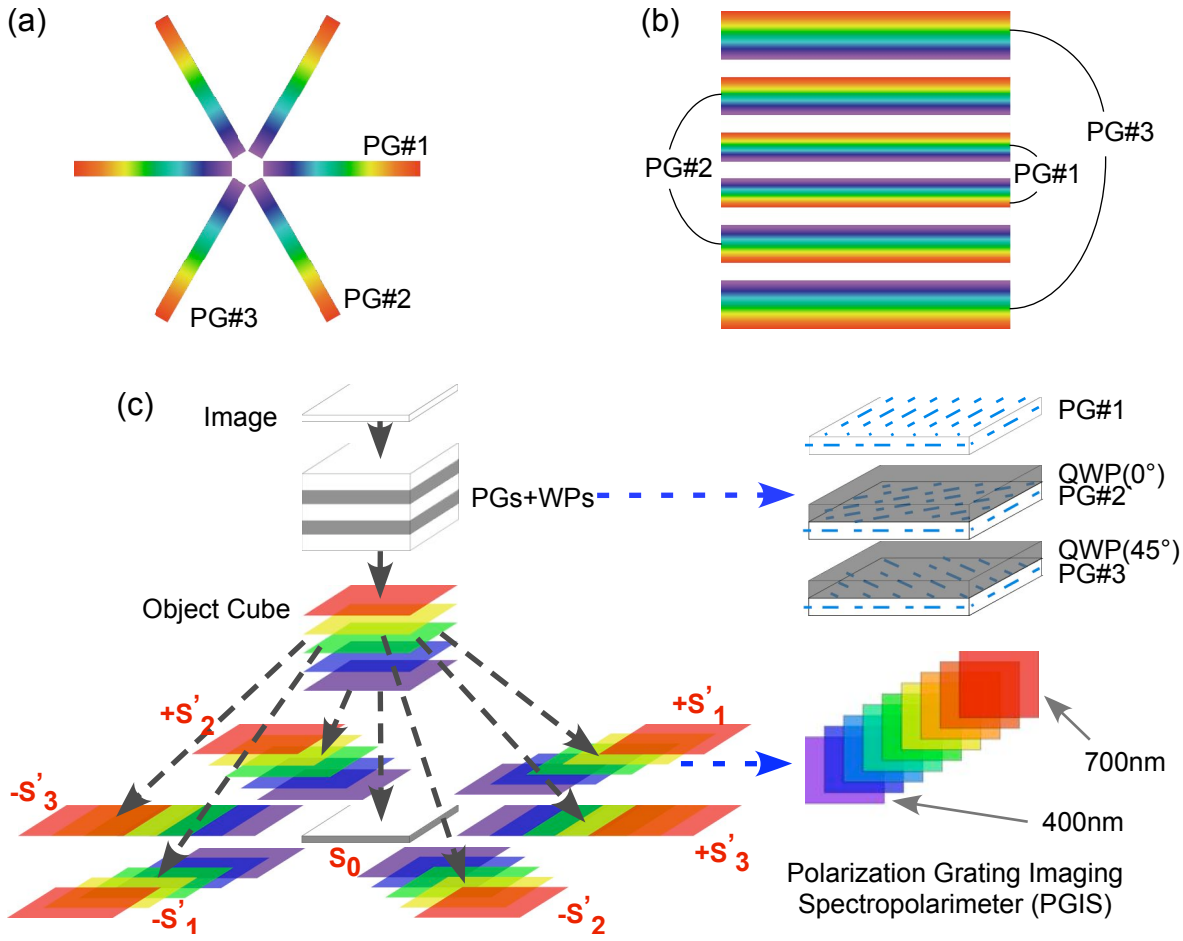

Figure 6.7: Image registration schemes for a hyper-spectral imaging polarimeter based on PGs using a single detector (CCD or photo-detector arrays): (a) axial arrangement (PGs are oriented at 60° with respect to each other); (b) parallel arrangement (PGs are aligned in parallel); (c) 2D dispersion pattern (PGs are stacked with relative angles (i.e., 60°)).

polarimeter with zero- and one-dimensional field of view, respectively. In order to measure the full spectropolarimetric data of a 2D image, a scanning element would be needed to sweep across only one spatial dimension of the input image (e.g., a pushbroom scanner or a rotating mirror). Design of a snapshot imaging spectropolarimeter was proposed by Kim et al. [122], which can capture all Stokes parameters directly from dispersed 2D images from a stack of three PGs and two quarter-waveplates onto a single imaging sensor (CCD or photo-detector arrays) utilizing computed tomographic techniques for the reconstruction of the object data cube (containing all intensity, spectrum, and polarization information

of the 2D scence). Since each PG stage inherently consolidates the two key functions in spectropolarimetry (wavelength and polarization sensitivity) into a single planar element, a wide variety of polarimeter designs optimized for multi-, hyper-, and imaging polarimetry are possible.

6.2 Polarization Gratings: A New Polarimetric Component for Astronomical Instruments

The use of PGs as a polarizing beam splitter offers a new potential for advances in astronomical polarimetry. Flexibility in wavelength tuning of diffraction spectrum and material properties of liquid crystal polymers make PGs a strong candidate as a key polarizing element in a mid-IR polarimeter. The potential use of the PG technology for a mid-IR (5-40μm) polarimetry for NASAs SOFIA 2.5m airborne telescope has been extensively evaluated in Ref. [123].

Polarization in the MIR is usually due to emission and absorption by aligned aspheric dust grains; polarization due to scattering from typical (astrophysical) sized dust is not observed at wavelengths $> 5\mu$m. The polarization gives access to the presence, orientation and distribution of magnetic fields in astrophysical objects, and the nature and mineralogy of the dust grains in them and in the interstellar medium, and is much more sensitive to chemical and physical differences than spectroscopy alone [123].

The Stratospheric Observatory for Infrared Astronomy (SOFIA) offers a near uninterrupted spectral coverage and sensitivity in the mid-infrared waveband. First (airborne)

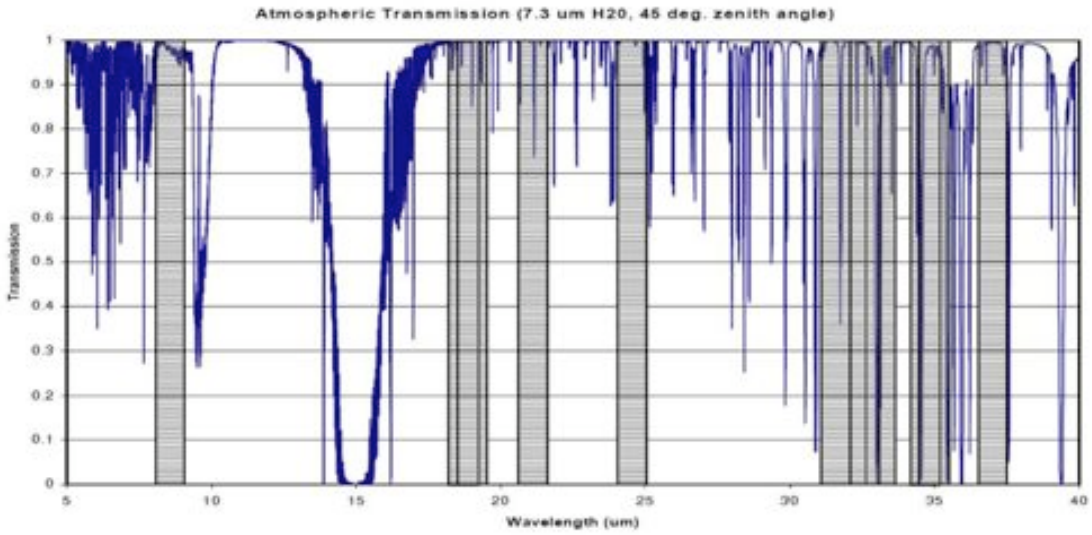

Figure 6.8: The atmospheric transmission expected for SOFIA, and the shaded areas show the initial filter selection for FORCAST (from Ref. [123]).

light of the telescope is expected in 2009, with regular science operations expected in 2010. Through the very high altitude of observations (12.5km) and its corresponding reduction in precipitatable water vapor, observations in an otherwise opaque part of the atmosphere are possible, opening observations in that wavelength space. Instruments such as FORCAST fully exploit this capability, in this example offering observing windows throughout the 5–40μm range.

The SOFIA Mid-InfraRed Polarimeter (SMIRPh) is currently under construction using the traditional and commonly implemented methodology of a crystalline Wollaston prism and half-wave retarder to offer dual beam polarimetry [161]. Typically, this dual beam polarimeter offers very high throughput, low instrumental polarization and high accuracy. However, at wavelengths longer than $\sim 20\mu$, there appears to be no suitable birefringent crystalline materials for a Wollaston prism and half wave retarder.

Polarization gratings have been proposed to be used as a thin-film, polarizing beam splitter, which is functionally analogous a Wollaston prism. This beamsplitter is made up of a thin polymer film ($< 300\mu$m) comprising a liquid crystal polymer coated optionally on a reflective or transparent substrate, and can be made with almost any surface area. Although its natural eigen-polarizations are circular, the PG beamsplitter can be paired with a quarter-waveplate (QWP) in order to separate incident light based on any eigen-polarization desired, as discussed in the previous Section 6.1.

Here we report our preliminary work as we consider the behavior of PGs at MIR wavelengths (5-40μm). We assert that two primary questions drive this initial work: (i) Do our current liquid crystal polymer materials manifest any birefringence over this wavelength range? and (ii) What is the absorption over this wavelength range?

6.2.1 Primary material properties of liquid crystal polymers in MIR

We first performed basic characterization of liquid crystal materials in the entire range of IR spectrum (i.e., 5–40μm). The indices of refraction and the extinction coefficients of reactive mesogen RMS03-001C (Merck) were measured on a J. A. Woollam Infrared Ellipsometer System at CREOL. This reactive mesogen results in a densely cross-linked polymer via UV photopolymerization, which is robust to optical, thermal, mechanical, and chemical degradation. A uniformly aligned layer was arranged on a glass substrate, with a thickness of 9.4μm, in such a way that the extra-ordinary index (i.e., the uniaxial

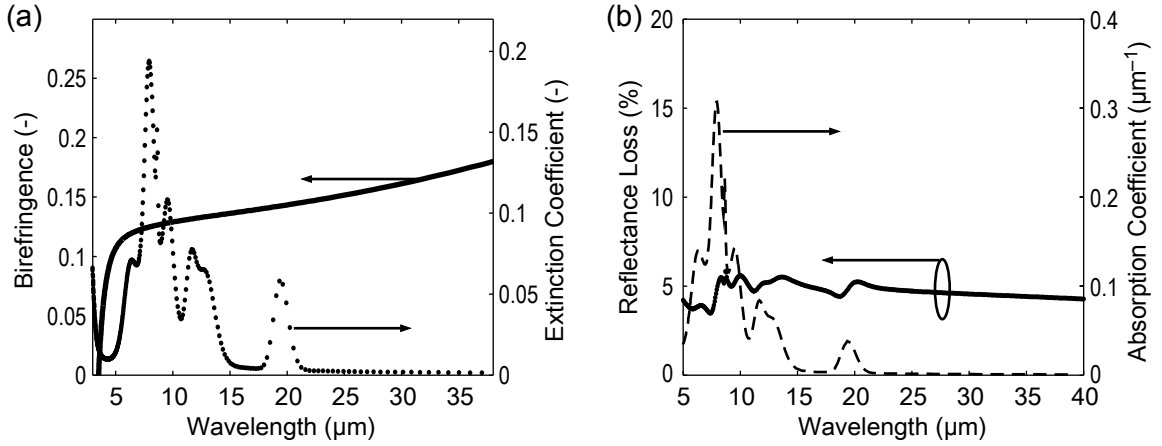

Figure 6.9: Preliminary measurements on RMS03-001C liquid crystal polymer films: (a) birefringence and extinction coefficient; and (b) Fresnel interface reflectance loss and absorption coefficient.

symmetry axis) was in the plane of the substrate. All measurements were performed at room temperature.

From the measured ordinary n_o and extraordinary n_e indices, the birefringence $\Delta n_l = n_e - n_o$ was found, which is shown in Fig. 6.9(a) along with the measured extinction coefficient k. Notice that a strong birefringence (~ 0.15) is indeed present, a value that compares very favorably to that offered by crystalline materials at optical and near-IR wavelengths. Note also that the extinction coefficient is particularly low at wavelengths $>\sim 20\mu$m, the very range at which conventional crystalline Wollaston prisms no longer function. The absorption coefficient ($\alpha = 4\pi\kappa/\lambda$) is shown in Fig. 6.9(b).

The total throughput T_{tot} of the PG thin-film is composed of several elements, and may be estimated in both reflective and transmissive modes by the following

$$T_{tot} = \eta^i_{tot}\eta_{abs}\eta_{refl} = \eta^i_{tot}e^{-\alpha d}(1-R)^2 \tag{6.15}$$

where η^i_{tot} is a sum of intrinsic diffraction efficiencies ($\eta^i_{-1} + \eta^i_0 + \eta^i_{+1}$) of the grating itself, to be calculated below. The quantity $\eta_{abs} = e^{-\alpha d}$ is the fraction of light not absorbed through a film of thickness d (which must be $d \sim 3\lambda_0/(2\Delta n_l)$, as discussed below). The quantity $\eta_{refl} = (1-R)^2$ is the fraction of light not reflected at the two air-polymer interfaces, where the reflectance of each interface determined by the Fresnel equation $R = ((n1)^2 + \kappa^2)/((n+1)^2 + \kappa^2)$, shown in Fig. 3b for our measured n and κ. For simplicity, we

have neglected the influence of the substrate, which in reflective PGs is likely to be only a refinement on the estimate in Eq. 6.15.

6.2.2 Behavior of polarization gratings with illumination in MIR

Until now we have exclusively examined the material properties of the LC polymer. Now we begin to examine the polarization, diffraction, and throughput behavior of PGs formed with that LC polymer. A series of "circular-type" (narrowband) PGs were formed with a 131μm grating period ($\pm 4.65^\circ$ first-order diffraction angle for 10.6μm wavelength) on undoped Si substrates.

We arranged a polarized collimated CO_2 laser beam (10.6μm wavelength) into the PG, normally incident, and measured the power going in the off- and on-axis directions. Ideally, all of the input light would be found in either of the two ± 1-order directions ($\pm 4.65^\circ$ off-axis). For a PG with 25μm thickness, we report the transmittance in all diffraction directions in Fig. 6.10, for three input polarizations (linear, and left- and right-handed circular polarizations).

Overall, it is clear that the PG operates very much as a polarizing beam splitter, similar to all prior effects observed at visible/NIR wavelengths. Upon illumination with linear polarization, the beam is nearly equally split into the ± 1-orders. Strong diffraction into one of the first orders is observed when the input polarization is circular. The most crucial evidence of polarization sensitive diffraction of the PG at this wavelength is the

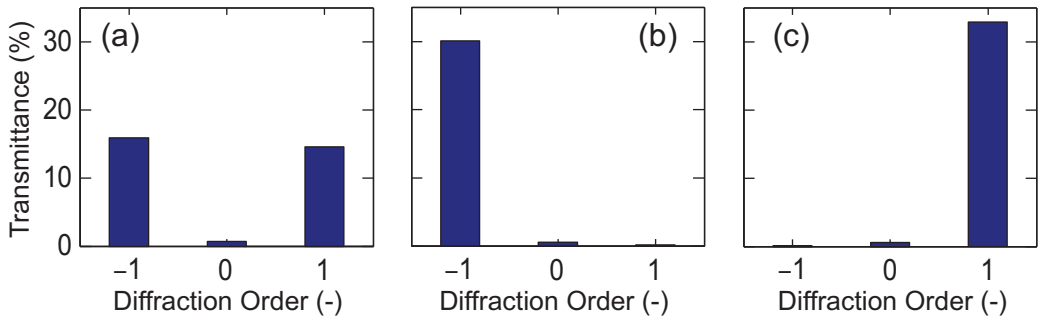

Figure 6.10: Measured beam powers of diffracted orders from a polymer PG sample ($\Lambda = 131\mu$m, $d = 10.6\mu$m with a CO^2 laser beam (10.6μm wavelength) with different polarizations: (a) linear polarization; (b) left-handed circular polarization; (c) right-handed circular polarization. Highly efficient ($> 99.8\%$) and strongly polarization sensitive ($400:1$ extinction ratio) diffraction have been confirmed at this IR wavelength.

measured polarization extinction ratios up to $\sim 400:1$, which are calculated as the ratio of the first-order powers for orthogonal circular polarizations. We may attribute most losses to material absorptions and interface reflections without noticeable scattering from the PG. It is important to note that there is $\sim 30\%$ loss from the Si substrate due to Fresnel reflections.

We prepared a series of PGs with a range of LC polymer thicknesses, and with otherwise identical parameters. In Fig. 6.11(a), we report the total forward-going transmittance (in all orders) at various thicknesses. We then found the least-square-error fit with Eq. 6.15 to determine the absorption coefficient at this wavelength as $\alpha = 0.032\mu\text{m}^{-1}$, very similar to the value measured by ellipsometry.

We also calculated the zero- and total first-order efficiency, which enables us to observe the behavior of the grating itself, where the influence of the substrate, interface reflections, and all absorption is normalized out. This is useful because we can estimate the birefringence at this wavelength. The measured diffraction efficiency is shown in Fig. 6.11(b), where it is notable that the maximum measured total-first order diffraction efficiency was 98.2% ($\pm 1\%$); this confirms that apart from absorption and Fresnel reflections at interfaces, the PG itself is a nearly 100% efficient diffraction grating (just as it is at visible/NIR wavelengths).

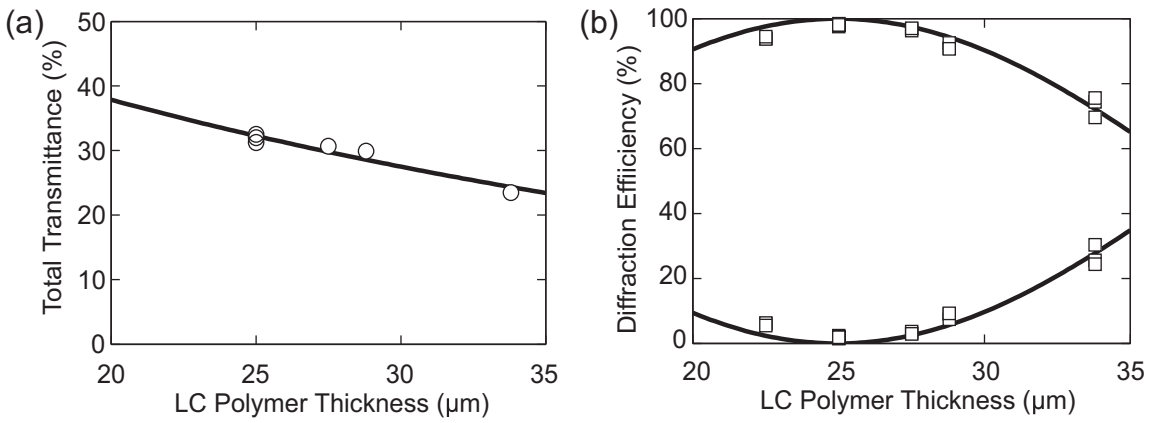

Figure 6.11: Total transmittance and intrinsic diffraction efficiencies of PGs with different LC polymer thicknesses (22–34μm) and their comparison with analytically estimated values.

6.2.3 Optimum broadband design using achromatic PGs

The bandwidth 5–40μm is extremely large ($\Delta\lambda/\lambda_0 = 156\%$), and as a result, more than one PG is necessary to cover this range. In addition, more than one type of FPA detector is needed, and both of these facts constrain the optical system design. Here, we identify an optimum design of the number and properties of PGs optimized to enable the highest efficiency as possible.

We experimentally confirm $> 98\%$ efficiency but this high efficiency may be held only at wavelengths close (within $\lambda/\lambda_0 \sim 12\%$) to the half-wave retardation condition ($\Delta n_l d = \lambda_0/2$). Nevertheless, several 'achromatic' PGs with modified nematic director profiles have been identified [133, 141], with high efficiency bandwidths λ/λ_0 increased by up to eight-fold. In the most preferred achromatic PG for this application, the thickness depends on the center wavelength of the high efficiency window according to $d \sim 3\lambda/(2\Delta n_l)$. In Fig. 6.12, we show the calculated diffraction efficiency of three achromatic PGs using the Finite-Difference Time-Domain (FDTD) simulation tool WOLFSIM [134, 135]. These three wavelength windows (5–11.2μm, 11.2–25μm, and 25–40μm) were chosen based on the FPA detector technologies and the desire to keep the spectral dispersion consistent. The ideal PG diffraction efficiency ($\Sigma\eta^i_{\pm 1}$) is therefore $> 99\%$ for the entire 5–40μm range.

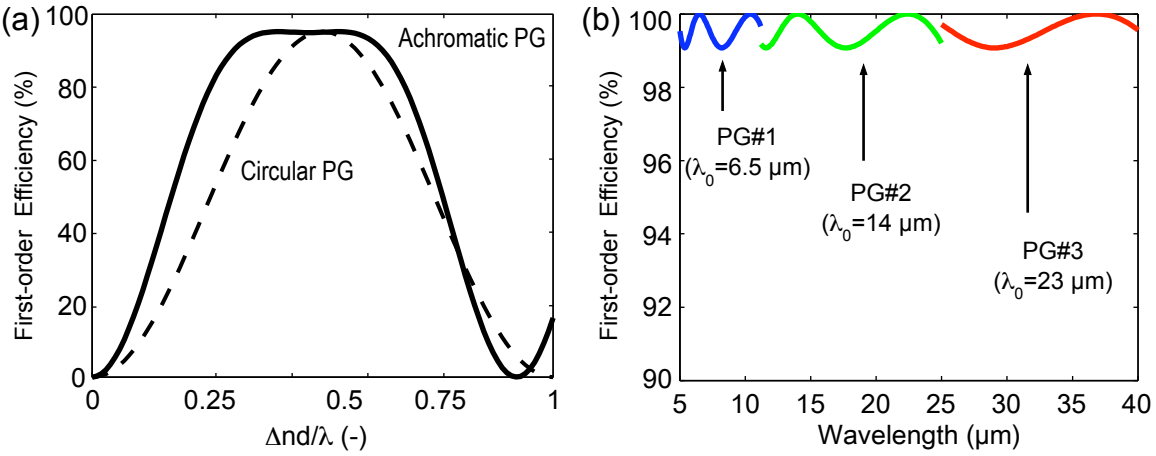

Figure 6.12: Design of broadband PGs for the entire MIR wavelengths (5–40μm): (a) the diffraction spectra of the first-order efficiency of an achromatic PG; (b) optimum bandwidth design using three achromatic PGs for three different spectrum windows (5–11.2μm, 11.2–25μm, and 25–40μm).

It is important to note that both the initial fabrication of and measurements on the liquid crystal polymer measured above were all made at room temperature. Nevertheless, the optical and mechanical behaviors of PGs at the operational cryogenic temperatures are undoubtedly critical for SMIRPh. Whilst we are still in the initial phase of studying temperature effects, we can note two points: (i) The liquid crystal material composing the PG is a highly cross-linked poly-acrylate network, which we have observed to remain mechanically intact even with manual handling at liquid nitrogen temperatures; and (ii) It is well known that the birefringence of these materials increases as temperature decreases [162]. With both of these positive points in mind, we are actively working to quantitatively understand the optical/physical behavior and limitations of our polymer PGs at cryogenic temperatures.

In summary, we have shown that liquid crystal polymer materials show the necessary birefringence at the MIR wavelengths of operation. We also have confirmed high efficiency and polarization sensitive diffraction of polymer PG samples at an IR wavelength (10.6μm). Future work will continue optimization work on the transmission of the PGs, and refining our preliminary measurements, which are likely pessimistic as the absorption bands are likely significantly more narrow than we show above. In addition, we plan to characterize the PGs at cryogenic temperatures. The optimum broadband design using achromatic PGs will be also studied.

Chapter 7

Concentric Polarization Gratings as Vectorial Fresnel Zone Plates: a new opportunity for beam shaping

Shaping of a beam can be done by a precise control of wavefront via refraction/diffraction/interference. One of the most classical methods for beam shaping is to use curved/angled surfaces of a medium which has a different index of refraction from that of the other region. Volume lenses, curved mirrors, and prisms are good examples of this type of beam shaping elements which are commonly found in any optics laboratory. Micro-optical devices based on liquid crystal technologies and electro-wetting have been introduced to miniature or improve classical optics. Especially, optical phase array (OPA) and MEMS-based micro-mirror technologies enable similar spatial modulation in the wavefront even in a dynamic environment.

In this Chapter, we introduce a new vector-version of Fresnel zone plates that can produce ideal Fresnel lens effect by shaping polarization states using concentric polarization grating patterns. We, first, briefly overview Fresnel-type lenses as thin-plate lenses and review some recent developments of liquid crystal lenses. Then, we introduce a concentric pattern of polarization gratings (with radially modulated periods corresponding to Fresnel zones) as a polarization-type Fesnel zone plate. Finally, we report our development of concentric PGs formed as both an electrically switchable LC device and liquid crystal poly-

mer thin films. Excellent optical performance including good focusing and high efficiency ($\geq 98\%$) and polarization-selective lens properties have been demonstrated.

7.1 Fresnel lenses and zone plates as a thin lens

Lenses are the most popular optical elements that are found from daily-life products such as eye-glasses, cameras, and DVD players to sophisticated optical systems such as microscopes, observatory telescopes, and most advanced lithography systems. Although fabrication of lenses is still challenging at the current technological era, even cheap lenses can perform excellent jobs on converging (negative lenses) or diverging (positive lenses) the beam depending on the lens geometry. These classical lenses, however, are often limited by its volume structure with surface curvatures that cannot be easily scaled. In addition, highly-graded optical materials for making lenses are usually expensive and not always available some wavelength regions.

A Fresnel lens is a thin-plate type of lens invented by Augustin-Jean Fresnel. This thin lens is made up of fractional prismatic structures by breaking the conventional spherical lens into a set of concentric annular sections known as *Fresnel zones* as shown in Fig. 7.1(a). Each of these zones effectively beaks down the continuous curvature of a standard lens into a set of surfaces of the same shape, with discontinuities between them. A substantial reduction in thickness can be done by employing such fractional compartment of small surface elements and lenses with a large aperture can be easily manufactured using a small volume of material in a thin plate. While a Fresnel lens is typically useful for large optical systems such as lighthouses, traffic lights, automobile headlamps, and projectors, it is not quite often to use in high-quality imaging systems due to its poor image quality. One

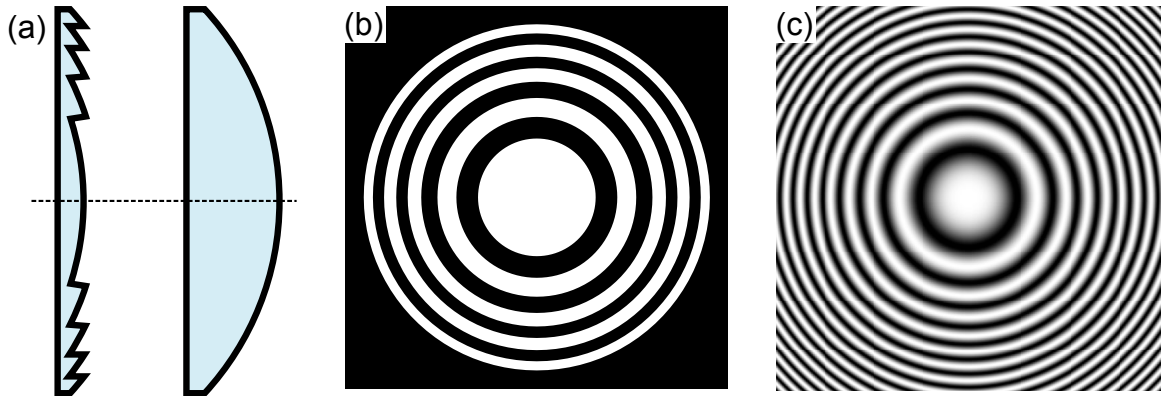

Figure 7.1: Fresnel-type thin-plate lenses: (a) a Fresnel lens compared to a classical volume lens; (b) a binary-type Fresnel zone plate; (c) a sinusoidal-type Fresnel zone plate.

of the main reasons is the discrete pattern of individual zone elements (often, saw-toothed structures). For non-ideal structures (i.e., smooth tips, angled edges) or non-collimated beams, the effective surface curvature of the Fresnel lens is distorted from that of the original lens. There is a general trade-off of the resolution of zones between thickness and lens quality.

A zone plate, often called a Fresnel zone plate (FZP), also can be used to focus light similar to a Fresnel lens but operating by diffraction instead of refraction. A zone plate consists of a set of radially symmetric rings with alternating transparent and opaque zones. Figs. 7.1(b) and 7.2(c) illustrate two different types of FZPs with binary and sinusoidal profiles in opacity. To obtain constructive interference at the focus, the radius of the m-th zone should be determined as follows [35]

$$r_n = \sqrt{m\lambda f + n^2\lambda^2/4} \simeq \sqrt{mf\lambda} \tag{7.1}$$

where λ is the wavelength, f is the distance of the focus from the zone plate. The effective focal length also can be determined by the radius (r_N) and resolution (Δr_N) of the outermost zone as follows

$$f = \frac{2r_N\Delta r_N}{\lambda} \tag{7.2}$$

and the maximum possible resolution of the zone plate is given by

$$\Delta l = 1.22\Delta r_N, \tag{7.3}$$

which is equivalent to the diffraction limit based on the Raleigh criterion. While a binary zone plate produces multiple foci along the axis of the plate at odd fractions (f/3, f/5, f/7, etc.), a sinusoidal zone plate can have a single focal point (for one wavelength). A primary means for creating binary zone plates is lithography but holographic techniques can be employed to make sinusoidal patterns, which are equivalent to transmission holograms of a converging lens.

The use of liquid crystals to implement switchable lenses has been proposed by many research groups. Generally, they can be divided into two types according to their structures. One type is based on the patterned relief surface substrates then it is filled with liquid crystals [163, 164]. The other type is based on patterned electrodes to generate a special distribution of electric field to align LC molecules, forming an index profile as a

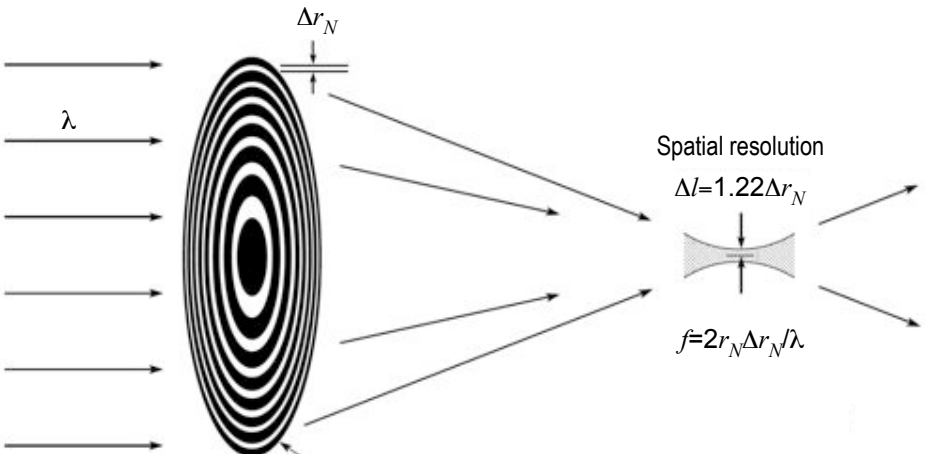

Figure 7.2: Focusing of a Fresnel zone plate and its diffraction-limited spatial resolution.

lens [165, 166, 167, 168, 169]. Both types of LC lenses have their own problems: the first type of LC-filled lenses are often limited because of their large thickness of the active area, high operating voltage, and poor transmittance due to optical scattering; the LC lenses with patterned electrodes require a complicated design of electrodes and it is difficult to get ideal LC profiles due to fringing fields between electrodes and interaction of neighboring LCs. The properties of most LC lenses are dependent on polarization state of illuminating light due to the anisotropy of LCs. A simple solution to make polarization-independent lenses was proposed by overlying LC layers with orthogonal orientations [170]. This method, however, produces issues of a precise alignment of two LC lens elements.

A number of binary FZPs were proposed using alternating zones in two orthogonal LC directions [171, 172]. While this type of FZPs operates on a spatial modulation of polarization state of light instead of phase or intensity, this polarization operation was not well recognized. The polarization properties of diffracted beam from a binary LC FZP were studied by Lin et al. [173]. A polarization-type FZP with quasi-continuous patterns (more than binary) was introduced and demonstrated using a computer-generated space-variant sub-wavelength dielectric grating that effectively modulates polarization state of light [174]. Advantages of a continuous grating profile with $\sim$ 100% efficiency was also theoretically predicted and an IR FZP was experimentally demonstrated to have 94.5% efficiency at 10.6 μm wavelength. A similar LC FZP was demonstrated at a visible wavelength (i.e., 633

nm) using micro-rubbing techniques for LC alignment [175] and focusing properties and electro-optical response of the LC FZP were also studied by the same authors. All of these initial efforts to create a highly-efficient polarization-type (or vectorial) FZP, however, have been limited by their fabrication difficulties to pattern defect-free, continuous polarization grating profiles.

7.2 Polarization-type Fresnel zone plates based on a continuous, concentric polarization grating pattern

The polarization-type FZP has a radially symmetric birefringence profile similar to a sinusoidal amplitude FZP. The spatial distribution of the azimuthal orientation of local birefringence (Fig. 7.3(a)) in the m-th zone can be written as follows [175]

$$\phi = \frac{\pi}{\lambda}(f - \sqrt{f^2 - r^2}) + \left(m + \frac{1}{2}\right)\pi \tag{7.4}$$

where $r = \sqrt{x^2 + y^2}$ is the distance from the center ($[x,y]=[0,0]$) of the FZP. We now call this type of FZPs as a concentric polarization grating (CPG) because its birefringence pattern is identical to that of the circular PG but with radially modulated periodicity. 100% efficiency also can be achieved at a single focal point when the CPG produces a half-wave retardation and the input is circularly polarized. Fig. 7.3(b) shows an intensity profile of the CPG with a half-wave thickness between crossed polarizers, which is interestingly identical to the profile of a sinusoidal amplitude FZP. Another interesting view of the CPG is the phase profile of the emerging beam immediately after the CPG when it is illuminated with circularly polarized light. The resulting phase profile is also identical to that of an ideal Fresnel lens as shown in Fig. 7.3(c) and 7.3(d). The CPG shows polarization-selective lens properties: it functions as a convex (or positive) lens for right-handed circular light while it acts as a concave (or negative) lens for left-handed light. Similar to the PG, the diffracted beam has the opposite handedness of the input polarization (i.e., left- to right-handed or right- to left-handed).

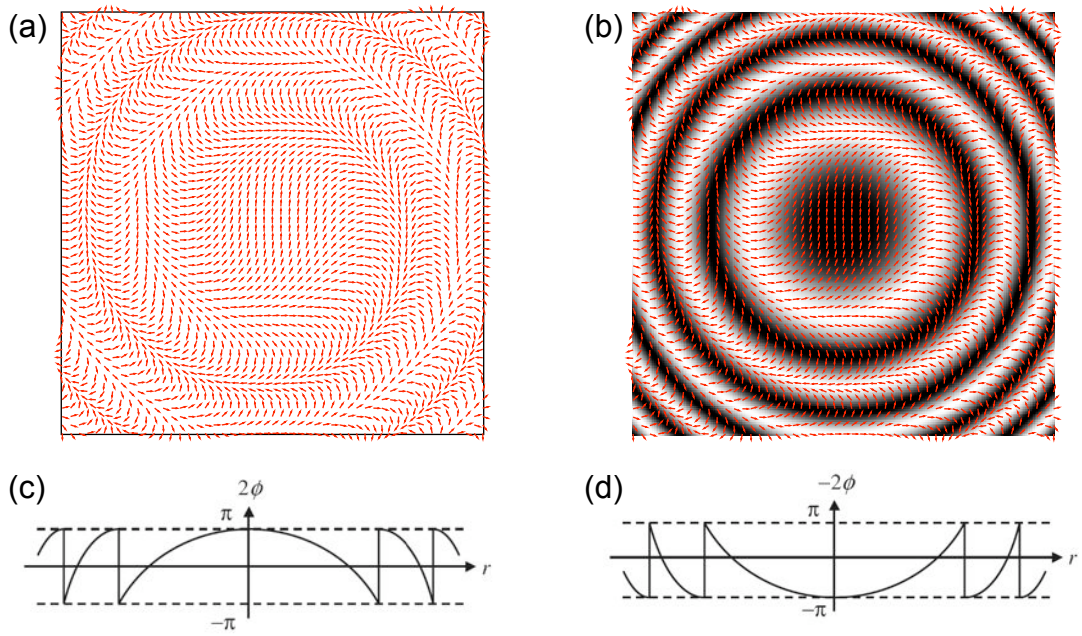

Figure 7.3: Concentric polarization gratings (CPGs): the spatial distribution of (a) a birefringence profile and (b) an intensity profile between crossed polarizers, equivalent to a sinusoidal FZP; (c) and (d) the phase profiles of the emerging beam immediately after the CPG for circular input polarizations (right- and left-handed, respectively).

7.3 Fabrication of concentric polarization gratings as a polarization hologram

We have demonstrated high-quality concentric polarization gratings (CPGs) that manifests excellent focusing properties with nearly 100% efficiency. We utilize polarization holography and photoalignment techniques for liquid crystal materials. Figs. 7.4(a) and 7.4(b) show a schematic view and a real picture of the holography setup based on the Michelson interferometer. A collimated beam (diameter $D \sim 20$ mm) from a HeCd UV laser (at 325 nm) with linear polarization (vertical, LVP) is split and recombined by a non-polarizing beam splitter. The polarization of one of the beam after a beam splitter is flipped into the orthogonal linear polarization (horizontal, LHP) as it travels twice of a quarter-waveplate (effectively by a half-wave retardation). A recording lens is inserted in one of the beam paths as shown in Fig. 7.4. Polarization states of these two recording beams are converted to orthogonal circular polarizations (i.e., vertical linear to left-handed circular

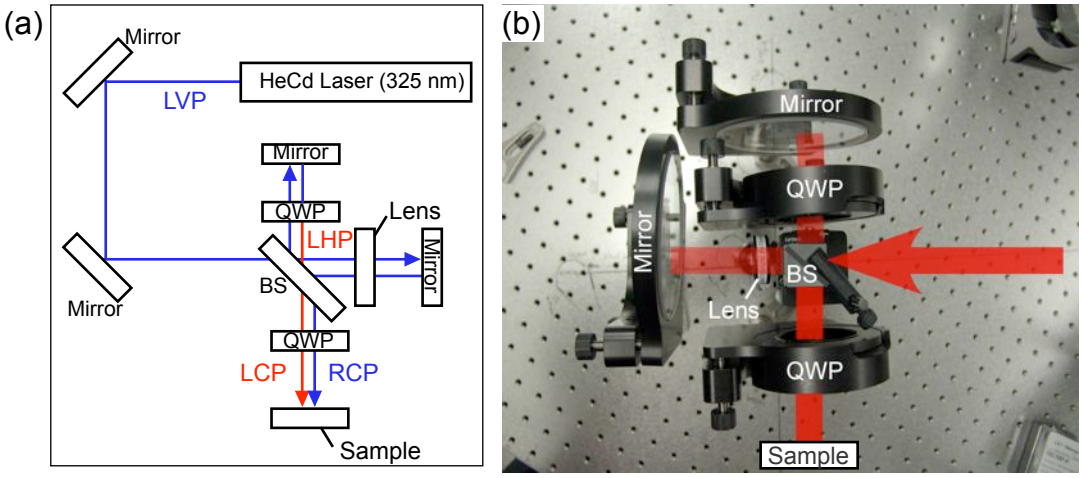

Figure 7.4: Polarization holography setup based on the Michelson interferometer: (a) a schematic view of the UV holography setup; (b) a picture of the actual optics setup in the lab. The linearly polarized beam from a UV laser is split and recombined by a non-polarizing beam splitter of the Michelson setup and two recording beams with orthogonal circular polarizations are superimposed at the sample position. A lens was inserted in a path of one of the two recording beams as shown in the actual picture.

or horizontal linear to right-handed circular), which result in a polarization interference equivalent to the birefringence profile of the CPG. The sample is placed where two beams are exactly overlapped and the resulting polarization hologram is recorded into the polarization sensitive layer (as a photoalignment layer for LCs) of the sample.

We fabricated CPG samples as electrically switchable LC devices and liquid crystal polymer (LCP) thin films. We used two different linear photopolymerizable polymer (LPP) materials, ROP-103/2CP (from Rolic) for LC cells and LIA-01 (from Dainippon Ink and Chemical) for LCP films. We also used a nematic liquid crystal MLC-12100-000 (from Merck, $\Delta n_l = 0.113$ at 589 nm, $T_{NI} = 92°$C) for LC cells and a RM prepolymer/sovent mixture RMS08-075 (Merk, $\Delta n_l = 0.159$ at 589 nm) for LCP samples. The fabrication processes for both LC cells and LCP samples are very similar to those for LCPGs and RMPGs, respectively. More details of fabrication will be discussed elsewhere.

To confirm the CPG profile of LC alignment, the CPG samples were observed with a polarizing microscope. Figs. 7.5(a)–7.5(b) show polarizing microscope images of a CPG polymer sample with different polarizer angles (0°, 90°, ±45°). Very well-defined sinusoidal profiles were observed without defects or discontinuities and the intensity profile varies as

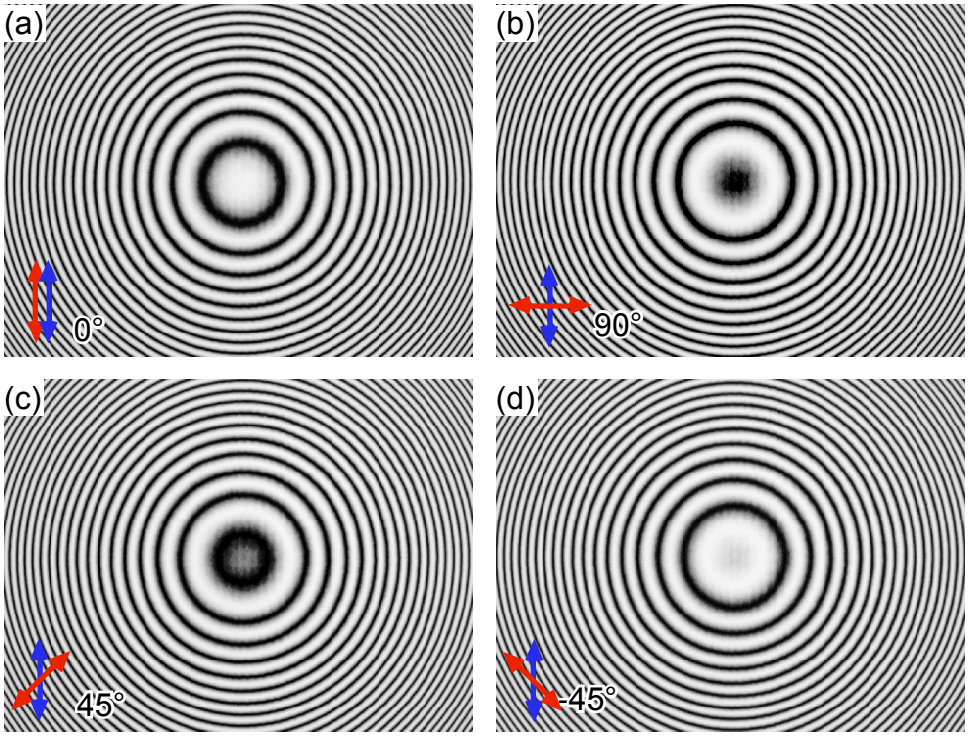

Figure 7.5: Polarizing microscope images of a CPG polymer sample with four different polarizer angles: (a) 0°; (b) +90°; (c) +45°; (d) −45°.

the analyzer rotates with respect to the bottom polarizer (fixed at an angle). These pictures show us that a nearly ideal CPG pattern was recorded and it was successfully captured in the liquid crystal layer, which is permanently fixed via photopolymerization for this LCP sample.

We also characterized lens properties of the CPG samples. We measured a focal length $f \simeq 16$ cm and $\sim 98\%$ efficiency at the focal point at a green laser wavelength (532 nm). Note that the thickness of the CPG samples were optimized for a half-wave retardation at the same wavelength ($d \simeq 1.65$ μm and $d \simeq 2.4$ μm for CPG polymer and LC samples, respectively). Figs. 7.6(a) and 7.6(b) show the polarization-selective lens properties of CPG samples. We took pictures of a green laser beam (diameter $D \simeq 1$ cm) on a screen placed at the focus of the CPG as rotating a quarter-waveplate to control the input polarization state. For right-handed circular polarization, the beam is focused as shown in Fig. 7.6(a) so that the CPG behaviors as a positive lens. On the other hand, the beam is diverged

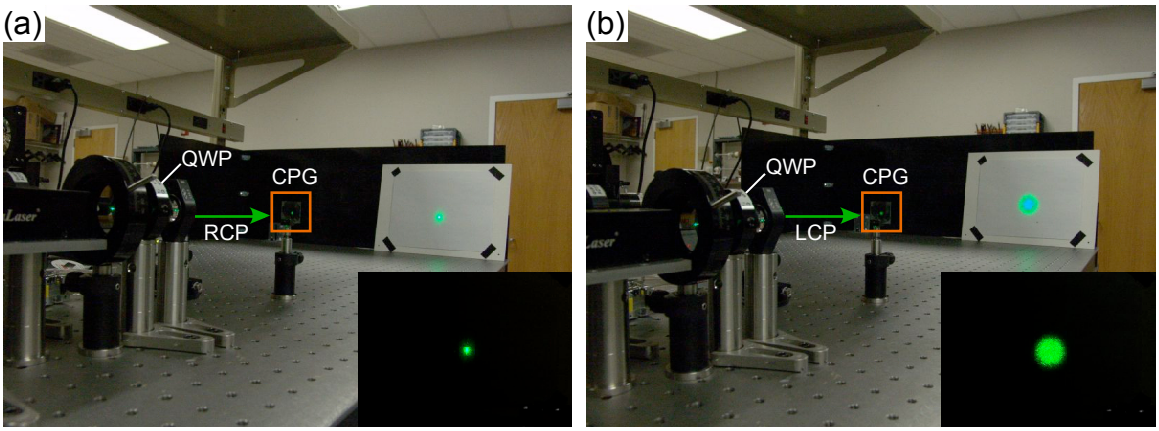

Figure 7.6: Polarization-selective lens properties of CPG samples: pictures of a laser beam (at 532 nm) with (a) right- and (b) left-handed circular polarization. The same CPG can function as both a positive lens and a negative lens for right- and left-handed circular polarization, respectively. The emerging beams are always circularly polarized (either right- or left-handed) regardless the input polarization state.

for left-handed input and the CPG acts as a negative lens. We should also note that the emerging beam is always circularly polarized regardless the input polarization state and it has the opposite handedness for circularly polarized input. Electrical switching of lens effect also has been demonstrated using CPG LC cells as shown in Figs. 7.7(a) and 7.7(b). These pictures were taken by placing a CPG cell in front of a camera with and without applying a voltage across the LC cell. The focused images with the CPG in the "ON" state (no voltage applied) show very good image qualities. The switching times for the particular sample ($d \simeq 2.4$ μm) was measured ~ 8 ms.

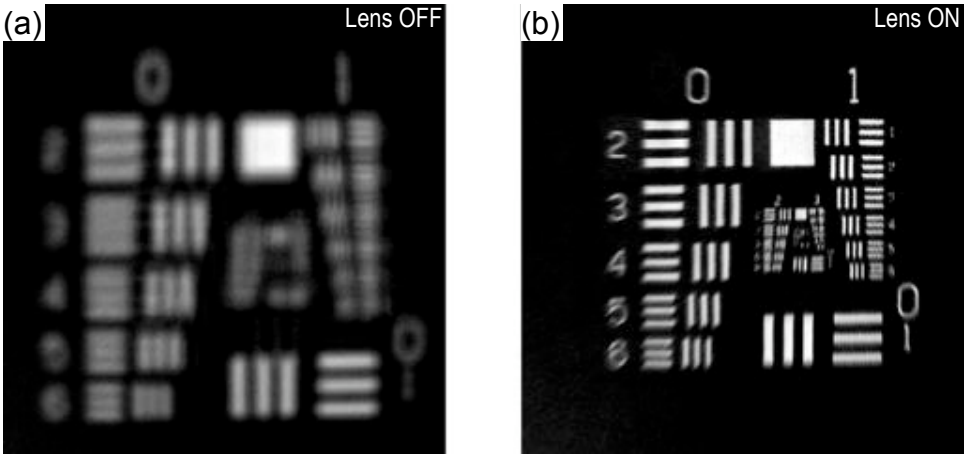

Figure 7.7: Electrical switching of the CPG LC cell. Images were taken by placing a CPG cell in front of a camera (a) with and (b) without applying a voltage across the LC cell.

Chapter 8

Discussion and Conclusions

Achromatic polarization gratings have been proposed as a broadband polarizing beam splitter which is embodied as a thin liquid crystal layer. Our extensive numerical analysis predicts diffraction behavior of the PG beyond the limit of the paraxial approximation, where the analytical solutions cannot properly explain the phenomena, and it also suggests a practical guideline to design and evaluate PGs. We have introduced and experimentally demonstrated achromatic PGs that perform ideal diffraction properties of the circular PG over a broad range of spectrum, which was the first realization of achromatic diffraction at nearly 100% efficiency. Three key innovative technologies based on PGs have been developed in displays, beam steering, and spectropolarimetry. The last, but very interesting, innovation in this Dissertation was the concentric polarization grating as a vectorial Fresnel zone plate, which functions as a polarization-selective, thin-plate lens.

8.1 Summary and Conclusions

We reported a rigorous numerical analysis of the polarization grating with the minimum possible assumptions using our in-house simulation tool WOLFSIM based on the finite-difference time-domain method. We have studied the effect of grating parameters on diffraction properties of PGs, especially where the theoretical predictions become invalid (i.e., beyond paraxial domain). We evaluated the grating regime (thin or thick gratings) for the PG and discovered that a dimensionless parameter ($\rho \propto \Delta n_l(\lambda/\Lambda)^2$) can be used as a criterion to determine where the PG can perform its ideal properties ($\rho < 1$), which is

the first *honest* analysis of the grating regime for anisotropic diffraction gratings. We also suggested to use the relationship between grating parameters (Λ, Δn_l, d) to achieve both high efficiency ($\sim 100\%$) and large diffraction angles at the same time. We demonstrated small-period PGs as small as $\Lambda = 1.35$ μm, fabricated as liquid crystal polymer films, with excellent diffraction properties. In particular, 1.35 μm PGs were created and perform $> 95\%$ efficiency at 650 nm (the diffraction angle $\theta_{\pm 1} = 28.8^{\circ}$). Experimental results show a great agreement with the numerically predicted efficiencies. Angular sensitivity and the effect of a finite grating have been studied and confirmed that the PG exhibits excellent angle performance compared to any other type of diffraction gratings and only a few periods of a pixelated PG can perform the nearly ideal properties in both efficiency and polarization.

The achromatic design of PGs is one of the key inventions of this Dissertation research, which realizes, for the first time, 100% efficient diffraction over a fairly wide spectrum (actually, $\sim 56\%$ of the center wavelength for $\geq 99\%$ efficiency versus 12.8% of the non-achromatic PG) and leads to development of a number of interesting advanced technologies. Relatively simple and robust fabrication process for achromatic PGs has been developed using UV holography and commercially available liquid crystal materials. We routinely fabricate very high-quality PGs with a wide range of grating periods ($\Lambda \simeq 1.35$ μm to several 100s μm) for different wavelength regions (visible, near-infrared, midwave-infrared). The resulting achromatic PGs demonstrate $\geq 99\%$ efficiency for almost all visible wavelengths from 470 nm to 630 nm and the same polarization properties as non-achromatic PGs. Another type of the achromatic PG, namely the *super*-achromatic PG, based on three layers with a relative phase shift has been experimentally demonstrated to have a even broader bandwidth for high diffraction efficiency with a significant improvement factor ($\times 2$ of the first achromatic PG and $\times 7$ of the non-achromatic PG) in both visible and near-infrared wavelength ranges.

Polymer-PG display has been developed as a viable solution for light-efficient LC display without using polarizers. A significant improvement (up to a factor of 2) in brightness can be achieved by replacing polarizers with transmissive, thin-film polarizing beam splitters, polymer PGs, using a conventional LC displays (virtually any LC mode can be used). Polarization-independent light modulation by the polymer PG display has been demonstrated with single-pixel LC displays with several different LC modes (including VAN, ECB, and TN-modes). We confirmed more than $\times 2$ brightness improvement

compared to polarizer-based LCDs. We also developed a prototype projector based on the polymer-PG display using a commercial microdisplay. The polymer-PG projection display exhibits double the brightness than the original display using polarizers with all excellent imaging qualities preserved. The extinction ratio of antiparallel PGs (equivalent to crossed polarizers) remains a limiting factor to prevent high contrast-ratio displays. We also discovered that the use of simple retardation films effectively reduces polarization-related light leakages.

Novel beam steering concepts based on PG diffraction were introduced in Chapter 5. First, we developed a non-mechanical, wide-angle beam steering system using stacked PGs and LC waveplates. $\pm 15^\circ$ beam steering with 5° resolution was demonstrated using only two pairs of PGs and LC waveplates (few mm of the total thickness). We also introduced a new beam steering concept, 'Risley grating,' using a pair of rotating PGs. This thin-plate version of the Risley prism can function continuous beam steering within a field-of-regard (FOR) that is determined by the diffraction angle of the PG. We derived governing equations to describe the steering angle using the direction Cosine method. Continuous beam steering with 62° FOR was realized at an infrared wavelength (1550 nm) using a pair of 6 μm-period LCPGs ($\pm 31^\circ$ diffraction angles at 1550 nm) and high throughputs from 92% to 89% (efficiency from 92% to 97%) were measured for all steering angles. Losses in transmittance and efficiency are considered mainly due to reflection losses at the LC-glass interfaces and the polarization-related leakages from PGs, respectively. The use of index-matching substrates and polarization compensation techniques have been suggested to increase the steering efficiency even further.

The Chapter 7 comprised of a brief introduction of the vectorial Fresnel zone plate (we named the concentric polarization grating or CPG) and our recent demonstration of ideal Fresnel lens effect by the CPGs that were fabricated as both switchable LC lens and highly crosslinked polymer films. We apply a polarization holography setup based on the Michelson interferometer to record a conventional spherical lens as a spatially distributed polarization hologram. Both types of CPG samples show good imaging properties as thin-plate diffraction lenses as well as polarization-selective lens properties (it acts as a positive or negative lens depending on the handedness of circular polarization). CPG LC lenses also show good electro-optical properties including fast switching times at a modest operating voltage (i.e., 8 ms at 10 Vrms). The results on high-quality CPGs suggest a new potential of

polarization holograms for beam shaping; holographic techniques with polarization-sensitive materials enable many possibilities creating complex vector beams with preserving high optical qualities.

In summary, we have shown a new possibility of the use of a special type of anisotropic gratings as broadband polarizing beam splitters for a number of different applications. In last few years, we have developed effective fabrication processes for creating high-quality polarization gratings even with a very small period (between 1 μm and 2 μm) using holographic photoalignment techniques and liquid crystal materials with high linear birefringence. Achromatic PGs were created by a relatively simple fabrication method and used to advance existing technologies and also lead to innovative technologies. Finally, the holographic fabrication process for high-quality CPGs proposes a practical method for creating complex vector holograms with arbitrary, spatially distributed polarization patterns.

8.2 Suggestions for future work

Until now, we have seen a great potential of polarization gratings as an efficient polarizing element that can be employed in many interesting optical systems including displays, polarimeters, beam steering/shaping, spectrometers, and so on. Although a comprehensive study of these special anisotropic gratings has been done in both theory and experiment by the Author and others, many aspects of PG diffraction behavior still remain not fully understood yet. In this Section, we briefly summarize current challenges and limitations of applications based on PGs and present suggestions for future work to advance the technology.

8.2.1 Challenges and advances in PG fabrication

Fabrication of small-period PGs using high Δn_l materials

Recent advances in photoalignment technologies of LCs significantly improve the fabrication process for PGs with polarization holography. The anchoring energy of photoalignment materials is critical to obtain good alignment of LCs. As the grating period decreases, a stronger anchoring energy is required to prevent defects in LC profiles. We have demonstrated 1.35 μm-period gratings with nearly perfect LC alignment. However, it is very

challenging to fabricate high-quality PGs below 1 μm period, which has not been demonstrated experimentally. In addition, liquid crystal materials with high Δn_l are required to obtain high diffraction efficiency at these small grating periods. Therefore, development of new photoalignment materials with higher anchoring energy and high Δn_l LCs may be required to overcome the current limitation of PG fabrication.

We have tried to use a new reactive mesogen prepolymer/solvent mixture RMS09-038 (from Merk, $\Delta n_l = 0.39$ at 589 nm). Although this material shows the best performance ($> 95\%$ efficiency for 1.35 μm PGs at 650 nm) among other similar RM materials with lower Δn_l, processing of the material is very challenging because of instability of main molecules. Crystallization of reactive mesogen molecules immediately occur as the temperature of the mixture is below a certain point ($\sim 60^\circ$). Figs. 8.1(a) and 8.1(b) show microscope images of crystallized particles formed during spin-coating process. Interestingly, crystallized RM molecules show very regular patterns which may indicate phase separation to another LC phase (i.e., smectic A) during this crystallization process. Further optimization of processing and possible modification of chemicals can improve the coating qualities as well as diffraction properties of PGs.

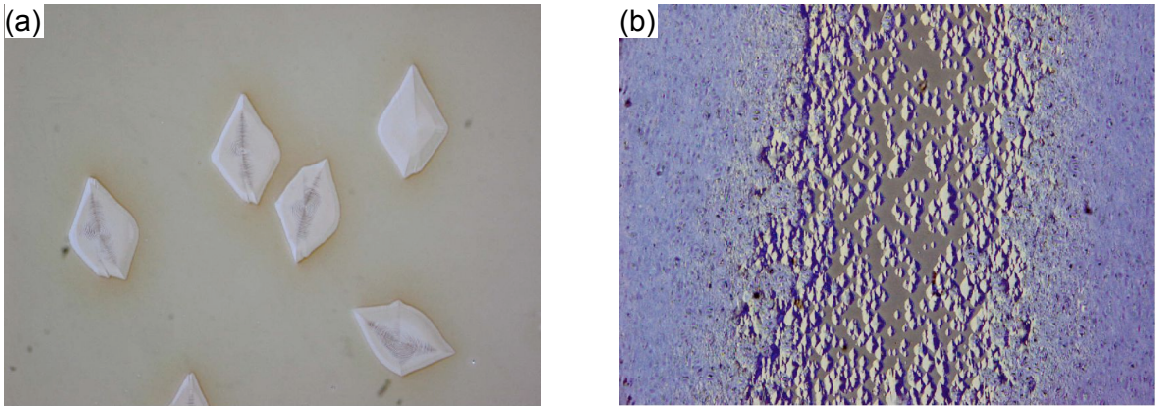

Figure 8.1: Microscope images of crystallized reactive mesogen molecules with a high Δn_l material (RMS09-038, $\Delta n_l = 0.39$ at 589 nm): (a) individual RM crystals; (b) a RMPG sample with typical coating problems with particles (RM crystals).

Proximity lithographic fabrication of PGs

Holographic recording of polarization grating patterns is the key technology for the successful fabrication of PGs. Although the current exposure method employ an interference of two orthogonal beams, a PG itself can be used to create the same polarization hologram at least in the near field. The resulting PG pattern, however, is expected to have half the period of the original PG (now named the 'master' PG) because of the difference between the period of interference ($2\Lambda \sin\theta_i = \lambda$) and patterned birefringence ($\Lambda \sin\theta_g = \lambda$). The resulting PG pattern can be recorded by placing the sample (named the 'copy' PG) immediately after the master PG, which method is basically the proximity lithography commonly used in micro-fabrication process. Initial experiments to fabricate a circular PG from a master grating on a fused silica substrate with period $\Lambda = 4$ μm (optimized for a half-wave retardation at 325 nm) via the proximity lithography. Fig. 8.2(a) shows the 0-order transmission spectrum of the master PG and Fig. 8.2(b) shows a comparison of PGs fabricated using the conventional holography and the proximity lithography. The copy PG shows a half grating period of the mater PG (2 μm versus 4 μm) and excellent diffraction properties including 99% efficiency at 633 nm and $> 500:1$ polarization contrast. Note that we used a photoalignment material LIA-01 (from Dainnipon Ink and Chemical) and a reactive mesogen prepolymer/solvent mixture RMS08-075 (from Merk, $\Delta n_l = 0.25$ at 532 nm). These preliminary results show

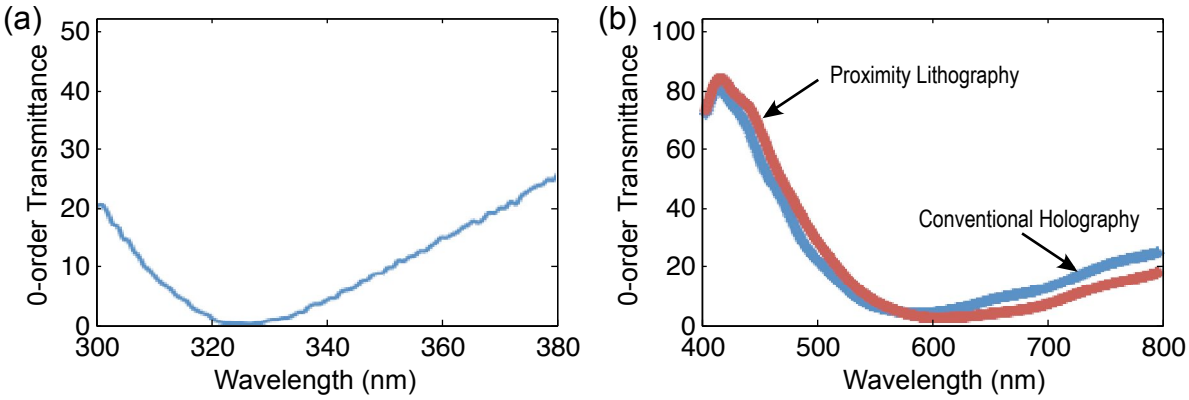

Figure 8.2: Proximity lithography as a fabrication method of PGs through a direct copy of the master PG: (a) the 0-order transmission spectrum of the master PG (optimized for a half-wave retardation at 325 nm); (b) the 0-order transmission spectra of the copy PG (compared with an identical PG fabricated by conventional polarization holography.

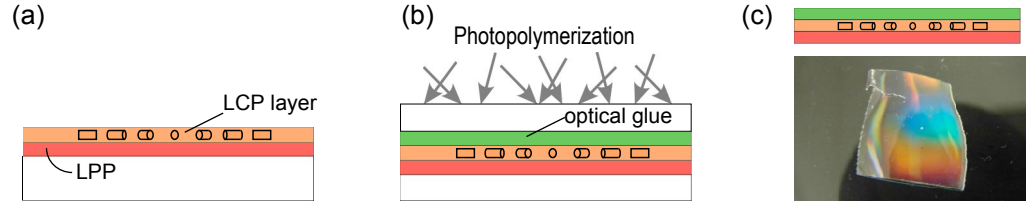

Figure 8.3: Fabrication of a flexible PG on a thin plastic film: (a) RMPG preparation; (b) glass assembling with optical glue; (c) de-lamination of the RMPG-glue film.

a good promise of the proximity lithography as an effective fabrication method for high-quality PGs at lower cost for mass-production.

Fabrication of liquid crystal polymer PGs on a flexible plastic film

PGs can be fabricated as a liquid crystal polymer film that is a highly crosslinked, rigid plastic sheet. It is very interesting to fabricate diffraction gratings on non-uniform surfaces or flexible substrates. Here, we propose a simple but effective fabrication method to transfer RMPGs onto a flexible substrate (i.e., thin plastic films). Figs. 8.3(a)–8.3(c) show the suggested method with following three steps: (i) fabricate RMPG layers on a normal solid substrate (a glass); (ii) assemble the RMPG sample with another glass substrate using an optical adhesive (UVS 61 from Norland) then cure the glue via UV exposure; (iii) break the glass substrate carefully then laminate the RMPG film with a relatively thick (i.e., ~ 10 μm) glue layer that serves as a flexible substrate. Fig. 8.3(c) also shows an actual flexible RMPG film. A number of alternative ways can be employed to produce similar plastic gratings. This thin-film grating can be laminated to any optical systems even with curved surfaces.

8.2.2 Polymer-PG display: toward ultra-bright pico-projectors

We have demonstrated the polymer-PG projection display with double the brightness as compared to the same system using polarizer-based display. However, low contrast ratio remains a main limitation of the polymer-PG display for practical pico-projector development. The extinction ration enhancement technique substantially improve the inherent extinction ratio of the polymer PGs but the system contrast ratio cannot reach to an acceptable level ($> 100:1$). Since most conventional light engines developed for pico-projectors

have $\sim 10^\circ$ divergence angle, $> 20^\circ$ diffraction angle of the PG ($\Lambda < 1.35$ μm for the shortest wavelength, 470 nm) is required to achieve high contrast images. To achieve this large diffraction angle and high efficiency at the same time, high Δn_l materials has to be considered. We believe the currently available high birefringence RM material (RMS09-038, $\Delta n_l = 0.39$ at 589 nm) can satisfy these requirements. In addition, more studies on polarization properties of PG diffraction at such large diffraction angles are highly suggested to improve the polarization compensation for the extinction ratio enhancement. We recently found that the LC/glass interfaces produce substantial light reflection ($\sim 3\%$) due to high index differences between glass and LCs with high Δn_l (the average LC index $\bar{n} = n_o + \frac{1}{2}\Delta n_l$) and affect the contrast ratio when the reflective display is used. The use of index-matched glasses for the LC materials can significantly reduce this reflection.

8.2.3 Uni-directional pointing of broadband beam using polarization gratings

Diffraction-based beam steering devices have a common problem of chromatic separation of the broadband beam due to the fundamental diffraction phenomena. The benefits of high steering efficiency and wide-angle scanning capability of PG-based beam steering systems can be maximized if it also allows uni-directional beam pointing even with broadband light (i.e., collimated white light). We propose a uni-directional pointing device based on two PGs and a waveplate with carefully engineered retardation for the spectrum of light source as shown in Fig. 8.4(a). We assume a white LED light source with intensity peaks at three wavelengths (red, green, blue). The beam is diffracted by the first achromatic PG (Fig. 8.4(b)) and then the polarization state at one wavelength is flipped to the orthogonal circular polarization by the waveplate (Fig. 8.4(c)). Finally, the second circular PG diffracts only two wavelengths at 100% efficiency but the center wavelength is not diffracted (0% efficiency of the second PG). Since two wavelengths have orthogonal circular polarizations, both beams are diffracted to the same direction of the center wavelength as shown in Fig. 8.4(c). The retardation engineering for optimized spectrum (Fig. 8.4(d)) can be done by a careful choice of materials and thicknesses of the each element.

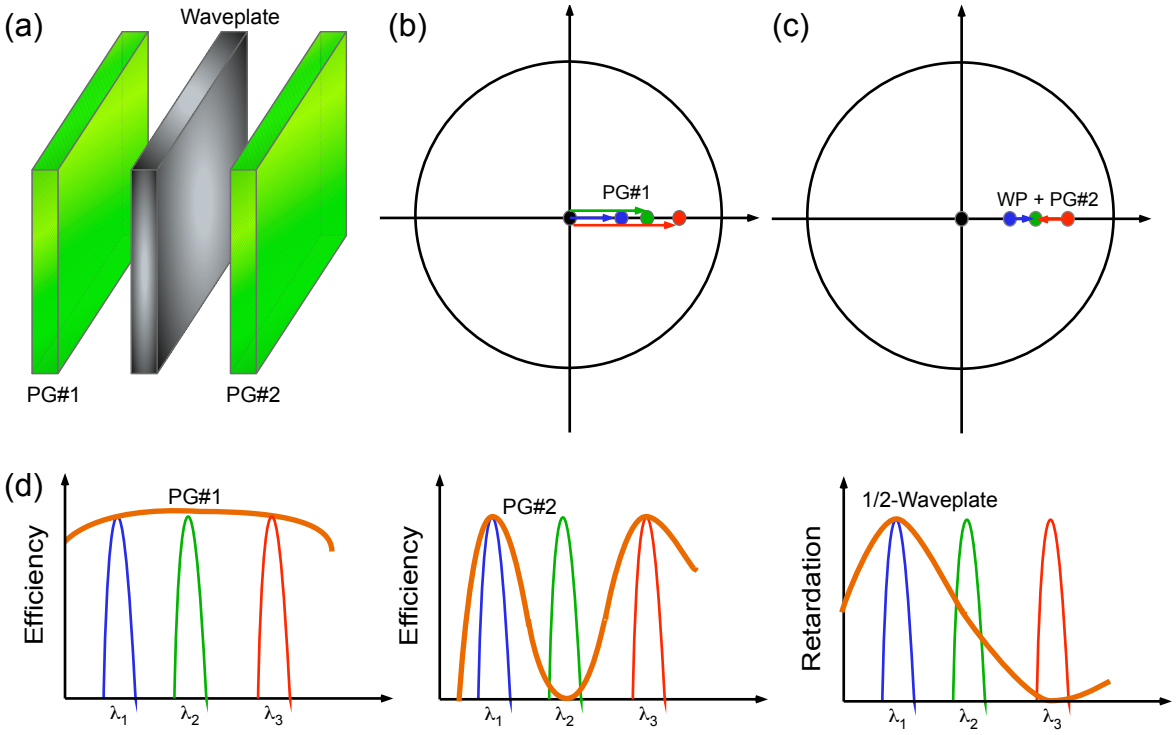

Figure 8.4: Uni-directional pointing of beadband beam using polarization gratings: (a) a schematic view of the pointing device using two PGs (one achromatic and one dispersive) and one waveplates; (b) the first achromatic PG diffraction at different wavelengths; (c) the second PG diffraction after a waveplate. The unidirectional pointing of the beam with intensity peaks at three different wavelengths is achieved by a precise engineering of the retardation spectra of individual elements as shown in the part (d).

8.2.4 Polarization holographic elements for vector beam shaping

We have shown that the polarization holography is an effective method to create complex polarization patterns and these spatially distributed polarization can be captured into a liquid crystal layer via photoalignment techniques. We, for the first time, demonstrated vectorial Fresnel zone plates as liquid crystal concentric polarization gratings using the polarization holography based on the Michelson interferometer. While our initial test was done with a simple spherical lens, any optical elements can be recorded as polarization holograms. One very interesting element is a fork grating [176] that generates a cylindrical vector beam. A polarization hologram corresponding to this grating pattern can be generated by inserting an axicon which has a conical surface as shown in Fig. 8.5. A number of different type of polarization holograms can be considered to create polarization diffractive

elements as *vector-beam shapers*.

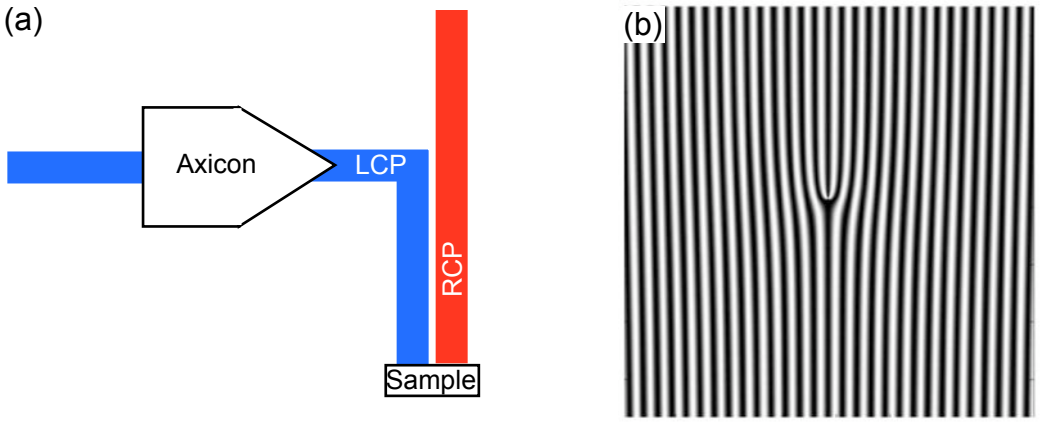

Figure 8.5: Polarization holographic elements for vector beam shaping: (a) polarization holography with a axicon; (b) a polarization-version of a fork grating

Bibliography

[1] J. C. Maxwell. A dynamical theory of the electromagnetic field. *Philos. Trans. R. Soc. Lond., A*, 155:459–512, 1865.

[2] E. Hecht. *Optics*. Addison-Wesley Pub. Co., San Francisco, 4th edition, 2002.

[3] E. Collett. *Polarized Light: fundamentals and applications*. Marcel Dekker, New York, 1993.

[4] L. Nikolova and T. Todorov. Diffraction efficiency and selectivity of polarization holographic recording. *Opt. Acta*, 31:579–588, 1984.

[5] F. Gori. Measuring stokes parameters by means of a polarization grating. *Opt. Lett.*, 24:584–586, 1999.

[6] J. Tervo and J. Turunen. Paraxial-domain diffractive elements with 100% efficiency based on polarization gratings. *Opt. Lett.*, 25:785–786, 2000.

[7] Chulwoo Oh and Michael J. Escuti. Numerical analysis of polarization gratings using the finite-difference time-domain method. *Phys. Rev. A*, 76(4):043815, 2007.

[8] E. Hasman, Z. Bomzon, A. Niv, G. Biener, and V. Kleiner. Polarization beam-splitters and optical switches based on space-variant computer-generated subwavelength quasi-periodic structures. *Opt. Commun.*, 209:45–54, 2002.

[9] Michael J. Escuti and W. Michael Jones. A polarization-independent liquid crystal spatial light modulator. *Proc. SPIE*, 6332(1):63320M, 2006.

[10] Hakob Sarkissian, Svetlana V. Serak, Nelson V. Tabiryan, Leon B. Glebov, Vasile Rotar, and BorisYa. Zeldovich. Polarization-controlled switching between diffraction

orders in transverse-periodically aligned nematic liquid crystals. *Opt. Lett.*, 31:2248–2250, 2006.

[11] C. Provenzano, P. Pagliusi, and G. Cipparrone. Highly efficient liquid crystal based diffraction grating induced by polarization holograms at the aligning surfaces. *Appl. Phys. Lett.*, 89:121105, 2006.

[12] T. Todorov, L. Nikolova, and N. Tomova. Polarization holography. 1: A new high-efficiency organic material with reversible photoinduced birefringence. *Appl. Opt.*, 23:4309–4312, 1984.

[13] D. Sek, E. Schab-Balcerzak, M. Solyga, and A. Miniewicz. Polarisation-sensitive holographic recording in polyimide-containing azo-dye. *Syn. Mat.*, 127:89–93, 2002.

[14] L. Nikolova, T. Todorov, M. Ivanov, F. Andruzzi, S. Hvilsted, and P. S. Ramanujam. Polarization holographic gratings in side-chain azobenzene polyesters with linear an circular photoanisotropy. *Appl. Opt.*, 35:3835–3840, 1996.

[15] H. Ono and A. Emoto. Multiplex diffraction from functionalized polymer liquid crystals and polarization conversion. *Opt. Express*, 11:2379–2384, 2003.

[16] Martin Schadt, Klaus Schmitt, Vladimir Kozinkov, and Vladmir Chigrinov. Surface-induced parallel alignment of liquid crystals by linearly polymerized photopolymers. *Jpn. J. Appl. Phys.*, 31:2155–2164, 1992.

[17] Gregory P. Crawford, James N. Eakin, Marc D. Radcliffe, Andrew Callan-Jones, and Robert A. Pelcovits. Liquid-crystal diffraction gratings using polarization holography alignment techniques. *J. Appl. Phys.*, 98:123102, 2005.

[18] M. J. Escuti and W. M. Jones. Polarization independent switching with high contrast from a liquid crystal polarization grating. *SID Digest*, 37:39.34–, 2006.

[19] M. J. Escuti, C. Oh, C. Sanchez, C. W. M. Bastiaansen, and D. J. Broer. Simplified spectropolarimetry using reactive mesogen polarization gratings. *Proc. SPIE*, 6302:632614, 2006.

[20] F. Wyrowski. Upper bound of the diffraction efficiency of diffractive phase elements. *Opt. Lett.*, 16:1915–1917, 1991.

[21] H. Lajunen, J. Turunen, and J. Tervo. Design of polarization gratings for broadband illumination. *Opt. Express*, 13:3055–3067, 2005.

[22] David K. Cheng. *Fundamentals of engineering electromagnetics*. Addison Wesley, 1993.

[23] J. A. Kong. *Theory of Electromagnetic Waves*. J. Wiley and Sons, New York, 1975.

[24] Saleh. *Fundamentals of Phtonics*. Addison-Wesley Pub. Co., San Francisco, 4th edition, 2002.

[25] Pochi Yeh. *Introduction to photorefractive nonlinear optics*. Wiley & Sons, 1993.

[26] R. C. Jones. A new calculus for the treatment of optical systems. i. description and discussion of the calculus. *J. Opt. Soc. Am.*, 31:488–, 1941.

[27] A. Lien. Extended jones matrix representation for the twisted nematic liquid-crystal display at oblique incidence. *Appl. Phys. Lett.*, 57:2767–2769, 1990.

[28] G. G. Stokes. On the composition and resolution of streams of polarized light from different sources. *Trans. Cambridge Philos. Soc.*, 9:339–412, 1852.

[29] G. R. Fowles. *Introduction to Mordern Optics*. Holt, Rinehart and Winston, New York, 1968.

[30] P. Yeh and C. Gu. *Optics of Liquid Crystal Displays*. Wiley, New York, 1999.

[31] Erwin C. Loewen and Evgeny Popov. *Diffraction gratings and applications*. Marcel Dekker, 1997.

[32] T. K. Gaylord and M. G. Moharam. Analysis and applications of optical diffraction by gratings. *Proc. IEEE*, 73:894–937, 1985.

[33] W. R. Klein and B. D. Cook. Unified approach to ultrasonic light diffraction. *IEEE Trans. Ultrason. Ferr.*, SU14:123, 1967.

[34] M. G. Moharam and L. Yong. Criterion for bragg and raman-nath diffraction regimes. *Appl. Opt.*, 17:1757–1759, 1978.

[35] M. Born and E. Wolf. *Principles of Optics*. Cambridge University Press, New York, 7th edition, 1999.

[36] E. B. Grann, M. G. Moharam, and D. A. Pommet. Artificial uniaxial and biaxial dielectrics with use of two-dimensional subwavelength binary gratings. *J. Opt. Soc. Am. A*, 11:2695–2703, 1994.

[37] H. Kikuta, H. Yoshida, and K. Iwata. Ability and limitation of effective medium theory for subwavelength gratings. *Opt. Rev.*, 2:92–99, 1995.

[38] I. Richter, P.-C. Sun, F. Xu, and Y. Fainman. Design considerations of form birefringent microstructures. *Appl. Opt.*, 34:2421–2429, 1995.

[39] P. Lalanne and D. Lemercier-Lalanne. On the effective medium theory of subwavelength periodic structures. *J. Mod. Opt.*, 43:2063–2085, 1996.

[40] I. Richter, P.-C. Sun, F. Xu, and Y. Fainman. Artificial uniaxial and biaxial dielectrics with the use of photoinduced gratings. *J. Appl. Phys.*, 81:23–29, 1996.

[41] I. Celanovic, F. O'Sullivan, M. Ilak, J. Kassakian, and D. Perreault. Design and optimization of one-dimensional photonic crystals for thermophotovoltaic applications. *Opt. Lett.*, 29:863–865, 2004.

[42] M. L. Jepsen and H. J. Gerritsen. Liquid-crystal-filled gratings with high diffraction efficiency. *Opt. Lett.*, 21:1081–1083, 1996.

[43] M. L. Doucen and P. Pellat-Finet. Polarization properties and diffraction efficiencies of binary anisotropic gratings: general study and experiments on ferroelectric liquid crystals. *Opt. Commun.*, 151:321–330, 1998.

[44] J. Park, C. Yu, J. Kim, S. Chung, and S. Lee. Concept of a liquid-crystal polarization beamsplitter based on binary phase gratings. *Appl. Phys. Lett.*, 83:1918–1920, 2003.

[45] Pierre Gilles de Gennes and Jacques Prost. *The Physics of Liquid Crystals*. Oxford University Press, 1995.

[46] S. Chandrasekhar. *Liquid Crystals*. Cambridge U. Press, Cambridge, 1992.

[47] P. J. Collings and M. Hird. *Introduction to liquid crystals : chemistry and physics*. Taylor and Francis, London, 1997.

[48] Iain W. Stewart. *The Static and Dynamic Continuum Theory of Liquid Crystals: A Mathematical Introduction*. Taylor & Francis, 2004.

[49] S. M. Kelly. Anisotropic networks. *J. Mater. Chem.*, 37:1443–1446, 1995.

[50] Heiko Thiem, Peter Strohriegl, Maxim Shkunov, and Iain McCulloch. Photopolymerization of reactive mesogens. *Macromol. Chem. Phys.*, 206:2153–2159, 2005.

[51] D. J. BROER, J. LUB, and G. N. MOL. Wide-band reflective polarizers from cholesteric polymer networks with a pitch gradient. *Nature*, 378:467–469, 1995.

[52] Dirk J. Broer, Jos A.M.M. van Haaren, Peter van de Witte, and Cees Bastiaansen. New functional polymers for liquid crystal displays review of some recent developments. *Macromol. Symp.*, 154:1–13, 2000.

[53] Roel Penterman, Stephen I. Klink, Henk de Koning, Giovanni Nisato, and Dirk J. Broer. Single-substrate liquid-crystal displays by photo-enforced stratification. *Nature*, 417:55–58, 2002.

[54] Grietje N. Mol, Kenneth D. Harris, Cees W. M. Bastiaansen, and Dirk J. Broer. Thermo-mechanical responses of liquid-crystal networks with a splayed molecular organization. *Adv. Funct. Mater.*, 15:1155–1159, 2005.

[55] Kenneth D. Harris, Cees W. M. Bastiaansen, Johan Lub, and Dirk J. Broer. Self-assembled polymer films for controlled agent-driven motion. *Nano Lett.*, 5:1857–1860, 2005.

[56] A. L. Elias, K. D. Harris, C. W. M. Bastiaansen, D. J. Broer, and M. J. Brett. Photopatterned liquid crystalline polymers for microactuators. *J. Mater. Chem.*, 16:2903–2912, 2006.

[57] Scott J. Woltman, Gregory D. Jay, and Gregory P. Crawford. Liquid-crystal materials find a new order in biomedical applications. *Nat. Mater.*, 6:929–938, 2007.

[58] Timothy J. White, Svetlana V. Serak, Nelson V. Tabiryan, Richard A. Vaiaa, and Timothy J. Bunning. Polarization-controlled, photodriven bending in monodomain liquid crystal elastomer cantilevers. *J. Mater. Chem.*, 19:1080–1085, 2009.

[59] D. W. Berreman. Solid surface shape and the alignment of an adjacent nematic liquid crystal. *Phys. Rev. Lett.*, 28:1683–1686, 1972.

[60] K Takatoh, M Sakamoto, R Hasegawa, M Koden, N Itoh, and M Hasegawa. *Alignment Technology and Applications of Liquid Crystal Devices*. Taylor & Francis, 2005.

[61] Kunihiro Ichimaru, Yasuzo Suzuki, and Takahiro Seki. Reversible change in alignment mode of nematic liquid crystals regulated photochemically by "command surfaces" modified with an azobenzene monolayer. *Langmuir*, 4:1214–1216, 1988.

[62] Wayne M. Gibbons, Paul J. Shannon, Shao-Tang Sun, and Brian J. Swetlin. Surface-mediated alignment of nematic liquid crystals with polarized laser light. *Nature*, 351:49–50, 1991.

[63] M O'Neil and S. M. Kelly. Photoinduced surface alignment for liquid crystal displays. *J. Phys. D: Appl. Phys.*, 33:R67–R84, 2000.

[64] Kunihiro Ichimaru. Photoalignment of liquid-crystal systems. *Chem. Rev.*, 100:1847–1873, 2000.

[65] Vladimir G. Chigrinov, Vladimir M. Kozenkov, and Hoi-Sing Kwok. *Photoalignment of Liquid Crystalline Materials: Physics and Applications*. Wiley, 2008.

[66] Vladimir Chigrinov, Sergey Pikin, Andrey Verevochnikov, Vladimir Kozenkov, Maxim Khazimullin, Jacob Ho, Dan Ding Huang, and Hoi-Sing Kwok. Diffusion model of photoaligning in azo-dye layers. *Phys. Rev. E*, 69:061713, 2004.

[67] M. Schadt, H. Seiberle, and A. Schuster. Optical patterning of multi-domain liquid crystal displays with wide viewing angles. *Nature*, 381:123102, 1996.

[68] Martin Schadt. Liquid crystal displays and novel optical thin films enabled by photo-alignment. *Mol. Cryst. Liq. Cryst.*, 364:151–169, 2001.

[69] Masaki Hasegawa and Yoichi Taira. Nematic homogeneous photo alignment by polyimide exposure to linearly polarized uv. *J. Photopolym. Sci. Technol.*, 8:241–248, 1995.

[70] V. G. Nazarenko, O. P. Boiko, A. B. Nych, Yu. A. Nastishin, V. M. Pergamenshchik, and P. Bos. Selective light-induced desorption: The mechanism of photoalignment of liquid crystals at adsorbing solid surfaces. *Europhys. Lett.*, 75:448–454, 2006.

[71] Alexei D. Kiselev, Vladimir Chigrinov, and Dan Ding Huang. Photoinduced ordering and anchoring properties of azo-dye films. *Phys. Rev. E*, 72:061703, 2005.

[72] V. P. Vorflusev, H.-S. Kitzerow, and V. G. Chigrinov. Azimuthal anchoring of liquid crystals at the surface of photo-induced anisotropic films. *Appl. Phys. A*, 64:615–618, 1997.

[73] V. P. Vorflusev, H.-S. Kitzerow, and V. G. Chigrinov. Azimuthal anchoring energy in photoinduced anisotropic films. *Jpn. J. Appl. Phys.*, 34:L1137–L1140, 1995.

[74] Vladimir Chigrinov, Elena Prudnikova, Vladimir Kozenkov, and Hoi Kwok. Synthesis and properties of azo dye aligning layers for liquid crystal cells. *Liq. Cryst.*, 29:1321–1327, 2002.

[75] Martin Schadt. Liquid crystal materials and liquid crystal displays. *Annu. Rev. Mater. Sci.*, 27:305–379, 1997.

[76] Douglas J. McKnight, David G. Vass, and Richard M. Sillitto. Development of a spatial light modulator: a randomly addressed liquid-crystal-over-nmos array. *Appl. Opt.*, 28:4757–4762, 1989.

[77] D. A. Jared, R. Turner, and K. M. Johnson. Electrically addressed spatial light-modulator that uses a dynamic memory. *Opt. Lett.*, 16:1785–1787, 1991.

[78] D. J. Mcknight, K. M. Johnson, and R. A. Serati. 256×256 liquid-crystal-on-silicon spatial light-modulator. *Appl. Opt.*, 33:2775–2784, 1994.

[79] Ian Underwood, David G. Vass, Antony O'Hara, Dwayne C. Burns, Peter W. McOwan, and James Gourlay. Improving the performance of liquid-crystal-over-silicon spatial light modulators: issues and achievements. *Appl. Opt.*, 33:2768–2774, 1994.

[80] P. F. McManamon, T. A. Dorschner, D. L. Corkum, L. J. Friedman, D. S. Hobbs, M. Holz, S. Liberman, H. Q. Nguyen, D. P. Resler, R. C. Sharp, and E. A. Watson. Optical phased array technology. *Proc. IEEE*, 84(2):268–298, 1996.

[81] A. Linnenberger, S. Serati, and J. Stockley. Advances in optical phased array technology. *Proc. SPIE*, 6304:63040T, 2006.

[82] William J Hossack, Eirini Theofanidou, and Jason Crain. High-speed holographic optical tweezers using a ferroelectric liquid crystal microdisplay. *Opt. Express*, 11:2053–2059, 2003.

[83] Xu Wang, Daniel Wilson, Richard Muller, Paul Maker, and Demetri Psaltis. Liquid-crystal blazed-grating beam deflector. *Appl. Opt.*, 39:6545–6555, 2000.

[84] Allan S. P. Chang, Keith J. Morton, Hua Tan, Patrick F. Murphy, Wei Wu, and Stephen Y. Chou. Tunable liquid crystal-resonant grating filter fabricated by nanoimprint lithography. *IEEE Photonics Technol. Lett.*, 19:1457–1459, 2007.

[85] Dean Faklis and G. Michael Morris. Diffractive optics technology for display applications. *Projection Displays*, 2407(1):57–61, 1995.

[86] Paul F. McManamon, Edward A. Watson, Terry A. Dorschner, and Lawrence J. Barnes. Applications look at the use of liquid crystal writable gratings for steering passive radiation. *Opt. Eng.*, 32:2657–2664, 1993.

[87] J. Shi, P. J. Bos, B. Winker, and P. McManamon. Switchable optical phased prism arrays for beam steering. *Proc. SPIE*, 5553:102–111, 2004.

[88] J. Chen, P. J. Bos, D. R. Bryant, D. L. Johnson, S. H. Jamal, and J. R. Kelly. Simple four-domain twisted nematic liquid crystal display. *Appl. Phys. Lett.*, 67:1990–1992, 1995.

[89] P. J. Bos, J. Chen, J. W. Doane, B. Smith, C. Holton, and W. Glenn. An optically active diffractive device for a high-efficiency light valve. *J. SID*, 3:195–197, 1995.

[90] C. M. Titus and P. J. Bos. Efficient, polarization-independent, reflective liquid crystal phase grating. *Appl. Phys. Lett.*, 71:2239–2241, 1997.

[91] B. Wang, X. Wang, and P. J. Bos. Finite-difference time-domain calculations of a liquid-crystal-based switchable bragg grating. *J. Opt. Soc. Am. A*, 21:1066–1072, 2004.

[92] Yanli Zhang, Bin Wang, Philip J. Bos, Jennifer Colegrove, and David B. Chung. High-efficiency, liquid-crystal-based, controllable diffraction grating. *J. Opt. Soc. Am. A*, 22:2510–2515, 2005.

[93] T. Huang and K.H. Wagner. Coupled mode analysis of polarization volume hologram. *IEEE Journal of Quantum Electronics*, 31:372–390, 1995.

[94] Z. Bomzon, G. Biener, V. Kleiner, and E. Hasman. Spatial fourier-transform polarimetry using space-variant subwavelength metal-strip polarizers. *Opt. Lett.*, 26:1711–1713, 2001.

[95] G. Cipparrone, A. Mazzulla, and L.M. Blinov. Permanent polarization gratings in photosensitive langmuir-blodgett films for polarimetric applications. *J. Opt. Soc. Am. B*, 19:1157–1161, 2002.

[96] Clementina Provenzano, Gabriella Cipparrone, and Alfredo Mazzulla. Photopolarimeter based on two gratings recorded in thin organic films. *Appl. Opt.*, 45:3929–3934, 2006.

[97] W. M. Jones, B. L. Conover, and M. J. Escuti. Evaluation of projection schemes for the liquid crystal polarization grating operating on unpolarized light. *SID Digest*, 37:1015–1018, 2006.

[98] R. K. Komanduri, W. M. Jones, C. Oh, and M. J. Escuti. Polarization-independent modulation for projection displays using small-period lc polarization gratings. *J. SID*, 15:589–594, 2007.

[99] J. A. Davis, J. Adachi, C. R. Fernandez-Pousa, and I. Moreno. Polarization beam splitters using polarization diffraction gratings. *Opt. Lett.*, 26:587–589, 2001.

[100] J. Kim, C. Oh, M. J. Escuti, L. Hosting, and S. Serati. Wide-angle nonmechanical beam steering using thin liquid crystal polarization gratings. *Proc. SPIE*, 7093:709302, 2008.

[101] Paul F. McManamon, Philip J. Bos, Michael J. Escuti, Jason Heikenfeld, Steve Serati, Huikai Xie, and Edward A. Watson. A review of phased array steering for narrow-band electrooptical systems. *Proc. IEEE*, 97:1078–1096, 2009.

[102] G. Cincotti. Polarization gratings: Design and applications. *IEEE J. Quantum Electron.*, 39:1645–1652, 2003.

[103] C.M. van Heesch. *Polarization-Selective Diffraction for display applications*. PhD thesis, Eindhoven University of Technology, Eindhoven, Netherlands, 2007.

[104] Olef Bryngdahl. Polarization-grating moire. *J. Opt. Soc. Am.*, 62:839–848, 1972.

[105] Sh. D. Kakichashvili. Method of recording phase polarization holograms. *Sov. J. Quant. Electron.*, 4:795–798, 1974.

[106] T. Todorov, L. Nikolova, and N. Tomova. Polarization holography. 2: Polarization holographic gratings in photoanisotropic materials with and without intrinsic birefringence. *Appl. Opt.*, 23:4588–4591, 1984.

[107] I. D. Shatalin, V. I. Kakichashvili, and Sh. D. Kakichashvili. Polarization hologram with the 100-percent efficiency. *Sov. Tech. Phys. Lett.*, 13:1051–1055, 1987.

[108] J.M.C. Jonathan. Interferograms obtained from photodichroic recording of two partially coherent vibrations with opposite sense. *Opt. Commun.*, 40:239–242, 1982.

[109] M. Attia and J.M.C. Jonathan. Anisotropic gratings recorded from two circularly polarized coherent waves. *Opt. Commun.*, 47:85–90, 1983.

[110] N.C.R. Holme, L. Nikolova, P.S. Ramanujam, and S. Hvilsted. An analysis of the anisotropic and topographic gratings in a side-chain liquid crystalline azobenzene polyester. *Appl. Phys. Lett.*, 70:1518–1520, 1997.

[111] I. Naydenova, L. Nikolova, T. Todorov, N.C.R. Holme, P.S. Ramanujam, and S. Hvilsted. Diffraction from polarization holographic gratings with surface relief in side-chain azobenzene polyesters. *J. Opt. Soc. Am. B*, 15:1257–1265, 1998.

[112] L. Nikolova, T. Todorov, V. Dragostinova, T. Petrova, and N. Tomova. Polarization reflection holographic gratings in azobenzene-containing gelatine films. *Opt. Lett.*, 27:92–94, 2002.

[113] S. Slussarenko, O. Francescangeli, F. Simoni, and Y. Reznikov. High resolution polarization gratings in liquid crystals. *Appl. Phys. Lett.*, 71:3613–3615, 1997.

[114] Y. Okada-Shudo. Polarization holography with bacteriorhodopsin. *Proc. SPIE*, 4461:138–145, 2001.

[115] Gabriel Biener, Avi Niv, Vladimir Kleiner, and Erez Hasman. Near-field fourier transform polarimetry by use of a discrete space-variant subwavelength gratings. *J. Opt. Soc. Am. A*, 20:1940–1948, 2003.

[116] B. Wen, R. G. Petschek, and C. Rosenblatt. Nematic liquid-crystal polarization gratings by modification of surface alignment. *Appl. Opt.*, 41:1246–1250, 2002.

[117] Mario Ivanov and Tomoaki Eiju. Compact spectral ellipsometer with polarization grating. *Proc. SPIE*, 4580:664–672, 2001.

[118] G. Cincotti. Design and fabrication techniques for polarization gratings for polarization mode dispersion measurements. *J. Opt. A: Pure Appl. Opt*, 6:S100–S104, 2004.

[119] J. N. Eakin, Y. Xie, R. A. Pelcovits, M. D. Radcliffe, and G. P. Crawford. Zero voltage freedericksz transition in periodically alligned liquid crystals. *Appl. Phys. Lett.*, 85:1671–1673, 2004.

[120] C. Oh, R. K. Komanduri, B. L. Conover, and M. J. Escuti. Polarization-independent modulation using standard liquid crystal microdisplays and polymer polarization gratings. *Int. Disp. Res. Conf.*, 28:298–301, 2008.

[121] Ravi K. Komanduri. *Ultra-efficient liquid crystal projection displays: polarizer-free displays using continuous polarization gratings.* PhD thesis, North Carolina State University, 2009.

[122] J. Kim and M. J. Escuti. Snapshot imaging spectropolarimeter utilizing polarization gratings. *Proc. SPIE*, 7086:708603, 2008.

[123] C. Packham, M. J. Escuti, G. Boreman, I. Quijano, J. C. Ginn, B. Franklin, D. J. Axon, J. H. Hough, T. J. Jones, P. F. Roche, M. Tamura, C. M. Telesco, N. Levenson, J. M. Rodgers, and J. P. McGuire. Design of a mid-ir polarimeter for sofia. *Proc. SPIE*, 7014:70142H, 2008.

[124] Elena Nicolescu and Michael J. Escuti. Polarization-independent tunable optical filters based on liquid crystal polarization gratings. *Proc. SPIE*, 6654(1):665405, 2007.

[125] Elena Nicolescu and Michael J. Escuti. Compact spectrophotometer using polarization-independent liquid crystal tunable optical filters. *Proc. SPIE*, 6661(1):666105, 2007.

[126] E. Nicolescu and M. J. Escuti. Polarization-independent tunable optical filters based on bilayer polarization gratings. *Proc. SPIE*, 7050:705018, 2008.

[127] Lei Shi, Paul F. McManamon, and Philip J. Bos. Liquid crystal optical phase plate with a variable in-plane gradient. *J. Appl. Phys.*, 104:033109, 2008.

[128] Sarik R. Nersisyan, Nelson V. Tabiryan, Landa Hoke, Diane M. Steeves, and Brian Kimball. Polarization insensitive imaging through polarization gratings. *Opt. Express*, 17:1817–1830, 2009.

[129] P. Hariharan. *Basics of Holography.* Cambridge Univeristy Press, 2002.

[130] R. K. Komanduri and M. J. Escuti. Elastic continuum analysis of the liquid crystal polarization grating. *Phys. Rev. E*, 76:021701, 2007.

[131] Ravi K. Komanduri, Chulwoo Oh, and Michael J. Escuti. Reflective liquid crystal polarization gratings with high efficiency and small pitch. *Proc. SPIE*, 7050:70500J, 2008.

[132] A. Taflove and S. C. Hagness. *Computational Electrodynamics: Finite-Difference Time-Domain Method.* Artech House, Norwood, MA, 2nd edition, 2000.

[133] C. Oh. Finite-difference time-domain analysis of periodic anisotropic media. Master's thesis, North Carolina State University, Raleigh, NC, 2006.

[134] C. Oh and M. J. Escuti. Time-domain analysis of periodic anisotropic media at oblique incidence: An efficient fdtd implementation. *Opt. Express*, pages –, 2006.

[135] Wideband optical fdtd simulator (wolfsim) – http://www.ece.ncsu.edu/oleg/wiki/wolfsim.

[136] W. H. Southwell. Gradient-index antireflection coatings. *Opt. Lett.*, 8:584–586, 1983.

[137] I. Richter, Z. Ryzi, and P. Fiala. Analysis of binary diffraction gratings: comparison of different approaches. *J. Mod. Opt.*, 45:1335–1355, 1998.

[138] H. Kogelink. Coupled wave theory for thick hologram gratings. *Bell Syst. tech. J.*, 48:2909–2947, 1969.

[139] H. Lajunen, J. Tervo, and J. Turunen. High-efficiency broadband diffractive elements based on polarization gratings. *Opt. Lett.*, 29:803–805, 2004.

[140] C. Oh and M. J. Escuti. Achromatic polarization gratings as highly efficient thin-film polarizing beamsplitters for broadband light. *Proc. SPIE*, 6682:668211, 2007.

[141] Chulwoo Oh and Michael J. Escuti. Achromatic diffraction from polarization gratings with high efficiency. *Opt. Lett.*, 33:2287–2289, 2008.

[142] Terry Scheffer. Supertwisted nematic (stn) liquid crystal displays. *Annu. Rev. Mater. Sci.*, 27:555–583, 1997.

[143] Ravi K. Komanduri, Chulwoo Oh, Michael J. Escuti, and D. J. Kekas. Polarization independent liquid crystal microdisplays. *SID Digest*, 39:236–239, 2008.

[144] M. Bauer, C. Boeffel, F. Kuschel, and H. Zaschke. Evaluation of chiral dopants for lcd applications. *J. SID*, 14:805–812, 2006.

[145] B. Liang and C. L. Lin. Crucial influence on d/p range in bistable chiral tilted-homeotropic nematic liquid crystal cells. *J. Appl. Phys.*, 102:124504, 2007.

[146] W. H. Southwell. Multilayer coating design achieving a broadband 90° phase shift. *Appl. Opt.*, 19:2688–2692, 1980.

[147] P. Hariharan and Philip E. Ciddor. Achromatic switchable polarization rotators. *Opt. Eng.*, 36:952–956, 1997.

[148] P. Hariharan and P. E. Ciddor. Broad-band superachromatic retarders and circular polarizers for the uv, visible and near infrared. *J. Mod. Opt.*, 51:2315–2322, 2004.

[149] Jesus Lancis, Gladys Minguez-Vega, Enrique Tajahuerce, Vicent Climent, Pedro Andres, and Jose Caraquitena. Chromatic compensation of broadband light diffraction: Abcd-matrix approach. *J. Opt. Soc. Am. A*, 21:1875–1885, 2004.

[150] H. H. Refai, J. J. Sluss, and M. P. Tull. Digital micromirror device for optical scanning applications. *Opt. Eng.*, 46:085401, 2007.

[151] Ata Akatay and Hakan Urey. Design and optimization of microlens array based high resolution beam steering system. *Opt. Express*, 15:4523–4529, 2007.

[152] L. B. Glebov. Photosensitive holographic glass - new approach to creation of high power lasers. *Glass Technol.: Eur. J. Glass Sci. Technol.*, 48:123–128, 2007.

[153] Neil R. Smith, Don. C. Abeysinghe, Joseph W. Haus, and Jason Heikenfeld. Agile wide-angle beam steering with electrowetting microprisms. *Opt. Express*, 14:6557–6563, 2006.

[154] F. A. Rosell. Prism scanner. *J. Opt. Soc. Am.*, 50:521–526, 1960.

[155] Christopher T. Amirault and Charles A. DiMarzio. Precision pointing using a dual-wedge scanner. *Appl. Opt.*, 24:1302–1308, 1985.

[156] James W. Bilbro, C. DiMarzio, D. Fitzjarrald, S. Johnson, and W. Jones. Airborne doppler lidar measurements. *Appl. Opt.*, 25:3952–3960, 1986.

[157] Gerald F. Marshall. Risley prism scan patterns. *Proc. SPIE*, 3787:74–86, 1999.

[158] G. Garcia-Torales, M. Strojnik, and G. Paez. Risley prisms to control wave-front tilt and displacement in a vectorial shearing interferometer. *Appl. Opt.*, 41:1380–1384, 2002.

[159] Bradley D. Duncan, Philip J. Bos, and Vassili Sergan. Wide-angle achromatic prism beam steering for infrared countermeasure applications. *Opt. Eng.*, 42:1038–1047, 2003.

[160] James E. Harvey and Cynthia L. Vernold. Description of diffraction grating behavior in direction cosine space. *Appl. Opt.*, 37:8158–8160, 1998.

[161] C. Packham and T. J. Jones. Mmt-pol: an adaptive optics optimized 1-5m polarimeter. *Proc. SPIE*, 7014:70145F, 2008.

[162] D.J. Broer, J. Boven, G.N. Mol, and G. Challa. In-situ photopolymerization of oriented liquid-crystalline acrylate, 3: Oriented polymer networks from a mesogenic diacrylate. *Makromol. Chem.*, 190:2255–2268, 1989.

[163] S. Sato. Liquid crystal lens-cell with variable focal length. *Jpn. J. Appl. Phys.*, 18:1679–1684, 1979.

[164] S. Sato, A. Sugiyama, and R. Sato. Variable-focus liquid- crystal fresnel lens. *Jpn. J. Appl. Phys.*, 24:L626–L628, 1985.

[165] S. T. Kowel, D. S. Cleverly, and P. G. Kornreich. Focusing by electrical modulation of refraction in a liquid crystal cell. *Appl. Opt.*, 23:278–289, 1984.

[166] T. Nose and S. Sato. A liquid crystal microlens obtained with a non-uniform electric field. *Liq. Cryst.*, 5:1425–1433, 1989.

[167] T. Nose, S. Masuda, and S. Sato. Optical properties of a liquid crystal microlens with a symmetric electrode structure. *Jpn. J. Appl. Phys.*, 30:L2110–L2112, 1991.

[168] A. F. Naumov, M. Yu. Loktev, I. R. Guralnik, and G. Vdovin. Liquid-crystal adaptive lenses with modal control. *Opt. Lett.*, 23:992–994, 1998.

[169] S. Masuda, S. Takahashi, T. Nose, S. Sato, and H. Ito. Liquid-crystal microlens with a beam-steering function. *Appl. Opt.*, 26:4772–4778, 1997.

[170] G. Williams, N. J. Powell, A. Purvis, and M. G. Clark. Electrically controllable liquid crystal fresnel lens. *Proc. SPIE*, 1168:352–357, 1989.

[171] J. S. Patel and K. Rastani. Electrically controlled polarization-independent liquid-crystal fresnel lens arrays. *Opt. Lett.*, 16:532–534, 1991.

[172] Yun-Hsing Fan, Hongwen Ren, and Shin-Tson Wu. Switchable fresnel lens using polymer-stabilized liquid crystals. *Opt. Express*, 11:3080–3086, 2003.

[173] Tsung-Hsien Lin, Yuhua Huang, Andy Y. G. Fuh, and Shin-Tson Wu. Polarization controllable fresnel lens using dye-doped liquid crystals. *Opt. Express*, 14:2359–2364, 2006.

[174] Erez Hasman, Vladimir Kleiner, Gabriel Biener, and Avi Niv. Polarization dependent focusing lens by use of quantized pancharatnam-berry phase diffractive optics. *Appl. Phys. Lett.*, 82:328–330, 2003.

[175] Michinori Honma and Toshiaki Nose. Liquid-crystal fresnel zone plate fabricated by microrubbing. *Jan. J. Appl. Phys.*, 44:287–290, 2005.

[176] Ljiljana Janicijevic and Suzana Topuzoski. Fresnel and fraunhofer diffraction of a gaussian laser beam by fork-shaped gratings. *J. Opt. Soc. Am. A*, 25:2659–2669, 2008.

Appendices

A. Numerical Analysis of Linear Polarization Gratings

Linear PGs are distinct from circular PGs because they have a periodic modulation in the magnitude of their linear and circular birefringences (Fig. 2.19(b)), attainable in various materials [12, 14, 15]. Classification into two cases is convenient: (A) $\Delta n_l = \Delta n_c$ and (B) $\Delta n_l \neq \Delta n_c$.

The presence of the circular birefringence (Δn_c) makes the diffraction properties of Linear PGs distinct. When $\Delta n_l = \Delta n_c$, interesting diffraction properties result: again only three diffracted orders are present, but the first-order beams are linearly polarized and their efficiencies are strongly dependent on the extent of linear polarization present in the incident light. Analytic expressions can be derived using Jones calculus (a re-formulation of Ref. [14]) under the same assumptions as before:

$$\eta_0 = \cos^2(\pi \Delta n d/\lambda) \tag{A-1a}$$

$$\eta_{\pm 1} = \frac{1 \mp S_1'}{2} \sin^2(\pi \Delta n d/\lambda) \tag{A-1b}$$

where $\Delta n = \Delta n_l = \Delta n_c$ and $S_1' = S_1/S_0$ is the normalized Stokes parameter [3] of the input light. Since the polarization states of the ± 1-orders will be orthogonal and linearly polarized, the label 'Linear PG' applies.

The numerical and analytic diffraction spectra of linear PGs correspond well, and

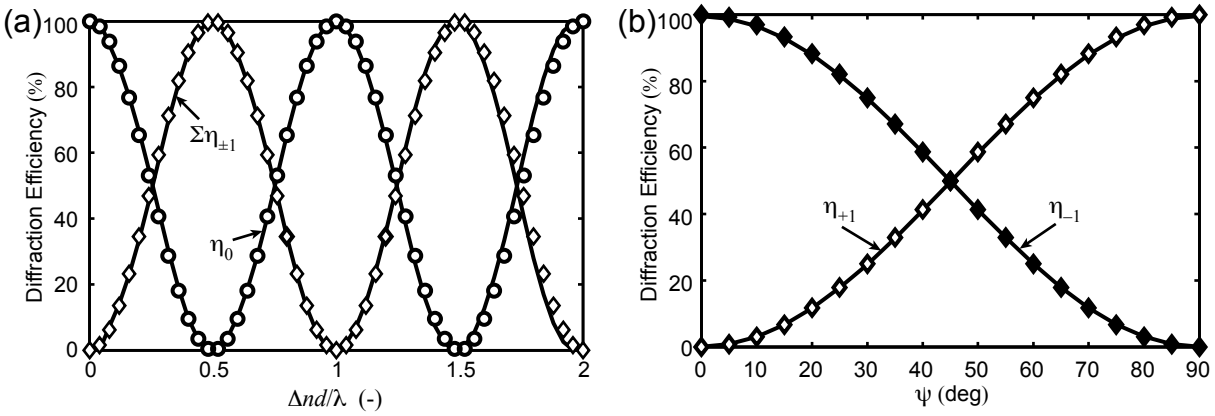

Figure A-1: Diffraction behavior of the Linear PG ($\Delta n_l = \Delta n_c = \Delta n = 0.2$) – (a) diffraction efficiency spectra and (b) polarization-sensitive first-order diffraction ($\Delta n d/\lambda = 1/2$) – numerically calculated (curves) and analytically estimated (◯, ◇, and ♦) using Eqs. (A-1). ($\Lambda = 20\lambda_0$, $\bar{n} = 1.6$)

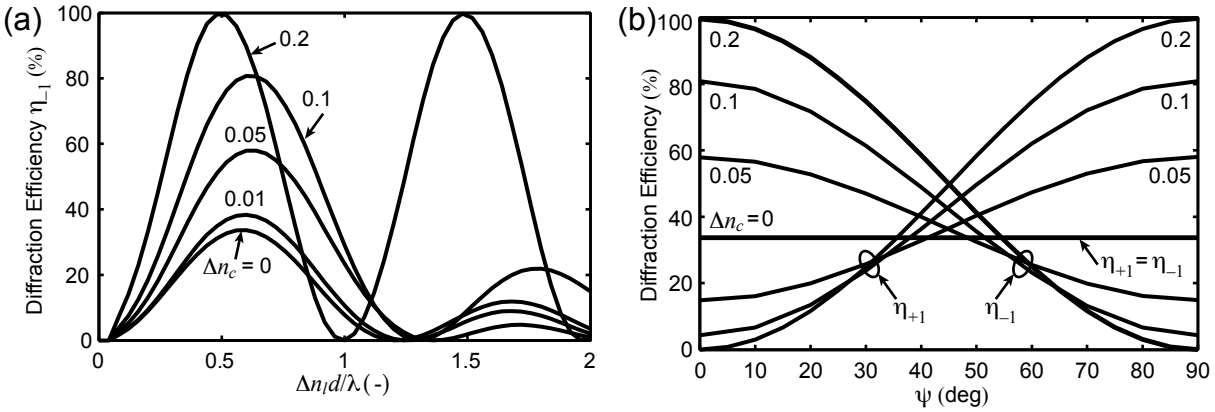

Figure A-2: Diffraction behavior of the Linear PG ($\Delta n_c \neq \Delta n_l$) for different values of circular birefringence Δn_c; (a) diffraction efficiency spectra and (b) polarization-sensitive first-order diffraction ($\Delta n_l d/\lambda = 1/2$). ($\Lambda = 20\lambda$, $d = 5\lambda$, $\bar{n} = 1.6$, and $\Delta n_l = 0.2$)

are shown in Fig. A-1(a), with $\Lambda = 20\lambda_0$, $d = 5\lambda_0$, $\bar{n} = 1.6$, and $\Delta n = 0.2$. As expected, only three diffraction orders are present, and the maximum first-order efficiency approaches 100% (actually, 99.73%). We also verified the polarization states of each diffraction order; the 0-order has the same polarization state as the input and the +1- and −1-orders have horizontal and vertical linear polarizations. We also examined the paraxial limit for the ideal diffraction of the linear PG, in the same manner as Section 3.1 and Fig. 3.4. The resulting behavior of the linear PG was the same as for the circular PG with respect to the grating regime and conditions for high diffraction efficiency, and the discussion in that Section (3.1) therefore also applies to Linear PGs. Note that we omit the figures for linear PGs because they appear identical.

The polarization sensitivity is shown in Fig. A-1(b) with respect to the orientation angle of the linearly polarized incident light ($S_1' = \cos(2\psi)$). We emphasize that the first-diffraction orders of Linear PGs respond to the orientation and extent of *linear polarization* in the incident light, while Circular PGs respond to the ellipticity and extent of *circular polarization*. The FDTD near-field maps of Linear PG with a monochromatic source appear identical to Fig. 3.3(a) and 3.3(b) for vertical linear incident polarization and right-handed circular incident polarization, respectively, and are therefore omitted.

Unlike the two previous PGs examined so far, Linear PGs with $\Delta n_c \neq \Delta n_l$ exhibit non-zero higher diffraction orders ($\eta_{|m|\geq 2} \neq 0$), similar to thin phase and amplitude gratings.

However, diffraction properties depend strongly [14] on the birefringence ratio $\Delta n_c/\Delta n_l$, and we can identify several interesting cases: for $\Delta n_c = 0$, light diffracted into odd orders of Linear PGs alter the incident light as if traveling through a $\lambda/2$-waveplate whose fast axis is at 45°; for $\Delta n_l = 0$, the odd orders act as a 90° polarization rotator. In both of these extremes, the diffraction efficiencies follow $\eta_m = J_m^2(\pi\Delta n d/\lambda)$.

Diffraction spectra for various $\Delta n_c/\Delta n_l$ ratios with linearly polarized input are shown in Fig. A-2(a), where $\Delta n_l = 0.2$, $\Lambda = 20\lambda_0$, $d = 5\lambda_0$, and $\bar{n} = 1.6$. When $\Delta n_c = 0$, it should be noted that only the magnitude (and not the orientation) of its linear birefringence is varying spatially, and as such, these Linear PGs show very similar diffraction behaviors to conventional phase gratings: multiple diffraction orders and no polarization sensitivity. However, as Δn_c increases, the maximum diffraction efficiency increases, and the first-orders become sensitive to the incident polarization (i.e. $\propto S_1'$). Both of these effects can be observed (Fig. A-2(b)) in the polarization contrast between the $m = \pm 1$ orders. It is important to note the local influence that a Linear PG imposes on incident light: the linear birefringence locally modifies the polarization orientation, while simultaneously the circular birefringence modifies its ellipticity — both in a spatially-dependent fashion. When the variation in the two types of anisotropy is balanced, Linear PGs manifest properties in response to linear incident polarizations which are analogous to Circular PGs illuminated with circular polarizations.

B. Jones Matrix Analysis of Achromatic PGs with Twist

The Jones matrix for a circular PG can be expressed as

$$\mathbf{T}_{PG} = \mathbf{R}(-\phi) \begin{bmatrix} e^{-i\Gamma} & 0 \\ 0 & e^{i\Gamma} \end{bmatrix} \mathbf{R}(\phi) \tag{B-2}$$

where $\Gamma = \pi\Delta nd/\lambda$ is the retardation, $\mathbf{R}$ is the rotation matrix, and $\phi = \phi(x) = \pi x/\Lambda$.

The circular PG with a twist can be approximated as a stack of multiple (N) thin circular PG layers with a small phase shift $\Delta\phi$ in the azimuth. The Jones matrix for this stratified grating structure can be written as

$$\begin{aligned} \mathbf{T}_{PG,twist} &= \prod_{m=1}^{N} \mathbf{R}\left(-m\Delta\phi\right) \mathbf{T}_{PG}(\Delta\Gamma) \mathbf{R}\left(m\Delta\phi\right) \\ &= \mathbf{R}\left(-\Phi\right) \left[\mathbf{T}_{PG}(\Delta\Gamma) \mathbf{R}\left(\Delta\phi\right)\right]^{N} \end{aligned} \tag{B-3}$$

where N is the number of circular PG layers, $\Delta\Gamma = \Gamma/N$ is the retardation of each layer, and $\Phi = N\Delta\phi$ is the total twist angle.

Now we introduce an auxiliary matrix $\mathbf{W} = \mathbf{T}_{PG}\mathbf{R}\left(\Delta\phi\right)$:

$$\mathbf{W} = \begin{bmatrix} W_{11} & W_{12} \\ W_{21} & W_{22} \end{bmatrix}, \tag{B-4}$$

where

$$W_{11} = \left(e^{-i\Delta\Gamma}\cos^2(\phi) + e^{i\Delta\Gamma}\sin^2(\phi)\right)\cos(\Delta\phi) - \left(e^{-i\Delta\Gamma} - e^{i\Delta\Gamma}\right)\sin(\phi)\cos(\phi)\sin(\Delta\phi) \tag{B-5a}$$

$$W_{12} = \left(e^{-i\Delta\Gamma}\cos^2(\phi) + e^{i\Delta\Gamma}\sin^2(\phi)\right)\sin(\Delta\phi) + \left(e^{-i\Delta\Gamma} - e^{i\Delta\Gamma}\right)\sin(\phi)\cos(\phi)\cos(\Delta\phi) \tag{B-5b}$$

$$W_{21} = -\left(e^{-i\Delta\Gamma}\sin^2(\phi) + e^{i\Delta\Gamma}\cos^2(\phi)\right)\sin(\Delta\phi) + \left(e^{-i\Delta\Gamma} - e^{i\Delta\Gamma}\right)\sin(\phi)\cos(\phi)\cos(\Delta\phi) \tag{B-5c}$$

$$W_{22} = \left(e^{-i\Delta\Gamma}\sin^2(\phi) + e^{i\Delta\Gamma}\cos^2(\phi)\right)\cos(\Delta\phi) + \left(e^{-i\Delta\Gamma} - e^{i\Delta\Gamma}\right)\sin(\phi)\cos(\phi)\sin(\Delta\phi) \tag{B-5d}$$

As $N \to \infty$, we can simplify W_{11} as follows

$$W_{11} \cong \cos(\Delta\phi) - i(\Delta\Gamma)\cos(2\phi) \tag{B-6a}$$

$$W_{12} \cong \Delta\phi - i(\Delta\Gamma)\sin(2\phi) \tag{B-6b}$$

$$W_{21} \cong -\Delta\phi - i(\Delta\Gamma)\sin(2\phi) \tag{B-6c}$$

$$W_{22} \cong \cos(\Delta\phi) + i(\Delta\Gamma)\cos(2\phi) \tag{B-6d}$$

Using Chebychev's identity, we can find a matrix $\mathbf{W'} = \mathbf{W}^N$ as follows

$$\begin{aligned} \mathbf{W'} &= \begin{bmatrix} W'_{11} & W'_{12} \\ W'_{21} & W'_{22} \end{bmatrix} \\ &= \begin{bmatrix} \frac{W_{11}\sin(NZ)-\sin(N-1)Z}{\sin(Z)} & \frac{W_{12}\sin(NZ)}{\sin(Z)} \\ \frac{W_{21}\sin(NZ)}{\sin(Z)} & \frac{W_{22}\sin(NZ)-\sin(N-1)Z}{\sin(Z)} \end{bmatrix} \end{aligned} \tag{B-7}$$

where W'_{ij} is the (i,j) component of $\mathbf{W'}$ and $Z = \cos^{-1}\left[\frac{1}{2}(W_{11} + W_{22})\right]$.

We can further simplify $\mathbf{W'}$ using approximations: as $N \to \infty$, $\sin(NZ)/NZ \cong \sin X/X$ and $\cos(NZ) \cong \cos X$, where $X = \sqrt{\phi^2 + \Gamma^2}$.

$$W'_{11} \cong \cos(X) - i\Gamma\cos(2\phi)\mathrm{sinc}(X) \tag{B-8a}$$

$$W'_{12} \cong [\Phi - i\Gamma\sin(2\phi)]\,\mathrm{sinc}(X) \tag{B-8b}$$

$$W'_{11} \cong -[\Phi + i\Gamma\sin(2\phi)]\,\mathrm{sinc}(X) \tag{B-8c}$$

$$W'_{11} \cong \cos(X) + i\Gamma\cos(2\phi)\mathrm{sinc}(X) \tag{B-8d}$$

where $\mathrm{sinc}(X) = [\sin(X)]/X$. Substituting $\mathbf{W'}$ into Eq. B-3, we finally get the Jones matrix for the PG with twist:

$$\mathbf{T}_{PG,twist} = \begin{bmatrix} T_{11} & T_{12} \\ T_{21} & T_{22} \end{bmatrix} = \mathbf{R}(-\Phi)\mathbf{W'} \tag{B-9}$$

where T_{ij} is the (i,j) component of $\mathbf{T}_{PG,twist}$:

$$T_{11} = \cos(\Phi)\cos(X) + \Phi\sin(\Phi)\mathrm{sinc}(X) - i\frac{\Gamma}{2}\mathrm{sinc}(X)e^{i\Phi}e^{i2\phi} - i\frac{\Gamma}{2}\mathrm{sinc}(X)e^{-i\Phi}e^{-i2\phi} \tag{B-10a}$$

$$T_{12} = -\sin(\Phi)\cos(X) + \Phi\cos(\Phi)\mathrm{sinc}(X) - \frac{\Gamma}{2}\mathrm{sinc}(X)e^{i\Phi}e^{i2\phi} + \frac{\Gamma}{2}\mathrm{sinc}(X)e^{-i\Phi}e^{-i2\phi} \tag{B-10b}$$

$$T_{21} = \sin(\Phi)\cos(X) - \Phi\cos(\Phi)\mathrm{sinc}(X) - \frac{\Gamma}{2}\mathrm{sinc}(X)e^{i\Phi}e^{i2\phi} + \frac{\Gamma}{2}\mathrm{sinc}(X)e^{-i\Phi}e^{-i2\phi} \tag{B-10c}$$

$$T_{22} = \cos(\Phi)\cos(X) + \Phi\sin(\Phi)\mathrm{sinc}(X) + i\frac{\Gamma}{2}\mathrm{sinc}(X)e^{i\Phi}e^{i2\phi} + i\frac{\Gamma}{2}\mathrm{sinc}(X)e^{-i\Phi}e^{-i2\phi} \tag{B-10d}$$

where $X = \sqrt{\Phi^2 + \Gamma^2}$. The Jones matrix $\mathbf{T}_{PG,twist}$ can be split into three matrices $\mathbf{T}_0$, $\mathbf{T}_{+1}$, and $\mathbf{T}_{-1}$:

$$\mathbf{T}_{PG,twist} = \mathbf{T}_0 + e^{i2\phi}\mathbf{T}_{+1} + e^{-i2\phi}\mathbf{T}_{-1} \tag{B-11}$$

where

$$\mathbf{T}_0 = \cos(X)\mathbf{R}(-\Phi) + \Phi\left[\frac{\sin(X)}{X}\right]\mathbf{R}(\pi/2 - \Phi) \tag{B-12a}$$

$$\mathbf{T}_{\pm 1} = e^{\pm i\Phi}\frac{\Gamma}{2}\mathrm{sinc}(X)\begin{bmatrix} -i & \mp 1 \\ \mp 1 & i \end{bmatrix} \tag{B-12b}$$

where $\mathbf{T}_m$ $(m = 0, \pm 1)$ is a transmission matrix corresponding to the m^{th}-order of diffraction. Still, only three diffracted orders exist and the first orders have orthogonal circular polarizations regardless the incident polarization. However, the polarization state of the 0-order generally becomes elliptical due to the effect of twist.

Let us consider a Jones vector $\mathbf{E}_{inc}$ with normalized intensity for the incoming electric field:

$$\mathbf{E}_{inc} = \begin{bmatrix} E_x \\ E_y \end{bmatrix} = \begin{bmatrix} \cos(\alpha) \\ e^{i\delta}\sin(\alpha) \end{bmatrix} \tag{B-13}$$

where α is an auxiliary angle $(0 \le \alpha \le \pi/2)$ for the polarization ellipse and $\delta = \delta_y - \delta_x$ is the phase difference between E_x and E_y. The outgoing electric field of each diffracted order can be obtained as follows

$$\mathbf{E}_m = \mathbf{T}_m\mathbf{E}_{inc} \quad (m = 0, \pm 1) \tag{B-14}$$

Still, only three diffracted orders exist and the first orders have orthogonal circular polarizations regardless the incident polarization. However, the polarization state of the 0-order generally becomes elliptical due to the effect of twist. The normalized intensity (or efficiency) in each diffracted order is given by:

$$\eta_m = \mathbf{E}_m^\dagger \mathbf{E}_m \quad (m = 0, \pm 1) \tag{B-15}$$

where $\mathbf{E}^\dagger$ denotes the Hermitian adjoint of $\mathbf{E}$. Diffraction efficiencies of a single circular PG with a twist can be expressed as

$$\eta_0 = \cos^2 X + \Phi^2 \left(\frac{\sin X}{X}\right)^2 \tag{B-16a}$$

$$\Sigma\eta_{\pm 1} = 1 - \eta_0 = \sin^2 X - \Phi^2 \left(\frac{\sin X}{X}\right)^2 \tag{B-16b}$$

where $X = \sqrt{\Phi^2 + \Gamma^2}$. We omit the individual expressions for the first order efficiencies ($\eta_{\pm 1}$) because of complexity. The efficiencies can be calculated by using computer softwares such as Matlab from Eqs. B-12 and B-15.

Now we consider the other circular PG with the same twist angle but opposite twist sense. Since we want to have two symmetric gratings, the anisotropy profile of two gratings should be in phase at the interface as shown in Fig. 3.10(b) and 3.10(c). The Jones matrix $\mathbf{T}'_{PG,twist}$ for the second circular PG can be obtained simply by replacing ϕ and Φ with $\phi + \Phi$ and $-\Phi$ from Eqs. B-12, respectively:

$$\mathbf{T}'_{PG,twist} = \mathbf{T}'_0 + e^{i2(\phi+\Phi)}\mathbf{T}'_{+1} + e^{-i2(\phi+\Phi)}\mathbf{T}'_{-1} \tag{B-17}$$

and

$$\mathbf{T}'_0 = \cos(X)\mathbf{R}(\Phi) - \Phi\left[\frac{\sin(X)}{X}\right]\mathbf{R}(\pi/2 + \Phi) \tag{B-18a}$$

$$\mathbf{T}'_{\pm 1} = e^{\mp i\Phi}\frac{\Gamma}{2}\mathrm{sinc}(X)\begin{bmatrix} -i & \mp 1 \\ \mp 1 & i \end{bmatrix} \tag{B-18b}$$

where $\mathbf{T}_m$ $(m = 0, \pm 1)$ is a transmission matrix corresponding to the m^{th}-order of diffraction. Since the handedness of twist does not affect the field distribution in the diffraction, the efficiencies are found same as those of the first circular PG in Eq. B-16.

The Jones matrix $\mathbf{T}_{APG}$ for the achromatic PG (APG) composed of two chiral circular PGs with opposite twist sense can be obtained simply by multiplying the Jones

matrices for each PG:

$$\mathbf{T}_{APG} = \mathbf{T}'_{PG,twist}\mathbf{T}_{PG,twist} \tag{B-19}$$

Again, $\mathbf{T}_{APG}$ can be split into three parts corresponding to each diffracted order:

$$\mathbf{T}_{APG} = \mathbf{T}_{0,APG} + e^{i2\phi}\mathbf{T}_{+1,APG} + e^{-i2\phi}\mathbf{T}_{-1,APG} \tag{B-20}$$

and

$$\mathbf{T}_{0,APG} = \left\{\cos^2(X) + \left(\Phi^2 - \Gamma^2\right)\mathrm{sinc}(X)^2\right\}\begin{bmatrix} 1 & 0 \\ 0 & 1 \end{bmatrix} \tag{B-21a}$$

$$\mathbf{T}_{\pm1,APG} = -ie^{\pm i\Phi}\Gamma\mathrm{sinc}(X)\begin{bmatrix} T^{(\pm)}_{11,APG} & T^{(\pm)}_{12,APG} \\ T^{(\pm)}_{21,APG} & T^{(\pm)}_{22,APG} \end{bmatrix} \tag{B-21b}$$

where

$$T^{(\pm)}_{11,APG} = \cos(\Phi)\cos(X) + \Phi\sin(\Phi)\mathrm{sinc}(X) \mp i\left[\sin(\Phi)\cos(X) - \Phi\cos(\Phi)\mathrm{sinc}(X)\right] \tag{B-22a}$$

$$T^{(\pm)}_{12,APG} = -\sin(\Phi)\cos(X) + \Phi\cos(\Phi)\mathrm{sinc}(X) \mp i\left[\cos(\Phi)\cos(X) + \Phi\sin(\Phi)\mathrm{sinc}(X)\right] \tag{B-22b}$$

$$T^{(\pm)}_{21,APG} = -\sin(\Phi)\cos(X) + \Phi\cos(\Phi)\mathrm{sinc}(X) \mp i\left[\cos(\Phi)\cos(X) + \Phi\sin(\Phi)\mathrm{sinc}(X)\right] \tag{B-22c}$$

$$T^{(\pm)}_{22,APG} = -\cos(\Phi)\cos(X) - \Phi\sin(\Phi)\mathrm{sinc}(X) \pm i\left[\sin(\Phi)\cos(X) - \Phi\cos(\Phi)\mathrm{sinc}(X)\right] \tag{B-22d}$$

Interestingly, the transmission matrix for the 0-order diffraction is reduced to a identity matrix with a magnitude depending on the twist angle (Φ) and retardation (Γ). We can interpret that the polarization effect of twist is canceled out by two chiral layers with opposite twist sense. Therefore, the polarization of the 0-order remains same as the incident polarization.

Similar to Eqs. B-16, the final expressions for diffraction efficiencies of the achromatic PG can be obtained as follows

$$\eta_0 = \left[\cos^2 X + \left(\Phi^2 - \Gamma^2\right)\left(\frac{\sin X}{X}\right)^2\right]^2 \tag{B-23a}$$

$$\eta_{\pm1} = A^2\left(\frac{1 \mp S'_3}{2}\right)\left(\cos^2 X + \Phi^2\mathrm{sinc}^2 X\right) \tag{B-23b}$$

where $\Gamma = \pi\Delta nd/\lambda$ and $X = \sqrt{\Phi^2 + \Gamma^2}$. We omit the individual expressions for the first order efficiencies ($\eta_{\pm 1}$) because of complexity. Again, the efficiencies can be calculated by using computer softwares such as Matlab from Eqs. B-22 and B-23.

C. Jones Matrix Analysis of Super-Achromatic PGs

Again, the Jones matrix for a circular PG can be expressed as

$$\mathbf{T}_{PG} = \mathbf{R}(-\phi) \begin{bmatrix} e^{-j\Gamma} & 0 \\ 0 & e^{j\Gamma} \end{bmatrix} \mathbf{R}(\phi) \tag{C-24}$$

where $\Gamma = \pi\Delta nd/\lambda$ is the retardation, $\mathbf{R}$ is the rotation matrix, and $\phi = \phi(x) = \pi x/\Lambda$. The above equation can be rewritten as follows

$$\mathbf{T} = \cos(\Gamma) - j\sin(\Gamma) \begin{bmatrix} -\cos(2\phi) & \sin(2\phi) \\ \sin(2\phi) & \cos(2\phi) \end{bmatrix} \tag{C-25}$$

Now consider a stack of three PGs of which grating directions are all parallel but shifted by an angle Φ for the middle PG with respect to the others. The transfer matrices for each grating are given by

$$\mathbf{T}_{1,3} = \cos(\Gamma) - j\sin(\Gamma) \begin{bmatrix} -\cos(2\phi) & \sin(2\phi) \\ \sin(2\phi) & \cos(2\phi) \end{bmatrix} = \cos(\Gamma) - j\sin(\Gamma)\mathbf{U} \tag{C-26}$$

$$\mathbf{T}_{2} = \cos(\Gamma) - j\sin(\Gamma) \begin{bmatrix} -\cos(2\phi') & \sin(2\phi') \\ \sin(2\phi') & \cos(2\phi') \end{bmatrix} = \cos(\Gamma) - j\sin(\Gamma)\mathbf{U}' \tag{C-27}$$

where $\phi' = \phi + \Phi$ and $\mathbf{U}$ and $\mathbf{U}'$ are auxiliary matrices for the first and last PGs and the second PG, respectively. The Jones matrix for all three PGs can be written as follows

$$\mathbf{T} = \mathbf{T}_3 \times \mathbf{T}_2 \times \mathbf{T}_1 \tag{C-28}$$

After significant mathematical steps (similar to Appendix B), we get the diffraction efficiencies as follows

$$\eta_0 = \{\cos^3(\Gamma) - [1 + 2\cos(2\Phi)]\cos(\Gamma)\sin^2(\Gamma)\}^2 \tag{C-29}$$

$$\eta_{\pm 1} = \frac{1 \mp S_3'}{2}\sin^2(\Gamma)\left\{1 - 4[1 + \cos(2\Phi)]\cos(2\Phi)\cos^2(\Gamma) + 4[1 + \cos(2\Phi)]^2\cos^4(\Gamma)\right\} \tag{C-30}$$

D. Direction Cosine Description of Two Rotating Gratings

Diffraction behaviors of gratings can be conveniently described in the direction cosine space. Especially, the conical diffraction is traced by linear relationships between two projected dimensions (α, β). Here we derive the governing equations for the exiting diffraction angle from two rotating inline PGs in the direction cosine space.

An arbitrary vector in the Cartesian coordinate space can be expressed in the direction cosine space as follows

$$\vec{A} = A_x\vec{i} + A_y\vec{j} + A_x\vec{k} \tag{D-31a}$$

$$= A(\alpha\vec{i} + \beta\vec{j} + \gamma\vec{k}) \tag{D-31b}$$

where $A = |\vec{A}|$ is the magnitude of the vector and α, β, and γ are projections of the direction vector ($\vec{u}_A = \vec{A}/A$) onto x-, y-, and z-axes and can be expressed by the angles between the direction vector and $\vec{i}$, $\vec{j}$, and $\vec{k}$ as follows

$$\alpha = A_x/A = cos(\theta_x) \tag{D-32a}$$

$$\beta = A_y/A = cos(\theta_y) \tag{D-32b}$$

$$\gamma = A_z/A = cos(\theta_z) \tag{D-32c}$$

It is convenient to express α, β, and γ with the polar and azimuth angles (θ, ϕ) in the Spherical coordination space because these angles are useful to describe angular behaviors.

$$\alpha = \sin(\theta)\cos(\phi) \tag{D-33a}$$

$$\beta = \sin(\theta)\sin(\phi) \tag{D-33b}$$

$$\gamma = \cos(\theta) \tag{D-33c}$$

It is also noted that $\alpha^2 + \beta^2 + \gamma^2 = 1$ and γ can be always found from α and β by $\gamma^2 = 1 - (\alpha^2 + \beta^2)$. From this relationship, we can treat any problem in the α-β space and then find the complete solution.

The diffraction equation at an arbitrarily oblique angle (θ_i, ϕ_i) can be expressed

in the direction cosine space as follows

$$\alpha_m = -\alpha_i + m\left[\frac{\lambda\cos(\psi)}{\Lambda}\right] = -\alpha_i + m\Delta\alpha \tag{D-34a}$$

$$\beta_m = -\beta_i + m\left[\frac{\lambda\sin(\psi)}{\Lambda}\right] = -\beta_i + m\Delta\beta \tag{D-34b}$$

$$\gamma_m = \sqrt{1-\alpha_m^2-\beta_m^2} \tag{D-34c}$$

where the subscript m is the order of diffraction, $\Delta\alpha = (\lambda/\Lambda)\cos(\psi)$ and $\Delta\beta = (\lambda/\Lambda)\sin(\psi)$, ψ is the angle between the grating vector ($\vec{g}$) and the α- or x-axis, and α_i, β_i, and γ_i are given by

$$\alpha_i = \sin(\theta_i)\cos(\phi_i) \tag{D-35a}$$

$$\beta_i = \sin(\theta_i)\sin(\phi_i) \tag{D-35b}$$

$$\gamma_i = \cos(\theta_i) \tag{D-35c}$$

Now, we can consider a special case of two circular polarization gratings that are aligned inline but rotating around the propagation axis (the z-axis). The orientation angles of each grating from the x-axis are ϕ_1 and ϕ_2, respectively. The offsets of nearest diffracted orders are give by $\Delta\alpha_{1,2} = (\lambda/\Lambda)cos(\phi_{1,2})$ and $\Delta\beta_{1,2} = (\lambda/\Lambda)sin(\phi_{1,2})$. The direction of the outgoing beam from the first PG can be written as follows

$$\alpha^{(1)} = -\alpha_i + \Delta\alpha_1 \tag{D-36a}$$

$$\beta^{(1)} = -\beta_i + \Delta\beta_1 \tag{D-36b}$$

$$\gamma^{(1)} = \sqrt{1-\left(\alpha^{(1)}\right)^2-\left(\beta^{(1)}\right)^2} \tag{D-36c}$$

We assume that the incident polarization is left-handed circular, which leads to only +1-order in the diffraction of the first PG with right-handed circular polarization. We also assume that the second PG is identical to the first PG so that only -1-order can exist in the diffraction from the second PG. The direction of the outgoing beam from the second PG can be written as follows

$$\alpha^{(2)} = -\alpha^{(1)} - \Delta\alpha_2 \tag{D-37a}$$

$$\beta^{(2)} = -\beta^{(1)} - \Delta\beta_2 \tag{D-37b}$$

$$\gamma^{(2)} = \sqrt{1-\left(\alpha^{(2)}\right)^2-\left(\beta^{(2)}\right)^2} \tag{D-37c}$$

For normal incidence, we can simplify Eq. D-37:

$$\alpha^{(2)} = -(\Delta\alpha_1 + \Delta\alpha_2) = -(\lambda/\Lambda)\left[\cos(\phi_1) + \cos(\phi_2)\right] \tag{D-38a}$$

$$\beta^{(2)} = -(\Delta\beta_1 + \Delta\beta_2) = -(\lambda/\Lambda)\left[\sin(\phi_1) + \sin(\phi_2)\right] \tag{D-38b}$$

$$\gamma^{(2)} = \sqrt{1 - \left(\alpha^{(2)}\right)^2 - \left(\beta^{(2)}\right)^2} \tag{D-38c}$$

Finally, we get the angles for the emerging beam as follows

$$\phi = \tan^{-1}(\beta/\alpha) \tag{D-39a}$$

$$\theta = \cos^{-1}(\gamma) \tag{D-39b}$$